

# Synthesis and Characterization of Molecular Precursors for IV-VI Materials

*By*

**ADISH TYAGI**

**CHEM01201304003**

**Bhabha Atomic Research Centre, Mumbai**

*A thesis submitted to the  
Board of Studies in Chemical Sciences  
In partial fulfillment of requirements  
for the Degree of*

**DOCTOR OF PHILOSOPHY**

*of*

**HOMI BHABHA NATIONAL INSTITUTE**



**December, 2018**

# Homi Bhabha National Institute

## Recommendations of the Viva Voce Committee

As members of the Viva Voce Committee, we certify that we have read the dissertation prepared by Adish Tyagi entitled "Synthesis and characterization of molecular precursors for IV-VI materials" and recommend that it may be accepted as fulfilling the thesis requirement for the award of Degree of Doctor of Philosophy.

Chairman - Prof. K. I. Priyadarsini *K. Indira Priyadarini* Date: 24.5.19

Guide / Convener - Dr. G. Kedarnath *G. Kedarnath* Date: 24/5/19

Examiner - Prof. H. B. Singh *H. B. Singh* Date: 24/05/2019

Member 1- Prof. A. K. Tyagi *A. K. Tyagi* Date: 24/05/2019

Member 2- Prof. S. Kannan *S. Kannan* Date: 24/5/19

Member 3- Prof. S. K. Ghosh *S. K. Ghosh* Date: 24/05/2019.

Final approval and acceptance of this thesis is contingent upon the candidate's submission of the final copies of the thesis to HBNI.

I/We hereby certify that I/we have read this thesis prepared under my/our direction and recommend that it may be accepted as fulfilling the thesis requirement.

Date: 24/5/19

Place: Mumbai

*G. Kedarnath*  
24/5/19  
Guide  
(G. Kedarnath)

## **STATEMENT BY AUTHOR**

This dissertation has been submitted in partial fulfillment of requirements for an advanced degree at Homi Bhabha National Institute (HBNI) and is deposited in the Library to be made available to borrowers under rules of the HBNI.

Brief quotations from this dissertation are allowable without special permission, provided that accurate acknowledgement of source is made. Requests for permission for extended quotation from or reproduction of this manuscript in whole or in part may be granted by the Competent Authority of HBNI when in his or her judgment the proposed use of the material is in the interests of scholarship. In all other instances, however, permission must be obtained from the author.

**(Adish Tyagi)**

## **DECLARATION**

I, hereby declare that the investigation presented in the thesis has been carried out by me. The work is original and has not been submitted earlier as a whole or in part for a degree / diploma at this or any other Institution / University.

**(Adish Tyagi)**



## List of Publications arising from the thesis

### Journal

1. Diorganotin(IV) 2-pyridyl and 2-pyrimidyl thiolates: Synthesis, structures and their utility as molecular precursors for the preparation of tin sulfide nano-sheets. Adish Tyagi, G. Kedarnath, A. Wadawale, V. K. Jain, M. Kumar B. Vishwanadh, *RSC Adv.*, **2015**, 5, 62882-62890.
2. Diorganotin(IV) 4,6-dimethyl-2-pyrimidyl selenolates: synthesis, structures and their utility as molecular precursors for the preparation of SnSe<sub>2</sub> nano-sheets and thin films. Adish Tyagi, G. Kedarnath, A. Wadawale, A. Y. Shah, V. K. Jain, *RSC Adv.*, **2016**, 6, 8367-8376.
3. Synthesis, characterization and photovoltaic properties of phase pure Cu<sub>2</sub>SnSe<sub>3</sub> nanostructures using molecular precursors. Adish Tyagi, A. Y. Shah, G. Kedarnath, A. Wadawale, V. Singh, D. Tyagi, C. A. Betty, C. Lal, V. K. Jain, *J. Mater. Sci. Mater El.*, **2018**, 29, 8937.
4. Facile one-pot synthesis of tin selenide nanostructures using diorganotin bis(5-methyl-2-pyridylselenolates) Adish Tyagi, G. Karmakar, A. Wadawale, A. Y. Shah, G. Kedarnath, V. Singh, V. K. Jain, *J. Organomet. Chem.*, **2018**, 873, 15-21.
5. Accessing copper-tin-sulfide nanostructures from diorganotin(IV) and copper(I) 2-pyrazinyl thiolates Adish Tyagi, G. K. Kole, A. Y. Shah, A. Wadawale, A.P. Srivastava, M. Kumar, G. Kedarnath, V. K. Jain, *J. Organomet. Chem.*, **2019**, 887, 24-31.

### Communicated/ Under preparation

1. Diorganotin thiolates for SnS thin films

## Conferences

1. Organotin(IV) 4,6-dimethyl-2-pyrimidyl selenolates: Versatile precursors for tin selenide,  
Adish Tyagi, G. Kedarnath, A. Wadawale A. Shah and V. K. Jain, 5<sup>th</sup> DAE-BRNS Interdisciplinary Symposium on Materials Chemistry, Bhabha Atomic Research Centre, Mumbai, December, 2014.
2. Tin chalcogenolates: Precursors for tin chalcogenide nanomaterials.  
Adish Tyagi, G. Kedarnath, A. Wadawale A. Shah and V. K. Jain, 6<sup>th</sup> DAE-BRNS Interdisciplinary Symposium on Materials Chemistry, Bhabha Atomic Research Centre, Mumbai, December 2016.
3. Cu<sub>2</sub>SnSe<sub>3</sub> nanocrystals from molecular precursors,  
Adish Tyagi, A.Y. Shah, V. Singh, A. Wadawale, G. Kedarnath, V.K. Jain, SSCB 2017, Bhabha Atomic Research Centre, Mumbai, November 2017.

**(Adish Tyagi)**

**DEDICATED**

***To My Family...***

## ACKNOWLEDGEMENTS

This dissertation would not have been possible without the help and motivation from numerous people including my family, friends and well-wishers who contributed in many ways to the successful completion of this thesis.

First and foremost my sincere gratitude and heartfelt regard goes to my *beloved parents* for their unconditional love and unwavering support. They have been the driving force and inspiration in all pursuits of my life.

When it comes to scientific field, first and foremost, I would like to express my sincere thanks to my mentor ***Dr. V. K. Jain*** who has introduced me to the subject of “Organometallic Chemistry”. He has constantly encouraged me to remain focused to achieve my goal. I would like to express my sincere gratitude to my guide ***Dr. G. Kedarnath*** for his support, patience and encouragement. His knowledge and experience helped me a lot during the course of my Ph.D. work. Besides my guide, I would like to thank my doctoral committee members; ***Dr. K. I. Priyadarsini, Dr. A. K. Tyagi, Dr. S. Kannan and Dr. S. K. Ghosh*** for their time, encouragement and critical evaluation during the course of my Ph.D.

My sincere thanks to my friends and lab mates: ***Dr. Siddhartha Kolay, Shri Gourab Karmakar and Shri Pravin Mane*** for all their precious help, scientific contribution, valuable discussions, and cooperation. Special thanks to ***Shri Amey. P. Wadawale*** for solving crystal structures and for deposition of thin films, ***Dr. Bal Govind Vats*** for p-XRD, ***Dr. Alpa Y. Shah*** for PEC measurements, ***Shri Kamal. P. Chaudhari, Shri Manoj. K. Pal and Dr. Nisha Kushwah*** for recording NMR spectra, ***Shri Suresh M. Chopade*** for the elemental analysis, ***Shri Vishal Singh and Dr. Amit Srivastava*** for SEM and TEM studies, ***Dr. K. Bhattacharya*** for DRS measurements.

I am indebted to my seniors ***Drs. Liladhar Kumbhare, Sandip Dey and Prasad Phadnis*** who always supported me and kept me on my theoretical toes. I would like to thank

all academic and administrative staff of the chemistry division for everything they have done for me.

I am grateful to all my *teachers*; I would not have been here without their guidance, blessings and support.

I am fortunate to have lovely friends *Vikrant* and *Niti* for their support, love and motivation. I am grateful to my childhood friends *Rahul Rana* and *Rahul Prabhakar* who are constant source of support, laughter and joy. Special thanks to my precious friends *Parveen, Govind, Rakeshji, Deepak, Abhishek, Vijay, Ashwini, Amar* for their support and all good times we had together.

Words cannot express my gratitude for the support and care I have received from my brother *Shri Anmol Tyagi*. I would like to acknowledge the selfless love and respect I received from my niece *Anika Tyagi*. I would like to thank my wife *Shradha Tyagi* for her strong support, love and patience. Without her encouragement and understanding, I would not have been able to make it.

This list of incredible people who fill my life is endless and I regret not being able to explicitly name everybody.

# CONTENTS

	Page No.
<b>Synopsis</b>	i
<b>List of Figures</b>	xv
<b>List of Tables</b>	xxviii
<b>CHAPTER 1: General Introduction</b>	1
1.1 Introduction and Historical Background of Nanomaterials	1
1.2 Classification of Nanomaterials	2
1.3 Semiconductors	3
1.4 Band structure	4
1.5 Intrinsic and Extrinsic Semiconductors	5
1.6 Direct and Indirect Band gap Semiconductors	8
1.7 Semiconductor nanomaterials	9
1.8 General properties of tin and tin based chalcogenides	13
1.8.1 General properties of tin	13
1.8.2 General properties of tin based chalcogenides	14
1.9 Synthetic methodologies for tin based chalcogenides	23
1.9.1 Precursors for tin sulfide	24
1.9.2 Precursors for tin selenide	29
1.10 Scope of the Present Work	34
<b>CHAPTER 2: Characterization Techniques</b>	36
2.1 Materials and Methods	36
2.2 Experimental techniques	37
2.2.1 Analysis	37

2.2.2 Crystallography	37
2.2.3 Nuclear magnetic resonance (NMR) Spectroscopy	44
2.2.4 Powder X-ray diffraction	44
2.2.5 Scanning electron microscope (SEM)	46
2.2.6 Transmission electron microscope (TEM)	46
2.2.7 Selected area electron diffraction (SAED)	47
2.2.8 Photoelectrochemical Cell (PEC)	48
2.2.9 Other techniques	50
<b>CHAPTER 3: Preparation of tin sulfide nanostructures using organotin pyridyl and pyrimidyl thiolates</b>	<b>52</b>
3.1 Introduction	53
3.2 Experimental	54
3.2.1 General consideration	54
3.2.2 Synthesis of [HSpymMe <sub>2</sub> ]	54
3.2.3 Synthesis of [Me <sub>2</sub> Sn(2-Spy) <sub>2</sub> ]	54
3.2.4 Synthesis of [Et <sub>2</sub> Sn(2-Spy) <sub>2</sub> ]	55
3.2.5 Synthesis of [ <sup>t</sup> Bu <sub>2</sub> Sn(2-Spy) <sub>2</sub> ]	55
3.2.6 Synthesis of [Et <sub>2</sub> SnCl(2-Spy) <sub>2</sub> ]	56
3.2.7 Synthesis of [ <sup>t</sup> Bu <sub>2</sub> SnCl(2-Spy) <sub>2</sub> ]	56
3.2.8 Synthesis of [Me <sub>2</sub> SnCl(2-SpymMe <sub>2</sub> )]	57
3.2.9 Synthesis of [Et <sub>2</sub> SnCl(2-SpymMe <sub>2</sub> )]	57
3.2.10 Synthesis of [ <sup>t</sup> Bu <sub>2</sub> SnCl(2-SpymMe <sub>2</sub> )]	58
3.2.11 Preparation of tin sulfide nanostructures	58
3.2.12 Preparation of thin films by Aerosol Assisted Chemical Vapor Deposition (AACVD)	58

3.2.13 Crystallography	59
3.3 Results and discussion	59
3.3.1 Synthesis and spectroscopy	59
3.3.2 X-ray Crystallography	61
3.3.3 Thermal studies	65
3.3.4 Preparation and characterization of tin sulfide nanostructures	68
3.3.5 Surface properties of the nanostructures	73
3.3.6 Deposition and characterization of tin sulfide thin films	75
3.3.8 Optical properties of SnS nanostructures	76
<b>CHAPTER 4: Preparation of tin selenide nanostructure using organotin pyridyl and pyrimidyl selenolates</b>	78
4.1 Introduction	79
4.2 Experimental	80
4.2.1 General consideration	80
4.2.2 Synthesis of bis(5-methyl-2-pyridyl)diselenide [(2-Sepy(5-Me)) <sub>2</sub> ]	80
4.2.3 Synthesis of bis(4,6-dimethyl-2-pyrimidyl)diselenide [(2-SepymMe <sub>2</sub> ) <sub>2</sub> ]	81
4.2.4 Synthesis of [Me <sub>2</sub> Sn(2-Sepym(5-Me)) <sub>2</sub> ]	81
4.2.5 Synthesis of [Et <sub>2</sub> Sn(2-Sepym(5-Me)) <sub>2</sub> ]	82
4.2.6 Synthesis of [ <sup>t</sup> Bu <sub>2</sub> Sn(2-Sepym(5-Me)) <sub>2</sub> ]	82
4.2.7 Synthesis of [Me <sub>2</sub> Sn(2-SepymMe <sub>2</sub> ) <sub>2</sub> ]	83
4.2.8 Synthesis of [Et <sub>2</sub> Sn(2-SepymMe <sub>2</sub> ) <sub>2</sub> ]	83
4.2.9 Synthesis of [ <sup>n</sup> Bu <sub>2</sub> Sn(2-SepymMe <sub>2</sub> ) <sub>2</sub> ]	84
4.2.10 Synthesis of [ <sup>t</sup> Bu <sub>2</sub> Sn(2-SepymMe <sub>2</sub> ) <sub>2</sub> ]	84
4.2.11 Synthesis of [Me <sub>2</sub> SnCl(2-SepymMe <sub>2</sub> ) <sub>2</sub> ]	84



4.2.12 Synthesis of [ $^{119}\text{Sn}$ ] $\text{Bu}_2\text{SnCl}(\text{2-SepymMe}_2)$	85
4.2.13 Synthesis of [ $^{119}\text{Sn}$ ] $\text{Bu}_2\text{SnCl}(\text{2-SepymMe}_2)$	85
4.2.14 Preparation of tin selenide nanostructures	86
4.2.15 Preparation of thin films by Aerosol Assisted Chemical Vapor Deposition (AACVD)	87
4.2.16 Crystallography	87
4.3 Results and Discussion	87
4.3.1 Synthesis and Spectroscopy	87
4.3.2 X-ray Crystallography	92
4.3.3 Thermogravimetric Studies	101
4.3.4 Preparation and characterization of tin selenide nanostructures	102
4.3.5 Preparation and characterization of tin selenide thin films	115
4.3.6 Optical properties	116
4.3.7 Photo response measurements of Si/SnSe <sub>2</sub> based PEC	120
<b>CHAPTER 5: Accessing ternary tin chalcogenide nanostructures from molecular precursors</b>	122
5.1 Introduction	123
5.2 Experimental	125
5.2.1 General Consideration	125
5.2.2 Synthesis of 2-pyrazinylthiol (2-HSpyz)	125
5.2.3 Bis(3-methyl-2-pyridyl)diselenide [(2-Sepy(3-Me)) <sub>2</sub> ]	125
5.2.4 Synthesis of [ $^{119}\text{Sn}$ ] $\text{Bu}_2\text{Sn}(\text{Spyz})_2$	126
5.2.5 Synthesis of $[\text{Cu}(\text{Spyz})(\text{PPh}_3)_2]$	126
5.2.6 Synthesis of $[\text{Me}_2\text{Sn}(\text{2-Sepy}(\text{3-Me}))_2]$	127
5.2.7 Synthesis of $[\text{Cu}(\text{Sepy}(\text{3-Me}))_4]$	127

5.2.8 Preparation of CTS, SnS and Cu <sub>1.8</sub> S nanostructures	128
5.2.9 Preparation of Cu <sub>2</sub> SnSe <sub>3</sub> , SnSe <sub>2</sub> and Cu <sub>2</sub> Se nanostructures	129
5.2.10 Crystallography	130
5.3 Results and discussion	130
5.3.1 Synthesis, Spectroscopy and X-ray crystallography	130
5.3.2 Thermogravimetric analyses	138
5.3.3 Preparation and characterization of the nanostructures	139
5.3.4 Optical properties	161
5.3.5 Photoelectrochemical studies	163
<b>CHAPTER 6: Conclusion and Future Work</b>	167
<b>REFERENCES</b>	174

# Synopsis

Discovery of 2D carbon allotrope, graphene, has ignited intensive research in a wide range of layered material [1-2]. However, the absence of band gap has prevented the graphene to be utilized in nanoelectronics. This diverted the focus to other layered materials which possess band gap, in particular metal chalcogenides. Tuning of band gap enables the layered metal chalcogenides to display a wide range of unique chemical and physical properties which have been exploited for diverse applications such as optoelectronic, photovoltaic devices, transistors, lithium ion battery, hydrogen generation by photocatalytic splitting of water, etc. [3-4].

Beyond transition metal chalcogenides, various main group metal chalcogenides (III–VI (e. g. GaS, GaSe, In<sub>2</sub>Se<sub>3</sub>); IV–VI (e. g. GeS, SnS, SnSe, SnSe<sub>2</sub>, PbS, PbSe, etc.) and V–VI (e. g. Bi<sub>2</sub>Se<sub>3</sub>, Bi<sub>2</sub>Te<sub>3</sub>, etc.)) also exhibit layered structure in their nano regime. The interest in the narrow band gap IV–VI layered semiconductor nanostructures is increasing due to their promising optoelectronic properties which have relevance in photovoltaic [5], photodetector [6] and thermoelectric devices [7]. Among them lead chalcogenide nanocrystals (PbE; E = S, Se, Te) have been extensively investigated and were the first of the IV–VI class of semiconductor nanocrystals to gain interest as practical photovoltaic (PV) and thermoelectric materials. In spite of promising results obtained from lead chalcogenide-based optoelectronic devices, the toxicity of lead and the potential of lead exposure are considered a significant threat to public health [8].

This led to the emergence of tin based chalcogenides materials which has a potential to promote their value in sustainable electronic and photonic systems due to their earth abundant, low cost and environmentally benign characteristics [9]. Tin chalcogenides exist in several crystal phases such as hexagonal, monoclinic and orthorhombic phases depending

upon the oxidation state of the tin.  $\text{SnE}$  ( $\text{E} = \text{S}, \text{Se}$ ) crystallizes into orthorhombic phase while hexagonal and monoclinic phases are denoted by  $\text{SnE}_2$ . The crystal structure of  $\text{SnE}_2$  is similar to that of layered molybdenum chalcogenides, a representative and most extensively investigated layered inorganic material [10].

Besides binary tin chalcogenides, there is another interesting family of tin, which is a ternary system. Compared to binary system, ternary materials not only exhibit outstanding physical, chemical and electronic properties but also provide some distinct advantages that binary systems do not possess and one such important advantage being that, the ternary systems have greater number of degrees of freedom for tailoring their band gap *via* stoichiometric variation.

Various synthetic approaches have been adopted for the preparation of these materials. Among them the solution based methods which include solvothermal technique, hot injection method, polyol or aqueous solution methods are the most popular one. However these methods employed toxic and sensitive reagents for the preparation of nanomaterials. Of late metallo-organic precursor route has emerged as a versatile technique for the synthesis of metal chalcogenide nanoparticles and deposition of thin films which offer key advantages over other routes in terms of phase purity and better stoichiometry. However, this route has met with a little success in the case of tin chalcogenides and related ternary materials possibly due to limited exploration of tin complexes with chalcogen ligands as molecular precursors. Moreover there are some issues associated with the reported precursors such as i) use of hazardous chemicals during the preparation (phosphine) or utilization ( $\text{H}_2\text{S}$ ) of precursors [11], ii) improper stoichiometry and incorporation of impurities (elemental/ phase) in the final product [12], iii) poor solubility of precursors due to the formation of non-crystalline polymers stabilized through bridging chalcogenolate ligands.

Thus, the quest for novel precursors for the preparation of binary and ternary tin chalcogenides of desired phase, composition, shape and band gap has become necessary. In view of the above, it was considered worthwhile to design and synthesize organotin complexes with substituted and non-substituted internally functionalized chalcogen ligands which can serve as molecular precursors for binary and ternary tin chalcogenide materials. Internally functionalized chalcogenolate ligands viz. 2-pyridyl and 2-pyrimidyl chalcogenolates, assist in suppressing oligomerization of metal chalcogenolates, *via* chelation as observed by Sharma *et al.*[13]. The facile cleavage of C-E bond in these complexes makes them potential precursor candidates for the preparation of binary and ternary tin chalcogenide nanostructures and thin films.

Accordingly, various tin complexes with substituted and non-substituted 2-pyridyl, 2-pyrimidyl and 2-pyrazinyl chalcogenolates ligands were synthesized and characterized using different characterization techniques e.g. elemental analysis, multi-nuclear NMR, thermogravimetry, single crystal X-ray diffraction. These complexes were utilized for the preparation of binary and ternary tin chalcogenides nanostructures and thin films, and characterized by p-XRD, electron microscopic techniques (SEM, TEM, EDS, SAED), solid state diffuse reflectance spectroscopy (DRS). Phase, composition and band gap tunability of the nanostructures have been demonstrated by varying the temperature, growth duration and choice of reaction solvent. The details of the above work are compiled in five chapters as follows:

## **Chapter 1: Introduction**

This chapter of the thesis gives brief introduction on semiconductor nanomaterials with special emphasis on binary and ternary tin chalcogenide nanomaterials. Basic chemistry and structure of tin monochalcogenides, tin dichalcogenides and ternary copper tin

chalcogenide system with brief account of important properties leading to their utility in the field of photovoltaics and thermoelectric devices have been discussed. The chapter also provides a brief discussion on various synthetic strategies including precursor route and advantage of latter over the other methods. Different precursors used for the preparation of tin chalcogenide nanomaterials are discussed in the present chapter. A brief note on the objective and motivation of the present work has also been included in this chapter.

## **Chapter 2: Characterization techniques**

This chapter describes general materials and chemicals used during the present investigation followed by a brief discussion on experimental tools and techniques such as elemental analysis, hetero-nuclear NMR spectroscopy, thermogravimetry (TGA), powder X-ray diffraction (p-XRD), single crystal X-ray (SCXRD), Scanning electron microscopy (SEM), Energy dispersive X-ray analysis (EDS), Transmission electron microscopy (TEM) and Selected area electron diffraction (SAED) employed during the course of present study.

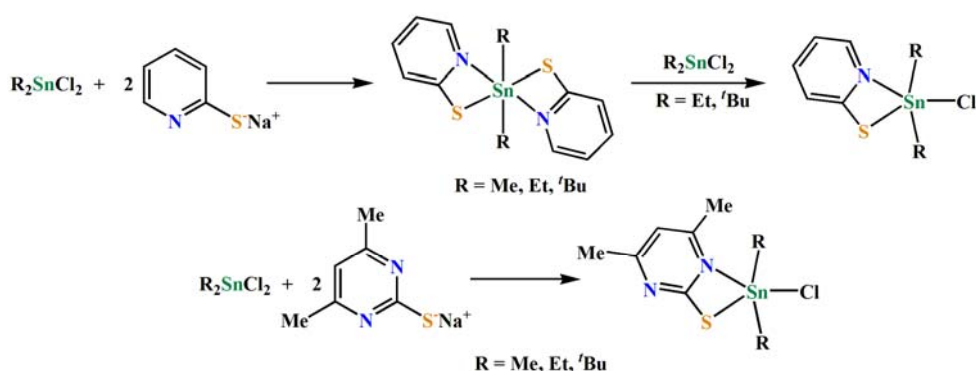
## **Chapter 3: Preparation of tin sulfide nanostructures using organotin pyridyl and pyrimidyl thiolates.**

This chapter presents a detailed study of synthesis, characterization of tin complexes with pyridyl- and pyrimidyl- thiolates. These complexes were utilized as molecular precursors for the preparation of tin sulfide nanosheets in different high boiling solvents. The resulting nanosheets were characterized by various techniques such as p-XRD, SEM, EDS, TEM, SAED. Band gap tuning of the nanosheets was achieved by varying the sheet thickness.

Tin sulfide nanostructures received considerable attention in recent times due to their excellent semiconducting properties and remarkable electronic properties. Molecular precursor route serve as a versatile method to synthesize nanostructures adopting solution or

wet chemical route and can also be utilized for the deposition of nano-structured thin films using aerosol assisted chemical vapor deposition (AACVD) method. In addition, the molecular precursor route proved to be better method to obtain phase pure and narrowly distributed nanostructures and also handling the precursors is convenient compared to multiple source precursors. There are only few reports dealing with the utility of molecular precursors for the preparation of nanostructures in solution. Accordingly, diorganotin 2-pyridyl- and 2-pyrimidyl- thiolate complexes were synthesized and were used for the preparation of tin sulfide nanostructures. Scheme 1 depicts the synthesis of the complexes.

The complexes were characterized by elemental analysis followed by multinuclear NMR ( $^1\text{H}$ ,  $^{13}\text{C}$ ,  $^{119}\text{Sn}$ ) spectroscopy.  $^1\text{H}$  and  $^{13}\text{C}$  NMR spectra showed expected resonances and peak multiplicities. The pyridyl/ pyrimidyl ring proton resonances of all the complexes shifted to down field with reference to the corresponding signals for free ligand. The  $^{119}\text{Sn}\{^1\text{H}\}$  NMR spectra showed single resonances in the range  $-45$  to  $-119$  ppm confirming the existence of one tin containing specie in the solution.



**Scheme 1**

The molecular structures of the complexes  $[\text{R}_2\text{Sn}(\text{2-Spy})_2]$  ( $\text{R} = \text{Et}, t\text{Bu}$ ) and  $[\text{R}_2\text{SnCl}(\text{2-SpymMe}_2)]$  ( $\text{R} = \text{Me}, \text{Et}, t\text{Bu}$ ) have been established by single crystal X-ray diffraction analysis (SCXRD). Molecular structures of  $[\text{Et}_2\text{Sn}(\text{2-Spy})_2]$  and  $[\text{Et}_2\text{SnCl}(\text{2-SpymMe}_2)]$  have been established by single crystal X-ray diffraction analysis (SCXRD).

SpymMe<sub>2</sub>)] are shown in fig. 1. Thermogravimetric analysis (TGA) of the complexes showed that [R<sub>2</sub>Sn(2-Spy)<sub>2</sub>] (R = Me, Et or <sup>t</sup>Bu) undergo an ill defined two-step decomposition finally leading to tin. The complexes, [R<sub>2</sub>SnCl(2-SpymMe<sub>2</sub>)] (R = Me, Et or <sup>t</sup>Bu) decompose in a single step. The weight loss was significantly higher than expected for either formation of SnS or Sn. It is likely that the complexes undergo dismutation into R<sub>2</sub>SnCl<sub>2</sub> and R<sub>2</sub>Sn(2-SpymMe<sub>2</sub>)<sub>2</sub> and the former vaporizes while latter decomposes to stable tin sulfide.

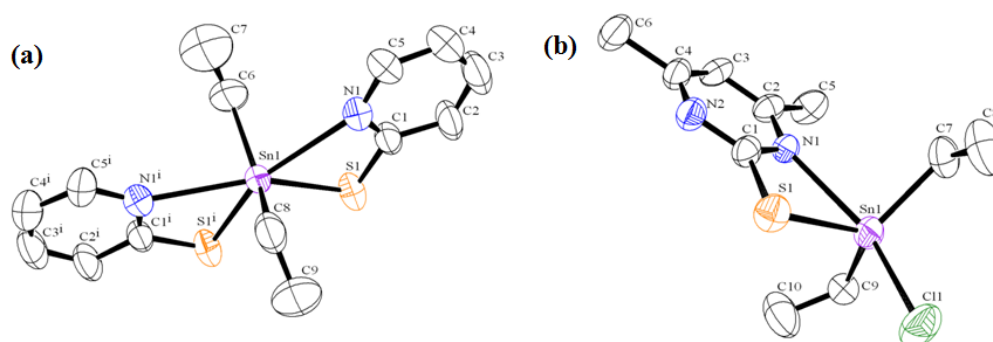


**Fig. 1** Crystal structures of a) [Et<sub>2</sub>Sn(2-Spy)<sub>2</sub>] and b) [Et<sub>2</sub>SnCl(2-SpymMe<sub>2</sub>)] with atomic number scheme. (H atoms are omitted for clarity).

It is likely that the complexes disproportionate into R<sub>2</sub>SnCl<sub>2</sub> and R<sub>2</sub>Sn(2-SpymMe<sub>2</sub>)<sub>2</sub> and the former vaporizes while the latter decomposes to stable tin sulfide. Based upon the thermal studies results two representative diethyltin complexes were chosen to assess their suitability of molecular precursor for tin sulfide.

The precursors were thermolysed in oleyl amine (OLA) and trioctylphosphine oxide (TOPO). Thermolysis of [Et<sub>2</sub>Sn(2-Spy)<sub>2</sub>] and [Et<sub>2</sub>SnCl(2-SpymMe<sub>2</sub>)] in OLA for different duration, results in the formation of crystalline orthorhombic SnS with hexagonal and nearly rectangular sheets as inferred from p-XRD, SEM, EDS, TEM and SAED studies. The direct band gap of the nanosheets can be tuned in the range of 1.6-1.9 eV by varying the thickness of the sheets.

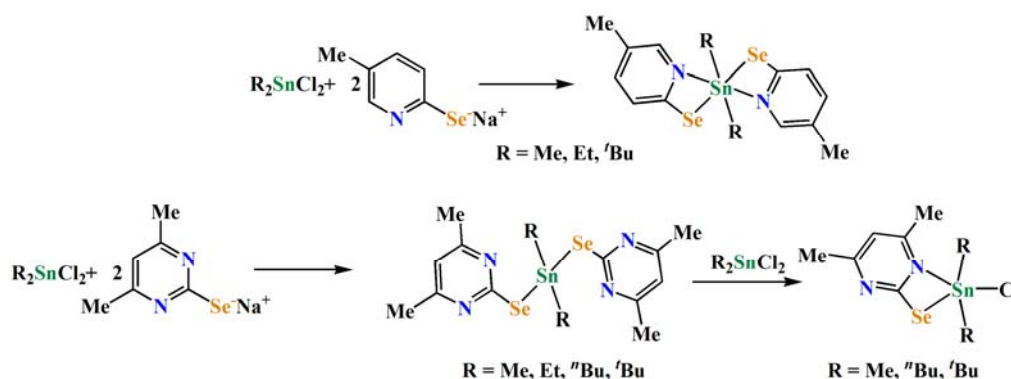


## Chapter 4: Preparation of tin selenide nanostructure using organotin pyridyl and pyrimidyl selenolates.

Successful utilization of molecular precursors for the preparation of tin sulfide nanostructures motivated us to extend this strategy for the preparation of tin selenide nanostructure. This chapter describes the synthesis and characterization of tin complexes with pyridyl- and pyrimidyl- selenolates followed by their utilization as molecular precursors for the preparation of tin selenide nanostructures and thin films. The band gap tuning of  $\text{SnSe}_2$  was achieved by varying the growth duration and the details are included in this chapter.

Tin selenides are emerging members of group IV-VI materials due to their earth abundant, low cost and environmentally benign characteristics. Tin selenides exist in two narrow band gap forms, namely  $\text{SnSe}$  and  $\text{SnSe}_2$ . The unique combination of anisotropy and optical properties including slow carrier relaxation rate, render  $\text{SnSe}$  as a suitable candidate for thermoelectric, photovoltaic and infrared optoelectronic devices, whereas the layered structure of  $\text{SnSe}_2$  have been utilized for infrared photo detection, solar cells and anode material to improve lithium ion diffusivity in lithium ion battery. Relevance of tin selenide nanostructures in optoelectronic and thermoelectric devices, prompted us to explore their preparation through molecular precursor route.

Accordingly, a series of complexes,  $[\text{R}_2\text{Sn}(2\text{-Sepy}(5\text{-Me}))_2]$  ( $\text{R} = \text{Me}, \text{Et}$  or  $t\text{Bu}$ ) and  $[\text{R}_2\text{Sn}(2\text{-SepymMe}_2)_2]$  ( $\text{R} = \text{Me}, \text{Et}, n\text{Bu}, t\text{Bu}$ ) were synthesized as given in scheme 2.



*Scheme 2*

The complexes were characterized by elemental analysis followed by multinuclear NMR ( $^1\text{H}$ ,  $^{13}\text{C}$ ,  $^{77}\text{Se}$ ,  $^{119}\text{Sn}$ ) spectroscopy. The  $^1\text{H}$  and  $^{13}\text{C}\{^1\text{H}\}$  NMR spectra showed expected resonances and peak multiplicities. The  $^{77}\text{Se}\{^1\text{H}\}$  NMR spectra of all the complexes displayed a single resonance which were flanked by tin satellites with  $^1\text{J}(^{119}\text{Sn}-^{77}\text{Se})$  couplings varying between 668 to 887 Hz and 723-977 Hz for 2-pyridyl- and 2-pyrimidyl- selenolate derivatives, respectively. The magnitude of  $^1\text{J}(^{119}\text{Sn}-^{77}\text{Se})$  coupling constant is reduced with reference to the analogous pyrimidyl derivatives indicative of weaker Sn-Se interaction leading longer Sn-Se bond lengths in the pyridyl selenolate complexes which is in accordance with single crystal X-ray analysis. Existence of only one tin containing species in solution is confirmed by the  $^{119}\text{Sn}\{^1\text{H}\}$  NMR spectra which displayed a single resonance flanked by selenium satellites. The molecular structure was established unambiguously for most of the complexes from SCXRD and crystal structures of representative *tert*-butyl derivatives are shown in fig. 2. The bis complexes  $[\text{tBu}_2\text{Sn}(2\text{-Sepy}(5\text{-Me}))_2]$  and  $[\text{tBu}_2\text{Sn}(2\text{-SepymMe}_2)_2]$  show intramolecular Sn---N interaction, however the interaction is stronger in the former compared to the latter as revealed from Sn-N distance. TG analysis shows that decomposition of the complexes leads to the formation of either SnSe ( $[\text{R}_2\text{Sn}(2\text{-Sepy}(5\text{-Me}))_2]$ ; R = Me, Et,  $^t\text{Bu}$  and  $[\text{tBu}_2\text{Sn}(2\text{-SepymMe}_2)_2]$ ), SnSe<sub>2</sub> ( $[\text{R}_2\text{Sn}(2\text{-SepymMe}_2)_2]$ ; R = Et,  $^n\text{Bu}$ ) or Sn ( $[\text{tBu}_2\text{SnCl}(2\text{-SepymMe}_2)]$ ) *via* single step or two overlapping steps.

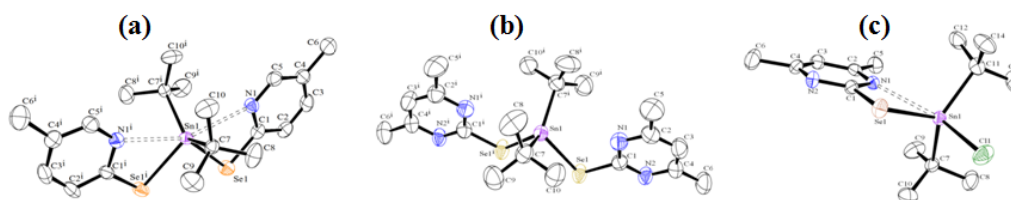


**Fig.2** Crystal structure of (a)  $[\text{tBu}_2\text{Sn}(2\text{-Sepy}(5\text{-Me}))_2]$ , (b)  $[\text{tBu}_2\text{Sn}(2\text{-SepymMe}_2)_2]$  (7), (c)  $[\text{tBu}_2\text{SnCl}(2\text{-SepymMe}_2)]$  with atomic number scheme.

Thermolysis of the complex  $[\text{tBu}_2\text{Sn}(2\text{-Sepy}(5\text{-Me}))_2]$ , in different solvents afforded the formation of SnSe with irregular sheet morphology (OLA), SnSe<sub>2</sub> with hexagonal morphology (ODE) or mixture of both in mixed solvents whereas exclusively SnSe<sub>2</sub> sheet (with rough and smooth edges) like morphology could be obtained from the thermolysis of complexes  $[\text{R}_2\text{Sn}(2\text{-SepymMe}_2)_2]$ ; R = Et, <sup>n</sup>Bu, <sup>t</sup>Bu in OLA for different time durations as deduced from p-XRD, EDS, SAED, SEM, TEM and HR-TEM. The morphology as deduced from SEM are shown in fig. 3.

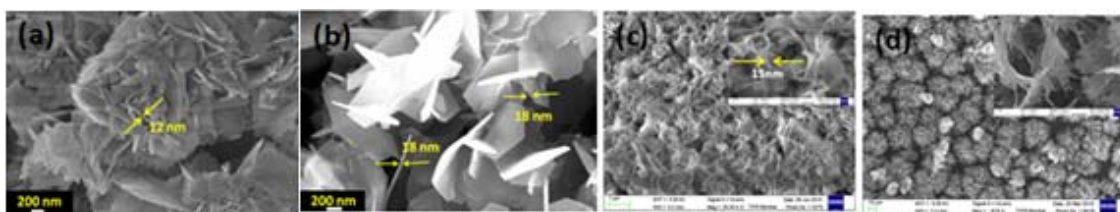


**Fig.3** SEM images of (a) SnSe, (b) SnSe<sub>2</sub> obtained by thermolysis of  $[\text{R}_2\text{Sn}(2\text{-Sepy}(5\text{-Me}))_2]$  in OLA and ODE, respectively, (c) SnSe<sub>2</sub> obtained by thermolysis of  $[\text{tBu}_2\text{Sn}(2\text{-SepymMe}_2)_2]$  in OLA and (d) SnSe<sub>2</sub> thin film obtained by  $[\text{tBu}_2\text{Sn}(2\text{-SepymMe}_2)_2]$  through AACVD, respectively.

The complex,  $[\text{tBu}_2\text{Sn}(2\text{-SepymMe}_2)_2]$  was also employed for the deposition of SnSe<sub>2</sub> thin films through AACVD. The films were characterized by p-XRD, SEM and EDS studies. SEM image of hierarchical flower like structure of SnSe<sub>2</sub> film is shown in fig. 3d. The band gap of the SnSe<sub>2</sub> nanosheets could be tuned from 1.7 to 2.3 eV as function of growth duration.

Photoelectrochemical studies (PEC) of SnSe and SnSe<sub>2</sub> obtained from the thermolysis of  $[\text{tBu}_2\text{Sn}(2\text{-Sepy}(5\text{-Me}))_2]$  measured under the light intensity of 200  $\mu\text{W}/\text{cm}^2$  shows the photo-switching behavior of SnSe<sub>2</sub> under alternating light and dark conditions while no such behavior was observed for SnSe nanostructures.

## **Chapter 5: Accessing ternary tin chalcogenide nanostructures from molecular precursors.**

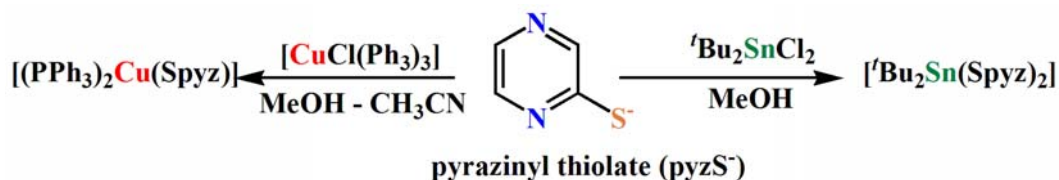
After accomplishing the synthesis of binary tin chalcogenides through molecular precursors, the strategy was extended for the preparation of ternary tin chalcogenides ( $\text{Cu}_2\text{SnS}_3$  and  $\text{Cu}_2\text{SnSe}_3$ ). For ternary nanostructures, it is essential to select suitable combination of precursor material having similar kind of reactivities and comparable decomposition temperatures. Keeping this in mind the precursors were designed and details are provided in this chapter. This chapter is divided into two sections which describe the synthesis, and utilization of molecular precursors for the preparation of i)  $\text{Cu}_2\text{SnS}_3$  and ii)  $\text{Cu}_2\text{SnSe}_3$ , respectively.

Copper-tin-chalcogenides and their derivatives constitute an interesting family of semiconductor materials. They are projected as alternates for technologically well-established photovoltaic materials such as CdTe, PbSe,  $\text{CuInSe}_2$  which are based on either toxic (Cd, Pb) or scarce (In, Te) elements. There is hardly any report in the literature dealing with the preparation of these materials from molecular precursors. Accordingly, tin and copper complexes with pyrazinyl thiolates and pyridyl selenolates have been explored as molecular precursors.

### **5.1 Preparation of $\text{Cu}_2\text{SnS}_3$ from diorganotin(IV) and copper(I) 2-pyrazinyl thiolates**

Air stable di-*tert*-butyltin(IV) and copper(I) complexes of 2-pyrazinylthiol (2-HSpyz),  $[\text{tBu}_2\text{Sn}(\text{Spyz})_2]$  and  $[\text{Cu}(\text{Spyz})(\text{PPh}_3)_2]$ . These complexes were employed as molecular precursors for the preparation of binary ( $\text{SnS}$  and  $\text{Cu}_{1.8}\text{S}$ ) and ternary  $\text{Cu}_2\text{SnS}_3$  (CTS) nanostructures. p-XRD, Raman spectroscopy, SEM, EDS, TEM, HR-TEM, DRS and PEC studies were carried out to determine the crystal structure, phase purity, morphology, band gap and photo-response behavior of nanostructures. The choice of reaction solvent

governs the phase purity and morphology of  $\text{Cu}_2\text{SnS}_3$  nanostructures was established during the investigation. The synthesis of the complexes is shown in scheme 3.



*Scheme 3*

The complexes have been characterized by elemental analysis, multinuclear NMR, SCXRD. The TG analysis of the  $[\text{tBu}_2\text{Sn}(\text{Spyz})_2]$  and  $[(\text{PPh}_3)_2\text{Cu}(\text{Spyz})]$  (Fig. 4a.) revealed closely related decomposition temperatures with the formation of the corresponding metal sulfide. Thus, these complexes were chosen to assess their utility as molecular precursors for the preparation of ternary copper tin sulfide nanostructures. To study the effect of solvent on phase purity and morphology of nanostructures three distinct solvents were chosen based on their binding ability. Thermolysis of complexes either in OA or in a mixture of OA-OLA revealed the formation of monoclinic phase of  $\text{Cu}_2\text{SnS}_3$  as a major product slightly contaminated by cubic phase of  $\text{Cu}_{1.8}\text{S}$ , while in OLA, nearly spherical phase pure  $\text{Cu}_2\text{SnS}_3$  nanostructures which exhibit a band gap of 1.5 eV were obtained as evident from pXRD, Raman spectroscopy, SEM, EDS, TEM, HR-TEM and DRS studies. The ternary  $\text{Cu}_2\text{SnS}_3$  showed better photosensitivity compare to binary SnS and  $\text{Cu}_{1.8}\text{S}$  as inferred from PEC studies.

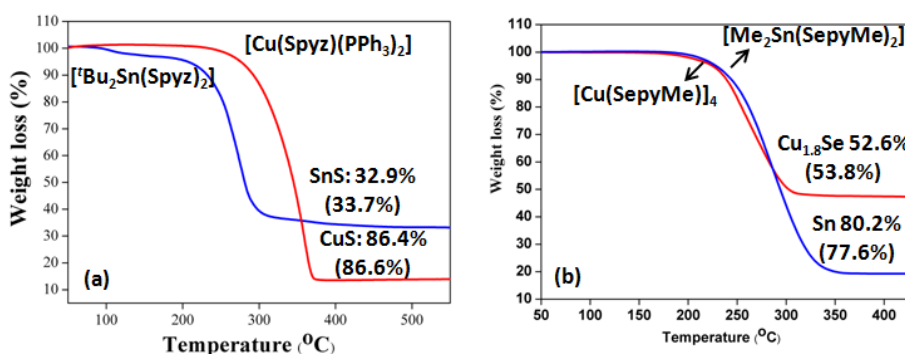


**Fig.4** TG curves for complexes a)  $[\text{Cu}(\text{Spyz})(\text{PPh}_3)_2]$  and  $[\text{tBu}_2\text{Sn}(\text{Spyz})_2]$  b)  $[\text{Cu}(2\text{-SepyMe})_4]$  and  $[\text{Me}_2\text{Sn}(2\text{-SepyMe})_2]$ , respectively.

## 5.2 Preparation of $\text{Cu}_2\text{SnSe}_3$ from diorganotin(IV) and copper(I) 2-pyridylselenolates

This section describes the synthesis of phase pure, photoresponsive  $\text{Cu}_2\text{SnSe}_3$  nanostructures using metal selenolates,  $[\text{Me}_2\text{Sn}(2\text{-SepyMe})_2]$  and  $[\text{Cu}(2\text{-SepyMe})_4]$  as molecular precursors in oleylamine (OLA) and tri-n-octylphosphine oxide (TOPO). The crystal structure, phase purity, morphology and band gap of nanostructures were evaluated from pXRD, Raman spectroscopy, SEM, TEM and DRS studies. The effect of temperature on final composition of nanostructures has also been investigated. The complexes were synthesized according to scheme 4.



**Scheme 4**

Precursors  $[\text{Me}_2\text{Sn}(2\text{-SepyMe})]$  and  $[\text{Cu}(2\text{-SepyMe})_4]$  were prepared according to literature methods [13, 14]. The X-ray structural characterization for the latter was reported earlier [14] while for the former is described as discrete monomer with distorted tetrahedral

geometry around tin defined by two Me groups and two selenium atoms of the selenolate ligand. The complexes underwent single step decomposition (TG analysis) with closely related decomposition temperature (fig. 4b). These complexes were simultaneously thermolysed at temperature 300 °C for 10 minutes in OLA to obtain the phase pure Cu<sub>2</sub>SnSe<sub>3</sub> nanostructures. Thermolysis of precursors at growth temperature less than 300 °C or in TOPO leads to the formation of tin deficient nanostructures as revealed from EDX studies. Absence of Cu<sup>2+</sup> ions in Cu<sub>2</sub>SnSe<sub>3</sub> was confirmed from the results of magnetic property measurements and electron paramagnetic resonance (EPR) studies. The optical band gap of Cu<sub>2</sub>SnSe<sub>3</sub> nanosheets (1.73 eV) derived from DRS measurements is in the range of optimum band gap required for solar energy absorption while the photo response of the nanosheets has been established with faster switching characteristics.

## **Chapter 6: Conclusions**

This chapter presents the conclusion of the present investigation. Various air stable, monomeric tin complexes using internally functionalized chalcogenolate ligands (2-pyridyl, 2-pyrimidyl and 2-pyrazinyl chalcogenolates) have been synthesized, isolated and characterized. The facile cleavage of C-E bond in these complexes serves them as versatile precursors for the preparation of photo-responsive binary and ternary tin chalcogenide nanostructures and deposition of thin films. PEC studies revealed that ternary nanostructures exhibit better photosensitivity compared to binary tin chalcogenides. Phase, composition and band gap tunability of the nanostructures has been demonstrated by varying the temperature, growth duration and choice of reaction solvent.

Overall, this thesis describes facile synthesis of binary and ternary tin chalcogenides *via* molecular precursor route in an efficient manner and thus it provides an easily adoptable alternative for large scale preparation of technologically important tin chalcogenide nanomaterials and thin films.

## References

1. P. Mir, M. Audiffred, T. Heine, Chem. Soc. Rev., 43 (2014) 6537.
2. K. S. Novoselov, A. K. Geim, S. V. Morozov, D. Jiang, Y. Zhang, S. V. Dubonos, I. V. Grigorieva, A. A. Firsov, Science, 306 (2004) 666.
3. R. Lv, J. A. Robinson, R. E. Schaak, D. Sun, Y. Sun, T. E. Mallouk, M. Terrones, Acc. Chem. Res., 48 (2015) 56.
4. D. Voiry, A. Mohite, M. Chhowalla, Chem. Soc. Rev., 44 (2015) 2702.
5. J. Gao, A. F. Fidler, V. I. Klimov, Nature Commun., 6 (2015) 8185.
6. R. Saran, R. J. Curry, Nature Photonics, 10 (2016) 81.
7. Y. Lee, S. H. Lo, C. Chen, H. Sun, D. Y. Chung, T. C. Chasapis, C. Uher, V. P. Dravid, M. G. Kanatzidis, Nature Commun., 5 (2014) 3640.
8. F. Bertolotti, D. N. Dirin, M. Ibanez, F. Krumeich, A. Cervellino, R. Frison, O. Voznyy, E. H. Sargent, M. V. Kovalenko, A. Guagliardi and N. Masciocchi, Nature Mater., 15 (2016) 987.
9. X. Zhou, Q. Zhang, L. Gan, H. Li, J. Xiong, T. Zhai, Adv. Sci., 3 (2016) 1600177.
10. H. Zhong, G. Yang, H. Song, Q. Liao, H. Cui, P. Shen, C. X. Wang, J. Phys. Chem. C, 116, (2012) 9319.
11. P. Boudjouk, D. J. Seidler, D. Grier, G. McCarthy, J. Chem. Mater., 8 (1996) 1189.
12. I. P. Parkin, L. S. Price, T. G. Hibbert, K. C. Molloy, J. Mater. Chem., 11 (2001) 1486.
13. R. K. Sharma, G. Kedarnath, A. Wadawale, C. A. Betty, B. Vishwanadh, V. K. Jain, Dalton Trans., 41 (2012) 12129.
14. R. Sharma, G. Kedarnath, V. K. Jain, A. Wadawale, C. Pillai, M. Nallathg, B. Vishwanadh, Dalton Trans., 40 (2011) 9194.



# List of Figures

	CHAPTER 1	Page No.
<b>Fig. 1.1</b>	Nanomaterials having different dimensions (a) 0D spheres and clusters, (b) 1D nanofibers, wires and rods, (c) 2D films, plates and networks	3
<b>Fig. 1.2</b>	Electronic band structure of metals, semiconductors and insulators.	4
<b>Fig. 1.3</b>	Classification of semiconductors.	5
<b>Fig. 1.4</b>	Band structure of extrinsic semiconductor; a) n-type with donor levels, b) p-type with acceptor levels.	7
<b>Fig. 1.5</b>	Energy vs crystal momentum for a) direct semiconductor and b) indirect semiconductor.	9
<b>Fig. 1.6</b>	Structure of SnSe a) $P_{nma}$ phase below 800 K and b) $C_{mcm}$ phase above 800 K, respectively.	17
<b>Fig. 1.7</b>	Crystal structure of layered hexagonal 2D $SnSe_2$ .	19
<b>Fig. 1.8</b>	Crystal structure of $Cu_2SnS_3$ based on cubic close packing of S with Cu and Sn in tetrahedral sites.	22
<b>Fig. 1.9</b>	Molecular structure of a) $[Sn(SCH_2CH_2S)_2]$ and b) $[(PhS)_4Sn]$ employed for the deposition of tin sulfide thin films.	28
<b>Fig. 1.10</b>	Molecular structure of Tribenzyltin chloride thiosemicarbazones for growth of SnS thin films.	28
<b>Fig. 1.11</b>	Molecular structure of diorganotin dithiocarbamates design and developed by O'Brien and coworkers	29
<b>Fig. 1.12</b>	Schematic representation of the preparation of $[Sn(Sepy)_2]$ its	32

molecular structure and formation of SnSe from the thermolysis of precursor

## CHAPTER 2

**Fig. 2.1** Schematic representation of Bragg's equation for X-ray diffraction. 44

**Fig. 2.2** Block diagram of Photoelectrochemical Cell. 49

## CHAPTER 3

**Fig. 3.1** Crystal structure of a)  $[\text{Et}_2\text{Sn}(\text{2-Spy})_2]$ , b)  $[\text{tBu}_2\text{Sn}(\text{2-Spy})_2]$ , c)  $[\text{tBu}_2\text{ClSn}(\text{2-Spy})]$ , d)  $[\text{Me}_2\text{SnCl}(\text{2-SpymMe}_2)]$ , e)  $[\text{Et}_2\text{SnCl}(\text{2-SpymMe}_2)]$  and f)  $[\text{tBu}_2\text{SnCl}(\text{2-SpymMe}_2)]$  with atomic number scheme. The ellipsoids were drawn at 25% probability. 65

**Fig. 3.2** TG curve of a)  $[\text{Me}_2\text{Sn}(\text{2-Spy})_2]$ , b)  $[\text{Et}_2\text{Sn}(\text{2-Spy})_2]$ , c)  $[\text{tBu}_2\text{Sn}(\text{2-Spy})_2]$ , d)  $[\text{Me}_2\text{SnCl}(\text{2-SpymMe}_2)]$ , e)  $[\text{Et}_2\text{SnCl}(\text{2-SpymMe}_2)]$  and f)  $[\text{tBu}_2\text{SnCl}(\text{2-SpymMe}_2)]$ . 66

**Fig. 3.3**  $^{119}\text{Sn}\{^1\text{H}\}$  NMR spectra ( $\text{CDCl}_3$ ) of (a) Freshly prepared  $[\text{Et}_2\text{SnCl}(\text{SpymMe}_2)]$  (b) sublimed product from the complex at 200 °C under vacuum. The formation of  $[\text{Et}_2\text{Sn}(\text{SpymMe}_2)_2]$  indicates disproportionation of the complex into  $[\text{Et}_2\text{Sn}(\text{SpymMe}_2)_2]$  and  $\text{Et}_2\text{SnCl}_2$ . 67

**Fig. 3.4** a) Simulated XRD pattern of orthorhombic SnS (JCPDS-39-0354). XRD profiles of SnS nanosheets obtained by b) thermolysis of  $[\text{Et}_2\text{Sn}(\text{2-Spy})_2]$  in OLA at 300 °C for 10 minutes and by thermolysis of  $[\text{Et}_2\text{SnCl}(\text{SpymMe}_2)]$  in OLA at 300 °C for c) 5 and d) 10 minutes. 70

- Fig. 3.5** SEM, TEM images and SAED patterns of a), b) and c) SnS hexagonal sheets obtained by thermolysis of  $[\text{Et}_2\text{Sn}(2\text{-Spy})_2]$  and d), e) and f) rectangular sheets obtained by thermolysis of  $[\text{Et}_2\text{SnCl}(\text{SpymMe}_2)]$  in OLA at 300 °C for 10 minutes, respectively. 72
- Fig. 3.6** a) XRD, b) TEM image and c) SAED pattern of the residue obtained by thermolysis of  $[\text{Et}_2\text{SnCl}(\text{SpymMe}_2)]$  in TOPO-OLA at 320 °C for 10 minutes. (\* corresponds to  $\text{SnS}_2$ ) 72
- Fig. 3.7** FT-IR spectra of a) oleylamine (OLA), b) SnS nanosheets obtained by thermolysis of  $[\text{Et}_2\text{Sn}(2\text{-Spy})_2]$  in OLA at 300 °C for 10 minutes and by thermolysis of  $[\text{Et}_2\text{SnCl}(\text{SpymMe}_2)]$  in OLA at 300 °C for c) 5 and d) 10 minutes, respectively. 73
- Fig. 3.8** A representative thermogravimetric curve of SnS nanosheets obtained by thermolysis of  $[\text{Et}_2\text{SnCl}(\text{SpymMe}_2)]$  in OLA at 300 °C. 74
- Fig. 3.9** XRD pattern and SEM image of orthorhombic SnS thin films a) and c) on glass substrate, b) and d) on Si substrate, respectively. 75
- Fig. 3.10** a) Solid-state diffuse reflectance spectrum of SnS rectangular sheets obtained by thermolysis of  $[\text{Et}_2\text{SnCl}(\text{SpymMe}_2)]$  in OLA at 300 °C for 5 minutes and their Kubelka-Munk conversion plots of b)  $[\text{F(R)hv}]^2$  vs energy and c)  $[\text{F(R)hv}]^{1/2}$  vs energy from which direct and indirect band gaps were determined. 76

## CHAPTER 4

- Fig. 4.1**  $^{77}\text{Se}\{^1\text{H}\}$  NMR spectra of a)  $[\text{Me}_2\text{Sn}(2\text{-Sepy}(5\text{-Me}))_2]$  and b)  $[\text{Me}_2\text{Sn}(2\text{-SepymMe}_2)_2]$ . 89

<b>Fig. 4.2</b>	$^{119}\text{Sn}\{^1\text{H}\}$ NMR spectra of a) $[\text{Me}_2\text{Sn}(2\text{-Sepy}(5\text{-Me}))_2]$ and b) $[\text{Me}_2\text{Sn}(2\text{-SepymMe}_2)_2]$ .	90
<b>Fig. 4.3</b>	Variable temperature $^{119}\text{Sn}\{^1\text{H}\}$ NMR spectrum of $[\text{tBu}_2\text{SnCl}(2\text{-SepymMe}_2)]$ acquired in $\text{CDCl}_3$ .	91
<b>Fig. 4.4</b>	Molecular structure of $(2\text{-Sepy}(\text{Me}-5))_2$ , with atomic number scheme .	94
<b>Fig. 4.5</b>	Crystal structure of a) $[\text{Me}_2\text{Sn}(2\text{-Sepy}(5\text{-Me}))_2]$ , b) $[\text{Et}_2\text{Sn}(2\text{-Sepy}(5\text{-Me}))_2]$ and c) $[\text{tBu}_2\text{Sn}(2\text{-Sepy}(5\text{-Me}))_2]$ with partial atomic number scheme. Ellipsoids are drawn with 25% probability.	95
<b>Fig. 4.6</b>	Crystal structure of a) $[\text{tBu}_2\text{Sn}(2\text{-SepymMe}_2)_2]$ , b) $[\text{nBu}_2\text{Sn}(2\text{-SepymMe}_2)_2]$ and c) $[\text{tBu}_2\text{SnCl}(2\text{-SepymMe}_2)]$ with partial atomic number scheme. Ellipsoids are drawn at 50%, 25% and 10% probability for a), b) and c), respectively.	96
<b>Fig. 4.7</b>	TG curve of a) $[\text{Me}_2\text{Sn}(2\text{-Sepy}(5\text{-Me}))_2]$ , b) $[\text{Et}_2\text{Sn}(2\text{-Sepy}(5\text{-Me}))_2]$ , c) $[\text{tBu}_2\text{Sn}(2\text{-Sepy}(5\text{-Me}))_2]$ , d) $[\text{Me}_2\text{Sn}(2\text{-SepymMe}_2)_2]$ , e) $[\text{Et}_2\text{Sn}(2\text{-SepymMe}_2)_2]$ , f) $[\text{nBu}_2\text{Sn}(2\text{-SepymMe}_2)_2]$ , g) $[\text{tBu}_2\text{Sn}(2\text{-SepymMe}_2)_2]$ and h) $[\text{tBu}_2\text{Sn}(2\text{-SepymMe}_2)_2]$ , respectively.	102
<b>Fig. 4.8</b>	a) and b) Simulated XRD patterns of orthorhombic phase of $\text{SnSe}$ (JCPDS no. 23-0602) and hexagonal $\text{SnSe}_2$ (JCPDS no. 48-1224), respectively. XRD profiles of tin selenide nanostructures obtained by thermolysis of $[\text{tBu}_2\text{Sn}(2\text{-Sepy}(5\text{-Me}))_2]$ at $220^\circ\text{C}$ for 10 minutes in c) ODE, d) OLA, e) OA, f) 1:1 v/v mixture of OLA/ODE and g) 1:1 v/v mixture of OLA/	104

OA, respectively.

**Fig. 4.9** The SEM, TEM and HRTEM images of nanostructures obtained by thermolysis of  $[\text{tBu}_2\text{Sn}(\text{2-Sepy}(5\text{-Me}))_2]$  at  $220^\circ\text{C}$  for 10 minutes corresponds to (a, b, c) hexagonal  $\text{SnSe}_2$  in ODE, (d, e, f) orthorhombic  $\text{SnSe}$  in OLA (g, h, i) hexagonal  $\text{SnSe}_2$  contaminated with slight amount of orthorhombic  $\text{SnSe}$  in OA, respectively. 107

**Fig. 4.10** a), b), c) SEM, TEM and HRTEM of nanostructure obtained in (1:1) (v/v) mixture of ODE:OLA, d) SEM micrograph of nanostructure obtained in (1:1) (v/v) mixture of OLA:OA, e) HRTEM image of rectangular sheet obtained in OA from the thermolysis of  $[\text{tBu}_2\text{Sn}(\text{2-Sepy}(5\text{-Me}))_2]$  at  $220^\circ\text{C}$  for 10 minutes. 108

**Fig. 4.11** a) Simulated XRD pattern of hexagonal  $\text{SnSe}_2$  (JCPDS-40-1465). XRD profiles of  $\text{SnSe}_2$  nanosheets obtained by b) thermolysis of  $[\text{Et}_2\text{Sn}(\text{2-SepymMe}_2)_2]$ , c)  $[\text{nBu}_2\text{Sn}(\text{2-SepymMe}_2)_2]$  and d)  $[\text{tBu}_2\text{Sn}(\text{2-SepymMe}_2)_2]$  in OLA at  $210^\circ\text{C}$  for 2 minutes (\* indicates the impurity peak of Se). Simulated pattern has been avoided for clarity. 110

**Fig. 4.12** a) Simulated XRD pattern of hexagonal  $\text{SnSe}_2$  (JCPDS-40-1465). XRD profiles of  $\text{SnSe}_2$  nanosheets obtained by b) thermolysis of  $[\text{Et}_2\text{Sn}(\text{2-SepymMe}_2)_2]$ , c)  $[\text{nBu}_2\text{Sn}(\text{2-SepymMe}_2)_2]$  and d)  $[\text{tBu}_2\text{Sn}(\text{2-SepymMe}_2)_2]$  in OLA at  $210^\circ\text{C}$  for 5 minutes (\* indicates the impurity peak of Se). 110

**Fig. 4.13** a) Simulated XRD pattern of hexagonal  $\text{SnSe}_2$  (JCPDS-23- 111

0602). XRD profiles of SnSe<sub>2</sub> nanosheets obtained by b) thermolysis [Et<sub>2</sub>Sn(2-SepymMe<sub>2</sub>)<sub>2</sub>], c) [<sup>n</sup>Bu<sub>2</sub>Sn(2-SepymMe<sub>2</sub>)<sub>2</sub>] and d) [<sup>t</sup>Bu<sub>2</sub>Sn(2-SepymMe<sub>2</sub>)<sub>2</sub>] in OLA at 210 °C for 10 minutes.

**Fig. 4.14** SEM images of SnSe<sub>2</sub> nanosheets obtained by a) thermolysis of [Et<sub>2</sub>Sn(2-SepymMe<sub>2</sub>)<sub>2</sub>], c) [<sup>n</sup>Bu<sub>2</sub>Sn(2-SepymMe<sub>2</sub>)<sub>2</sub>] and d) [<sup>t</sup>Bu<sub>2</sub>Sn(2-SepymMe<sub>2</sub>)<sub>2</sub>] in OLA at 210 °C for 2 minutes (Inset show magnified images of the same). 113

**Fig. 4.15** SEM images of SnSe<sub>2</sub> nanosheets obtained by a) thermolysis of [Et<sub>2</sub>Sn(2-SepymMe<sub>2</sub>)<sub>2</sub>], b) [<sup>t</sup>Bu<sub>2</sub>Sn(2-SepymMe<sub>2</sub>)<sub>2</sub>] in OLA at 210 °C for 10 minutes (Inset show magnified images of the same). 113

**Fig. 4.16** a) TEM image and b) SAED pattern of SnSe<sub>2</sub> nanosheets obtained by thermolysis of [Et<sub>2</sub>Sn(2-SepymMe<sub>2</sub>)<sub>2</sub>] in OLA at 210 °C for 2 minutes while c) and d) are TEM and HR-TEM image of SnSe<sub>2</sub> nanosheets obtained by thermolysis of [<sup>t</sup>Bu<sub>2</sub>Sn(2-SepymMe<sub>2</sub>)<sub>2</sub>] in OLA at 210 °C for 2 minutes (Inset show needle like structures formed by rolling of nanosheets). 114

**Fig. 4.17** XRD profile and SEM images a) as prepared SnSe<sub>2</sub> thins films obtained by AACVD of [<sup>t</sup>Bu<sub>2</sub>Sn(2-SepymMe<sub>2</sub>)<sub>2</sub>] on silicon substrate at 375 °C for 1 h and b) annealed thin film of as prepared thin film at 375 °C for 1 h. 116

**Fig. 4.18** Plots of [F(R)hv]<sup>2</sup> vs energy generated by Kubelka-Munk transformation of solid-state diffuse reflectance data of a) orthorhombic SnSe b) hexagonal SnSe<sub>2</sub> nanostructures obtained 117

by thermolysis of  $[\text{tBu}_2\text{Sn}(2\text{-Sepy}(5\text{-Me}))_2]$  at 220 °C for 10 minutes in OLA and ODE, respectively for determining direct band gap energies.

**Fig. 4.19** Plots of  $[\text{F(R)hv}]^2$  vs energy generated by Kubelka-Munk transformation of solid-state diffuse reflectance data of  $\text{SnSe}_2$  nano-sheets obtained by thermolysis of a)  $[\text{Et}_2\text{Sn}(2\text{-SepymMe}_2)_2]$  and b)  $[\text{tBu}_2\text{Sn}(2\text{-SepymMe}_2)_2]$  in OLA at 210 °C for 2, 5 and 10 minutes, respectively for determining direct band gap energies. 118

**Fig. 4.20** Plots of  $[\text{F(R)hv}]^2$  vs energy generated by Kubelka-Munk transformation of solid-state diffuse reflectance data of a) as-deposited  $\text{SnSe}_2$  thin films obtained by AACVD of  $[\text{tBu}_2\text{Sn}(2\text{-SepymMe}_2)_2]$  on silicon substrate at 375 °C for 1 h and b) annealed thin films to determine direct band gap energies. 119

**Fig. 4.21** a) I-V characteristics of  $\text{SnSe}_2$  nanostructures under dark (black) and light (red) conditions, b) Current vs. time plot of hexagonal  $\text{SnSe}_2$  nanostructures under light intensity of 200  $\mu\text{W}/\text{cm}^2$  and bias voltage of 0.5 V 120

## CHAPTER 5

**Fig. 5.1** a)  $^{31}\text{P}\{^1\text{H}\}$  NMR (121.49 MHz,  $\text{CDCl}_3$ ) spectrum of  $[\text{Cu}(\text{Spyz})(\text{PPh}_3)_2]$  shows a resonance at -2.87 ppm. The minor peak at 29.80 is due to  $\text{Ph}_3\text{PO}$ . b)  $^{119}\text{Sn}\{^1\text{H}\}$  NMR(111.94 MHz,  $\text{CDCl}_3$ ) spectrum of  $[\text{tBu}_2\text{Sn}(\text{Spyz})_2]$  shows a single resonance at -18.45 ppm. 132

- Fig. 5.2** Molecular structure of  $[\text{tBu}_2\text{Sn}(\text{Spyz})_2]$  with partial atomic numbering scheme. Hydrogen atoms are omitted for clarity. Ellipsoids are drawn with 50% probability. The shorter distance between Sn and N atoms, Sn1-N1 and Sn1-N3 are 2.88 and 2.90 Å respectively, suggest weak interaction exist between them. 133
- Fig. 5.3** Molecular structure of  $[\text{Cu}(\text{Spyz})(\text{PPh}_3)_2]$  with partial atomic numbering scheme. There are two molecules in asymmetric unit. Hydrogen atoms are omitted for clarity. Ellipsoids are drawn with 50% probability. 134
- Fig. 5.4** Packing diagram of  $[\text{Cu}(\text{Spyz})(\text{PPh}_3)_2]$ . One molecular complex unit exhibits weak intermolecular  $\text{N}\cdots\text{H}-\text{C}(\text{N})$  interaction. The parameters are: N – C distance 3.487 Å, N – H distance 2.632 Å, N-H-C angle 153.03°. The other molecule is devoid of any such interactions. 134
- Fig. 5.5** Crystal structure of  $[\text{Me}_2\text{Sn}(2\text{-Sepy}(3\text{-Me}))_2]$  with atomic number scheme. The ellipsoids were drawn at 25% probability (H atoms are omitted for clarity). Selected interatomic parameters: Bond distance (Å): Sn1-C13, 2.15(2); Sn1-C14, 2.128 (18); Sn1-Se1, 2.611 (2); Sn1-Se2, 2.666 (3); Sn1-N1, 2.74; Sn1-N2, 2.76. Bond angles (°): C13-Sn1-C14, 122.0 (10); C13-Sn1-Se1, 109.4 (6); C13-Sn1-Se2, 110.4 (7); C14-Sn1-Se1, 111.0(6); C14-Sn1-Se2, 110.6 (7), Se1-Sn-Se2, 88.29 (8); N1-Sn1-N2, 146.86. 136
- Fig. 5.6** Thermogravimetric analysis data for complexes a)  $[\text{tBu}_2\text{Sn}(\text{Spyz})_2]$  and b)  $[\text{Cu}(\text{Spyz})(\text{PPh}_3)_2]$ , respectively. 138



- Fig. 5.7** a), b), c) are the simulated XRD patterns of orthorhombic SnS (JCPDS no. 75-0925), cubic Cu<sub>1.8</sub>S (JCPDS no. 04-004-7716), monoclinic CTS (JCPDS no. 04-010-5719) respectively. p-XRD profiles of CTS nanostructures obtained by co-thermolysis of [<sup>t</sup>Bu<sub>2</sub>Sn(Spyz)<sub>2</sub>] and [Cu(Spyz)(PPh<sub>3</sub>)<sub>2</sub>] at 300 °C for 20 minutes by heat up method in d) OA-OLA, e) OA and f) OLA as solvent/capping agent respectively. (# indicates impurity peaks of orthorhombic SnS while \* indicates the impurity peak of cubic Cu<sub>1.8</sub>S). 141
- Fig. 5.8** a), b) are the simulated XRD patterns of orthorhombic SnS (JCPDS no. 75-0925), monoclinic CTS (JCPDS no. 04-010-5719) respectively. c) XRD profiles of CTS nanostructures obtained by co-thermolysis of [<sup>t</sup>Bu<sub>2</sub>Sn(Spyz)<sub>2</sub>] and [Cu(Spyz)(PPh<sub>3</sub>)<sub>2</sub>] at 275 °C for 20 minutes by heat up method in OLA as solvent/capping agent. (\* indicates binary impurity from orthorhombic phase of SnS). 142
- Fig. 5.9** a), b) are the simulated XRD patterns of orthorhombic SnS (JCPDS no. 75-0925), cubic Cu<sub>1.8</sub>S (JCPDS no. 04-004-7716), respectively. XRD profiles of c) orthorhombic SnS d) cubic Cu<sub>1.8</sub>S nanostructures obtained by thermolysis of [<sup>t</sup>Bu<sub>2</sub>Sn(Spyz)<sub>2</sub>] and [Cu(Spyz)(PPh<sub>3</sub>)<sub>2</sub>], respectively, at 300 °C for 20 minutes by heat up method in OLA as solvent/capping agent. 145
- Fig. 5.10** XRD patterns of a) cubic Cu<sub>1.8</sub>S, b) monoclinic CTS and c) orthorhombic SnS obtained by thermolysis of [<sup>t</sup>Bu<sub>2</sub>Sn(Spyz)<sub>2</sub>] 145

and  $[\text{Cu}(\text{Spyz})(\text{PPh}_3)_2]$  either individually or in combination at 300 °C for 20 minutes by heat up method in OLA as solvent/capping agent.

**Fig. 5.11** Raman spectra of a) monoclinic CTS and b) cubic  $\text{Cu}_{1.8}\text{S}$  obtained by thermolysis of precursors in OLA at 300 °C. 146

**Fig. 5.12** EDX and elemental imaging of nanostructures obtained from the co-thermolysis of  $[\text{tBu}_2\text{Sn}(\text{Spyz})_2]$  and  $[\text{Cu}(\text{Spyz})(\text{PPh}_3)_2]$  in OLA at 300 °C for 20 minutes. 148

**Fig. 5.13** SEM of CTS nanostructures obtained from co-thermolysis of  $[\text{tBu}_2\text{Sn}(\text{Spyz})_2]$  and  $[\text{Cu}(\text{Spyz})(\text{PPh}_3)_2]$  in a) OA, b) OA-OLA at 300 °C and c) OLA at 275 °C for 20 minutes. 148

**Fig. 5.14** SEM, TEM and HRTEM of a), b), c) monoclinic CTS obtained from co-thermolysis of  $[\text{tBu}_2\text{Sn}(\text{Spyz})_2]$  and  $[\text{Cu}(\text{Spyz})(\text{PPh}_3)_2]$ ; d), e), f) orthorhombic SnS obtained from thermolysis of  $[\text{tBu}_2\text{Sn}(\text{Spyz})_2]$ ; g), h), i) cubic  $\text{Cu}_{1.8}\text{S}$  obtained from thermolysis of  $[\text{Cu}(\text{Spyz})(\text{PPh}_3)_2]$  at 300 °C for 20 minutes in OLA as solvent/capping agent. 149

**Fig. 5.15** (a) Simulated XRD pattern of cubic  $\text{Cu}_2\text{SnSe}_3$  (ICDD file no. 03-065-4145). XRD profiles of CTSe nanostructures obtained by thermolysis of  $[\text{Me}_2\text{Sn}(2\text{-Sepy}(3\text{-Me}))_2]$  and  $[\text{Cu}(2\text{-Sepy}(3\text{-Me}))_4]$  in OLA at (b) 230, (c) 260 and (d) 300 °C using heat up method and (e) in OLA at 300 °C using hot injection method (f) 300 °C in TOPO using heat up method. 152

**Fig. 5.16** p-XRD pattern of (a)  $\text{Cu}_2\text{Se}$  obtained by thermolysis of  $[\text{Cu}(2\text{-Sepy}(3\text{-Me}))_4]$  in OLA at 300 °C using heat up method. 153

- Sepy(3-Me))]<sub>4</sub>, (b) SnSe<sub>2</sub> obtained by thermolysis of [Me<sub>2</sub>Sn(2-Sepy(3-Me))<sub>2</sub>] and (c) cubic Cu<sub>2</sub>SnSe<sub>3</sub> obtained by co-thermolysis of [Me<sub>2</sub>Sn(2-Sepy(3-Me))<sub>2</sub>] and [Cu(2-Sepy(3-Me))]<sub>4</sub> in OLA at 300 °C by heat up method.
- Fig. 5.17** a) SEM, b) TEM and c) SAED pattern of CTSe nanostructures obtained by co-thermolysis of [Me<sub>2</sub>Sn(2-Sepy(3-Me))<sub>2</sub>] and [Cu(2-Sepy(3-Me))]<sub>4</sub> in OLA at 300 °C by heat up method. 154
- Fig. 5.18** SEM micrographs of nanostructures obtained by co-thermolysis of [Me<sub>2</sub>Sn(2-Sepy(3-Me))<sub>2</sub>] and [Cu(2-Sepy(3-Me))]<sub>4</sub> in a) TOPO (heat up method), b) OLA (hot injection method) at 300 °C. 155
- Fig. 5.19** Elemental mapping of CTSe nanostructure obtained by co-thermolysis of [Me<sub>2</sub>Sn(2-Sepy(3-Me))<sub>2</sub>] and [Cu(2-Sepy(3-Me))]<sub>4</sub> in OLA at 300 °C using heat up method. 156
- Fig. 5.20** Raman spectra of a) CTSe, b) Cu<sub>2</sub>Se and c) SnSe<sub>2</sub> nanostructures obtained either by thermolysis of [Me<sub>2</sub>Sn(2-Sepy(3-Me))<sub>2</sub>] and [Cu(2-Sepy(3-Me))]<sub>4</sub> individually or together in OLA at 300 °C by heat up method. 157
- Fig. 5.21** (a) X-ray photoelectron survey scan for CTSe nanostructures obtained by co-thermolysis of [Me<sub>2</sub>Sn(2-Sepy(3-Me))<sub>2</sub>] and [Cu(2-Sepy(3-Me))]<sub>4</sub> in OLA at 300 °C by heat up method. (b) Cu 2p, (c) Sn 3d and (d) Se 3d core level spectra. 158
- Fig. 5.22** Temperature dependent magnetic susceptibility CTSe nanostructures obtained by co-thermolysis of [Me<sub>2</sub>Sn(2-

Sepy(3-Me))<sub>2</sub>] and [Cu(2-Sepy(3-Me))]<sub>4</sub> in OLA at 300 °C by heat up method. Inset shows field dependent magnetization curve for Cu<sub>2</sub>SnSe<sub>3</sub> at 5K.

**Fig. 5.23** EPR spectrum of CTSe nanostructures obtained by co-thermolysis of [Me<sub>2</sub>Sn(2-Sepy(3-Me))<sub>2</sub>] and [Cu(2-Sepy(3-Me))]<sub>4</sub> in OLA at 300 °C by heat up method. 160

**Fig. 5.24** Plots of  $[F(R)hv]^2$  vs energy generated by Kubelka-Munk transformation of solid-state diffuse reflectance data of a) monoclinic CTS obtained from co-thermolysis of [<sup>t</sup>Bu<sub>2</sub>Sn(Spyz)<sub>2</sub>] and [Cu(Spyz)(PPh<sub>3</sub>)<sub>2</sub>], b) orthorhombic SnS obtained from thermolysis of [<sup>t</sup>Bu<sub>2</sub>Sn(Spyz)<sub>2</sub>] and c) cubic Cu<sub>1.8</sub>S obtained from thermolysis of [Cu(Spyz)(PPh<sub>3</sub>)<sub>2</sub>] at 300 °C for 20 minutes in OLA as solvent/capping agent, respectively for determining direct band gap energies. 162

**Fig. 5.25** Stack Plots of  $[F(R)hv]^2$  vs energy generated by Kubelka-Munk transformation of solid-state diffuse reflectance data of CTSe nanostructures obtained by co-thermolysis of [Me<sub>2</sub>Sn(2-Sepy(3-Me))<sub>2</sub>] and [Cu(2-Sepy(3-Me))]<sub>4</sub> in OLA at 300 °C by (a) hot injection method and (b) heat up method. 163

**Fig. 5.26** I-V characteristics of a) CTS, b) Cu<sub>1.8</sub>S and c) SnS nanostructures obtained by thermolysis of precursors in OLA at 300 °C for 20 minutes under dark (black) and light (red) conditions. 164

**Fig. 5.27** I-V characteristics of CTSe nanostructure (Efficiency = 1.7 %; 164

$V_{oc} = 339 \text{ mV}$ ;  $J_{sc} = 33.3 \mu\text{A}/\text{cm}^2$ ; Fill factor = 0.3) obtained by co-thermolysis of  $[\text{Me}_2\text{Sn}(2\text{-Sepy}(3\text{-Me}))_2]$  and  $[\text{Cu}(2\text{-Sepy}(3\text{-Me}))_4]$  in OLA at  $300^\circ\text{C}$ .

**Fig. 5.28** Current vs Time plot phase pure a) monoclinic CTS and b) cubic  $\text{Cu}_{1.8}\text{S}$ , nanostructures obtained at  $300^\circ\text{C}$  for 20 minutes using OLA as reaction solvent. 165

**Fig. 5.29** (a) Current vs. time plot of CTSe nanostructures obtained by thermolysis of co-thermolysis of  $[\text{Me}_2\text{Sn}(2\text{-Sepy}(3\text{-Me}))_2]$  and  $[\text{Cu}(2\text{-Sepy}(3\text{-Me}))_4]$  in OLA at  $300^\circ\text{C}$ ; (b) expanded view of one of the cycles. 165

# List of Tables

CHAPTER 1		Page No.
<b>Table 1.1</b>	Classifications and applications of semiconductors.	11
<b>Table 1.2</b>	Summary of typical binary and ternary tin chalcogenides and their properties.	21
CHAPTER 2		
<b>Table 2.1</b>	Crystallographic and structural determination data for $[\text{Et}_2\text{Sn}(2\text{-Spy})_2]$ , $[\text{tBu}_2\text{Sn}(2\text{-Spy})_2]$ and $[\text{tBu}_2\text{SnCl}(2\text{-Spy})]$ .	38
<b>Table 2.2</b>	Crystallographic and structural determination data for $[\text{Me}_2\text{SnCl}(2\text{-SpymMe}_2)]$ , $[\text{Et}_2\text{SnCl}(2\text{-SpymMe}_2)]$ and $[\text{tBu}_2\text{SnCl}(2\text{-SpymMe}_2)]$ .	39
<b>Table 2.3</b>	Crystallographic and structural determination data for $(\text{Sepy}(5\text{-Me}))_2$ and $[\text{R}_2\text{Sn}(2\text{-Sepy}(5\text{-Me}))_2]$ ( $\text{R} = \text{Me}, \text{Et}, \text{tBu}$ ).	40
<b>Table 2.4</b>	Crystallographic and structural determination data for $[\text{tBu}_2\text{Sn}(2\text{-SepymMe}_2)_2]$ , $[\text{nBu}_2\text{Sn}(2\text{-SepymMe}_2)_2]$ and $[\text{tBu}_2\text{SnCl}(2\text{-SepymMe}_2)]$ .	41
<b>Table 2.5</b>	Crystallographic and structural determination data for $[\text{tBu}_2\text{Sn}(\text{Spyz})_2]$ and $[\text{Cu}(\text{Spyz})(\text{PPh}_3)_2]$ .	42
<b>Table 2.6</b>	Crystallographic and structural determination data for $[\text{Me}_2\text{Sn}(2\text{-Sepy}(3\text{-Me}))_2]$ .	43
CHAPTER 3		
<b>Table 3.1</b>	Selected inter-atomic parameters ( $\text{\AA}/^\circ$ ) for $[\text{R}_2\text{Sn}(2\text{-Spy})_2]$ ( $\text{R} = \text{Et}, \text{tBu}$ ).	62

<b>Table 3.2</b>	Selected inter-atomic parameters (Å/°) for [ <sup>t</sup> Bu <sub>2</sub> SnCl(2-Spy)].	63
------------------	---	----

<b>Table 3.3</b>	Selected inter-atomic parameters (Å/°) for [R <sub>2</sub> SnCl(2-SpymMe <sub>2</sub> )] (R = Me, Et, <sup>t</sup> Bu).	64
------------------	---	----

## CHAPTER 4

<b>Table 4.1</b>	<sup>77</sup> Se{ <sup>1</sup> H} and <sup>119</sup> Sn{ <sup>1</sup> H} NMR data in CDCl <sub>3</sub> of diorganotin selenolate complexes with coupling constant values.	91
------------------	---	----

<b>Table 4.2</b>	Selected bond lengths (Å) and angles (°) of [(2-Sepy(5-Me)) <sub>2</sub> ].	96
------------------	---	----

<b>Table 4.3</b>	Selected bond lengths (Å) and angles (°) of [Me <sub>2</sub> Sn(2-Sepy(5-Me)) <sub>2</sub> ] and [ <sup>t</sup> Bu <sub>2</sub> Sn(2-Sepy(5-Me)) <sub>2</sub> ].	97
------------------	--	----

<b>Table 4.4</b>	Selected bond lengths (Å) and angles (°) of [Et <sub>2</sub> Sn(2-Sepy(5-Me)) <sub>2</sub> ].	98
------------------	---	----

<b>Table 4.5</b>	Selected bond lengths (Å) and angles (°) of [ <sup>t</sup> Bu <sub>2</sub> Sn(2-SepymMe <sub>2</sub> ) <sub>2</sub> ] and [ <sup>t</sup> Bu <sub>2</sub> SnCl(2-SepymMe <sub>2</sub> )].	99
------------------	--	----

<b>Table 4.6</b>	Selected bond lengths (Å) and angles (°) of [ <sup>n</sup> Bu <sub>2</sub> Sn(2-SepymMe <sub>2</sub> ) <sub>2</sub> ].	100
------------------	--	-----

<b>Table 4.7</b>	Reaction conditions, structural, compositional and optical parameters of tin selenides.	105
------------------	---	-----

<b>Table 4.8</b>	XRD data for tin selenide nanosheets obtained by the thermolysis of [R <sub>2</sub> Sn(2-SepymMe <sub>2</sub> ) <sub>2</sub> ] (R = Et, <sup>n</sup> Bu and <sup>t</sup> Bu).	112
------------------	---	-----

## CHAPTER 5

<b>Table 5.1</b>	Selected bond lengths (Å) and angles (°) of [ <sup>t</sup> Bu <sub>2</sub> Sn(Spyz) <sub>2</sub> ] and [Cu(Spyz)(PPh <sub>3</sub> ) <sub>2</sub> ].	137
------------------	---	-----

<b>Table 5.2</b>	Reaction condition, structural, morphological, compositional and optical parameters of nanostructures.	143
<b>Table 5.3</b>	Lattice parameter of nanostructures (CTS, SnS and Cu <sub>1.8</sub> S) synthesized in OLA at 300 °C.	144
<b>Table 5.4</b>	Reaction conditions, structural and elemental composition and optical band gap data of nanostructures.	153
<b>Table 5.5</b>	Raman spectroscopic data for CTSe.	158



# Chapter 1

## General Introduction

### 1.1 Introduction and Historical Background of Nanomaterials:

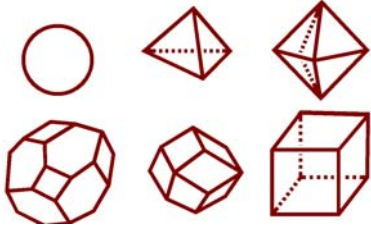
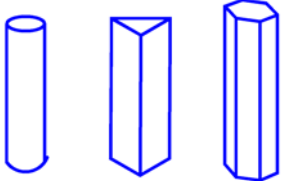

Nanomaterials are considered as materials having size intermediate between bulk and individual molecule with at least any one dimension in the range of 1 to 100 nm [1]. These came into existence immediately after the big bang when nanomaterials were formed in early meteorites. The utility of nanomaterials for mankind can be traced back to Roman period. Craftsmen's in those days were adept at impregnating glass with metal particles to achieve dramatic colour effects. For instance, the Lycurgus cup (from 4<sup>th</sup> century Rome), a glass cup, is a stunning decorative Roman treasure which appears green in reflected light and red in transmitted light. This effect is due to the presence of Au and Ag nanocrystals on the walls of the cup [2]. Systematic studies on nanomaterials began to appear as early as seventeenth century. Michael Faraday in 1857 [3] carried out pioneering work on colloidal metals (divided metals) and produced ruby colored gold sols. He observed that colloidal metal sols were thermodynamically unstable and can be stabilized kinetically against aggregation. Ostwald carried out extensive research on colloidal particles and published his findings in a book entitled "The world of neglected dimensions" in 1915. Meanwhile, numerous methods were discovered to make colloidal metal particles. Zsigmondy [4] discovered that formaldehyde can be used to make gold sols from the corresponding salts under mild alkaline conditions. The renewed interest in atomic scale materials, has been initiated after a lecture "There's Plenty of Room at the Bottom", a visionary lecture given by American Physicist Richard Feynman at CalTech in 1959 [5] and reasoned that "*The principle of physics as far as I can see, do not speak against the possibility of manoeuvring things atom by atom*". He saw miniaturisation of

science as an “*invitation into a new field of physics*” and predicted some of the impacts nanoscience could have.

Reducing the size of a material to such a scale can create severe divergence in its physical properties due to increase in surface area to volume ratio. As the size of the material is reduced, the number of atoms exposed on the surface increase exponentially compared to atoms in bulk. For example Au and Ag, in bulk form were considered as chemically inert but they become extremely reactive in nano regime and exhibit pronounced catalytic activity [6].

## **1.2 Classification of Nanomaterials**

The morphology of nanomaterials can be categorized in terms of dimensionality (Fig. 1.1). Zero dimensional (0D) nanomaterials are best exemplified by the quantum dots (QDs) with dimensions in nanometer scale size in all three directions [7]. QDs find various applications due to their distinct advantages, such as narrow and symmetric emission with tunable colors, broad and strong absorption. Rods, cylinders, wires and tubes are examples of one-dimensional (1D) nanostructures which exhibit unique optical/electronic properties due to anisotropic shape [8]. Two dimensional (2D) nanomaterials, like discs, ribbons, plates and thin films typically of semiconductor material, are defined by the flow of electrons which is only confined in one dimension, because the other two dimensions are allowed to continue to grow through free propagation [9]. Ability to control the dimensions and morphology of nanomaterial is one of the challenging issues in materials chemistry. Recent studies reveal that factors like the reaction temperature and duration of reaction, surfactants and precursor concentrations play a profound role in governing the shape and dimensions of nanomaterials.

0 D	
1 D	
2 D	

**Fig.1.1** Nanomaterials having different dimensions (a) 0D spheres and clusters, (b) 1D nanofibers, wires and rods, (c) 2D films, plates and networks, [9].

### 1.3 Semiconductors

A semiconductor is a material that has an electrical conductivity between a conductor (metals) and insulator. The conductivity value of semiconductors varies from ( $10^4$  to  $10^{-8} \Omega \text{ cm}^{-1}$ ). The semiconductors are also classified in terms of band gap which is: energy required by an electron to cross over from the valence band to the conduction band. Materials with an electronic band gap typically between 0.6 and 4 eV are termed as semiconductors whilst those with larger band gaps, often greater than 5 eV are categorised as insulators. At absolute zero temperature, a semiconductor behave like an insulator while at room temperature, a few electrons acquire enough thermal energy to overcome the energy gap between valence band and conduction band [10].

## 1.4 Band structure

The electronic band structure of a solid illustrates the range of “allowed” or “forbidden” energies that an electron can have within the solid. The band structure of a material determines several characteristics, in particular its electronic and optical properties. Energy band is formed when large number of atoms (of the order  $10^{20}$  or more) combine together to form crystal lattice, their atomic orbital splits, as in coupled oscillations to produce molecular orbitals proportional to the number of atoms with nearly same energies. The adjacent energy levels are so close that they can be considered as continuous band of energies. However, there is a forbidden space or region or gap between these energy bands corresponding to the intervals of energy that are void of orbitals, no matter how many atoms *viz.* atomic orbitals are aggregated [11]. The size and existence of this band gap allows us to visualize the difference between metals, semiconductors and insulators (Fig. 1.2). In metal there is overlap between conduction band and valence band, therefore they have very high conductivity. In insulator and semiconductors, the valence band is full while conduction band is completely empty. The electrons are bound to valence band and are not free to move.

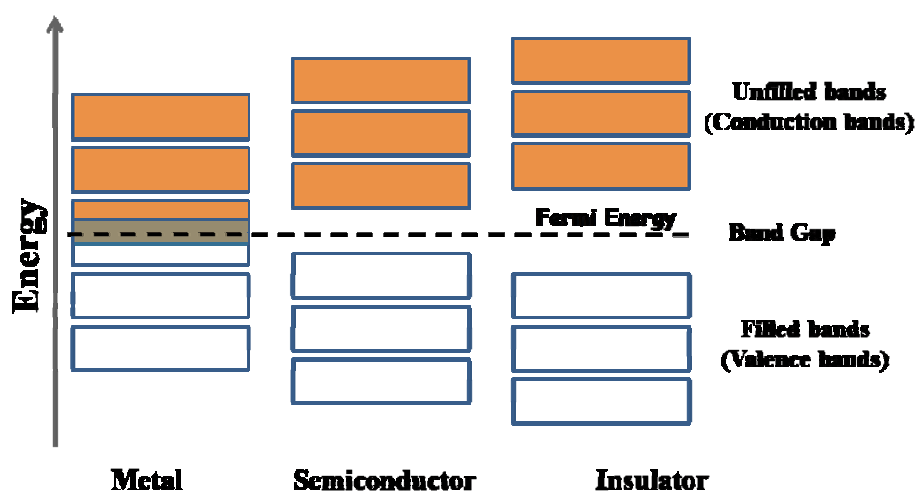


*Fig. 1.2 Electronic band structure of metals, semiconductors and insulators.*

The only difference between insulators and semiconductors is the size of band gap which is larger in case of insulator (Fig 1.2). Band gap of semiconductor often lies in the range of IR-Vis-UV region. Thus, at room temperature some electrons in the valence band acquire thermal energy greater than forbidden gap and jump to conduction band where they can participate in conduction [10, 12].

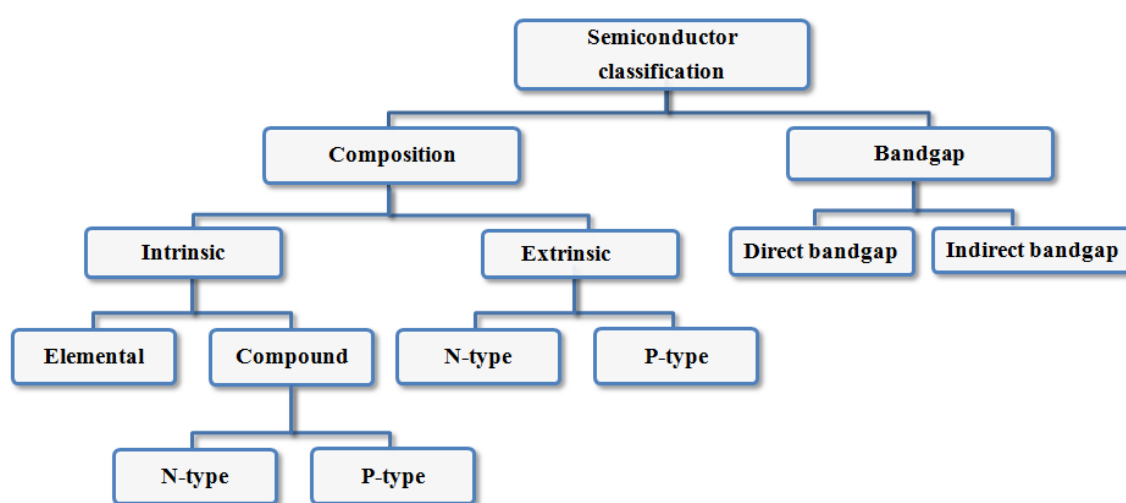


**Fig. 1.3** Classification of semiconductors

## 1.5 Intrinsic and Extrinsic Semiconductors

The conductivity of semiconductors depends not only on temperature but also on the amount and nature of impurities present in the material. Presence of different kind of impurities in a semiconductor can alter its conductivity up to 10 orders of magnitude. This offers a possibility to manipulate the semiconductor properties according to our requirements by controlling the amount of particular impurities in the material. The addition of precise amount of impurities for tailoring the properties of a semiconductor is called doping and the impurity being added is called dopant. On the basis of doping of

impurities, the semiconductors can be classified as Intrinsic and Extrinsic semiconductors (Fig. 1.3).

An intrinsic semiconductor is a pure form of semiconductor devoid of any impurity. It is also called an undoped semiconductor. At finite temperatures the only charge carriers are the electrons in the conduction band and the holes in the valence band that arise as a result of the thermal excitation of electrons to the conduction band. Intrinsic semiconductor has equal density of these intrinsic charge carriers (electron and holes). The Fermi level always lies in the middle of bandgap (i.e.  $E_f = E_g/2$ ) and is temperature independent. Pure crystalline silicon and germanium and compound such as CdSe, SnS or SnSe are included as examples of intrinsic semiconductors.

An intrinsic semiconductor when doped with a specific impurity atom/dopant to preferentially modify its conductivity is known as extrinsic semiconductor. Dopants are used in a very small concentration i.e., of the order of ppm (parts per million) to ppb (parts per billion), so that the crystal lattice of intrinsic semiconductor remains undisturbed. Impurity atoms act as either charge carriers donors or acceptors to the intrinsic semiconductor by changing the electron and hole concentrations of the semiconductor. The density of electrons and holes in extrinsic semiconductor is not equal. An electron donor dopant, when incorporated in the crystal donates additional valence electrons into the crystal lattice, thereby increasing the electron (negative charge) carrier concentration of semiconductor, making it n-type. For example, addition of small amount of pentavalent impurity, like arsenic (As), to Si will generate n-type semiconductor. These additional electrons are weakly bound to the parent impurity atoms and are capable of jumping to the conduction level even at low temperatures. These extra electrons create a donor electron level just below the conduction band (Fig. 1.4a). The donor level does not display band like properties and is discrete. The thermal energy can cause these

electrons to jump from donor level to the conduction band, making them available for conduction and are responsible for the large increase in conductivity. The energy difference between donor level and conduction band of As doped Si is 0.1 eV which is considerably less than the band gap of Si (1.1 eV). Therefore, less thermal energy is required for electronic excitation in As doped Si compared to pure Si. The Fermi level in n-type materials is temperature dependent and it is just above the donor level energy ( $E_d$ ) slightly below the conduction band.

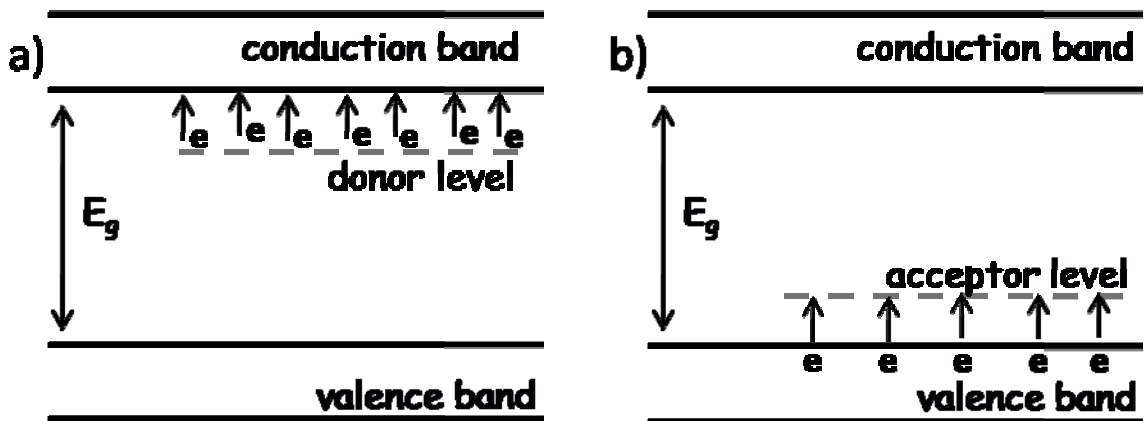


**Fig. 1.4** Band structure of extrinsic semiconductor; a) n-type with donor levels, b) p-type with acceptor levels.

Similarly, a trivalent dopant like boron (B) or gallium (Ga) when added to an intrinsic semiconductor (Si), forms three bonds with three Si atoms and an extra electron from the valence band of Si moves to the acceptor level of trivalent impurity (B) leaving behind the holes in the valence band. Similar to the donor levels in n-type materials, the acceptor levels in p-type materials do not display band-like qualities and electrons are not free to move (i.e. they are localized energy levels). However, the movement of these holes in the valence band causes conduction of the material. Since the acceptor atoms accept electrons from the valence band their energy levels are located close to the valence

band (Fig. 1.4b). In p-type, the Fermi level is located slightly below the acceptor energy level ( $E_a$ ), and just above the valence band [13].

## 1.6 Direct and Indirect Band gap Semiconductors

Semiconductors can further be classified on the basis of band gap as direct band gap and indirect band gap semiconductors (Fig. 1.3). The bottom of conduction band (minimal energy state) and the top of the valence band (maximal energy state) are characterized by the crystal momentum (k-vector). If the k-vectors are same then it is direct band gap semiconductors while for different value k-vectors are different then the semiconductor is termed as indirect band gap semiconductor (Fig. 1.5). In direct band gap semiconductors such as GaAs, CdSe or GaN, the momentum of electrons and holes are same in conduction and valence band, thus electron promotion from valence band to conduction band occur without a change in crystal momentum. Only potential energy of an electron will change during the transition. However, in indirect band gap semiconductor e.g., Ge or Si, the transition of an electron from valence band to conduction band violates conservation of momentum and is forbidden. However, transition does occur but with phonon assistance. Carrier life time is relatively small in case of direct band gap semiconductor compared to indirect band gap semiconductors. The processes in indirect band gap semiconductors proceed at much slower rate relative to direct processes [10, 13]. For this reason, Si is not used for the generation of optical signal and Lasers.

The optical band gaps of the semiconductor materials were determined from a plot of Kubelka-Munk function [14],  $F(R)$  as given in equation 1.

$$F(R) = A(h\nu - E_g)^{m/2} \quad (1.1)$$

Where  $h\nu$  = photon energy and  $m$  is a constant that depends on the nature of optical transition. For a direct transition,  $m$  is 1 (if allowed) or 3 (if forbidden), while for indirect



transitions,  $m$  is 4 (if allowed) or 6 (if forbidden). For a semiconductor,  $F(R)$  is proportional to the absorbance,  $A$ . Hence, the energy intercept of a plot of  $A^2$  (for direct allowed transition) and  $A^{1/2}$  (for indirect allowed transition) versus  $h\nu$  yields the corresponding optical band gap,  $E_g$ , when the linear region is extrapolated to the zero ordinate.

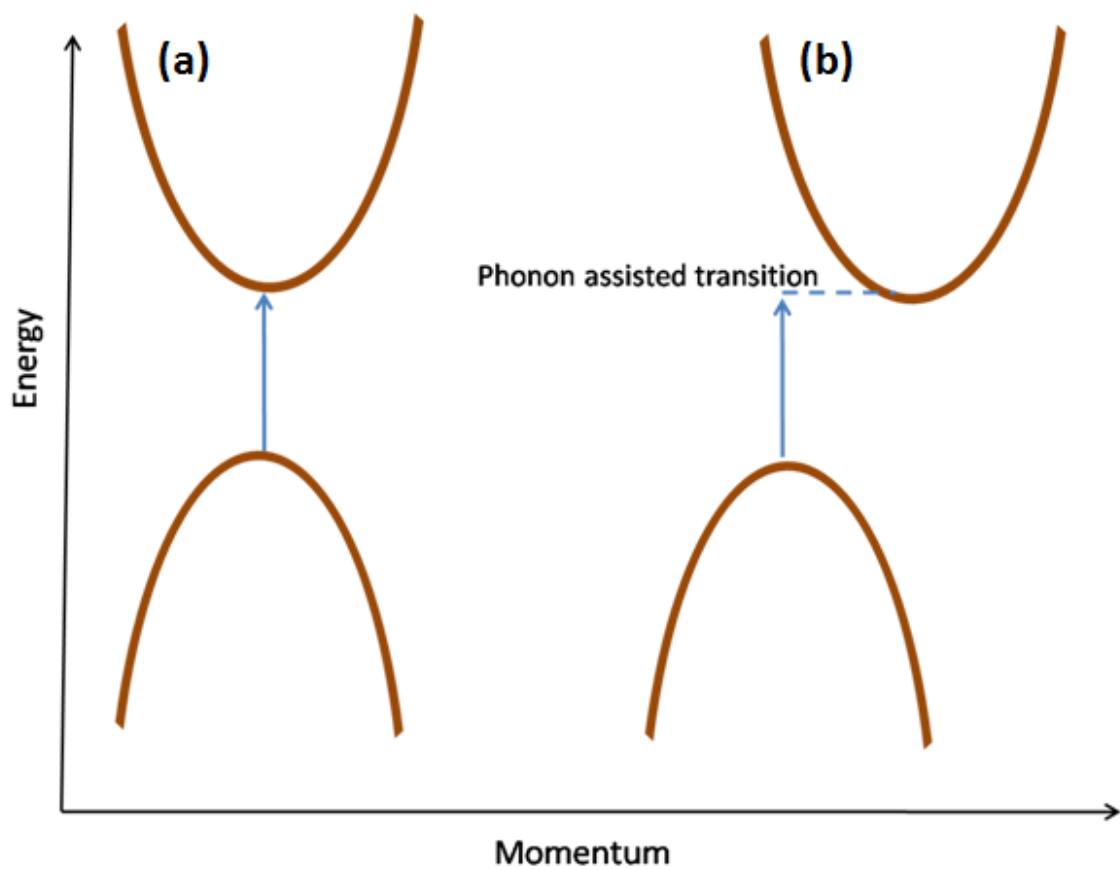


**Fig.1.5** Energy vs crystal momentum for a) direct semiconductor and b) indirect semiconductor.

## 1.7 Semiconductor nanomaterials

Semiconductor nanomaterials have gained considerable attention in recent past with their potential use in a wide range of technological applications [15, 17]. Nanoparticles of

semiconducting materials with all three dimensions in the range of 1–20 nm possess unique properties. Bulk semiconductors have composition-dependent band gap energy ( $E_g$ ). By absorbing a photon of energy greater than  $E_g$ , the electron from valence band gets excited leaving an orbital hole in valence band. The electron and hole in conduction and valence band respectively, may be mobilized in the presence of an electric field to yield a current. However, their lowest energy state is an electrostatically bound electron-hole pair, known as the exciton. The exciton has a finite size within the crystal defined by the Bohr exciton diameter ( $a_B$ ), which can vary from 1 nm to more than 100 nm depending on the material. If the size of a semiconductor nanocrystal is smaller than the Bohr diameter, the charge carriers become spatially confined, leading to transitions from continuous to discrete energy levels. Subsequently, size dependent electrical and optical properties will be observed [18]. At a given temperature, this variation in properties occurs at relatively large size in semiconductors compared to metals. The advantages associated with semiconductor nanoparticles for solar cell applications are, a) their absorption can be easily tuned to match the spectral distribution of sunlight with variation in size and b) the large intrinsic dipole moment of quantum dots can lead to rapid charge separation. Semiconductors in their bulk form as well as in nano dimensions find applications in various frontier areas. Summary of general applications of semiconductor nanoparticles are listed in Table 1.1.

Despite of appealing features of semiconductor nanoparticles, there is health risk associated with their exposure. The health risk originates from two effects:

- (i) Toxic effects of the constituent elements of the semiconductor nanoparticle.
- (ii) Toxic effects induced by the small dimensions of the particles. The latter influences their circulation in the body and accumulation in different organs. Moreover their high surface to volume ratio leads to the formation of reactive molecules causing

oxidative stress. It is predicted that skin and eyes followed by GI tract and lungs are the primary target organs of semiconductor nanomaterials toxicity. [26]

**Table 1.1** *Classifications and applications of semiconductors*

Semiconductor	Example	Applications	References
Group IV	Si, Ge, Diamond	Solar Cells, HPGe, Diamond detector.	[19, 20]
II-VI	ZnO, ZnS, ZnSe, CdS, CdSe, CdTe, CdZnTe	IR detectors, Solar cell, $\gamma$ -ray spectroscopy, Anti- bacterial property.	[19, 21]
III-V	AlN, GaN, InN, InP, GaAs	Light emitting diodes.	[19]
IV-VI	GeS, GeSe, SnS, SnSe, PbS, PbSe, Cu <sub>2</sub> SnS <sub>3</sub> (CTS), Cu <sub>2</sub> SnSe <sub>3</sub> (CTSe), Cu <sub>2</sub> ZnSnS <sub>4</sub> (CZTS), Cu <sub>2</sub> ZnSnSe <sub>4</sub> (CZTSe)	H <sub>2</sub> production, waste water treatment, photovoltaic, IR detectors, Thermal imaging, Thermoelectric material.	[22, 23]
V-VI	Sb <sub>2</sub> S <sub>3</sub> , Sb <sub>2</sub> Se <sub>3</sub> , Bi <sub>2</sub> S <sub>3</sub> , Bi <sub>2</sub> Se <sub>3</sub> , CuSbSe <sub>2</sub>	Thermoelectric material, Topological Insulator, Solar cell material.	[24, 25]

### **Nanostructured Metal Chalcogenide Semiconductors: IV-VI materials**

The discovery of graphene (a 2D carbon allotrope), has ignited intensive research in a wide range of 2D layered material [27-30]. Monolayer graphene finds promising applications in ultrahigh frequency photosensors [31] because of linear dispersion of the Dirac electrons [32]. However, the absence of band gap has prevented the graphene to be utilised in nanoelectronics.

This diverted the focus to other layered materials which possess band gap, in particular metal chalcogenides. Metal chalcogenides is like graphene having strong bonding within the layer and weak van der Waals interactions between neighbouring layers. Contrary to graphene, these metal chalcogenides possess band gaps which can be further adjusted over a broad range by varying thickness. The band gap tuning enables the 2-D layered metal chalcogenides to display a wide range of unique chemical and physical properties which have been used for diverse applications such as optoelectronic, photovoltaic devices, transistors, lithium ion battery, hydrogen generation by photocatalytic splitting of water and many more [33-36]. Few layered transition metal chalcogenides ( $\text{MoS}_2$  [37, 38],  $\text{WS}_2$  [39, 40] etc.) have been extensively explored in various fields such as gas sensing [41, 42], photodetectors [43, 44], and flexible devices [45-48].

Besides transition metal chalcogenides, several main group metal chalcogenides (III–VI (e. g.,  $\text{GaS}$ ,  $\text{GaSe}$ ,  $\text{In}_2\text{Se}_3$ ); IV–VI (e. g.,  $\text{GeS}$ ,  $\text{SnS}$ ,  $\text{SnSe}$ ,  $\text{SnSe}_2$ ,  $\text{PbS}$ ,  $\text{PbSe}$ , etc.) and V–VI (e. g.,  $\text{Bi}_2\text{Se}_3$ ,  $\text{Bi}_2\text{Te}_3$ , etc.)) also exhibit layered structures. The interest in the narrow band gap IV–VI layered semiconductor nanostructures is increasing due to their promising optoelectronic properties which have relevance in photovoltaic [49,50], photodetector [51, 52] and thermoelectric devices [53-56]. Lead chalcogenide nanoparticle ( $\text{PbS}$ ,  $\text{PbSe}$  and  $\text{PbTe}$ ) were the first IV–VI semiconductor nanoparticles to

receive experimental interest as practical photovoltaic (PV) and thermoelectric materials. Their band gaps can be tuned across infrared and visible wavelengths through quantum confinement. In spite of the promising results obtained from lead chalcogenide-based PVs and thermoelectrics, the toxicity of lead and the potential of lead exposure are considered a significant threat to public health [57-59].

However, tin based chalcogenides materials are gaining interest due to their earth abundant, low cost and environmentally benign characteristics [22, 60, 61] which significantly promote their value in sustainable electronic and photonic systems. Unlike lead, inorganic tin compounds are not readily absorbed into the blood stream through ingestion or inhalation [62]. They are also projected as substitute for the technologically well-established materials of the same group which are based either on scarce (Ge) or toxic (Pb) elements. The main advantage that tin based chalcogenides offers over other mainstream PV materials such as over organic photovoltaics (OPVs) and lead perovskites is their greater stability. OPVs suffer from photodegradation of organic molecules, of the photoabsorber due to oxidation [63]. Lead perovskites have a similar stability issue, with the material being sensitive to oxygen and water [64-66]. Along with photovoltaics [23, 67, 69], tin based chalcogenides find extensive applications in the field of thermoelectric materials [69-71]. Before discussing the synthetic protocols of tin based chalcogenides, it may be relevant to discuss some salient features of tin and tin based chalcogenides (binary and ternary).

## **1.8 General properties of tin and tin based chalcogenides**

### **1.8.1 General properties of tin**

Tin (Sn) together with carbon, silicon, germanium and lead comprises the main group IV of the periodic table. All these elements possess the outer electronic configuration,  $ns^2np^2$ . Tin melts at 505 K and its boiling point is 2875 K. It mainly occurs

in two allotropic forms namely  $\alpha$  tin (gray, diamond cubic crystal structure) and  $\beta$  tin (white, tetragonal structure). Sn is classified as hard acid in Pearson's hard-soft-acid-base (HSAB) concept. The principal valence state of tin is Sn(IV) (stannic), though Sn(II) (stannous) inorganic compounds are fairly common.

Several stannous organometallic compounds with specially designed structures are reported in recent past. There is interesting redox chemistry between Sn(II) and Sn(IV) species, and its organometallic and metal-organic complexes are also fairly stable. Sn also has a wide-range of alloy compositions with various properties. Tin has ten stable isotopes, which is the largest number for any element leading to a very characteristic mass spectrum. Among these isotopes,  $^{115}\text{Sn}$  (0.3%),  $^{117}\text{Sn}$  (7.6%) and  $^{119}\text{Sn}$  (8.6%), each with spin  $\frac{1}{2}$  are magnetically active nuclei and hence suitable for NMR spectroscopy. Most tin NMR parameters refer to the  $^{119}\text{Sn}$  nucleus due to its slightly higher natural abundance and its greater sensitivity to NMR detection. Coupling between tin and other nuclei such as  $^1\text{H}$ ,  $^{13}\text{C}$ ,  $^{77}\text{Se}$ ,  $^{31}\text{P}$  etc. is possible and the corresponding coupling constant provides invaluable information about the structure of organotin compounds. The  $\gamma$ -active  $^{119\text{m}}\text{Sn}$  isotope, which is prepared by the neutron-irradiation of enriched  $^{118}\text{Sn}$ , is used in Mössbauer spectroscopy and like NMR it is also a powerful tool for investigating the tin compounds [72, 73].

### 1.8.2 General properties of tin based chalcogenides

Tin chalcogenides exist in several crystal phases such as hexagonal, monoclinic and orthorhombic phases depending upon the oxidation state of the Sn with each phase having unique characteristics.  $\text{SnE}$  ( $\text{E} = \text{S}, \text{Se}$ ) crystallizes into orthorhombic phase while  $\text{SnE}_2$  exist in hexagonal and monoclinic phases. The crystal structure of  $\text{SnE}_2$  is similar to that of layered molybdenum chalcogenides, extensively investigated transition metal 2D materials [22, 74].

### SnE (E = S, Se) systems

Tin monochalcogenides possess an electron configuration of  $4d^{10}5s^25p^0$  for  $\text{Sn}^{2+}$  and  $ns^2np^6$  for the corresponding anion. The Sn undergoes  $sp^2$  hybridization where two Sn(5p) electrons are engaged in bond formation while Sn(5s) electrons act as a lone pair [73]. The band structure for SnS and SnSe is depicted in a way that the valence band is derived from the p orbitals of  $\text{S}^{2-}$  or  $\text{Se}^{2-}$  with some s band character of the cation), while the bottom of the conduction band is derived with a major contribution from the empty p orbitals of  $\text{Sn}^{2+}$  [23, 75-77]. The lone pair present in the Sn orbital does not participate in bonding to an appreciable extent, but leads to distortion in regular octahedral geometry around the  $\text{Sn}^{2+}$  ion. SnS and SnSe are intrinsically p-type semiconductors as the tin vacancies in the lattice produce acceptor levels [78].

Computational calculation predicts a systematic decrease in the bulk band gap of tin monochalcogenides as we move down the chalcogen group from S to Se [ $E_g$  for SnS and SnSe is 2.1 and 1.3 eV, respectively]. Moreover, from tight binding calculations, it has been evaluated that both SnS and SnSe possess direct and indirect band gaps with a very small energy difference [75, 79, 80].

Tin monochalcogenide (SnS, SnSe) crystallize into orthorhombic crystal lattice with  $P_{nma}$  space group (lattice parameters  $a = 11.198 \text{ \AA}$ ,  $b = 4.000 \text{ \AA}$ ,  $c = 4.285 \text{ \AA}$  for SnS [81] and  $a = 11.501 \text{ \AA}$ ,  $b = 4.153 \text{ \AA}$ ,  $c = 4.445 \text{ \AA}$  for SnSe [82, 83]) at room temperature. The structures are derived from three dimensional highly deformed rock salt structure (NaCl) [84-86]. The Sn and S/Se atoms are arranged in double layers of tightly bound Sn-S/Se atoms in zig-zag accordion like projection (Fig. 1.6a)[87, 88]. The unit cell contains highly distorted  $\text{SnS}_7$  or  $\text{SnSe}_7$  coordination polyhedra, which have three short and four very long Sn-Se/S bonds with the lone pair of  $\text{Sn}^{2+}$  sterically occupied one of the

symmetrical site [84]. Moreover, its crystal packing is different along the  $b$  and  $c$  axial directions, which leads to its anisotropic nature.

Interestingly SnS and SnSe, known to undergo a temperature dependent structural evolution and second order displacive phase transition from less symmetric orthorhombic phase ( $P_{nma}$  space group) i.e.  $\alpha$  form to a five-fold coordinated higher symmetry  $\beta$  form having  $C_{mcm}$  space group (lattice parameters  $a = 4.12 \text{ \AA}$ ,  $b = 11.48 \text{ \AA}$ ,  $c = 4.17 \text{ \AA}$  for SnS [89] and  $a = 4.31 \text{ \AA}$ ,  $b = 11.70 \text{ \AA}$ ,  $c = 4.31 \text{ \AA}$  for SnSe [85, 89]) with a movement of cation and anion along the  $[100]$  direction, caused apparently by thermal expansion (Fig. 1.6) [86, 88, 90]. In  $C_{mcm}$  phase the bilayer structure is preserved and each atom is now coordinated to four neighbouring atoms at an equal distance in the x-y plane [90]. This type of second order displacive phase transition occurs at higher temperature (around 878 K for SnS and 800 K for SnSe). In addition, there is a known metastable phase of SnS ( $a = 6.00 \text{ \AA}$ ) that possesses a cubic structure [91]. It is worth mentioning that unlike SnS and SnSe which prefer to crystallize in orthorhombic phase, SnTe possesses a cubic  $F_{m3m}$  structure ( $a = 6.32 \text{ \AA}$ ), similar to the lead monochalcogenides, that is stable up to 1000 K where a congruent melt occurs [92].

The anharmonic and anisotropic bonding in the SnE structure leads to high Grüneisen parameters, ultralow thermal conductivity and record high thermoelectric figure of merit ZT of 2.6 (for SnSe) [84, 93]. Due to high figure of merit ZT, these materials are of great utility for thermoelectric devices. Along with high figure of merit, these materials have intense absorption ( $\sim 10^5 \text{ cm}^{-1}$ ) across the electromagnetic spectrum, a narrow band gap, hole concentration of  $10^{18} \text{ cm}^{-3}$ , Hall mobility (resistivity  $0.06 \text{ U cm}$ ) of  $90 \text{ cm}^2 \text{ V}^{-1} \text{ s}^{-1}$  at room temperature due to which they find extensive applications as photon absorber material in photovoltaic cells and optoelectronic devices [95-97].



SnS solar cell device is believed to deliver a maximum power conversion efficiency (PCE) of 24% for a single junction solar cell as predicted by Prince–Loferski diagrams [97,98]. But as of now, the highest PCE recorded for SnS solar cell device was about 4% much lower than the theoretically predicted value [99]. Issues linked to the poor performance such as small grain sizes, band gap misalignment near the interface, impurity of interface and off stoichiometry, needs to be addressed in order to improve the efficiency of SnS based single junction solar cell [99,100].

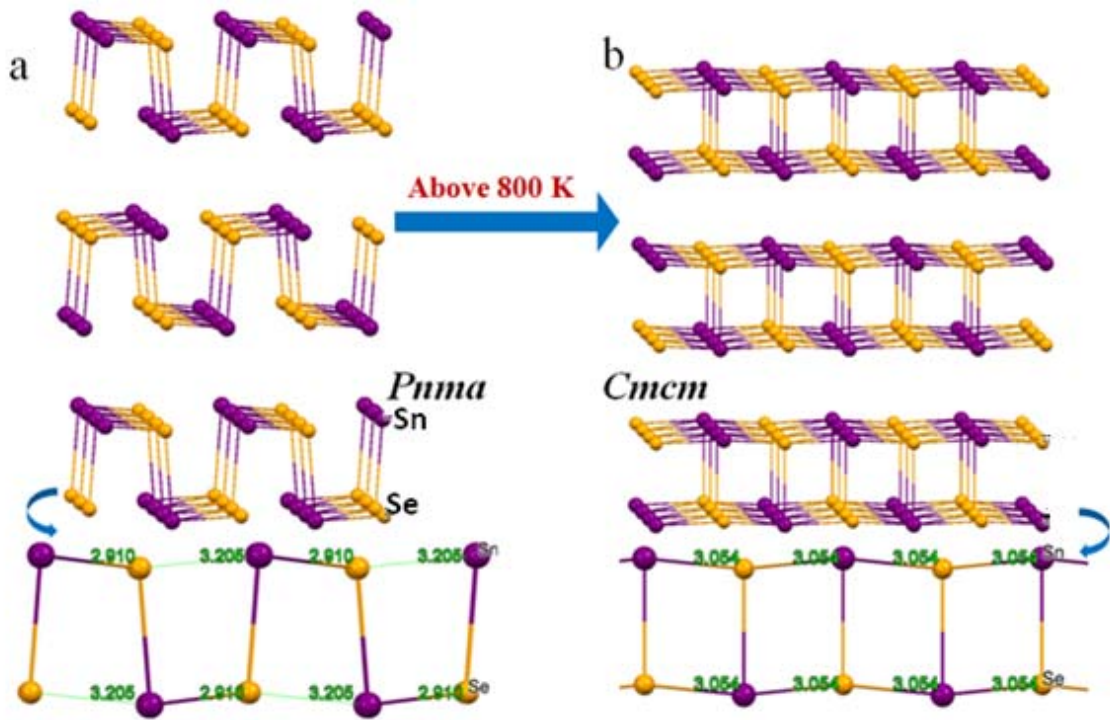


**Fig. 1.6** Structure of SnSe a)  $Pnma$  phase below 800 K and b)  $Cmc21$  phase above 800 K, respectively [adopted from Ref. 88].

## SnE<sub>2</sub> (E = S, Se) systems

Tin dichalcogenides (SnS<sub>2</sub> and SnSe<sub>2</sub>) like tin monochalcogenides (SnS and SnSe), possess a layered structure and exhibit rich structural polytypism which results from the various stacking sequences of identical E-Sn-E (E = S, Se) layers.

Tin dichalcogenides generally crystallizes in a CdI<sub>2</sub> type layered structure with space group  $P\bar{3}m1$  (lattice parameters  $a = 3.64 \text{ \AA}$ ,  $c = 5.89 \text{ \AA}$ , for SnS<sub>2</sub>) and ( $a = 3.81 \text{ \AA}$ ,  $c = 6.14 \text{ \AA}$ , for SnSe<sub>2</sub>) to form a native n-type semiconductor [22,101]. The Sn atoms are sandwiched between two layers of hexagonally packed chalcogenide atoms forming SnE<sub>6</sub> (E = S, Se) octahedral coordination at their edges (Fig. 1.7) [74,102]. Each layer possesses a thickness of 6-7  $\text{\AA}$  approximately. The intra-layer Sn-E (S, Se) bonds are predominantly covalent in nature while the adjacent chalcogenide layers are coupled by weak van der Waals forces [102,103]. The Sn atoms provide four electrons to fill the bonding molecular orbitals of SnE<sub>2</sub> such that the oxidation states of Sn and E atoms in SnE<sub>2</sub> are +4 and -2, respectively. The lone pair of electrons present on chalcogen atoms put an end to the surfaces of the layers and the non appearance of the dangling bonds renders those layers inert towards surface oxidation [104].

The semiconducting nature of SnSe<sub>2</sub> was recognised in 1955 during an exploration into the fundamental factors which are responsible for intrinsic semiconducting nature in the compounds formed by the metalloids Se and Te [61, 105]. Owing to their high charge carrier concentration ( $10^{17}$ – $10^{19} \text{ cm}^{-3}$ ), appreciable electron mobility ( $\mu_e$ : 0.6–85  $\text{cm}^2/\text{Vs}$ ), high absorption coefficient, tunable band gap for a wide range of electromagnetic spectrum from 1–2.2 eV, high electrical conductivity and appealing catalytic activity of tin dichalcogenides their utility in photovoltaic devices and lithium ion/sodium ion batteries has been demonstrated [60, 106-110]. In addition, their anisotropic structure in nano regime leads to negative correlation between enhanced electrical conductivity ( $\sigma$ )

and reduced thermal conductivity ( $\kappa$ ) which projects them as a promising material for thermoelectric applications [22, 104, 106].

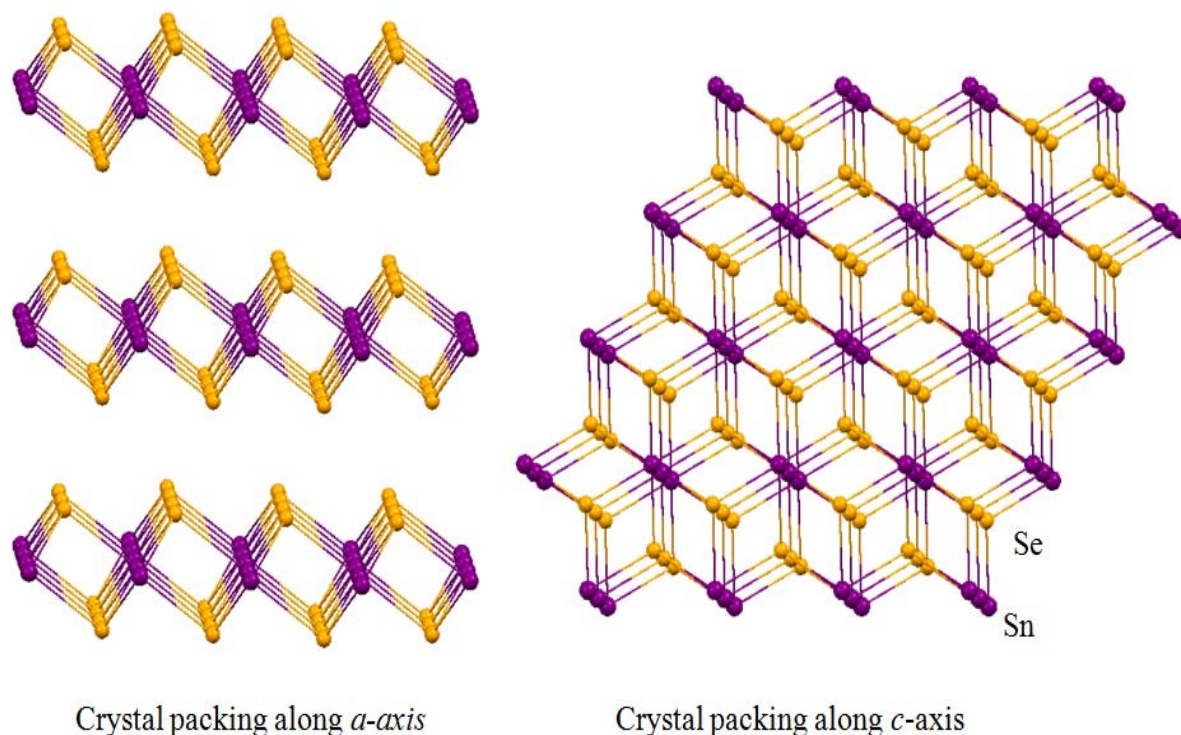


**Fig. 1.7** Crystal structure of layered hexagonal 2D  $\text{SnSe}_2$  [adopted from Ref. 22].

General properties of tin based binary and ternary chalcogenides nanostructures have been listed in table 2

### **Tin based ternary metal chalcogenides**

In addition to, binary tin chalcogenides, there is an interesting family of tin related ternary and quaternary systems. Compared to binary, ternary materials not only exhibit outstanding physical, chemical and electronic properties (high charge carriers mobility, intense photon absorption) but also provide some distinct advantages as discussed below that binary systems do not possess:

- (i) Ternary systems have greater number of degrees of freedom for tailoring their physical properties such as band gap via stoichiometric variation. For instance, band gap engineering or tuning in binary metal chalcogenide system can be attained only by varying the size whereas in ternary systems it can be accomplished fairly easily by varying the composition and size. Variation in ratio of constituent elements not only changes the band gap but sometimes also exhibits new structure [111, 112, 113].
- (ii) Unlike, binary semiconductors, off-stoichiometry ordered structures present in ternary systems do not lead to the formation of deep trap states which would compromise the use of these materials in optoelectronics [114].

However, one of the challenges often encountered during the synthesis of ternary nanostructures is controlling their composition and crystal structure. Due to structural complexities associated with ternary materials there is always a possibility of existence of binary impurities along with the final product.

Tin based ternary chalcogenides ( $\text{Cu}_2\text{SnS}_3$  (CTS) and  $\text{Cu}_2\text{SnSe}_3$  (CTSe)) have received considerable attention due to their solution processability and low cost. They are projected as substitutes for the technologically well established solar cell materials such as PbSe, PbTe, CdTe,  $\text{CuInSe}_2$ ,  $\text{Cu(In, Ga)Se}_2$ , etc. which are based either on scarce (Ga, In, Te) or toxic (Cd, Pb) elements [115, 116].

**Table 1.2** Summary of typical binary and ternary tin chalcogenides and their properties.

<b>Tin Chalcogenide</b>	<b>Crystal Structure</b>	<b>Lattice parameters (Å)</b>	<b>Electronic property</b>	<b>Bulk bandgaps (eV)</b>	<b>References</b>
SnS	Orthorhombic	a = 11.19, b = 4.00, c = 4.28	p-type	2.1	82
SnSe	Orthorhombic	a = 11.50, b = 4.15, c = 4.44	p-type	1.3	22
SnS <sub>2</sub>	Hexagonal	a = 3.64, c = 5.89	n-type	2.2	22
SnSe <sub>2</sub>	Hexagonal	a = 3.81, c = 6.14	n-type	1.0	60
Cu <sub>2</sub> SnS <sub>3</sub>	Different structural polymorphs such as cubic, tetragonal, monoclinic etc.	*	p-type	1.1	111
Cu <sub>2</sub> SnSe <sub>3</sub>	Different structural polymorphs such as cubic, tetragonal, monoclinic etc.	*	p-type	0.9	112

(\* Not given, due to different polymorphs)

Dicopper tin trisulfide (CTS) and dicopper tin triselenide (CTSe) are p-type semiconductors which have structure isomorphous to Cu<sub>2</sub>SiS<sub>3</sub>, where S or Se anions are bonded by four cations (Cu or Sn) lying at corners of slightly distorted tetrahedron [Fig. 1.8] [117,118]. Depending upon the distribution of these cations, different structural polymorphs, viz. cubic, tetragonal, monoclinic, triclinic and wurtzite phase of CTS and

CTSe have been isolated [111, 119]. The wurtzite structure of CTS and CTSe, which are metastable phases have been isolated by wet chemical methods [120, 121].

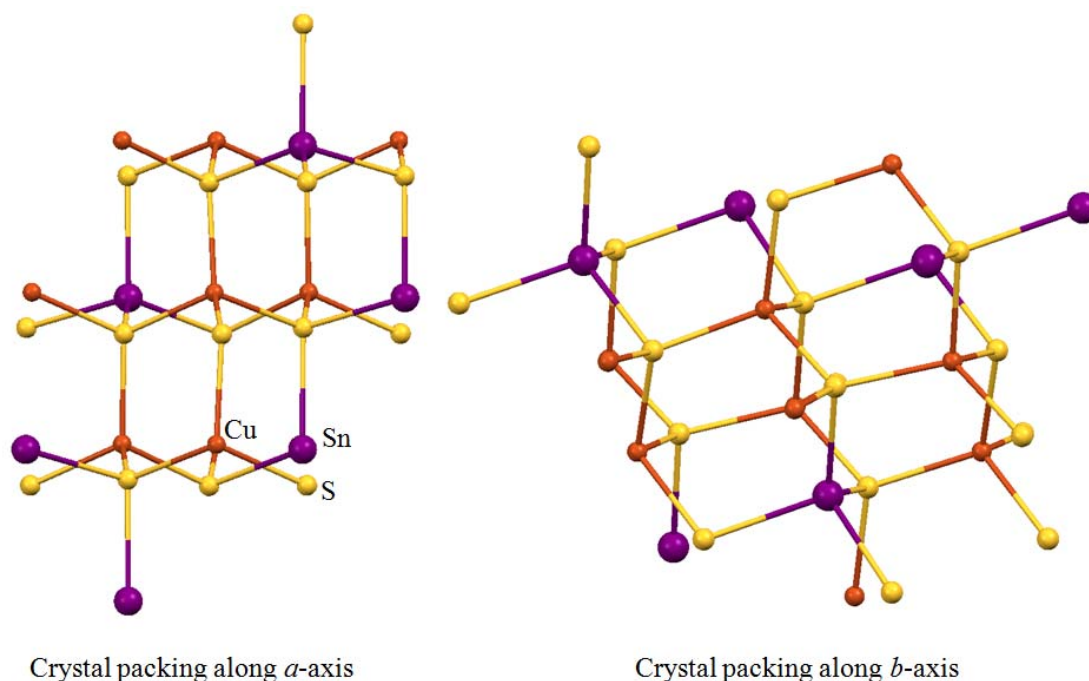


**Fig. 1.8** Crystal structure of  $\text{Cu}_2\text{SnS}_3$  based on cubic close packing of S with Cu and Sn in tetrahedral sites [adopted from Ref. 117].

Both CTS and CTSe stands out for their high absorption coefficient ( $> 10^5 \text{ cm}^{-1}$ ), tunable band gap varying between 0.9-1.7 eV which covers the optimal solar spectrum [122], good photostability, relatively high hole mobility [123] reasonably good electrical properties and are composed of earth abundant elements making it cost effective [124, 125]. While the fascinating properties of CTS and CTSe have garnered enormous attention as absorber material in solar cell application [120, 126] they have also been utilised in other fields of great significance such as electrode material for Li-ion battery [127], infrared photodetection [128], thermoelectrics [129, 130], supercapacitors [131], photocatalysis and gas sensing [132].

## 1.9 Synthetic methodologies for tin based chalcogenides

Various solution based methods such as solvothermal, hot injection, polyol, aqueous solution and molecular precursor/ single source precursor routes have been employed for the preparation of tin based binary and ternary chalcogenides nanomaterials. Except molecular precursor route, all other synthetic methods utilize a tin precursor (tin oleate, bis[bis(trimethylsilyl)amino]tin(II) or  $\text{SnCl}_2$ , etc.) and a suitable chalcogen (S or Se) source (thiourea, thioacetamide, S powder, trioctylphosphine-sulfur solution (TOPS) trioctylphosphine-selenium solution (TOPSe), Se powder, 1,3-dimethylimidazoline- 2-selenone or  $\text{SeO}_2$ , etc) for the preparation of tin chalcogenide nanomaterials. In the precursor route, generally an organometallic compound containing necessary atoms in a proper ratio, are employed for the preparation of desired nanomaterials. This route was pioneered by Bawendi, et al. for the synthesis of cadmium chalcogenide nanocrystals. The use of molecular precursor route provides some key advantages as discussed below over the other routes [134]:

1. Existence of preformed bonds can lead to materials with fewer defects and better stoichiometry and homogeneity of the resultant material.
2. Molecular precursors are generally air and moisture stable, have low toxicity and are therefore easy to handle and characterise.
3. Minimizations of the stoichiometric deviations due to possible handling errors as the numbers of starting materials are reduced.
4. Materials are obtained from molecular precursors at lower temperatures and are generally phase pure.
5. Molecular precursors can also be used for the deposition of nano-structured thin films using techniques such as metal organic chemical vapour deposition (MOCVD) or aerosol assisted chemical vapour deposition (AACVD).

6. Use of molecular precursors can minimise the use of toxic gases.
7. Pre-reactions can be limited during the deposition of thin films.

Nevertheless, there are few challenges associated with molecular precursor route such as

1. Poor solubility of precursors in common organic solvents due to the formation of non-crystalline polymers stabilized through bridging chalcogenolate ligands and are therefore difficult to purify and characterize.
2. In some cases incorporation of impurities was observed, as mentioned elsewhere.
3. Some precursors undergo improper decomposition leading to the formation of improper stoichiometry.
4. Additional synthetic steps are required compared to multi source precursor route.

In this direction, recent developments in precursor chemistry and their utilisation for the preparation of tin chalcogenide materials in form of nanostructures and thin films are discussed as follows:

### **1.9.1 Precursors for tin sulfide**

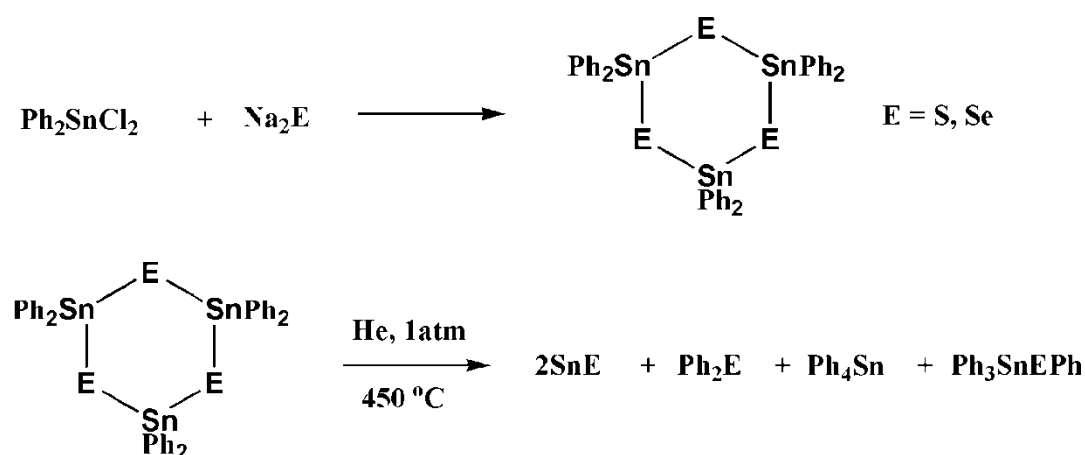
A variety of single source precursors such as tin thiolates, tin dithiocarbamates, tin thiosemicarbazone, etc. have been employed for the preparation of tin sulfide nanostructures and thin films. Koktysh, et al. [135] synthesized orthorhombic SnS nanocrystals (NCs) from bis(diethyldithiocarbamato)tin(II) in oleylamine at elevated temperature and achieved shape and size tunability of SnS NCs by controlling the reaction temperature, time and the nature of stabilizing ligand. These nanocrystals displayed strong absorption in the visible and near-infrared (NIR) spectral regions making them promising candidates for solar cell energy conversion.

Boudjouk and co-workers [136, 137] were the pioneers in the synthesis of molecular precursors employed arylated systems instead of alkylated systems for the preparation for tin chalcogenide materials. The former have synthesized, cyclic  $(\text{Ph}_2\text{SnE})_3$



as well as linear  $[(\text{Ph}_3\text{Sn})_2\text{E}]$  ( $\text{E} = \text{S}, \text{Se}, \text{Te}$ ) perphenylated derivatives of tin chalcogenides and utilized them for the preparation of  $\text{SnE}$  materials. These phenylated compounds offer various advantages over the alkylated systems: i) the phenylated precursor are destined to take advantage of the migrating ability of the phenyl group rather than its ability to form stable degradation products, ii) their thermolysis occurs in the liquid phase, and iii) the lower vapour pressure of phenylated molecules reduce the transmission of toxic vapours.

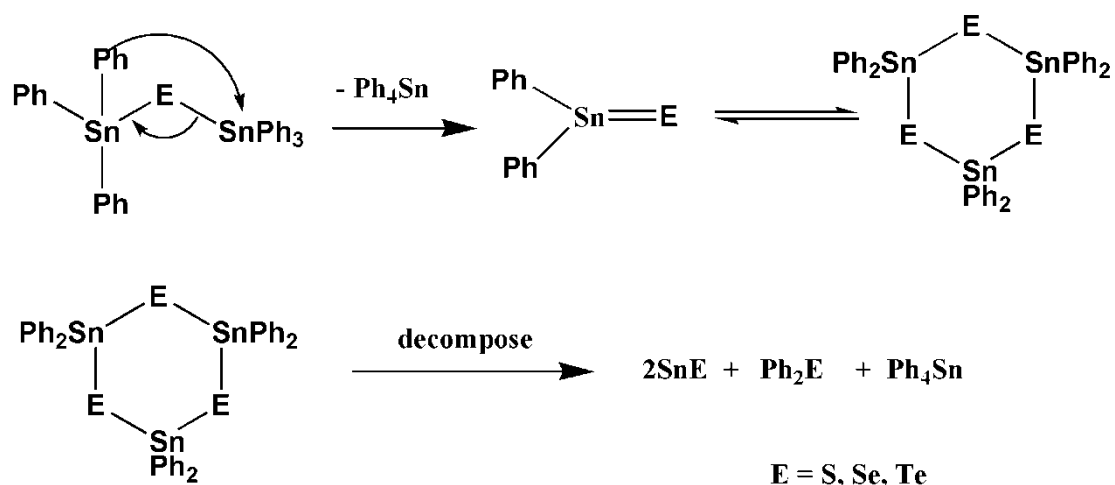
In case of cyclic precursors, proposed pyrolysis mechanism involves several intramolecular phenyl migrations leading to the formation of stable volatile by-products such as tetraphenyltin and diphenylchalcogenide. The steps leading to the formation of  $\text{SnE}$  materials from  $(\text{Ph}_2\text{SnE})_3$  are shown in scheme 1.1. Scanning electron microscopy micrographs of  $\text{SnS}$  and  $\text{SnSe}$  revealed the formation of rosette like clusture and prismatic like morphology, respectively. They also discovered that pyrolysis of mixtures of  $(\text{Ph}_2\text{SnS})_3$  and  $(\text{Ph}_2\text{SnSe})_3$  leads to the formation of solid solutions, with general composition  $\text{SnS}_x\text{Se}_{1-x}$  ( $x = 0$  to  $1$ ).



**Scheme 1.1** Synthesis and pyrolysis of perphenylated derivatives of tin chalcogenides

Pyrolysis linear precursor  $[(\text{Ph}_3\text{Sn})_2\text{E}]$  occurs *via* formation of cyclic intermediate which decompose into  $\text{SnE}$  and other volatile products (scheme 1.2). The resultant

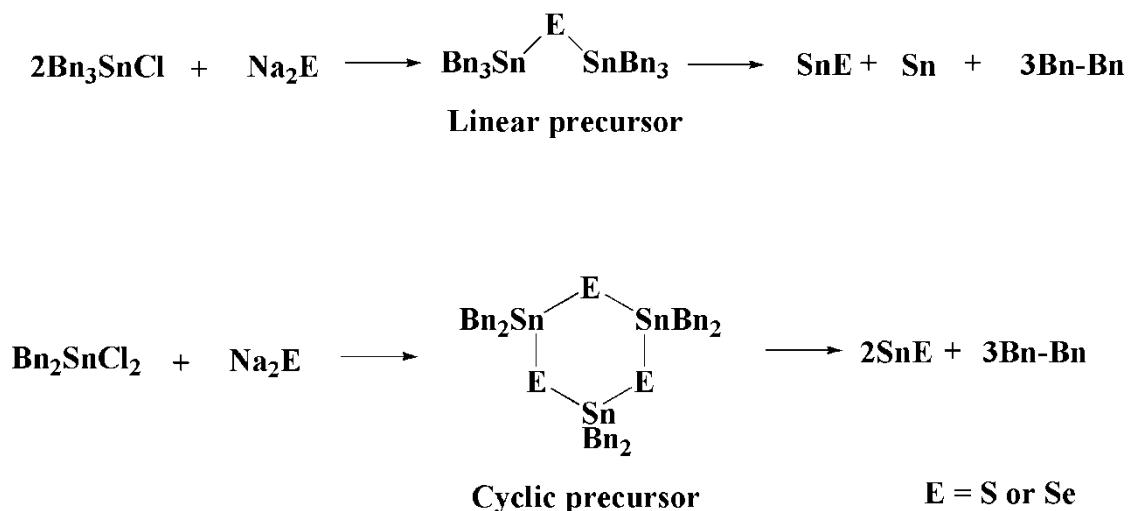
nanomaterials were found to be phase pure and highly crystalline in nature with less than 1% carbon contamination in the final product. SEM studies reveal that while SnS and SnSe adopts sheet like morphology, SnTe acquire cubo-octahedral habits.



**Scheme 1.2** Pyrolysis of linear precursor via cyclic intermediate

With the unexpected success of phenylated system for tin chalcogenide materials, Boudjouk et al. explored linear as well as cyclic benzyl substituted tin chalcogenides  $[(\text{Bn}_3\text{Sn})_2\text{E}]$ ,  $[\text{Bn}_2\text{SnE}]_3$  ( $\text{E} = \text{S, Se}$ ) [138] as single source precursors for the preparation of tin sulfide or tin selenide nanomaterials. The complexes were prepared by the reaction of benzyltin chloride with anhydrous sodium chalcogenide according to scheme 1.3. Pyrolysis of the linear complexes under argon yielded black powder which was analysed as tin chalcogenide ( $\text{SnS}$  or  $\text{SnSe}$ ) with some impurity of elemental tin. Unlike the linear precursors, cyclic precursors are found to be more atom efficient as they generate only target tin chalcogenide and bibenzyl. Benzylated systems are found to be more efficient for the preparation of metal chalcogenides as compared to phenylated systems because benzyl group undergoes homolytic cleavage contrary to phenylated system which involves series of phenyl migrations during the pyrolysis. Further, co-pyrolysis of the

precursors  $[(R_3Sn)_2S]$  and  $[(R_3Sn)_2Se]$  was also investigated which resulted into ternary  $Sn(S_xSe_{1-x})$  material.



*Scheme 1.3 Preparation and pyrolysis of benzylated tin chalcogenide*

In another study thermal decomposition of  $[Ph_2Sn(S_2CN(CH_2)_4)_2]$  and  $[Ph_3Sn(S_2CN(CH_2)_4)]$  were investigated. The analysis of the product showed the formation of a mixture of orthorhombic  $Sn_2S_3$  and  $SnS$  [139].

Apart from the preparation of nanostructures, molecular precursors have been used in the deposition of tin sulfide thin films. First single source precursor  $[Sn(SCH_2CH_2S)_2]$  (Fig. 1.9a) for the deposition of tin sulfide film through AACVD (aerosol assisted chemical vapour deposition) technique was developed by Parkin and co-workers [140]. In their investigation, they observed that in the presence of  $H_2S$  the precursor produced  $SnS$ ,  $SnS_2$  and  $Sn_2S_3$  films depending upon temperature. During the same period another group developed a tin(IV) thiolate precursor (Fig 1.9b) which was subsequently utilised for the deposition of tin sulfide thin film using AACVD technique. They observed that in the absence of  $H_2S$  as co-reactant, the precursor leads to deposition of  $Sn_3O_4$  film while in the presence of  $H_2S$ , it affords tin sulfide films [141].

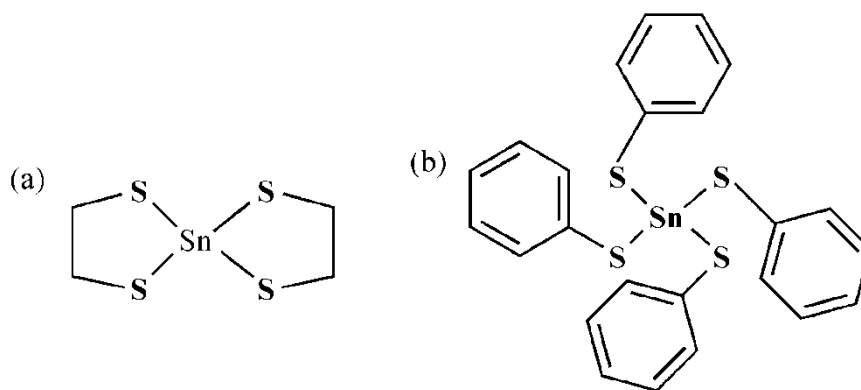


**Fig. 1.9** Molecular structure of a)  $[\text{Sn}(\text{SCH}_2\text{CH}_2\text{S})_2]$  [140] and b)  $[(\text{PhS})_4\text{Sn}]$  [141] employed for the deposition of tin sulfide thin films.

Similarly, Kana et. al. [142] carried out atmospheric pressure chemical vapor deposition (APCVD) of organotin dithiocarbamates  $[\text{Me}_2\text{Sn}(\text{S}_2\text{CN}(\text{C}_4\text{H}_9)\text{CH}_3)]$  and  $[\text{BuSn}(\text{S}_2\text{CN}(\text{C}_4\text{H}_9)\text{CH}_3)_3]$  in the presence of  $\text{H}_2\text{S}$  and obtained a mixture of  $\text{SnS}$  and  $\text{Sn}_2\text{S}_3$  films. Recently O'Brien et al. successfully deposited phase pure  $\text{SnS}$  thin films using tin thiosemicarbazone complexes of the type  $\text{Bz}_3\text{SnCl}(\text{L})$  ( $\text{L}$  = thiosemicarbazones of salicylaldehyde and 4-chlorobenzaldehyde) (Fig.1.10) [143]. Scanning electron microscope (SEM) micrographs revealed the formation of wafer like morphology. Noticeably, the morphologies of thin films are similar irrespective of the deposition temperature and also during experiment no  $\text{H}_2\text{S}$  was used.

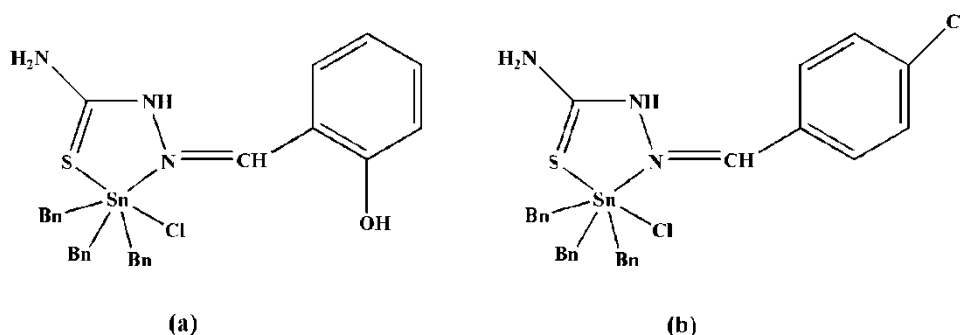


**Fig. 1.10** Molecular structure of Tribenzyltin chloride thiosemicarbazones for growth of  $\text{SnS}$  thin films [143].

O'Brien and co-workers also reported the synthesis of diorganotin dithiocarbamates,  $[\text{Bu}_2\text{Sn}\{\text{S}_2\text{CN}(\text{RR}')_2\}_2]$  ( $\text{R}, \text{R}' = \text{Et}$ ;  $\text{R} = \text{Me}, \text{R}' = \text{Bu}$ ;  $\text{R}, \text{R}' = \text{Bu}$ ;  $\text{R} = \text{Me}, \text{R}' = \text{hexyl}$ ) and  $[\text{Ph}_2\text{Sn}\{\text{S}_2\text{CN}(\text{RR}')_2\}_2]$  ( $\text{R}, \text{R}' = \text{Et}$ ;  $\text{R} = \text{Me}, \text{R}' = \text{Bu}$ ;  $\text{R}, \text{R}' = \text{Bu}$ ;  $\text{R} = \text{Me}, \text{R}' = \text{hexyl}$ ) (Fig. 1.11) [81] which were utilised for the deposition of sheet like tin(II) sulfide thin films in the temperature range 400 to 530 °C using AACVD. The crystal structure and phase purity of deposited film was confirmed by powder XRD.

From the above discussion it is evident that there are many reports on single source precursors for the deposition of tin sulfide thin films, however only few molecular precursors have been used for the preparation of tin sulfide nanostructures in the literature.

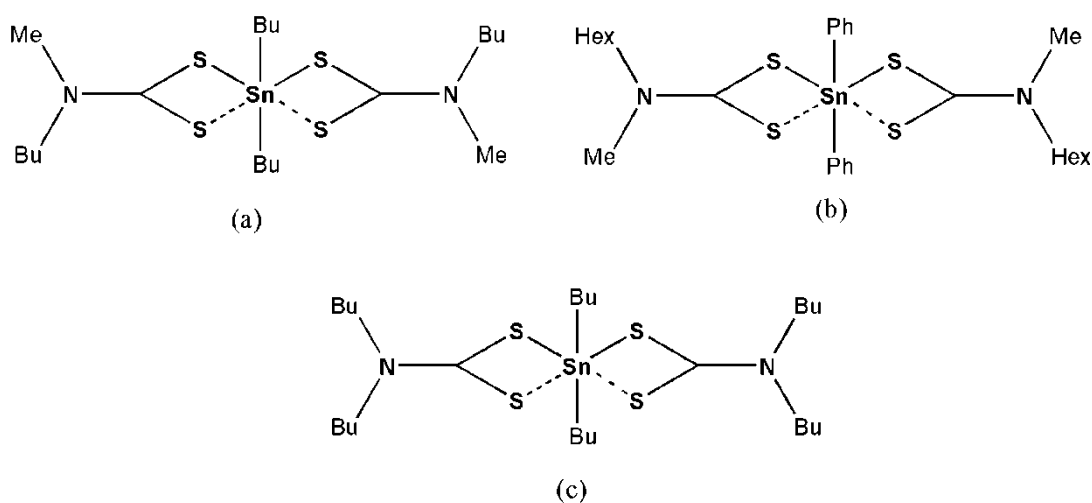


**Fig. 1.11** Molecular structure of diorganotin dithiocarbamates design and developed by O'Brien and coworkers [81].

### 1.9.2 Precursors for tin selenide

Preparation of tin selenide nanostructures and thin films employing aryl selenides, heterocyclic selenolates and aliphatic selenoethers of tin as single source molecular precursors has been well documented in the literature. In this direction Boudjouk and co-

workers contributed significantly. They have prepared several organotin complexes with aryl chalcogenide for the preparation of tin chalcogenide materials. Their work has been discussed in the previous section.

O'Brien and coworkers [144] reported bis(diphenylphosphinediselenoato)-tin(II)  $[\text{Sn}(\text{Ph}_2\text{PSe}_2)_2]$  as a molecular precursor for the deposition of SnSe and  $\text{Cu}_2\text{SnSe}_3$  thin films by the AACVD method, however the synthesis of precursor involves the use of highly toxic and expensive diphenyl phosphine which often cause phosphorus contamination and/ or formation of an entirely different products, such as metal phosphate or phosphide.

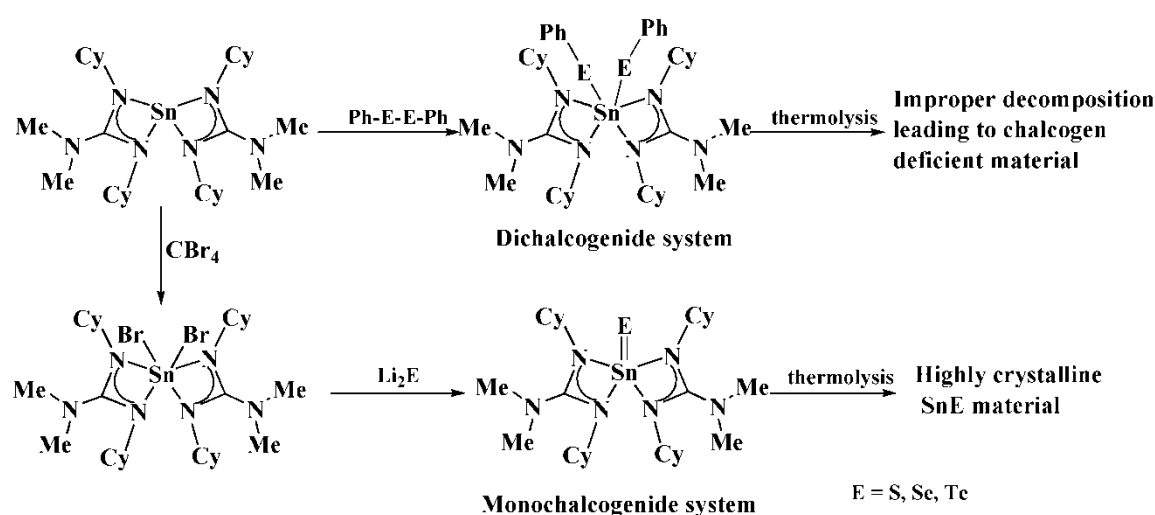
In order to avoid the presence of aryl phosphine ligands in molecular precursor, Khan et al. [145] have developed phosphine free bis(selenobenzoato)dibutyltin(IV) complex for the preparation of SnSe nanosheets and thin films by hot injection and AACVD method, respectively. The preferential growth and texture of films could be significantly manipulated by judicious control of the deposition temperature which imparts little effect over the stoichiometry of films. SnSe nanosheets exhibited bifunctional nature applicable for both hydrogen evolution reaction as well as oxygen evolution reaction as revealed by the photoelectrochemical studies.

Later, the same group has also reported another facile synthesis route for the synthesis of similar kind of selenotin(IV) complex and its thio analogue. The reported complexes are volatile in nature and undergo sublimation at elevated temperature. These complexes were used as molecular precursor to prepare binary tin chalcogenide ( $\text{SnS}$  and  $\text{SnSe}$ ) and their solid solution ( $\text{SnS}_x\text{Se}_{1-x}$ ) in the entire range. Two different synthetic routes viz. colloidal and melt methods were followed by them for the preparation of solid solution. Comparative analysis of the products obtained from two different synthetic routes clearly indicates that colloidal route enables superior control over the composition.

The volatility of complexes could be the reason behind the inefficient control in melt method. Moreover, composition dependent tuning of the band gap of  $(\text{SnS}_x\text{Se}_{1-x})$  solid solution has been demonstrated [156].

Recently, Ibrahim et al. [147] used tin(IV) guanidinate complexes as single source precursors for the production of tin(II) chalcogenides according to scheme 1.4.

Although both monochalcogenide and dichalcogenide systems were tested for the preparation of nanostructures, it was found that only monochalcogen system yields crystalline SnE system while the dichalcogen system undergo improper decomposition leading to chalcogen deficient material.



**Scheme 1.4** Preparation and thermolysis of Sn(IV) bisguanidate bisphenylchalcogenide and of Sn(IV) bisguanidate monochalcogenide complexes [adopted from Ref. 147].

In addition to aryl chalcogenides, heterocyclic compounds such as pyridyl selenolates of Sn(II) and Sn(IV) of formula  $[\text{Sn}(\text{Sepy})_n]$  ( $n = 2$  or  $4$ ) have also been prepared by Cheng et al. [148] either by metathesis or by the reduction of dipyridyl diselenide with elemental tin in refluxing toluene. The molecular structure of Sn(II) complex was found to be dimeric in nature with selenium bridges connecting the two

Sn(II) centres as determined from single crystal X-ray and shown in Fig. 1.12. Thermal decomposition of  $[\text{Sn}(\text{Sepy})_2]$  and  $[\text{Sn}(\text{Sepy})_4]$  gave SnSe and  $\text{SnSe}_2$ , respectively with the elimination of py-Se-py organic volatile product. Authors claim that the reported complexes are quite stable and can be used for vapour phase deposition.

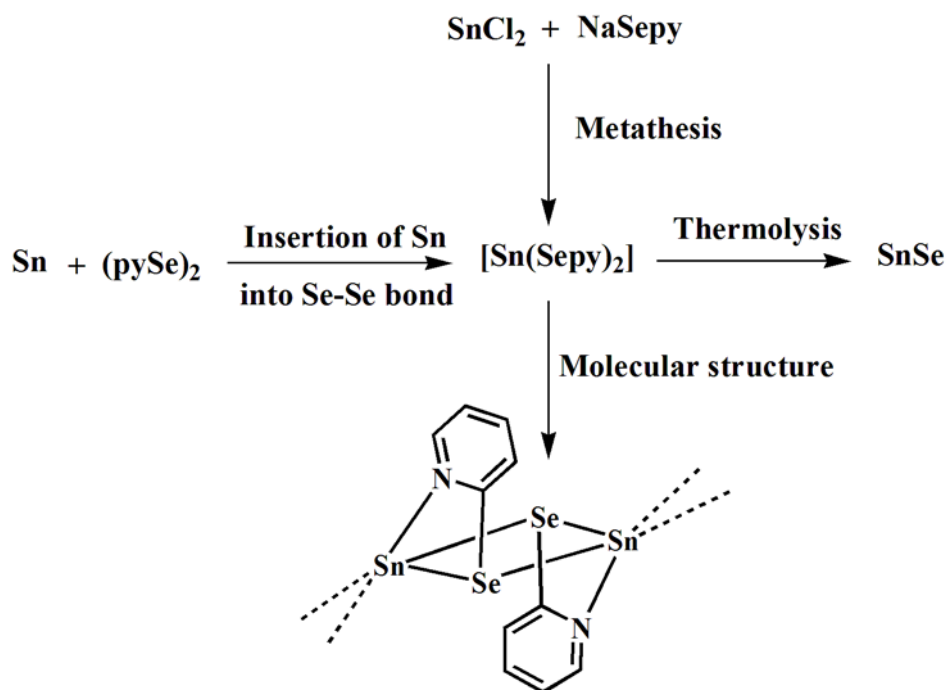


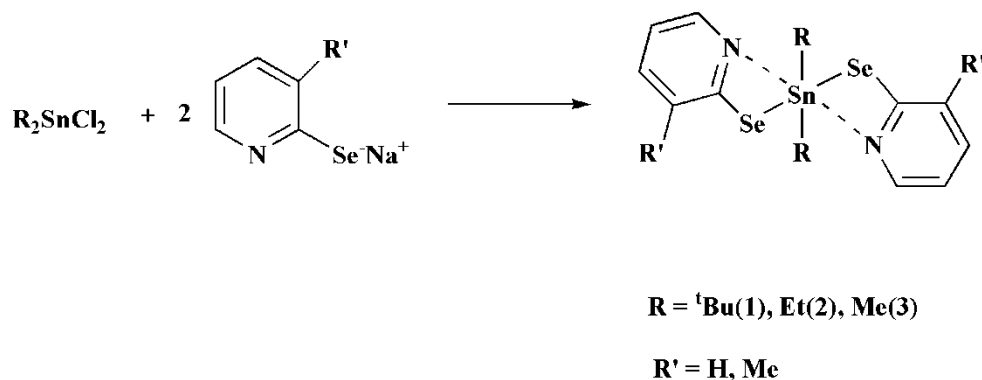
**Fig. 1.12** Schematic representation of the preparation of  $[\text{Sn}(\text{Sepy})_2]$  its molecular structure and formation of SnSe from the thermolysis of precursor [adopted from Ref. 148].

Similarly, Sharma et al. [149] synthesized complexes of diorganotin with pyridyl selenolate and its methyl derivative with the composition  $[\text{R}_2\text{Sn}\{2\text{-SeC}_5\text{H}_3(\text{R}'\text{-}3)\text{N}\}]_2$  ( $\text{R} = \text{Me}, \text{Et}, \text{'Bu}$ ) and ( $\text{R}' = \text{H}, \text{Me}$ ) according to scheme 1.5.

These complexes were used as single source precursors for the preparation of tin selenide nanostructures as well as for the deposition of thin films on different substrates by AACVD. They have also demonstrated that subtle variation either in molecular



structure of the precursor or in the experimental conditions could lead to nanostructures and thin films with different morphologies. Photo-response of SnSe thin films deposited on Si substrates has also been evaluated.



**Scheme 1.5** Preparation of diroganotinbis(3-methyl-2-pyridylselenolates) [149].

Recently, Reid and coworkers [150] employed aliphatic selenoethers of tin of the type  $[\text{SnCl}_4\{\text{'BuSe}(\text{CH}_2)_n\text{Se'Bu}\}]$  ( $n = 2$  or  $3$ ) as single source precursor for low pressure chemical vapor deposition (LPCVD) of microcrystalline, single phase  $\text{SnSe}_2$  films onto various substrate such as  $\text{SiO}_2$ , Si and TiN. Preferred crystallite orientation was observed for all the deposited thin films. The hall measurement studies revealed that deposited  $\text{SnSe}_2$  films are p-type with electrical resistivity higher than those deposited by spin coating and molecular beam epitaxy.

Other than tin-chalcogenide and -chalcogenolate complexes, cluster compound of type  $[(\text{N}_2\text{H}_4)_3(\text{N}_2\text{H}_5)_4\text{Sn}_2\text{Se}_6]$  separated from reaction of hydrazine with a mixture elemental tin and selenium has been used for the preparation of  $\text{SnSe}_2$  quantum dot sensitized solar cells by Dai and co-workers [68].

### 1.10 Scope of the Present Work

The emerging role of complexes as molecular precursors for the facile synthesis of metal chalcogenide nanostructures and thin films is evident from above discussion. However, it is also clear that this route has met with a little success in the case of tin chalcogenides possibly due to limited exploration of tin complexes with chalcogen ligands as molecular precursors, while there is hardly any report related to the preparation of ternary tin chalcogenides from molecular precursor route. This necessitates the exploration of chemistry of new precursor molecules for these materials and also to overcome the difficulties such as solubility, inappropriate decomposition leading to undesirable stoichiometry and incorporation of phosphorus impurities in the final product by the use of previously studied precursors. In view of the above, it was considered worthwhile to design and synthesize organotin complexes with substituted and non-substituted internally functionalized chalcogen ligands which can serve as molecular precursors for binary and ternary tin chalcogenide materials. Internally functionalized chalcogenolate ligands, *viz.* 2-pyridyl, 2-pyrimidyl and 2-pyrazinyl chalcogenolates, assist in suppressing oligomerization of metal chalcogenolates, *via* chelation and the facile cleavage of C-E bond in these complexes makes them potential candidate precursors for the preparation of binary and ternary tin chalcogenide nanostructures and thin films.

Accordingly, various tin complexes with substituted and non-substituted 2-pyridyl, 2-pyrimidyl and 2-pyrazinyl chalcogenolates ligands were synthesized and characterized using different characterization techniques, e.g. elemental analysis, multi-nuclear NMR, thermogravimetry, single crystal X-ray diffraction. These complexes were used for the preparation of binary and ternary tin chalcogenides nanostructures and thin films. Phase,

composition and band gap tunability of the nanostructures has been demonstrated by varying the temperature, growth duration and choice of reaction solvent.

For clarity, the present thesis is subdivided as follows:

- [1] Preparation of tin sulfide nanostructures using organotin pyridyl and pyrimidyl thiolates.
- [2] Preparation of tin selenide nanostructure using organotin pyridyl and pyrimidyl selenolates.
- [3] Accessing ternary tin chalcogenide nanostructures from molecular precursors.

# Chapter 2

## Characterization techniques

### 2.1 Materials and Methods

Glass-wares with inter-changeable standard conical ground joints were used throughout this investigation. Special glass-wares like Schlenk, two- and three- necked flasks with appropriate joints were used for performing reactions that involved use of  $\text{NaBH}_4$  for preparing sodium salts of ligands or for the preparation of nanomaterials and thin film deposition to avoid moisture and air. The precipitate formed during the synthesis was filtered through G-3 filter assemblies. All the glass-wares were kept overnight in an alkali bath [5%  $\text{NaOH}$  in ethanol-water (1:1 v/v) mixture] and then washed thoroughly with soap and water followed by rinsing with acetone and dried in an oven at 120- 130 °C for at least 6 h. The hot glass wares were kept in desiccators filled with silica gel for cooling. Inert atmosphere was maintained throughout the syntheses of metal complexes by flowing high purity argon or nitrogen through the reaction mixture.

Analytical reagent (AR) grade solvents procured from commercial sources were dried and purified by standard methods [151]. Hexane (67–68 °C), toluene (110 °C) were dried by refluxing them over sodium/benzophenone followed by distillation in an inert atmosphere when blue color persisted while diethyl ether (36 °C) was dried initially over anhydrous  $\text{CaCl}_2$ , followed by refluxing over  $\text{P}_2\text{O}_5$  and finally dried and distilled as mentioned in the former case. Dichloromethane (40 °C), chloroform (61 °C) was dried over anhydrous calcium chloride. Methanol (65 °C) was refluxed over magnesium methoxide (prepared from magnesium turnings and methanol in the presence of catalytic amount of iodine) for 4 h and distilled out. Acetonitrile (81 °C) was dried by refluxing over  $\text{P}_2\text{O}_5$  and distilled in an inert atmosphere.

High purity diorganotin dichlorides, cuprous chloride, 2-thiopyridine and high boiling solvents for nanomaterial syntheses such as oleylamine (OLA), 1-octadecene (ODE), oleic acid (OA), trioctylphosphine oxide (TOPO) were obtained from commercial sources.

## **2.2 Experimental techniques**

### **2.2.1 Analysis**

Melting points were determined in glass capillary tubes sealed at one end. Microanalyses (C, H, N and S) of the compounds were carried out on a Thermo Fischer Flash EA1112 elemental analyzer.

### **2.2.2 Crystallography**

The single crystal X-ray structural analyses of representative complexes were carried out on a Agilent Super Nova microfocuss X-ray source ( $\text{CuK}_\alpha$ ,  $\lambda = 1.5418 \text{ \AA}$ ) radiation or Rigaku AFC7S diffractometer using graphite monochromated  $\text{MoK}_\alpha$  ( $\lambda = 0.71069 \text{ \AA}$ ) radiation so that  $\theta_{\text{max}} = 27.5^\circ$ . The crystals were directly mounted on the diffractometer after examining the quality of crystal under a polarizing microscope. Sometimes crystals were cut to the desired size before mounting. The intensity data were corrected for Lorentz, polarization and absorption effects with an empirical procedure [152]. The structures were solved by direct methods using SHELX-97 [153] and refined by full-matrix least squares methods. The non-hydrogen atoms were refined anisotropically. The hydrogen atoms were fixed in their calculated positions. Molecular structures were drawn using ORTEP [154]. An ambient temperature, source of radiation, diffractometer and refinement details are given in Table 2.1-2.6.

**Table 2.1.** Crystallographic and structural determination data for  $[Et_2Sn(2-Spy)_2]$ ,  $[^tBu_2Sn(2-Spy)_2]$  and  $[^tBu_2SnCl(2-Spy)]$ .

	$[Et_2Sn(2-Spy)_2]$	$[^tBu_2Sn(2-Spy)_2]$	$[^tBu_2SnCl(2-Spy)]$
Chemical formula	$C_{14}H_{18}N_2S_2Sn$	$C_{18}H_{26}N_2S_2Sn$	$C_{13}H_{22}ClN_2SSn$
Formula weight	397.11	453.22	378.51
Crystal size/mm <sup>3</sup>	0.10 × 0.10 × 0.05	0.2 × 0.2 × 0.05	0.15 × 0.1 × 0.05
Crystal system / space group	Orthorhombic/ <i>Pnma</i>	Monoclinic/ <i>I2</i>	Orthorhombic/ <i>Pcmm</i>
Unit cell dimensions			
a/Å	9.9262(13)	10.360(6)	6.8450(18)
b/Å	17.2292(9)	7.085(4)	12.445(4)
c/Å	9.7256(8)	13.987(15)	19.516(3)
α	90	90	90
β	90	103.00(7)	90
γ	90	90	90
Volume/Å <sup>3</sup>	1663.3(3)	1000.4(14)	1662.6(8)
Z	4	2	4
D <sub>c</sub> /g cm <sup>-3</sup>	1.586	1.505	1.516
μ/mm <sup>-1</sup>	14.467	1.487	1.807
<i>F</i> (000)	792	460	760
Limiting indices	$-6 \leq h \leq 11; -19 \leq k \leq 20; -11 \leq l \leq 11$	$-10 \leq h \leq 20; 0 \leq k \leq 9; -13 \leq l \leq 11$	$-4 \leq h \leq 8; -15 \leq k \leq 9; -23 \leq l \leq 0$
No. of reflections collected / unique	1587/ 920	1242/1240	1627/1151
No. of data / restraints / parameters	1587/ 9/95	1242/1/109	1627/0/96
Final <i>R</i> <sub>1</sub> , <i>wR</i> <sub>2</sub> indices [ <i>I</i> > 2σ ( <i>I</i> )]	0.0706, 0.2017	0.0269, 0.0683	0.0666, 0.1723
<i>R</i> <sub>1</sub> , <i>wR</i> <sub>2</sub> (all data)	0.1017, 0.2518	0.027, 0.0684	0.0997, 0.1976
Goodness of fit on <i>F</i> <sup>2</sup>	1.091	1.083	1.096

**Table 2.2.** Crystallographic and structural determination data for  $[\text{Me}_2\text{SnCl}(2\text{-SpymMe}_2)]$ ,  $[\text{Et}_2\text{SnCl}(2\text{-SpymMe}_2)]$  and  $[\text{tBu}_2\text{SnCl}(2\text{-SpymMe}_2)]$ .

	$[\text{Me}_2\text{SnCl}(2\text{-SpymMe}_2)]$	$[\text{Et}_2\text{SnCl}(2\text{-SpymMe}_2)]$	$[\text{tBu}_2\text{SnCl}(2\text{-SpymMe}_2)]$
Chemical formula	$\text{C}_8\text{H}_{13}\text{ClN}_2\text{SSn}$	$\text{C}_{10}\text{H}_{17}\text{ClN}_2\text{SSn}$	$\text{C}_{14}\text{H}_{25}\text{ClN}_2\text{SSn}$
Formula weight	323.42	351.45	407.56
Crystal size/ $\text{mm}^3$	$0.20 \times 0.10 \times 0.01$	$0.15 \times 0.15 \times 0.05$	$0.1 \times 0.1 \times 0.1$
Crystal system / space group	Orthorhombic/ <i>Cmca</i>	Monoclinic/ $\text{P2}_1/\text{n}$	Monoclinic/ $\text{P2}_1/\text{n}$
Unit cell dimensions			
$a/\text{\AA}$	8.0000(10)	10.6207(15)	11.676(2)
$b/\text{\AA}$	20.119(4)	11.907(5)	13.758(3)
$c/\text{\AA}$	16.731(2)	11.589(2)	11.837(3)
$\alpha$	90	90	90
$\beta$	90	91.786(13)	93.373(17)
$\gamma$	90	90	90
Volume/ $\text{\AA}^3$	2692.9(7)	1464.9(7)	1898.2(7)
Z	8	4	4
$D_c/\text{g cm}^{-3}$	1.595	1.594	1.426
$\mu/\text{mm}^{-1}$	2.216	2.044	1.588
$F(000)$	1264	696	824
Limiting indices	$-9 \leq h \leq 5; -26 \leq k \leq 0; -12 \leq l \leq 21$	$-7 \leq h \leq 13; -15 \leq k \leq 15; -15 \leq l \leq 15$	$-8 \leq h \leq 15; -0 \leq k \leq 17; -15 \leq l \leq 15$
No. of reflections collected / unique	1571/814	3364/1534	4350/1925
No. of data / restraints / parameters	1571/0/79	3364/0/ 140	4350/7/174
Final $R_1, \omega R_2$ indices [ $I > 2\sigma(I)$ ]	0.0546, 0.1033	0.0538, 0.1120	0.0518, 0.1124
$R_1, \omega R_2$ (all data)	0.1411, 0.1280	0.1392, 0.1365	0.1523, 0.1441
Goodness of fit on $F^2$	0.976	0.990	0.985

**Table 2.3.** Crystallographic and structural determination data for (Sepy(5-Me))<sub>2</sub> and [R<sub>2</sub>Sn(2-Sepy(5-Me))<sub>2</sub>] (R = Me, Et, <sup>t</sup>Bu).

	(Sepy(5-Me)) <sub>2</sub>	[Me <sub>2</sub> Sn(2-Sepy(5-Me)) <sub>2</sub> ]	[Et <sub>2</sub> Sn(2-Sepy(5-Me)) <sub>2</sub> ]	[ <sup>t</sup> Bu <sub>2</sub> Sn(2-Sepy(5-Me)) <sub>2</sub> ]
Chemical formula	C <sub>12</sub> H <sub>12</sub> N <sub>2</sub> Se <sub>2</sub>	C <sub>14</sub> H <sub>18</sub> N <sub>2</sub> Se <sub>2</sub> Sn	C <sub>16</sub> H <sub>22</sub> N <sub>2</sub> Se <sub>2</sub> Sn	C <sub>20</sub> H <sub>30</sub> N <sub>2</sub> Se <sub>2</sub> Sn
Formula weight	342.16	490.91	518.96	575.07
Crystal size/mm <sup>3</sup>	0.15 × 0.10 × 0.05	0.1 × 0.05 × 0.05	0.1 × 0.1 × 0.05	0.2 × 0.1 × 0.05
Crystal system / space group	Monoclinic/P 21/n	Orthorhombic/Pnma	Orthorhombic/Pcmn	Monoclinic/'C 2/c'
Radiation λ/Å	Mo-Kα (0.71069 Å)	Mo-Kα (0.71069 Å)	Mo-Kα (0.71069 Å)	Mo-Kα (0.71069 Å)
Unit cell dimensions				
a/Å	6.6600(18)	12.527(6)	25.930(4)	15.700(4)
b/Å	6.194(2)	18.049(6)	18.220(3)	7.4200(12)
c/Å	31.393(14)	7.707(4)	8.050(2)	21.929(5)
α/°	90			
β/°	93.03(3)	90	90	114.683(15)
γ/°	90			
Volume/Å <sup>3</sup>	1293.3(8)	1742.5(13)	3803.3(14)	2321.2(9)
Z	4	4	8	4
D <sub>c</sub> /g cm <sup>-3</sup>	1.757	1.871	1.813	1.646
μ/mm <sup>-1</sup>	5.692	5.634	5.168	4.242
F(000)	664	936	2000	1128
Limiting indices	-10 ≤ h ≤ 10; -4 ≤ k ≤ 9; -47 ≤ l ≤ 22	-9 ≤ h ≤ 18; 0 ≤ k ≤ 27; -5 ≤ l ≤ 11	0 ≤ h ≤ 34; -13 ≤ k ≤ 24; -10 ≤ l ≤ 5	-11 ≤ h ≤ 23; -0 ≤ k ≤ 11; -33 ≤ l ≤ 30
θ range of data collection	2.599 - 32.503	2.87-32.48	2.65-28.28	2.731-32.50
No. of reflections collected / unique	4679/905	3229/865	4876/1641	4196/1490
No. of data / restraints / parameters	4679/0/147	3229/0/94	4876/0/210	4196/0/118
Final R <sub>1</sub> , ωR <sub>2</sub> indices [ <i>I</i> > 2σ( <i>I</i> )]	0.0648, 0.0725	0.0617, 0.0828	0.0632, 0.1375	0.0537, 0.0816
R <sub>1</sub> , ωR <sub>2</sub> (all data)	0.4044, 0.1234	0.3026, 0.1258	0.2636, 0.2138	0.2193, 0.1116
Goodness of fit on F <sup>2</sup>	0.878	0.907	0.852	0.940
Largest diff. peak and hole (e/Å <sup>3</sup> )	0.334 and -0.321	0.528 and -0.689	0.607 and -0.678	0.528 and -0.689



**Table 2.4.** Crystallographic and structural determination data for [<sup>t</sup>Bu<sub>2</sub>Sn(2-SepymMe<sub>2</sub>)<sub>2</sub>], [<sup>n</sup>Bu<sub>2</sub>Sn(2-SepymMe<sub>2</sub>)<sub>2</sub>] and [<sup>t</sup>Bu<sub>2</sub>SnCl(2-SepymMe<sub>2</sub>)].

	[ <sup>t</sup> Bu <sub>2</sub> Sn(2-SepymMe <sub>2</sub> ) <sub>2</sub> ]	[ <sup>n</sup> Bu <sub>2</sub> Sn(2-SepymMe <sub>2</sub> ) <sub>2</sub> ]	[ <sup>t</sup> Bu <sub>2</sub> SnCl(2-SepymMe <sub>2</sub> )]
Chemical formula	C <sub>20</sub> H <sub>32</sub> N <sub>4</sub> Se <sub>2</sub> Sn	C <sub>20</sub> H <sub>32</sub> N <sub>4</sub> Se <sub>2</sub> Sn	C <sub>14</sub> H <sub>25</sub> ClN <sub>2</sub> SeSn
Formula weight	605.11	605.11	454.46
Crystal size/mm <sup>3</sup>	0.20 × 0.20 × 0.10	0.20 × 0.15 × 0.05	0.10 × 0.05 × 0.05
Crystal system / space group	Monoclinic /C2/c	Triclinic /P1 <sup>-</sup>	Monoclinic/P2 <sub>1</sub> /c
Radiation λ/Å	Mo-Kα (0.71069 Å)	Mo-Kα (0.71069 Å)	Mo-Kα (0.71069 Å)
Unit cell dimensions			
a/Å	14.800(4)	11.659(6)	9.192(3)
b/Å	7.7490(7)	16.166(17)	12.655(3)
c/Å	21.526(4)	29.13(3)	15.9900(18)
α	90	84.62(9)	90
β	95.420(17)	84.17(5)	92.278(19)
γ	90	70.44(7)	90
Volume/Å <sup>3</sup>	2457.7(8)	5137(8)	1858.6(8)
Z	4	8	4
D <sub>c</sub> /g cm <sup>-3</sup>	1.635	1.565	1.624
μ/mm <sup>-1</sup>	4.013	3.840	3.468
F(000)	1192	2384	896
Limiting indices	-19 ≤ h ≤ 10 0 ≤ k ≤ 10 -27 ≤ l ≤ 27	-8 ≤ h ≤ 15 -19 ≤ k ≤ 21 -37 ≤ l ≤ 37	-11 ≤ h ≤ 11 -9 ≤ k ≤ 16 -11 ≤ l ≤ 20
No. of reflections collected / unique	2813/ 2067	23556/ 4580	4261/1963
No. of data / restraints / parameters	2813/ 0/ 128	23556/ 624/ 925	4261/0/ 181
Final R <sub>1</sub> , ωR <sub>2</sub> indices [ <i>I</i> > 2σ ( <i>I</i> )]	0.0342, 0.0823	0.1132, 0.2392	0.0482/0.1019
R <sub>1</sub> , ωR <sub>2</sub> (all data)	0.0636, 0.0922	0.4531, 0.3834	0.1745/0.1485
Goodness of fit on F <sup>2</sup>	1.044	0.906	1.016

**Table 2.5.** Crystallographic and structural determination data for [*t*-Bu<sub>2</sub>Sn(Spyz)<sub>2</sub>] and [Cu(Spyz)(PPh<sub>3</sub>)<sub>2</sub>].

	[ <i>t</i> -Bu <sub>2</sub> Sn(Spyz) <sub>2</sub> ]	[Cu(Spyz)(PPh <sub>3</sub> ) <sub>2</sub> ]
Chemical formula	C <sub>16</sub> H <sub>24</sub> N <sub>4</sub> S <sub>2</sub> Sn	C <sub>40</sub> H <sub>33</sub> CuN <sub>2</sub> P <sub>2</sub> S
Formula weight	455.20	699.22
Crystal size/mm <sup>3</sup>	0.15 × 0.15 × 0.05	0.333 × 0.248 × 0.092
Crystal system / space group	Orthorhombic/ <i>Pbca</i>	Triclinic/ <i>P<sub>1</sub></i>
Radiation λ/Å	Mo-Kα (0.71069 Å)	Cu-Kα (1.54184 Å)
Temperature/K	298(2)	293(2)
Unit cell dimensions		
<i>a</i> /Å	12.343 (3)	11.0868 (4)
<i>b</i> /Å	16.770 (2)	18.0414 (6)
<i>c</i> /Å	19.530 (2)	18.8952 (7)
α°	90	66.171 (3)
β°	90	85.023 (3)
γ°	90	89.302 (3)
Volume/Å <sup>3</sup>	4042.5 (11)	3443.1 (2)
<i>Z</i>	8	4
<i>D<sub>c</sub></i> /g cm <sup>-3</sup>	1.496	1.349
μ/mm <sup>-1</sup>	1.475	2.575
<i>F</i> (000)	1840	1448
Limiting indices	-8 ≤ <i>h</i> ≤ 18; -25 ≤ <i>k</i> ≤ 12; -29 ≤ <i>l</i> ≤ 0	13 ≤ <i>h</i> ≤ -13; 16 ≤ <i>k</i> ≤ -20; 22 ≤ <i>l</i> ≤ -23
θ range of data collection/°	2.643 – 32.474	2.864 – 73.288
No. of reflections collected / unique	7286/2767	13151/10047
No. of data / restraints / parameters	7286/0/215	13151/0/829
Final <i>R</i> <sub>1</sub> , ω <i>R</i> <sub>2</sub> indices [ <i>I</i> > 2σ( <i>I</i> )]	0.0602, 0.1098	0.0599, 0.1645
<i>R</i> <sub>1</sub> , ω <i>R</i> <sub>2</sub> (all data)	0.2097, 0.1506	0.0781, 0.1993
Goodness of fit on <i>F</i> <sup>2</sup>	0.966	1.052

**Table 2.6.** Crystallographic and structural determination data for  $[Me_2Sn(2\text{-Sepy}(3\text{-Me}))_2]$ .

	$[Me_2Sn(2\text{-Sepy}(3\text{-Me}))_2]$
Chemical formula	$C_{14}H_{18} N_2SnSe_2$
Formula weight	490.93
Crystal size/mm <sup>3</sup>	$0.30 \times 0.10 \times 0.05$
Crystal system / space group	Monoclinic/P $2_1/c$
Unit cell dimensions	
a/Å	8.000(2)
b/Å	17.4043)
c/Å	13.050(2)
$\alpha$	90
$\beta$	95.858(19)
$\gamma$	90
Volume/Å <sup>3</sup>	1807.5(6)
Z	4
$D_c/g\text{ cm}^{-3}$	1.804
$\mu/mm^{-1}$	5.431
Temperature(K)	298
$F(000)$	936
Limiting indices	$-5 \leq h \leq 11; 0 \leq k \leq 26; -19 \leq l \leq 19$
No. of reflections collected / unique	3666/ 1852
No. of data / restraints / parameters	3666/ 82/ 177
Final $R_1, \omega R_2$ indices [ $I > 2\sigma(I)$ ]	0.0619, 0.1795
$R_1, \omega R_2$ (all data)	0.1489, 0.2254
Goodness of fit on $F^2$	1.024
Largest diff. peak and hole ( $e/\text{\AA}^3$ )	1.146 and -1.227

### 2.2.3 Nuclear magnetic resonance (NMR) Spectroscopy

The  $^1\text{H}$ ,  $^{13}\text{C}\{^1\text{H}\}$ ,  $^{77}\text{Se}\{^1\text{H}\}$ , and  $^{119}\text{Sn}\{^1\text{H}\}$ , spectra were recorded on a Bruker Advanced-II-300 spectrometer operating at 300, 75.47, 57.23 and 111.92 MHz, respectively in a thin walled 5 mm NMR tubes. Chemical shifts are relative to internal chloroform peak ( $\delta = 7.26$  ppm for  $^1\text{H}$  and  $\delta = 77.0$  ppm for  $^{13}\text{C}$ ) and external  $\text{Me}_2\text{Se}$  for  $^{77}\text{Se}\{^1\text{H}\}$  ( $\text{Ph}_2\text{Se}_2$  in  $\text{CDCl}_3$  464 ppm) and 30%  $\text{Me}_4\text{Sn}$  in  $\text{C}_6\text{D}_6$  for  $^{119}\text{Sn}\{^1\text{H}\}$  NMR spectra. A  $90^\circ$  pulse was used in every case. A weighting function was applied in  $^{119}\text{Sn}\{^1\text{H}\}$  NMR spectra.

### 2.2.4 Powder X-ray diffraction

Powder X-ray diffraction [155] technique is one of the most widely used non-destructive techniques for characterization of crystalline materials and for determination of their unit cell, lattice parameters, phase and probable structures. Each crystalline compound has a characteristic unit cell which produces distinctive diffraction pattern when X-ray is shine on the material. The necessary condition for diffraction to occur is given by Bragg's law ( $n\lambda = 2d\sin\theta$ ), where  $n$  is the order of reflection,  $d$  is the inter-planar distance,  $\theta$  and  $\lambda$  are the incident angle and wavelength of the X-rays (Fig. 2.1).

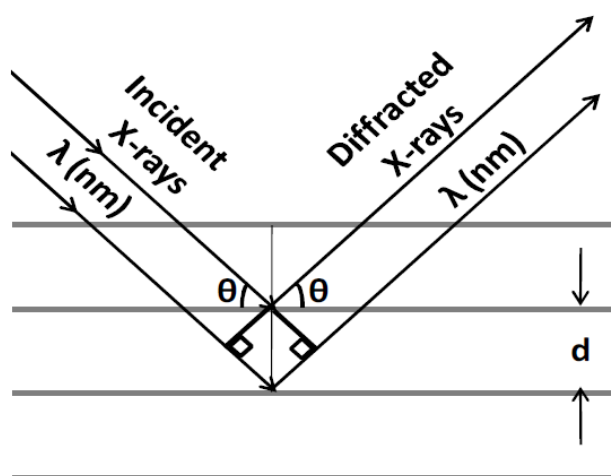


**Fig. 2.1** Schematic representation of Bragg's equation for X-ray diffraction.

The XRD patterns of any materials is based on the scattering of X-rays by the parallel planes, an array of atoms, ions or molecules. The location of the reflections (scattered X-rays) from the atomic planes of a crystal indicates the unit cell of crystal, while, the relative intensities of the reflections give the information about the kind and arrangement of the atoms within the unit cell.

In the present study the observed diffraction patterns were compared with JCPDS (Joint Committee on Powder Diffraction Standards, 1974) files available for reported crystalline samples. The average crystallite size of the nano powders was estimated from the XRD pattern using the Scherrer's formula [155] which is given by equation 2.1

$$d = 0.9\lambda/(\beta\cos\theta) \quad (2.1)$$

Where,  $d$  = size of the crystallite

$\lambda$  = wavelength of the X-ray radiation

$\beta$  = FWHM in radian

$\theta$  = angle at which that reflection occurs.

In this thesis, the samples were analysed on Philips 1710 diffractometer based on the Bragg-Brentano reflection geometry. The  $\text{CuK}_\alpha$  from sealed tube was used as the incident beam. A Ni foil was used as a filter and the diffracted beam was monochromatised with a curved graphite single crystal. The Philips (PW-1710) diffractometer is attached with a proportional counter (Argon filled) for the detection of X-rays. The X-ray tube rating was maintained at 30 kV and 20mA. The goniometer was calibrated for correct zero position using silicon standard. Samples are well grounded and made in the form of a slide. As all the micro crystals are randomly oriented, at any point on the sample different planes from crystals will be exposed to X-rays.

### **2.2.5 Scanning electron microscope (SEM)**

SEM in combination with EDX (energy dispersive X-ray analyzer) provides a high resolution image, elemental identification and quantitative compositional information of the sample [156]. An accelerated beam of mono-energetic electrons is focused on to the surface of the sample and is scanned over a small area in a raster pattern. The interaction of primary electron beam with the sample produces various types of signals such as back scattered, secondary and Auger electrons and X-ray photons of varied energies.

In the present investigation, SEM instruments used were from MIRERO Inc. AIS2100, Tescan Vega 2300T/40 and ULTRA 55 FESEM of Zeiss. Electron diffraction analyses of X-rays (EDX) experiments were carried out on Oxford Inca instrument. The surface morphology was studied by using Scanning Probe Microscope (SPM-Solver P47, NTMDT, Russia). The measurements were carried out in contact mode. Silicon nitride cantilevers having force constant of 3 N/m were employed for measurement. The samples were made in the form of slurry with isopropyl alcohol and spread over mirror polished single crystal of Si substrate prior to its mounting on the stub.

### **2.2.6 Transmission electron microscope (TEM)**

Transmission electron microscope [157] is a technique that uses the interaction between accelerated beam of mono-energetic electrons with the surface of the electron transparent (thickness is comparable to the wavelength of the electron beam) sample by a set of electromagnetic lenses to provide morphological and crystallographic information about the materials with atomic scale resolution. The image observed on a fluorescent screen is photographed with camera. Diffraction and contrast are two important aspects of TEM. Diffraction patterns form the basis of image formation in TEM. An image is constructed by diffraction pattern obtained either by one transmitted beam or more diffracted beam(s). In the

former case the image is known as the bright field image whereas in the latter it is referred as the dark field image. Such images which have been obtained by one beam alone are said to have mass thickness contrast and diffraction contrast.

The high-resolution transmission electron microscopy (HR-TEM) has been extensively used in analyzing the crystal structure and lattice imperfections in the materials on an atomic scale resolution. It utilizes both the transmitted and scattered beams to create an interference image which is basically a phase contrast image and can be as small as the unit cell of a crystal. In these cases, the outgoing modulated electron waves at very low angles interfere with itself during their propagation through the objective lens. All the electrons emerging from the specimen are combined at a point in the image plane. The HR-TEM has been employed for determining the lattice imperfections and crystal structures of nanomaterials at atomic resolution scale.

In the present study, JEOL-2000FX and Zeiss Libra 200 FE transmission electron microscope operating at accelerating voltages up to 200 kV was used for Transmission electron microscope (TEM) studies. The samples for TEM and Selected Area Electron Diffraction (SAED) were prepared by placing a drop of sample dispersed in acetone on a carbon coated copper grid.

#### **2.2.7 Selected area electron diffraction (SAED)**

The above mode enable us to obtain diffraction patterns of an object by focusing the electron beam of spot size (2-10 nm) with the projector lenses on the object surface [158]. The spots of SAED become disks whose radii depend on the condenser diaphragm. SAED patterns of a crystal permit to calculate its inter-planar distances. The former also helps in recognising the material under study is polycrystalline or single crystalline depending whether the pattern is disc or spot like. This aids in comparing the system under study with

the one reported in literature and thus help in determining the phase of the system. The interpretation of SAED pattern was done using the expression.

$$\lambda L = dr$$

$$\lambda L = \text{microscope constant}$$

$$d = \text{plane spacing}$$

$$r = \text{radii of the rings on SAED pattern}$$

$$\lambda = 12.26/(E(1 + 0.978 \times 10^{-6}E))^{1/2} \text{ \AA}$$

$$E = \text{Operating voltage in V (200 kV, for instrument used in the present study)}$$

### 2.2.8 Photoelectrochemical Cell (PEC)

A photoelectrochemical (PEC) cell is a device in which illumination of semiconductor electrode in a suitable electrolyte produces a change in electrode potential (on open circuit) or in the current flowing in the external circuit (short circuit current) thereby directly converting solar energy into electrical energy. PEC provides two key advantages over solid-solid junction; (i) attainment of junction is relatively easy in PEC thereby boosting separation of charges, (ii) relatively small loss in conversion efficiency when single crystals are replaced by polycrystals [159, 160].

In the present investigation photoelectrochemical cell were used to assess the utility of the tin chalcogenide nanostructures as low cost photon absorber material for solar cell. Photoelectrochemical cells were prepared by using silicon/(SnSe, SnSe<sub>2</sub>, Cu<sub>2</sub>SnE<sub>3</sub> (E = S, Se)) structure, Pt, Pt wire as the working, counter and pseudo reference electrodes, respectively and 0.6 M Na<sub>2</sub>S:0.8 M Na<sub>2</sub>SO<sub>3</sub> (1:2) as the electrolyte (Fig 2.2). Working electrode was prepared by drop casting a colloidal solutions of nanostructures in toluene on a rough surface of n-type Si wafer of (100) orientation having thickness of 300  $\mu$  and



resistivity 1-15  $\Omega\cdot\text{cm}$ . The process was repeated many times till a uniform coating was obtained on the silicon structure. Rough surface helps in good adhesion of the particles on the silicon substrate. The drop casted film was dried at 120  $^{\circ}\text{C}$  for 3 h. Fluorescent lamp (36 W, UV content < 3%) was used as radiation source with light intensity at the cell being 200  $\mu\text{W}/\text{cm}^2$ . Current-voltage (I-V) measurements have been evaluated on a potentiostat PARSTAT 273.

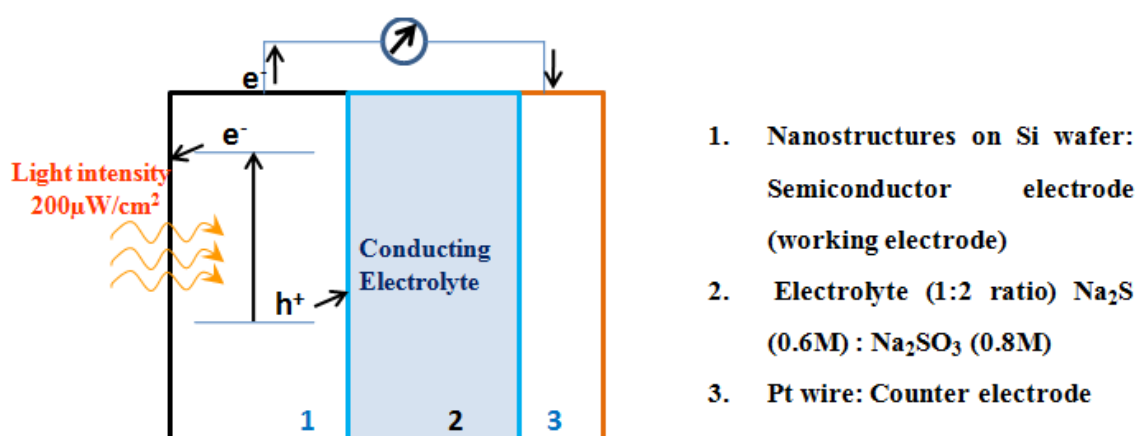


**Fig. 2.2** Block diagram of Photoelectrochemical Cell.

The performance of a photoelectrochemical cell is measured in terms of its conversion efficiency (Power output/Power input). As electrical power is the product of current and voltage, I-V measurements can be carried out. Efficiencies are obtained by measuring the current and voltage that are produced for different load resistances at constant standard light source and constant temperature.

$$\text{Conversion efficiency } (\eta\%) = \frac{J_{sc} \cdot V_{oc} \cdot FF \times 100\%}{P_{in}}$$

$$FF = \frac{P_{max}}{J_{sc} \cdot V_{oc}}$$

Where  $J_{sc}$  is the short current density and is equal to short circuit current ( $I_{sc}$ ) per area of the cell.  $I_{sc}$  is the short circuit current corresponds to the short circuit condition when the impedance is low and the voltage equals to zero (At  $V=0$ ).

$V_{oc}$  is the open-circuit voltage i.e. the voltage at which no current flows through the external circuit (At  $I=0$ ).  $I_{sc}$  and  $V_{oc}$  values will be obtained from I-V plot.

$P_{in}$  is taken as the product of irradiance of the incident light, measured in W/m or in Sun (1000 W/m<sup>2</sup>), with the surface area of the solar cell [m<sup>2</sup>].

FF: The fill factor is essentially a measure of quality of the solar cell. It is calculated by comparing the maximum power to the theoretical power (P) that would be output at both the open circuit voltage and short circuit current together.

### 2.2.9 Other techniques

Thermo gravimetric analyses (TGA) were carried out on a Nitzsch STA 409 PC-Luxx TG-DTA instrument, which was calibrated with  $\text{CaC}_2\text{O}_4 \cdot \text{H}_2\text{O}$ . The TG curves were recorded at a heating rate of 10 °C min<sup>-1</sup> under a flow of argon. Optical diffuse reflectance measurements in the 200-1800 nm (0.68 to 6.2 eV) regions were conducted on a two-beam spectrometer (V-670, JASCO) with a diffuse reflectance (DR) attachment consisting of an integration sphere coated with barium sulfate which was used as a reference for the same. Measured reflectance data were converted to absorption (A) using Kubelka–Munk remission function [161]. The band gaps of the samples were estimated by extrapolating the linear

portion of the plot to X (energy) axis. Magnetic susceptibility measurements for  $\text{Cu}_2\text{SnSe}_3$  (CTSe) nanocrystals were performed at 5 KOe between temperature range of 5 and 300 K using SQUID (Quantum make MPMS5) for zero field cooled (ZFC) and field cooled, and magnetization measurements were performed between 0 and 50 KOe at 5 and 300 K. EPR spectra were recorded using a Bruker EMM-1843 spectrometer operating at X-band frequency (9.4186 GHz) equipped with 100 kHz field modulation and phase sensitive detection to obtain the first derivative signal. Diphenylpicrylhydrazyl (DPPH) was used for calibration of the g-values of paramagnetic species. The simulation of the experimental spectra was performed using Bruker WINEPR Simfonia programme.

# Chapter 3

## Preparation of tin sulfide nanostructures using organotin pyridyl and pyrimidyl thiolates

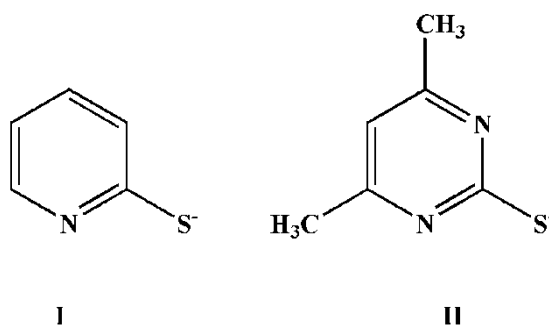
### Summary

Air stable, monomeric complexes of tin with 2-pyridylthiolate (Spy) and 4,6-dimethyl-2-pyrimidylthiolate (SpymMe<sub>2</sub>) of composition, [R<sub>2</sub>Sn(2-Spy)<sub>2</sub>] (R = Me, Et or 'Bu), [R<sub>2</sub>SnCl(2-Spy)] (R = Et or 'Bu) and [R<sub>2</sub>SnCl(2-SpymMe<sub>2</sub>)] (R = Me, Et or 'Bu) were prepared and characterized by elemental analyses and hetero-nuclear NMR (<sup>1</sup>H, <sup>13</sup>C, <sup>119</sup>Sn) spectroscopy. The molecular structures of [R<sub>2</sub>Sn(2-Spy)<sub>2</sub>] (R = Et, 'Bu), [R<sub>2</sub>SnCl(2-SpymMe<sub>2</sub>)] (R = Me, Et, 'Bu) were established unambiguously by single crystal X-ray diffraction analyses. The central tin atom acquires a skew trapezoidal bipyramidal configuration in the former [R<sub>2</sub>Sn(2-Spy)<sub>2</sub>] while distorted trigonal bipyramidal geometry in the latter three complexes [R<sub>2</sub>SnCl(2-SpymMe<sub>2</sub>)], respectively. Utility of these complexes as molecular precursors have been assessed by thermolysing diethyltin complexes [Et<sub>2</sub>Sn(2-Spy)<sub>2</sub>] and [Et<sub>2</sub>SnCl(2-SpymMe<sub>2</sub>)] in oleylamine (OLA). Thermolysis of the complexes afforded hexagonal and rectangular morphologies of phase pure orthorhombic SnS nano-sheets having thickness in the range of 30-80 nm. These nanosheets were characterized by solid state diffuse reflectance spectroscopy, XRD, EDX, SEM and TEM techniques. The band gap tuning of the nanosheets in the ranges of 1.61–1.90 eV were achieved by varying the thickness of sheets.

### 3.1 Introduction

Tin sulfide belongs to IV-VI semiconductor family and exists in three prominent forms  $\text{SnS}$ ,  $\text{SnS}_2$  and  $\text{Sn}_2\text{S}_3$  [79]. It has drawn significant attention as solar energy absorber for photovoltaic cells [100], new thermoelectric material [162] and for infrared detection [163] due to its abundant resources and good environmental compatibility [164]. The band gap values for  $\text{SnS}$ ,  $\text{SnS}_2$ ,  $\text{Sn}_2\text{S}_3$  are found to be 1.3, 2.18 and 0.95 eV, respectively [81]. Although all three forms of tin sulfide exhibit semiconducting property,  $\text{SnS}$  has received most attention because of its band gap which is nearby to optimal value of 1.5 eV required for solar cell applications. Moreover, the presence of tin vacancies in the crystal lattice makes  $\text{SnS}$  an intrinsically p-type semiconductor as a result no extrinsic doping is required. Owing to suitable characteristics  $\text{SnS}$  finds promising applications in optoelectronics and thermoelectric devices.

Various methods have been used for the preparation of SnS nanostructures and thin films [165-170]. However, the importance of molecular precursor route and its advantage over other methods prompted us to design new precursors for SnS nanostructures and thin films. Metal complexes based on internally functionalized chalcogenolate ligands have shown great potential in materials science [171–173]. 2-pyridyl- (I) and 2-pyrimidyl-chalcogenolate ion (II) represents an interesting family of hemilabile ligands with small bite angle containing both soft chalcogen and hard nitrogen atoms.



Recently, we have employed 2-pyridyl- (I) and 2-pyrimidylchalcogenolate (II) of group 12 (II), 13 (III) and 15 (V) metals for the preparation of metal chalcogenide nanomaterials and for the deposition of thin films [174-175]. In view of the above we have investigated the chemistry of organotin 2-pyridyl- and 2-pyrimidyl thiolate complexes. Accordingly, we have synthesized diorganotin(IV) complexes of 2-pyridyl- and 2-pyrimidylthiolate and utilized them as molecular precursors for the preparation of tin sulfide nanostructures. The results of this work are described herein.

## 3.2 Experimental

### 3.2.1 General consideration

Materials and techniques used during the investigation were discussed in Chapter 2.

### 3.2.2 Synthesis of [HSpymMe<sub>2</sub>]

4,6-dimethyl-2-pyrimidylthiolate was prepared according to literature method [176]. In a typical synthesis acetylacetone and thiourea in stoichiometric quantity were taken in ethanol. The mixture was refluxed for 4 hr. A crystalline yellow colour precipitate of the title compound was produced which was filtered and washed several times with 5:1 chloroform-methanol mixture (yield: 3.2 g, 87%), m.p. 215 °C. Anal. Calcd. for C<sub>6</sub>H<sub>8</sub>N<sub>2</sub>S: C, 51.39; H, 5.75; N, 19.98%. Found: C, 51.28; H, 5.77; N, 19.76%. <sup>1</sup>H NMR (D<sub>2</sub>O) δ: 2.49 (s, Me); 6.94 (s, CH-5). <sup>13</sup>C{<sup>1</sup>H} NMR (D<sub>2</sub>O) δ: 19.6 (Me); 111.5 (CH-5); 168.0 (C-2); 173.3 (C-4,6)).

### 3.2.3 Synthesis of [Me<sub>2</sub>Sn(2-Spy)<sub>2</sub>]

To a freshly prepared methanolic solution of NaSpy [from methanolic solutions of 2-HSpy (161 mg, 1.45 mmol) and NaOCH<sub>3</sub> [78 mg (14.4 ml of 0.1 M), 1.44 mmol)], solid Me<sub>2</sub>SnCl<sub>2</sub> (158 mg, 0.72 mmol) was added with vigorous stirring. The reaction mixture was stirred at room temperature for 2 h and the solvents were evaporated under vacuum. The residue was washed thoroughly with diethylether and the residue was

extracted with chloroform and passed through a G3 filtration assembly to remove NaCl. The filtrate was dried under reduced pressure and the residue was recrystallized from methanol to yield pale yellow crystals of the title complex (Yield: 174 mg, 65%), mp 138 °C. Anal. Calcd. for C<sub>12</sub>H<sub>14</sub>N<sub>2</sub>S<sub>2</sub>Sn: C, 39.05; H, 3.82; S, 17.38%. Found: C, 38.85; H, 3.75; S, 16.04%. <sup>1</sup>H NMR (CDCl<sub>3</sub>) δ: 1.01 (s, Me<sub>2</sub>Sn, 6 H, <sup>2</sup>J(Sn–H) = 75.9 Hz); 6.93 (t, CH-4, 2 H, 6.2 Hz); 7.30 (d, CH-3, 2 H, 7.8 Hz); 7.46 (t, CH-5, 2 H, 7.7 Hz); 8.07 (d, CH-6, 2 H, 4.2 Hz). <sup>13</sup>C{<sup>1</sup>H} NMR (CDCl<sub>3</sub>) δ: 7.1 (Me<sub>2</sub>Sn, <sup>1</sup>J(<sup>119</sup>Sn–<sup>13</sup>C) = 601 Hz; <sup>1</sup>J(<sup>117</sup>Sn–<sup>13</sup>C) = 575 Hz), 118.0 (C-4), 124.6 (C-5), 136.9 (C-3), 146.4 (C-6), 163.3 (C-S). <sup>119</sup>Sn{<sup>1</sup>H} NMR (CDCl<sub>3</sub>) δ: –119 ppm.

### 3.2.4 Synthesis of [Et<sub>2</sub>Sn(2-Spy)<sub>2</sub>]

Prepared in a similar fashion to [Me<sub>2</sub>Sn(2-Spy)<sub>2</sub>] and recrystallized from methanol as colorless crystals in 64% yield, mp 112 °C. Anal. Calcd. for C<sub>14</sub>H<sub>18</sub>N<sub>2</sub>S<sub>2</sub>Sn: C, 42.34; H, 4.57; S, 16.15%. Found: C, 41.98; H, 4.45; S, 15.64%. <sup>1</sup>H NMR (CDCl<sub>3</sub>) δ: 1.29 (t, SnCH<sub>2</sub>CH<sub>3</sub>, 6 H, 7.8 Hz); 1.59 (m, CH<sub>2</sub>CH<sub>3</sub>, 4 H); 6.92 (t, CH-5, 2 H, 6.2 Hz); 7.30 (d, CH-3, 2 H, 8.1 Hz); 7.45 (d,t, CH-5, 2 H, 1.5 (d), 8.4 (t) Hz); 8.12 (d, CH-6, 2 H, 4.8 Hz). <sup>13</sup>C{<sup>1</sup>H} NMR (CDCl<sub>3</sub>) δ: 10.4 (SnCH<sub>2</sub>CH<sub>3</sub>, <sup>2</sup>J(<sup>119</sup>Sn–<sup>13</sup>C) = 41 Hz), 19.1 (SnCH<sub>2</sub>, <sup>1</sup>J(<sup>119</sup>Sn–<sup>13</sup>C) = 588 Hz; <sup>1</sup>J(<sup>117</sup>Sn–<sup>13</sup>C) = 560 Hz); 117.9 (C-4), 124.7 (C-5), 136.8 (C-3), 146.6 (C-6), 164.0 (C-S). <sup>119</sup>Sn{<sup>1</sup>H} NMR (CDCl<sub>3</sub>) δ: –116 ppm.

### 3.2.5 Synthesis of [<sup>t</sup>Bu<sub>2</sub>Sn(2-Spy)<sub>2</sub>]

Prepared in a similar fashion to [Me<sub>2</sub>Sn(2-Spy)<sub>2</sub>] and recrystallized from methanol as colorless crystals in 74% yield, mp 126 °C. Anal. Calcd for C<sub>18</sub>H<sub>26</sub>N<sub>2</sub>S<sub>2</sub>Sn: C, 47.69; H, 5.78; N, 6.18; S, 14.14 %. Found: C, 46.79; H, 5.58; S, 11.50 %. <sup>1</sup>H NMR (CDCl<sub>3</sub>) δ: 1.35 (s, Bu<sup>t</sup><sub>2</sub>Sn, 18H, <sup>3</sup>J(<sup>119</sup>Sn–<sup>1</sup>H) = 109 Hz; <sup>3</sup>J(<sup>117</sup>Sn–<sup>1</sup>H) = 104 Hz); 6.91 (t, CH-4, 2H, 5.7 Hz); 7.30 (d, CH-3, 2H, 1.2 Hz); 7.42 (t, CH-5, 2H, 7.2 Hz); 8.18 (d, CH-6, 2H, 3.9

Hz).  $^{13}\text{C}$  { $^1\text{H}$ } NMR ( $\text{CDCl}_3$ )  $\delta$ : 30.9 ( $\text{Me}_3\text{C-Sn}$ ), 43.5(s, C-Sn) 118.1, 124.7, 136.5, 147.1, 164.0 (ring carbons).  $^{119}\text{Sn}$ { $^1\text{H}$ } NMR ( $\text{CDCl}_3$ )  $\delta$ : -81.1 ppm.

### 3.2.6 Synthesis of $[\text{Et}_2\text{SnCl}(\text{2-Spy})_2]$

To a toluene solution of  $[\text{Et}_2\text{SnCl}(\text{2-Spy})_2]$  (74 mg, 0.19 mmol) solid  $\text{Et}_2\text{SnCl}_2$  (46 mg, 0.19 mmol) was added and the contents were stirred at room temperature for 1 hr. The solvent was evaporated under vacuum and the residue was washed with hexane and again dried to give cream colored sticky mass (yield 70% ).  $^1\text{H}$  NMR ( $\text{CDCl}_3$ )  $\delta$ : 1.33 (t,  $\text{SnCH}_2\text{CH}_3$ , 7.8 Hz), 1.64 (m,  $\text{SnCH}_2$ ), 7.05 (t, 6 Hz), 7.27 (d, 8.4 Hz), 7.59 (t, 8.1 Hz), 7.94 (d, 5.3 Hz).  $^{13}\text{C}$ { $^1\text{H}$ } NMR ( $\text{CDCl}_3$ )  $\delta$ : 10.0 ( $\text{SnCH}_2\text{CH}_3$ ,  $^2\text{J}(\text{Sn-C}) = 38$  Hz), 17.9 ( $\text{SnCH}_2$ ,  $^1\text{J}(^{119}\text{Sn}-^{13}\text{C}) = 529$  Hz,  $^1\text{J}(^{117}\text{Sn}-^{13}\text{C}) = 505$  Hz), 119.0, 123.9, 138.9, 145.8, 164.7 ppm.  $^{119}\text{Sn}$ { $^1\text{H}$ } NMR ( $\text{CDCl}_3$ )  $\delta$ : -57 ppm.

### 3.2.7 Synthesis of $[\text{tBu}_2\text{SnCl}(\text{2-Spy})_2]$

To a toluene solution of  $[\text{tBu}_2\text{Sn}(\text{2-Spy})_2]$  [76.6 mg, 0.17 mmol] was added  $\text{tBu}_2\text{SnCl}_2$  [51.2 mg, 0.16 mmol] as solid and the resulting solution was stirred for 2 h at room temperature. The solvent were evaporated in vacuum to yield an off white solid (yield: 57 mg, 89 %) mp 116 °C. The compound was dissolved in chloroform (~ 5 ml) and left for slow evaporation to yield white crystals suitable for X-ray diffraction. Anal. Calcd for  $\text{C}_{12}\text{H}_{21}\text{ClN}_2\text{SSn}$ : C, 37.97; H, 5.57; N, 7.38; S, 8.44. Found C, 41.34; H, 5.72; N, 7.40; S, 7.58 %.  $^1\text{H}$  NMR ( $\text{CDCl}_3$ )  $\delta$ : 1.42 (s,  $\text{tBu}_2\text{Sn}$ , 18H,  $^3\text{J}(^{119}\text{Sn}-^1\text{H}) = 114$  Hz;  $^3\text{J}(^{117}\text{Sn}-^1\text{H}) = 109$  Hz); 7.01 (t, CH-4, 1H, 9 Hz); 7.32 (d, CH-3, 1H, 0.9 Hz); 7.57 (t, CH-5, 2H, 0.9 Hz); 8.06 (d, CH-6, 1H, 1.8 Hz).  $^{13}\text{C}$  { $^1\text{H}$ } NMR ( $\text{CDCl}_3$ )  $\delta$ : 30.2 ( $\text{Me}_3\text{C-Sn}$ ), 42.4 ( $\text{Me}_3\text{C-Sn}$ ), 118.5, 124.1, 138.6, 146.7, 166.1 (ring carbons).  $^{119}\text{Sn}$ { $^1\text{H}$ } NMR ( $\text{CDCl}_3$ )  $\delta$ : -87.7 ppm.



### 3.2.8 Synthesis of [Me<sub>2</sub>SnCl(2-SpymMe<sub>2</sub>)]

To a freshly prepared methanolic solution of NaspymMe<sub>2</sub> [from methanolic solutions of 2-HSpymMe<sub>2</sub> (153 mg, 1.09 mmol) and NaOCH<sub>3</sub> [58 mg (10.9 ml of 0.1 M), 1.07 mmol)], solid Me<sub>2</sub>SnCl<sub>2</sub> (119 mg, 0.54 mmol) was added with vigorous stirring which continued for 2 h. The solvents were removed under reduced pressure. The residue was washed thoroughly with diethylether and the residue was extracted with chloroform and filtered to remove NaCl. The filtrate was dried under vacuum to give yellow solid which was recrystallized from methanol to yield pale yellow crystals of title complex (Yield: 158 mg, 67.5%), mp 102 °C. Anal. Calcd. for C<sub>8</sub>H<sub>13</sub>ClN<sub>2</sub>SSn: C, 29.71; H, 4.05; S, 9.91%. Found: C, 29.32; H, 4.12; S, 10.35%. <sup>1</sup>H NMR (CDCl<sub>3</sub>) δ: 1.09 (s, Me<sub>2</sub>Sn, 6 H, <sup>2</sup>J(Sn-H) = 72 Hz); 2.36 (s, C<sub>4</sub>H(*Me*-4,6)N<sub>2</sub>, 6 H); 6.76 (s, *CH*-5, C<sub>4</sub>H(*Me*-4,6)N<sub>2</sub>). <sup>13</sup>C{<sup>1</sup>H} NMR (CDCl<sub>3</sub>) δ: 5.7 (SnCH<sub>3</sub>, <sup>1</sup>J(<sup>119</sup>Sn-<sup>13</sup>C) = 561 Hz; <sup>1</sup>J(<sup>117</sup>Sn-<sup>13</sup>C) = 536 Hz), 23.0 (C<sub>4</sub>H(4,6-*Me*)N<sub>2</sub>), 115.6 (C-5), 167.3 (C-4,6), 173.9 (C-S). <sup>119</sup>Sn{<sup>1</sup>H} NMR (CDCl<sub>3</sub>) δ: -66 ppm.

### 3.2.9 Synthesis of [Et<sub>2</sub>SnCl(2-SpymMe<sub>2</sub>)]

Prepared in a similar fashion to [Me<sub>2</sub>SnCl(2-SpymMe<sub>2</sub>)] and recrystallized from methanol as pale yellow crystals in 66% yield, mp 126 °C. Anal. Calcd. for C<sub>10</sub>H<sub>17</sub>ClN<sub>2</sub>SSn: C, 34.17; H, 4.88; S, 9.12%. Found: C, 34.59; H, 4.86; S, 9.80%. <sup>1</sup>H NMR (CDCl<sub>3</sub>) δ: 1.36 (t, SnCH<sub>2</sub>CH<sub>3</sub>, 6 H, 7.8 Hz); 1.63 (m, CH<sub>2</sub>CH<sub>3</sub>, 4 H); 2.35 (s, C<sub>4</sub>H(*Me*-4,6)N<sub>2</sub>, 6 H); 6.75 (s, *CH*-5, C<sub>4</sub>H(4,6-*Me*)N<sub>2</sub>). <sup>13</sup>C{<sup>1</sup>H} NMR (CDCl<sub>3</sub>) δ: 9.9 (SnCH<sub>2</sub>CH<sub>3</sub>, <sup>2</sup>J(<sup>119</sup>Sn-<sup>13</sup>C) = 41 Hz), 17.3 (SnCH<sub>2</sub>, <sup>1</sup>J(<sup>119</sup>Sn-<sup>13</sup>C) = 522 Hz; <sup>1</sup>J(<sup>117</sup>Sn-<sup>13</sup>C) = 500 Hz), 23.3 (C<sub>4</sub>H(4,6-*Me*)N<sub>2</sub>), 115.5 (C-5), 167.2 (C-4,6), 174.5 (C-S). <sup>119</sup>Sn{<sup>1</sup>H} NMR (CDCl<sub>3</sub>) δ: -58 ppm.

### 3.2.10 Synthesis of [ $t\text{Bu}_2\text{SnCl}(2\text{-SpymMe}_2)$ ]

Prepared in a similar fashion to [ $\text{Me}_2\text{SnCl}(2\text{-SpymMe}_2)$ ] and recrystallized from methanol as off white crystals in 72% yield, mp 98 °C. Anal. Calcd for  $\text{C}_{14}\text{H}_{25}\text{ClN}_2\text{SSn}$ : C, 41.25; H, 6.18; N, 6.87; S, 7.86 %. Found: C, 40.01; H, 5.93; S, 7.01 %.  $^1\text{H}$  NMR ( $\text{CDCl}_3$ )  $\delta$ : 1.47 (s,  $t\text{Bu}_2\text{Sn}$ , 18H,  $^3\text{J}(^{119}\text{Sn}-^1\text{H}) = 112$  Hz;  $^3\text{J}(^{117}\text{Sn}-^1\text{H}) = 108$  Hz); 2.39 (s,  $\text{C}_4\text{H}(\text{Me}-4,6)\text{N}_2$ , 6H); 6.76 (s, CH-5,  $\text{C}_4\text{H}(4,6\text{-Me})\text{N}_2$ ).  $^{13}\text{C}$   $\{^1\text{H}\}$  NMR ( $\text{CDCl}_3$ )  $\delta$ : 23.9 ( $\text{C}_4\text{H}(4,6\text{-Me})\text{N}_2$ ), 30.8 ( $\text{Me}_3\text{C-Sn}$ ), 43.7 ( $\text{Me}_3\text{C-Sn}$ ), 116.1, 117.2, 119.4, 167.1, 174.8.  $^{119}\text{Sn}\{^1\text{H}\}$  NMR ( $\text{CDCl}_3$ )  $\delta$ : -45.0 ppm.

### 3.2.11 Preparation of tin sulfide nanostructures

The nanostructures were prepared by hot injection method. In a typical experiment 8ml of oleyl amine (OLA) was taken in three necked round bottom flask and temperature was raised to 300 °C. To this, dispersion of [ $\text{Et}_2\text{Sn}(2\text{-Spy})_2$ ] (100 mg, 0.25 mmol) in OLA (2 ml) was injected under vigorous stirring and flowing argon. The reaction mixture was held at this temperature for different durations (10 and 20 min). After the desired growth time, the reaction temperature was cooled down rapidly to 98 °C and quenched by injecting toluene (4 ml). The resulting nanostructures were separated by precipitating with excess methanol followed by centrifugation to give a black powder. Similarly, [ $\text{Et}_2\text{SnCl}(2\text{-SpymMe}_2)$ ] (100 mg, 0.28 mmol) was thermolysed under same conditions (5 and 10 minutes). The [ $\text{Et}_2\text{SnCl}(2\text{-SpymMe}_2)$ ] was also thermolysed in TOPO (3 g, 7.76 mmol)/OLA at 320 °C and the nanostructures were isolated similarly.

### 3.2.12 Preparation of thin films by Aerosol Assisted Chemical Vapor Deposition (AACVD)

A toluene solution (25 ml) of [ $t\text{Bu}_2\text{Sn}(2\text{-Spy})_2$ ] (150mg, 0.33 mmol) was used to generate aerosol by an ultrasonic humidifier. The aerosol was transported over a period of

1 h using argon as a carrier gas (flow rates of 180 sccm) to a preheated glass and silicon wafer (110) orientation placed in a turbo furnace at 400 °C.

### 3.2.13 Crystallography

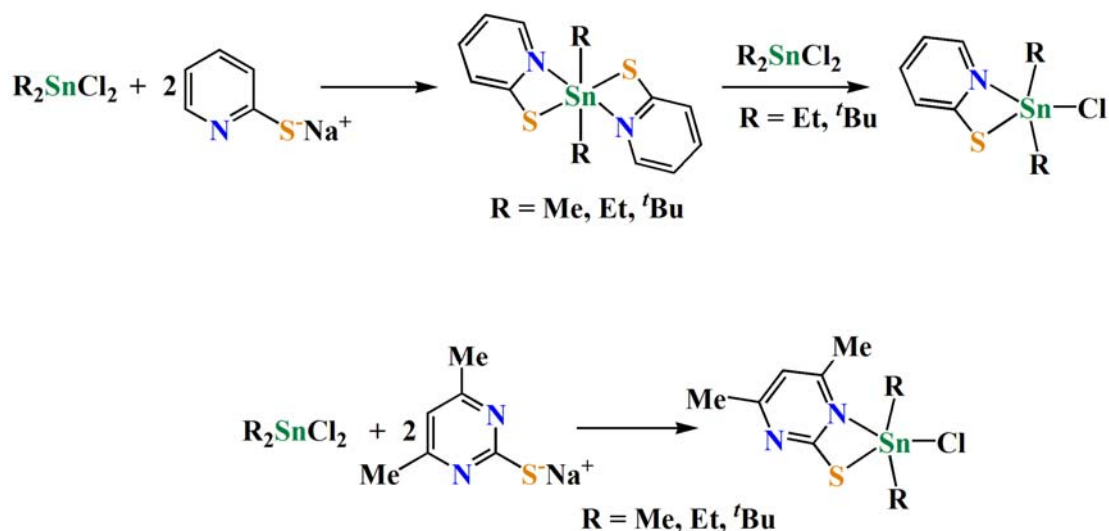
Intensity data for  $[\text{Et}_2\text{Sn}(\text{2-Spy})_2]$  was collected on a Agilent Super Nova microfucus X-ray source ( $\text{CuK}_\alpha$ ,  $\lambda = 1.5418 \text{ \AA}$ ) radiation,  $[\text{'Bu}_2\text{Sn}(\text{2-Spy})_2]$ ,  $[\text{'Bu}_2\text{SnCl}(\text{2-Spy})]$ ,  $[\text{Me}_2\text{SnCl}(\text{2-SpymMe}_2)]$ ,  $[\text{Et}_2\text{SnCl}(\text{2-SpymMe}_2)]$  and  $[\text{'Bu}_2\text{SnCl}(\text{2-SpymMe}_2)]$  were collected on a Rigaku AFC7S diffractometer using graphite monochromated  $\text{MoK}_\alpha$  ( $\lambda = 0.71069 \text{ \AA}$ ). The unit cell parameters determined from 25 reflections measured by a random search routine were given in Table 2.1 and 2.2 (Chapter 2).

## 3.3 Results and discussion

### 3.3.1 Synthesis and spectroscopy

Treatment of  $\text{R}_2\text{SnCl}_2$  ( $\text{R} = \text{Me}, \text{Et}$  or  $\text{'Bu}$ ) with two equivalents of sodium pyridyl/4,6-dimethyl-2-pyrimidyl thiolates,  $\text{Na}(\text{2-Spy})/\text{Na}(\text{2-SpymMe}_2)$ , in a toluene-methanol mixture gave diorganotin thiolate complexes of the type,  $[\text{R}_2\text{Sn}(\text{2-Spy})_2]$  and  $[\text{R}_2\text{SnCl}(\text{2-SpymMe}_2)]$ , respectively (Scheme1). Bis pyridyl thiolates upon reaction with  $\text{R}_2\text{SnCl}_2$  undergo redistribution reaction to afford diorganotinchloro-2-pyridylthiolate complexes.

The  $^1\text{H}$ ,  $^{13}\text{C}\{^1\text{H}\}$  and  $^{119}\text{Sn}\{^1\text{H}\}$  NMR spectra were recorded in  $\text{CDCl}_3$ .  $^1\text{H}$  and  $^{13}\text{C}$  NMR spectra showed expected resonances and peak multiplicities. The pyridyl/pyrimidyl ring proton resonances of all the complexes shifted to down field with reference to the corresponding signals for free ligand. There is an appreciable shift in the CH-6 proton resonances of the 2-pyridylthiolate complexes with respect to its position in free ligand.



**Scheme 3.1** Synthesis of tin pyridyl/pyrimidyl thiolate complexes

This may be attributed to tin-nitrogen coordination resulting in chelation of the ligand. The CH-5 proton resonance for  $[R_2\text{SnCl}(2\text{-SpymMe}_2)]$  is shielded with respect to the free ligand. The magnitude of  $^2J(^{119}\text{Sn}-^1\text{H})$  for  $[\text{Me}_2\text{Sn}(2\text{-Spy})_2]$  (~76 Hz) is smaller than expected for six coordinated dimethyltin complexes [177] while  $^2J(\text{Sn}-\text{H})$  (~72 Hz) for  $[\text{Me}_2\text{SnCl}(2\text{-SpymMe}_2)]$  is in accordance with five coordinate dimethyltin complexes.

The C–Sn–C angles for  $[\text{Me}_2\text{Sn}(2\text{-Spy})_2]$  and  $[\text{Me}_2\text{SnCl}(2\text{-SpymMe}_2)]$  have been estimated as  $129^\circ$  and  $125^\circ$ , respectively by Lockhart and Davidson's relationship  $[^1J(^{119}\text{Sn}-^{13}\text{C}) = 10.7 (\angle\text{C-Sn-C}) - 778]$  [178]. These C–Sn–C values can be compared with the one estimated by X-ray structural analysis ( $125.1(5)$  and  $126.5(4)^\circ$  for  $[\text{Me}_2\text{Sn}(2\text{-Spy})_2]$  and  $[\text{Me}_2\text{SnCl}(2\text{-SpymMe}_2)]$ , respectively, suggesting that the solid state structure is retained in the solution. The C–Sn–C angle in octahedral diorganotin complexes varies from  $110\text{--}180^\circ$  depending on a skew to regular *trans* arrangement of R groups on central tin atom [177]. Similarly the magnitude of  $^1J(\text{Sn}-\text{C})$  coupling constants are consistent with six  $[\text{Me}_2\text{Sn}(2\text{-Spy})_2]$  (Me and Et) and five ( $[\text{Me}_2\text{SnCl}(2\text{-Spy})]$ ,  $[\text{Me}_2\text{SnCl}(2\text{-SpymMe}_2)]$  (Me and Et)) coordinate diorganotin complexes [179].

The  $^{119}\text{Sn}\{^1\text{H}\}$  NMR spectra showed single resonances in the range  $-45$  to  $-119$  ppm and these signals within the series (bis or chloro) are deshielded on replacing methyl groups on tin by Et or  $^t\text{Bu}$  groups which could be due to +I effect of the larger alkyl group. Similarly,  $^{119}\text{Sn}$  NMR resonances for the complexes are deshielded with respect to their selenium analogues as S is more electronegative than selenium which results in more deshielding. The  $^{119}\text{Sn}$  NMR chemical shifts for  $[\text{R}_2\text{Sn}(\text{2-Spy})_2]$  and  $[\text{R}_2\text{SnCl}(\text{2-Spy})]$ ,  $[\text{R}_2\text{SnCl}(\text{2-SpymMe}_2)]$  are lower than the ranges reported for six-coordinated ( $-125$  to  $-400$  ppm) and five-coordinated ( $-90$  to  $-200$  ppm) diorganotin complexes with O-bonded and halide ligands [180]. The deviation from the expected ranges may be attributed to the difference in the polarities of Sn-S and Sn-O bonds.

### 3.3.2 X-ray Crystallography

The molecular structures of  $[\text{Et}_2\text{Sn}(\text{2-Spy})_2]$ ,  $[\text{tBu}_2\text{Sn}(\text{2-Spy})_2]$ ,  $[\text{Me}_2\text{SnCl}(\text{2-SpymMe}_2)]$ ,  $[\text{Et}_2\text{SnCl}(\text{2-SpymMe}_2)]$  and  $[\text{tBu}_2\text{SnCl}(\text{2-SpymMe}_2)]$  have been established by single crystal X-ray diffraction analysis are shown in Fig. 3.1.

Selected inter-atomic parameters are given in Tables 3.1-3.3.

The Sn-S distances in bis complexes are slightly longer than those found in the corresponding chloro derivatives. The overall coordination environment around tin in  $[\text{R}_2\text{Sn}(\text{2-Spy})_2]$  ( $\text{R} = \text{Et}, ^t\text{Bu}$ ) is similar to other analogous structures of  $\text{R}_2\text{Sn}(\text{Spy})_2$  ( $\text{R} = \text{Me}$  [181],  $\text{Ph}$  [182] and  $\text{c-Hex}$  [183]) which have a skew trapezoidal bipyramidal geometry. The effect of bulky tert-butyl group is evident on the overall coordination environment in  $[\text{tBu}_2\text{Sn}(\text{2-Spy})_2]$  complex. Unlike other diorganotin bis(2-pyridylthiolates),  $[\text{R}'_2\text{Sn}(\text{SR})_2]$  ( $\text{R}' = \text{Me}$  [181],  $\text{Ph}$  [182]) and  $[\text{Et}_2\text{Sn}(\text{2-Spy})_2]$  which shows weak Sn---N intramolecular interactions, (e.g.  $2.702(5)$  Å in  $[\text{Me}_2\text{Sn}(\text{Spy})_2]$  [181]) such interactions in the present case are vanishingly present. Consequently the C-Sn-C angles are reduced to  $134.3(3)^\circ$  (in  $[\text{tBu}_2\text{Sn}(\text{Spy})_2]$ ) from  $145.6(13)^\circ$  in  $[\text{Et}_2\text{Sn}(\text{Spy})_2]$ .

The N–Sn–N and S–Sn–S angle in  $[R_2Sn(2-Spy)_2]$  ( $R = Et, ^iBu$ ) are comparable to the one found in  $Me_2Sn(Spy)_2$  ( $152.1(2)^\circ$ ) [181] and  $[^nBu_2Sn\{SC_5H_3N(5-NO_2)\}_2]$  [184].

**Table 3.1** Selected inter-atomic parameters ( $\text{\AA}/^\circ$ ) for  $[R_2Sn(2-Spy)_2]$  ( $R = Et, ^iBu$ ).

$[Et_2Sn(2-Spy)_2]$		$[^iBu_2Sn(2-Spy)_2]$	
Sn1– S1	2.490(3)	Sn1 – S1	2.509(2)
Sn1– S1 <sup>i</sup>	2.490(4)	Sn1 – S1 <sup>i</sup>	2.509(2)
Sn1– C6	2.19(3)	Sn1 – C6	2.229(5)
Sn1– N1	2.661(10)	Sn1 – N1	2.957
S1– C1	1.753(14)	S1 – C1	1.717(11)
C6– Sn1–C8	145.6(13)	C6 – Sn1 – C6 <sup>i</sup>	134.3(3)
C6–Sn1–S1	99.5(8)	C6 – Sn1 – S1	107.23(16)
C6–Sn1–S1 <sup>i</sup>	99.5(8)	C6 – Sn1 – S1 <sup>i</sup>	104.76(15)
C8–Sn1–S1	104.1(4)	S1 – Sn1 – S1 <sup>i</sup>	89.51(10)
C8–Sn1– S1 <sup>i</sup>	104.1(4)	Sn1 – S1 – C1	90.9(3)
S1–Sn1– S1 <sup>i</sup>	92.28(17)	N1 – C1 – S1	116.4(7)
S1–Sn1– N1	60.9(3)	N1 – Sn – N1 <sup>i</sup>	151.63
S1 <sup>i</sup> –Sn1– N1	153.2(3)		
N1–Sn1– N1 <sup>i</sup>	145.88		
C1– S1– Sn1	88.8(5)		
C1 <sup>i</sup> – S1 <sup>i</sup> – Sn1	88.8(5)		

**Table 3.2** Selected inter-atomic parameters ( $\text{\AA}/^\circ$ ) for  $[\text{}^t\text{Bu}_2\text{SnCl}(2\text{-Spy})]$ .

$[\text{}^t\text{Bu}_2\text{SnCl}(2\text{-Spy})]$			
C6–Sn1	2.177(13)	N1–Sn1	2.489(10)
Cl1–Sn1	2.470(4)	S1–C1	1.739(16)
S1–Sn1	2.458(5)		
C6–Sn1–C6 <sup>i</sup>	131.1(6)	Cl1–Sn1–S1	91.64(19)
C6–Sn1–Cl1	96.9(3)	Cl1–Sn1–N1	154.4(3)
C6–Sn1–S1	113.1(3)	S1–Sn1–N1	62.8(3)
C5–Sn1–N1	93.5(3)	S1–C1–N1	112.6(10)
Cl1–Sn1–C6 <sup>i</sup>	96.9(3)		

The tin in  $[\text{R}_2\text{SnCl}(2\text{-SpymMe}_2)]$  ( $\text{R} = \text{Me}, \text{Et}$  and  ${}^t\text{Bu}$ ) adopts a distorted trigonal bipyramidal configuration defined by two alkyl groups, N, S and Cl donors. The chloride and the chelating 2-mercapto dimethylpyrimidyl group occupy equatorial plane while the two organic groups are axially disposed. The Sn–N distances are significantly higher in case of  ${}^t\text{Bu}$  analogue compared to Me and Et and also the one reported in  $[\text{Ph}_2\text{SnCl}(\text{Spy})]$  (2.413  $\text{\AA}$ ) [182]. This can be attributed to steric demand of  ${}^t\text{Bu}$  groups attached to tin which forces pyrimidyl ring to occupy space at a larger distance from the tin atoms.

**Table 3.3** Selected inter-atomic parameters ( $\text{\AA}/^\circ$ ) for  $[R_2\text{SnCl}(2\text{-SpymMe}_2)]$  ( $R = \text{Me}, \text{Et}, \text{'Bu}$ ).

[Me <sub>2</sub> SnCl(2-SpymMe <sub>2</sub> )]		[Et <sub>2</sub> SnCl(2-SpymMe <sub>2</sub> )]		[ <sup>t</sup> Bu <sub>2</sub> SnCl(2-SpymMe <sub>2</sub> )]	
Sn1–S1	2.443(3)	Sn1–C7	2.120(9)	C7–Sn1	2.183(7)
Sn1–C7	2.199(8)	Sn1–C9	2.123(9)	C11–Sn1	2.178(8)
Sn1–N1	2.505(8)	Sn1–Cl1	2.438 (2)	Cl1–Sn1	2.427(2)
Sn1–Cl1	2.436(3)	Sn1–S1	2.452(2)	S1–Sn1	2.438(2)
S1–C1	1.756(11)	Sn1–N1	2.525(5)	N1–Sn1	2.704
C7–Sn1–C7 <sup>i</sup>	126.5(4)	S1–C1	1.740(8)	S1–C1	1.743(8)
C7–Sn1–Cl1	100.4(2)	C7–Sn1–C9	128.0(4)	C7–Sn1–C11	127.0(3)
C7–Sn1–N1	90.5(2)	C7–Sn1–Cl1	101.7(3)	C7–Sn1–Cl1	97.8(2)
C7–Sn1–S1	114.0(2)	C7–Sn1–S1	112.5(3)	C7–Sn1–S1	117.2(2)
Cl1– Sn1–S1	91.87(10)	C7–Sn1–N1	90.0(3)	C7–Sn1–N1	94.52
Cl1– Sn1–N1	155.3(2)	C9–Sn1–Cl1	98.7(3)	C11–Sn1–Cl1	99.4(3)
S1– Sn1–N1	63.4(2)	C9–Sn1–S1	114.1(2)	C11–Sn1–S1	112.3(2)
		C9–Sn1–N1	91.4(3)	C11–Sn1–N1	93.11
		Cl1–Sn1–S1	91.48(9)	Cl1–Sn1–S1	90.86(9)
		Cl1–Sn1–N1	154.60(17)	Cl1 – Sn1 – N1	151.94
		S1–Sn1–N1	63.15(16)	S1 – Sn1 – N1	61.09



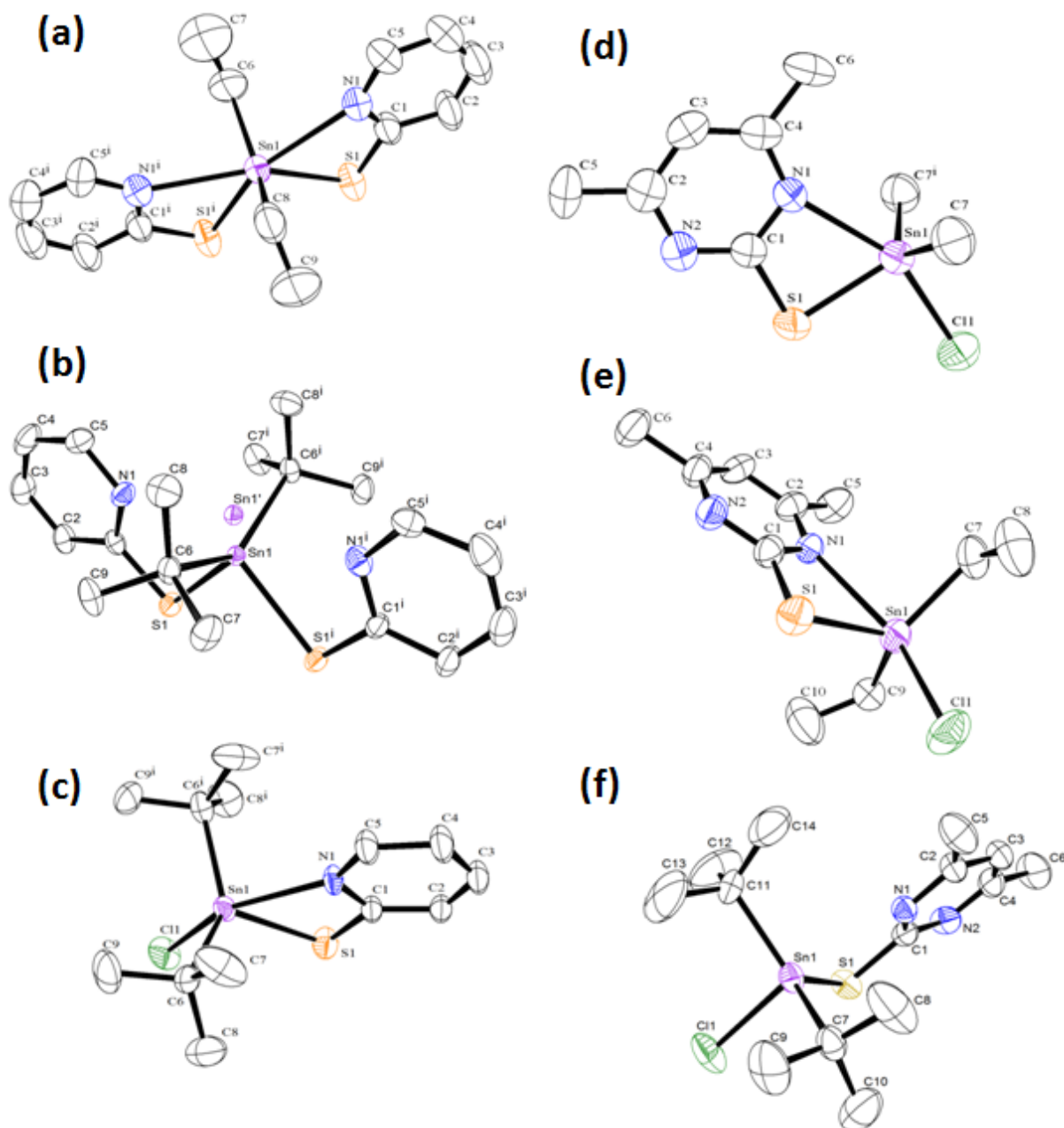


**Fig. 3.1** Crystal structure of a)  $[\text{Et}_2\text{Sn}(2\text{-Spy})_2]$ , b)  $[\text{tBu}_2\text{Sn}(2\text{-Spy})_2]$ , c)  $[\text{tBu}_2\text{ClSn}(2\text{-Spy})]$ , d)  $[\text{Me}_2\text{SnCl}(2\text{-SpymMe}_2)]$ , e)  $[\text{Et}_2\text{SnCl}(2\text{-SpymMe}_2)]$  and f)  $[\text{tBue}_2\text{SnCl}(2\text{-SpymMe}_2)]$  with atomic number scheme. The ellipsoids were drawn at 25% probability.

### 3.3.3 Thermal studies

Thermo gravimetric analyses (TGA) of these complexes were carried out to evaluate the thermal decomposition of the complexes under a flowing argon atmosphere

(Fig. 3.2). The complexes,  $[R_2Sn(2-Spy)_2]$  ( $R = Me, Et$ ) undergo an ill defined two-step decomposition. The first stage of decomposition corresponds to the formation of SnS as inferred from the weight loss (weight loss: found 57.1%, calcd. 59.7% for  $[Me_2Sn(2-Spy)_2]$  (**1**); found 62%, calcd. 62% for  $[Et_2Sn(2-Spy)_2]$ ). The second step corresponds to the decomposition of SnS to tin (weight loss: found 23.3%, calcd. 21.2%  $[Me_2Sn(2-Spy)_2]$  and found 21.3%, calcd. 21.2%  $[Et_2Sn(2-Spy)_2]$ ). On the contrary,  $[^tBu_2Sn(2-Spy)_2]$  undergo single step decomposition leading to the formation of SnS (weight loss found 66%, calcd. 64%)

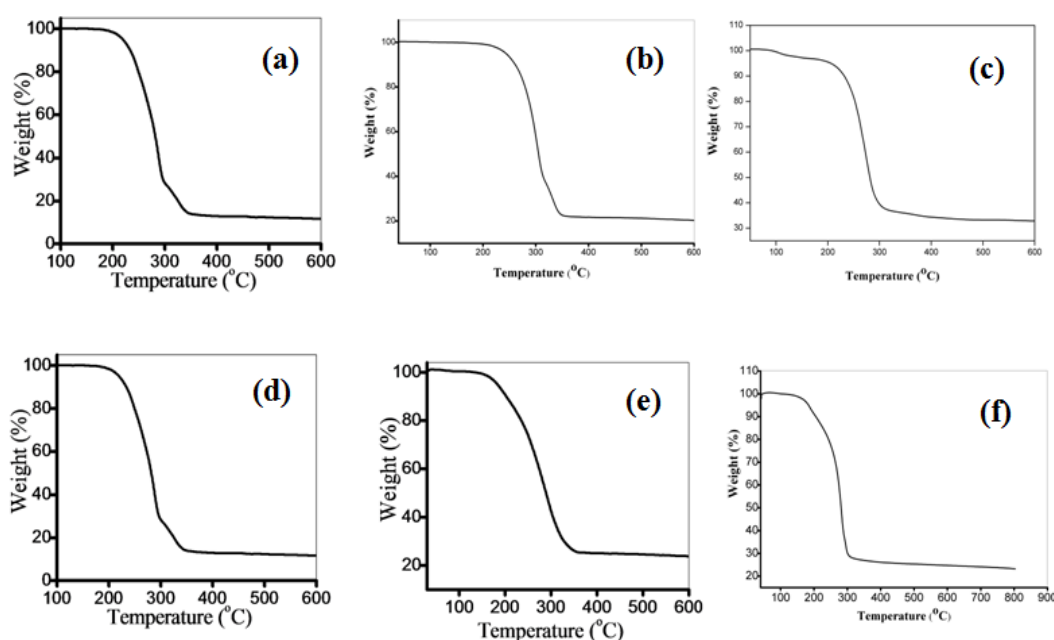


**Fig. 3.2** TG curve of a)  $[Me_2Sn(2-Spy)_2]$ , b)  $[Et_2Sn(2-Spy)_2]$ , c)  $[^tBu_2Sn(2-Spy)_2]$ , d)  $[Me_2SnCl(2-SpymMe_2)]$ , e)  $[Et_2SnCl(2-SpymMe_2)]$  and f)  $[^tBu_2SnCl(2-SpymMe_2)]$ .

The complexes,  $[R_2SnCl(2-SpymMe_2)]$  ( $R = Me, Et$ ) decompose in a single step at 200 °C for methyl and 288 °C for ethyl derivative. The weight loss was significantly higher than expected for either formation of SnS or Sn. It is likely that the complexes undergo disproportionation into  $R_2SnCl_2$  and  $R_2Sn(2-SpymMe_2)_2$  and the former

vaporizes while latter decomposes to stable tin sulfide. The disproportionation of the complexes at high temperature was also supported by the  $^{119}\text{Sn}\{^1\text{H}\}$  NMR studies (Fig. 3.3) of sublimed product from  $[\text{Et}_2\text{SnCl}(\text{2-SpymMe}_2)]$ . Appearance of peak at -111 ppm corresponds to  $[\text{Et}_2\text{Sn}(\text{2-SpymMe}_2)_2]$ . This indicates disproportionation of the complex into  $[\text{Et}_2\text{Sn}(\text{SpymMe}_2)_2]$  and  $\text{Et}_2\text{SnCl}_2$ . However,  $[\text{tBu}_2\text{SnCl}(\text{2-SpymMe}_2)]$  undergo single step decomposition to form Sn (weight loss found 72%, calcd. 72%).

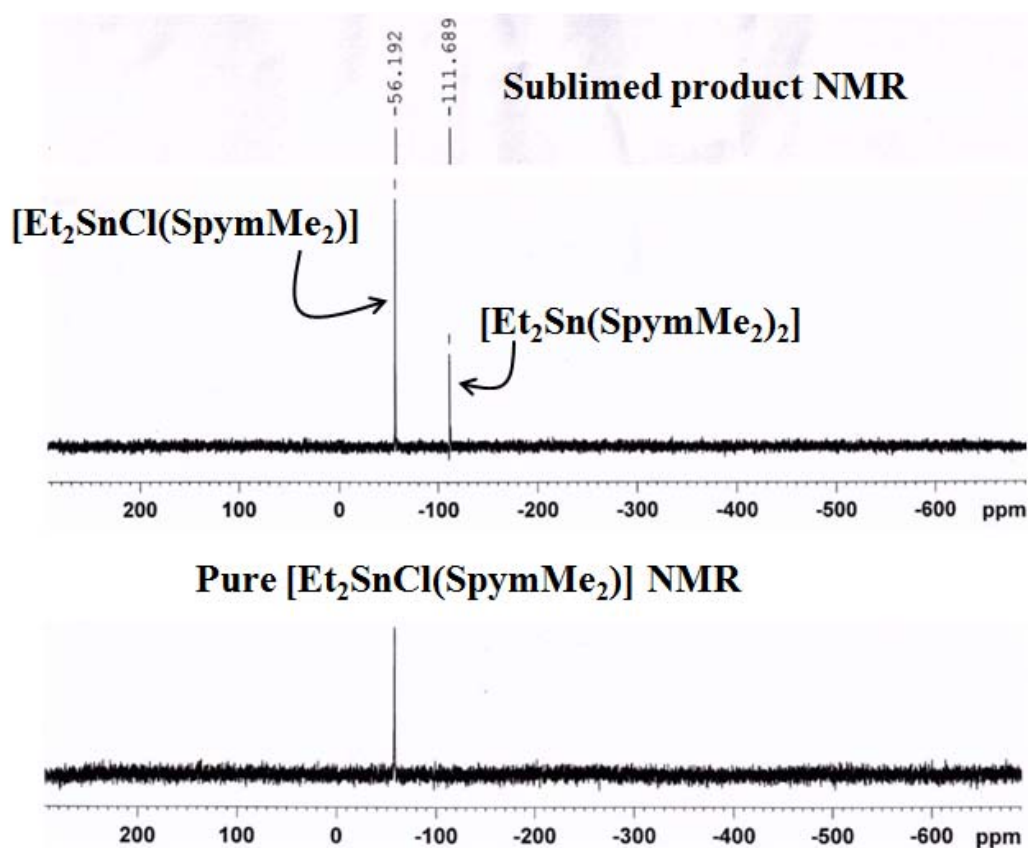


**Fig. 3.3**  $^{119}\text{Sn}\{^1\text{H}\}$  NMR spectra ( $\text{CDCl}_3$ ) of (a) Freshly prepared  $[\text{Et}_2\text{SnCl}(\text{SpymMe}_2)]$  (b) sublimed product from the complex at 200 °C under vacuum. The formation of  $[\text{Et}_2\text{Sn}(\text{SpymMe}_2)_2]$  indicates disproportionation of the complex into  $[\text{Et}_2\text{Sn}(\text{SpymMe}_2)_2]$  and  $\text{Et}_2\text{SnCl}_2$ .

### 3.3.4 Preparation and characterization of tin sulfide nanostructures

The TG data indicate that these complexes decompose to tin sulfide, thus two representative diethyltin complexes were chosen to assess their suitability of single source molecular precursor for tin sulfide. Tin sulfide nanostructures were prepared by employing  $[\text{Et}_2\text{Sn}(\text{2-Spy})_2]$  and  $[\text{Et}_2\text{SnCl}(\text{2-SpymMe}_2)]$ . The resulting products were characterized by solid state diffuse reflectance, FT-IR, thermo gravimetric analysis, X-ray powder diffraction (XRD), energy dispersive X-ray analysis (EDX) (Supplementary information), SEM, TEM and selective area electron diffraction (SAED) techniques.

#### Preparation of tin sulfide nanostructures

Tin sulfide nanostructures were prepared by injecting diethyltin complexes,  $[\text{Et}_2\text{Sn}(\text{2-Spy})_2]$  and  $[\text{Et}_2\text{SnCl}(\text{2-SpymMe}_2)]$ , in high boiling coordinating solvents like OLA or TOPO. Initially, the use of OLA as surface passivating agent (surfactant) to prepare tin sulfide nanostructures was driven by the fact that amines have good affinity for tin and secondly, ease of handling OLA during the purification of nanocrystals. However, the average size of nanostructures as calculated by Scherrer's formula comes out to be in the range of 30.9-39.7 nm. So, in order to achieve the nanostructures of smaller size, either reaction timing or the injection temperature may be reduced or strong coordinating ligand like TOPO can be used as a surfactant. However, reduction either in the injection temperature below 300 °C or the reaction time less than 5 minutes resulted in incomplete decomposition. Thus, TOPO was used as surfactant for thermolysis of  $[\text{Et}_2\text{SnCl}(\text{2-SpymMe}_2)]$  to prepare smaller nanostructures of tin sulfide. The initial pale yellow solution of the complex turned dark yellow on thermolysis in TOPO-OLA which gradually changed to red and dark brown from which tin sulfide nanoparticles were separated and characterized.

### Characterization of tin sulfide nanostructures

Thermolysis of  $[\text{Et}_2\text{Sn}(\text{2-Spy})_2]$  (0.25 mmol) and  $[\text{Et}_2\text{SnCl}(\text{2-SpymMe}_2)]$  (0.28 mmol) in OLA for different duration (experimental section) at 300 °C gave black residue of tin sulfide. The crystal structure and phase purity of the black residues was investigated using powder X-ray diffraction (p-XRD) technique. The XRD pattern of the residue obtained by thermolysis of  $[\text{Et}_2\text{Sn}(\text{2-Spy})_2]$  in OLA at 300 °C for 10 minutes exhibited peaks at 22.0, 25.9, 27.4, 30.5, 31.6, 32.0, 39.0, 42.5, 44.6, 45.5, 48.7, 51.3, 52.1, 53.4, 54.2, 56.6 and 59.5°. These peaks can be assigned to the reflections originating from (110), (120), (021), (101), (130), (040), (131), (210), (141), (002), (060), (151), (032), (160), (061), (132) and (250) planes of orthorhombic SnS (JCPDS-39-0354) (Fig. 3.4b). The lattice parameters for these nano-structures determined from the PXRD data using equation 1 (where h, k, and l are the lattice planes while a, b, c are lattice parameters and d is the inter-planar distance) are  $a = 4.340(13) \text{ \AA}$ ,  $b = 11.191(20) \text{ \AA}$ ,  $c = 3.984(10) \text{ \AA}$ , which are consistent with literature values ( $a = 4.329 \text{ \AA}$ ,  $b = 11.19 \text{ \AA}$ ,  $c = 3.983 \text{ \AA}$ ) for orthorhombic SnS (JCPDS-39-0354).

The intensity of these Bragg reflections indicates their crystalline nature. The average crystallite size as estimated by Scherrer's formula is 38 nm. Its composition is supported by EDX (from  $[\text{Et}_2\text{Sn}(\text{2-Spy})_2]$ , Sn:S atom ratio is 53.8:46.2 or 1.2:1).

$$\frac{1}{d^2} = \frac{h^2}{a^2} + \frac{k^2}{b^2} + \frac{l^2}{c^2} \quad (3.1)$$

Similarly, XRD profile of the residue obtained by thermolysis of  $[\text{Et}_2\text{SnCl}(\text{2-SpymMe}_2)]$  in OLA at 300 °C for 5 and 10 minutes showed peaks and their intensities corresponding to orthorhombic SnS (JCPDS-39-0354) (Fig. 3.4c and 3.4d). The

composition is supported by EDX analysis (from  $[\text{Et}_2\text{SnCl}(\text{2-SpymMe}_2)]$ ): Sn:S atom ratio is 52:48 or 1.1:1 (for 5 minutes); Sn:S atom ratio is 54.3:45.6 or 1.2:0.8 (for 10 minutes)).

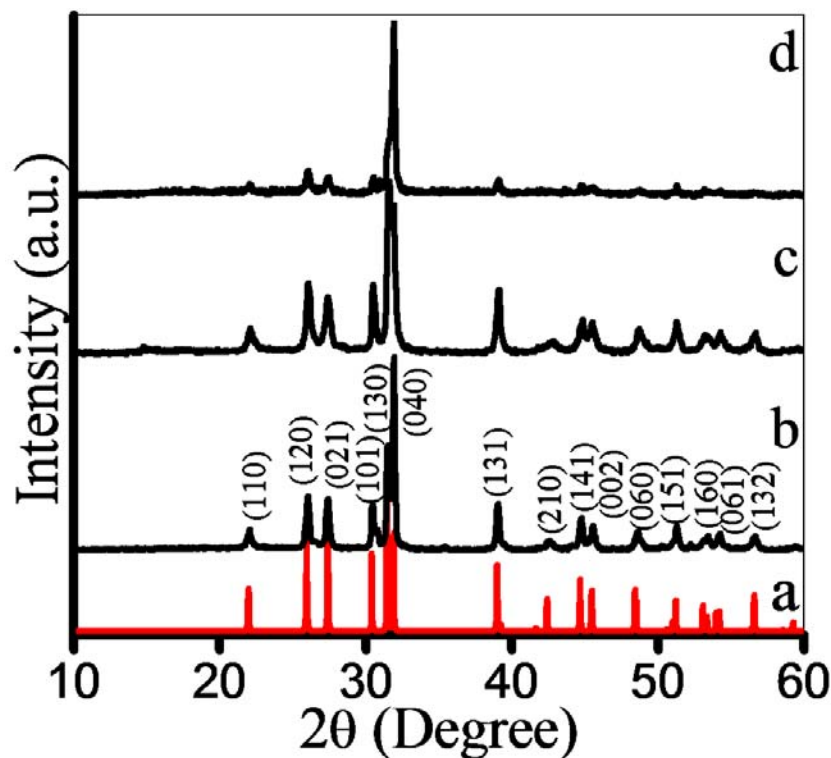


**Fig. 3.4** a) Simulated XRD pattern of orthorhombic SnS (JCPDS-39-0354). XRD profiles of SnS nanosheets obtained by b) thermolysis of  $[\text{Et}_2\text{Sn}(\text{2-Spy})_2]$  in OLA at 300 °C for 10 minutes and by thermolysis of  $[\text{Et}_2\text{SnCl}(\text{SpymMe}_2)]$  in OLA at 300 °C for c) 5 and d) 10 minutes.

The lattice parameters for these residues are  $a = 4.326(2) \text{ \AA}$ ,  $b = 11.217(3) \text{ \AA}$ ,  $c = 3.982(3)$  (for 5 min.) and  $a = 4.328(8) \text{ \AA}$ ,  $b = 11.194(1) \text{ \AA}$ ,  $c = 3.990(7)$  (for 10 min.), respectively which are in accord with the orthorhombic SnS (JCPDS-39-0354). Scherrer analysis of the intense reflection gave the average grain sizes of the two residues as 30.9 and 39.7 nm, respectively.

The SEM micrographs showed that the residues obtained by thermolysis of  $[\text{Et}_2\text{Sn}(\text{2-Spy})_2]$  and  $[\text{Et}_2\text{SnCl}(\text{2-SpymMe}_2)]$  have hexagonal and nearly rectangular sheet

structures, respectively (Fig. 3.5a and 3.5d). For instance, thermolysis of  $[\text{Et}_2\text{Sn}(\text{2-Spy})_2]$  afforded hexagonal sheets having edges of few microns while thermolysis of  $[\text{Et}_2\text{SnCl}(\text{2-SpymMe}_2)]$  gave nearly rectangular sheets with length and breadth of few hundred nanometers with thickness of 30-80 nm (majority being in the range of 35-60 nm). TEM images of tin sulfides (Fig. 3.5b and 3.5e) prepared by thermolysis of  $[\text{Et}_2\text{Sn}(\text{2-Spy})_2]$  and  $[\text{Et}_2\text{SnCl}(\text{2-SpymMe}_2)]$  in OLA showed hexagonal sheets (edges in the range of 200-350 nm) and a rectangular sheet (width of 310 nm, length of 390 and thickness of 58 nm), respectively. The SAED patterns (Fig. 3.5c and 3.5f) exhibited dot like pattern with sets of lattice planes, (040), (023), (063) (from  $[\text{Et}_2\text{Sn}(\text{2-Spy})_2]$ ) and (041), (200), (241) (from  $[\text{Et}_2\text{SnCl}(\text{2-SpymMe}_2)]$ ) related to orthorhombic SnS (JCPDS-39-0354) and were consistent with the XRD results. The dots like patterns suggest that SnS sheets are single crystalline in nature.

Unlike thermolysis in oylamine, the decomposition in TOPO-OLA gave a mixture of tin sulfides (SnS and  $\text{SnS}_2$ ), although the size of the resulting nanoparticles was smaller (by PXRD). The average size estimated from Scherrer's formula is 16.5 nm from thermolysis of  $[\text{Et}_2\text{SnCl}(\text{SpymMe}_2)]$  (Fig. 3.6a). The morphologies of tin sulfides obtained by thermolysis of  $[\text{Et}_2\text{SnCl}(\text{SpymMe}_2)]$  in TOPO-OLA showed square shaped sheets (edge of 49-127 nm) contaminated with nearly spherical structures (diameter 42 nm) (Fig. 3.6b). SAED pattern of square shaped sheets showed lattice fringes, (130), (121), (251) (square sheets) corresponds to orthorhombic of SnS (JCPDS-39-0354) (Fig. 3.6c).

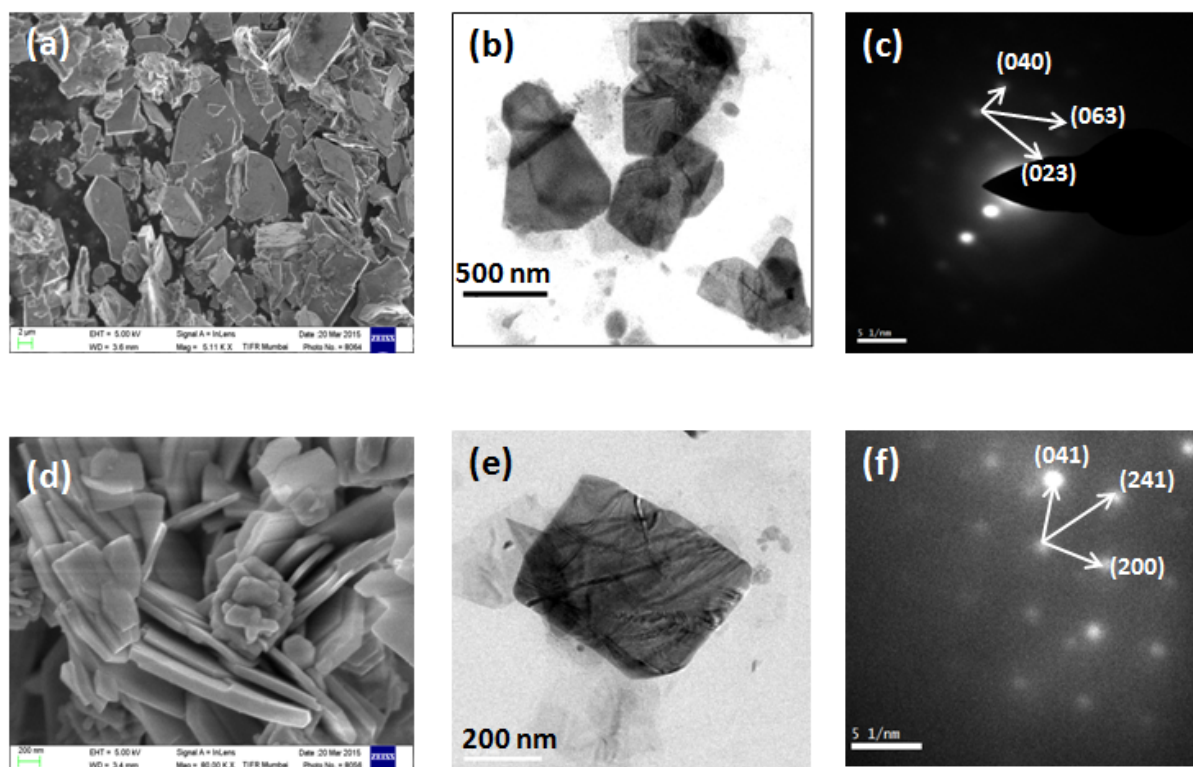


**Fig. 3.5** SEM, TEM images and SAED patterns of a), b) and c) SnS hexagonal sheets obtained by thermolysis of  $[\text{Et}_2\text{Sn}(2\text{-Spy})_2]$  and d), e) and f) rectangular sheets obtained by thermolysis of  $[\text{Et}_2\text{SnCl}(\text{SpymMe}_2)]$  in OLA at 300 °C for 10 minutes, respectively.

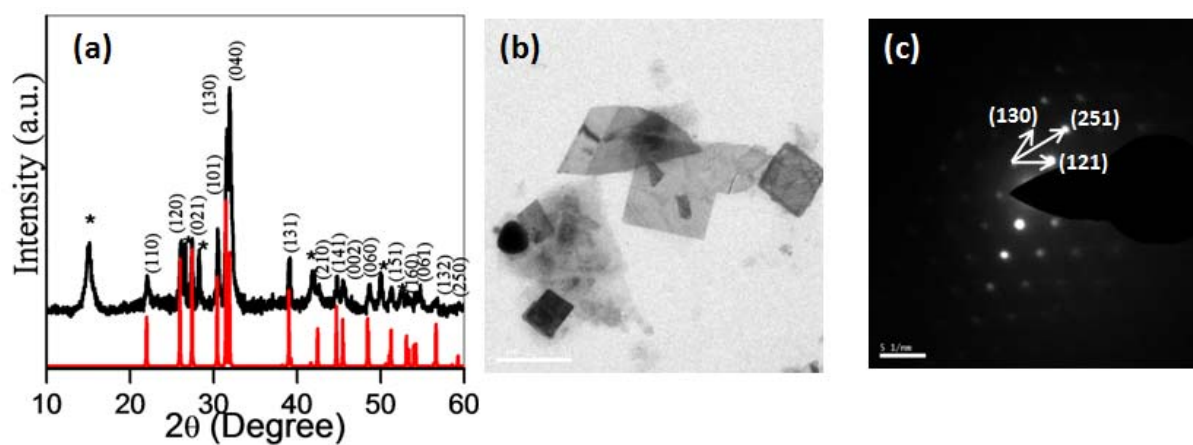


**Fig. 3.6** a) XRD, b) TEM image and c) SAED pattern of the residue obtained by thermolysis of  $[\text{Et}_2\text{SnCl}(\text{SpymMe}_2)]$  in TOPO-OLA at 320 °C for 10 minutes. (\* corresponds to SnS<sub>2</sub>)



### 3.3.5 Surface properties of the nanostructures

Since the thermolysis in oleylamine gave phase pure single composition of tin sulfide, further investigations were carried out on these samples. The surface characterization of tin sulfide nanostructures was studied by employing FT-IR spectroscopy (Fig. 3.7) and thermo gravimetric analysis (Fig. 3.8). FTIR spectra of SnS nano structures obtained by thermolysis of  $[\text{Et}_2\text{Sn}(2\text{-Spy})_2]$  and  $[\text{Et}_2\text{SnCl}(2\text{-SpymMe}_2)]$  showed different characteristic IR modes corresponding to  $\nu_{\text{N-H}}$  ( $3303\text{--}3308\text{ cm}^{-1}$ ),  $\nu_{\text{CH}_2}$  (anti-symmetric  $2914\text{ cm}^{-1}$  and symmetric  $2850\text{ cm}^{-1}$ ) stretches,  $\delta_{\text{N-H}}$  bending mode ( $1531\text{--}1546\text{ cm}^{-1}$ ) indicating the presence of alkyl amines [185].

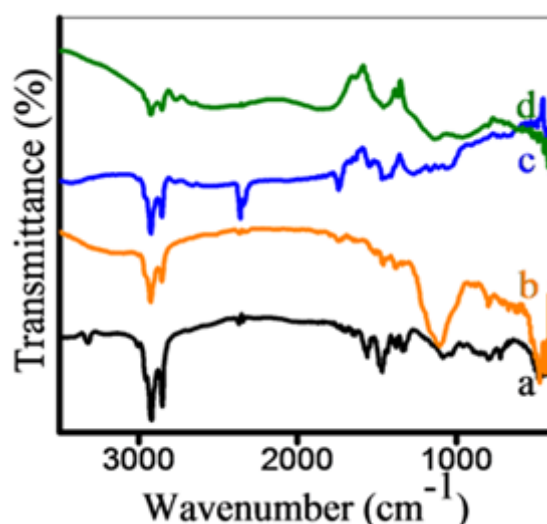


**Fig. 3.7** FT-IR spectra of a) oleylamine (OLA), b) SnS nanosheets obtained by thermolysis of  $[\text{Et}_2\text{Sn}(2\text{-Spy})_2]$  in OLA at  $300\text{ }^\circ\text{C}$  for 10 minutes and by thermolysis of  $[\text{Et}_2\text{SnCl}(\text{SpymMe}_2)]$  in OLA at  $300\text{ }^\circ\text{C}$  for c) 5 and d) 10 minutes, respectively.

The  $\nu_{\text{N-H}}$  stretches are broad which is generally observed for the nanostructures capped by amine ligands such as OLA. Both  $\nu_{\text{N-H}}$  and  $\delta_{\text{N-H}}$  bands are shifted to lower wave numbers with respect to the amine group of free OLA ( $\nu_{\text{N-H}} = 3373\text{ cm}^{-1}$  and  $\delta_{\text{N-H}} =$

1561 $\text{cm}^{-1}$ ) [185] suggesting  $-\text{NH}_2$  is bound to the surface of nanostructures. Thermo gravimetric analyses of the latter confirm the presence of amines on their surface.

Thermo gravimetric profile of the nanostructures synthesized in OLA showed overlapping step decomposition leading to an overall weight loss of  $\sim 17\%$  when the temperature is increased step-wise from room temperature to 800  $^{\circ}\text{C}$ . The differential curve of TGA displayed three peaks (a prominent and two small) consistent with decomposition steps at 189, 321 and 418  $^{\circ}\text{C}$  (Fig. 8). The first step involving a small weight loss of 2.9% below 189  $^{\circ}\text{C}$  may be attributed to the removal of crystalline and adsorbed water on the surface of the nanostructures [186]. After the first step, a gradual and slow thermal decomposition is observed in the temperature range of 200-600  $^{\circ}\text{C}$  which may be accounted for the loss of capping ligands (OLA). Such type of a gradual loss was also observed OLA capped  $\text{Cu}_2\text{ZnSnS}_4$  nanocrystals and was attributed to the long alkyl chains of OLA [187]. Different IR modes of FTIR spectra corroborated by thermo gravimetric analysis confirm the existence of OLA on the surface of the nanostructures.

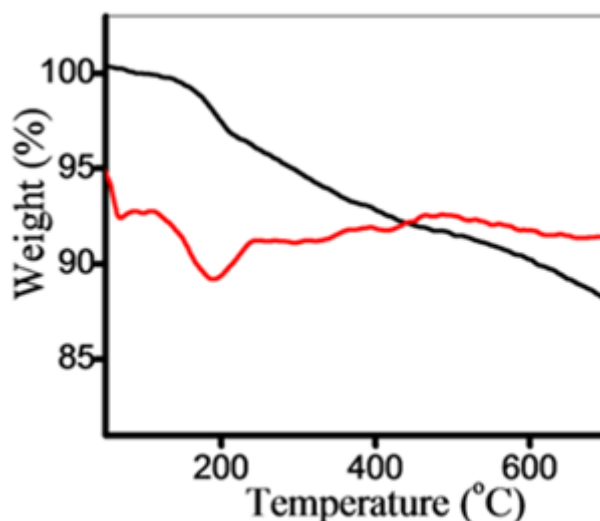


**Fig. 3.8** A representative thermogravimetric curve of SnS nanosheets obtained by thermolysis of  $[\text{Et}_2\text{SnCl}(\text{SpymMe}_2)]$  in OLA at 300  $^{\circ}\text{C}$ .

### 3.3.6 Deposition and characterization of tin sulfide thin films

One of the complexes [ $t\text{Bu}_2\text{Sn}(\text{Spy})_2$ ] was employed for the deposition of SnS thin films. The complex was chosen due to two reasons a) poor solubility of Me and Et derivatives in common organic solvent leads to very poor or no deposition and b)  $t\text{Bu}$  group is a good leaving group. Black to grey tin sulfide thin films were deposited on both glass and silicon substrate at temperature 400 °C.

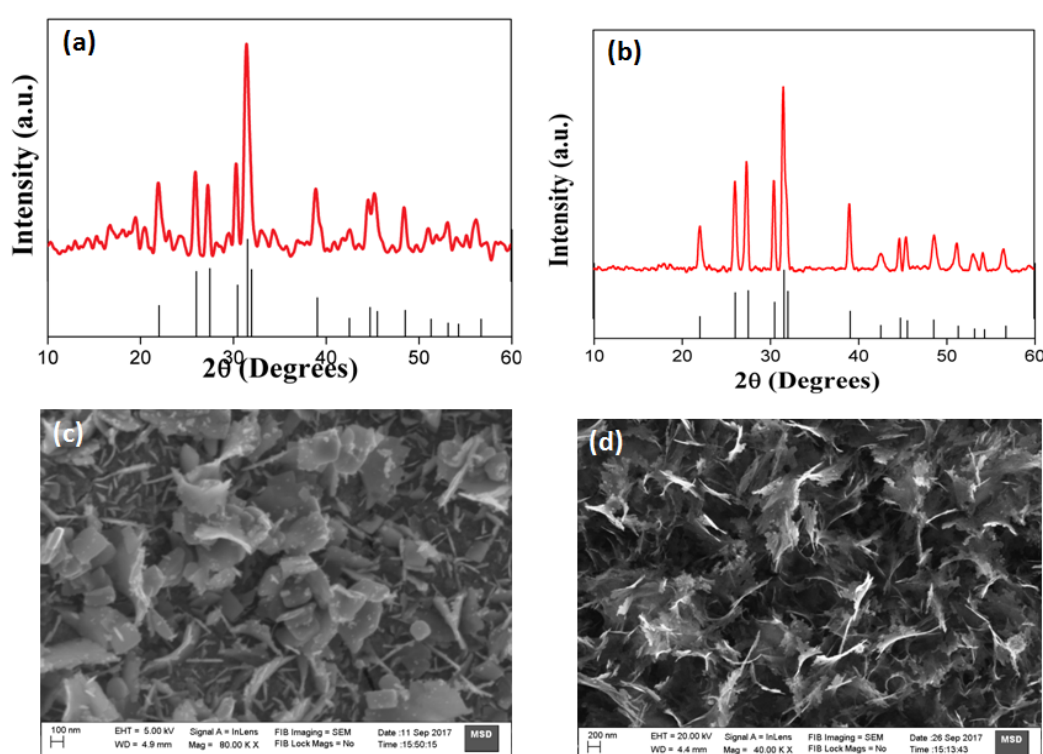


**Fig. 3.9** XRD pattern and SEM image of orthorhombic SnS thin films a) and c) on glass substrate, b) and d) on Si substrate, respectively.

It was observed that there is no deposition below 400 °C while above 400 °C (i.e. 450 °C) a sulfur deficient film was obtained due to volatile nature of sulfur. The films were characterized by XRD (Fig. 3.9a and 3.9b) and EDS for determining phase, crystal structure and composition of the thin films. XRD patterns and EDS analyses (Sn:S atom

ratio for the glass substrate is 1:0.96 while for the silicon substrate the ratio is 1:1.1) showed the formation of orthorhombic phase of SnS (JCPDS no 33-1375). SEM images (Fig. 3.9c and 3.9d) of the films on the glass substrate revealed nearly rectangular sheets while on silicon substrate it showed the formation of flakes like morphology. The intensity of XRD peaks and SEM micrographs also indicates that film deposited on the glass substrate is less crystalline and show poor coverage compared to the film obtained on silicon substrate.

### 3.3.7 Optical properties of SnS nanostructures

Optical properties of the tin sulfide nanostructures were studied using solid state diffuse reflectance spectroscopy. To determine the optical direct and indirect band gaps, Kubelka-Munk transformations were carried out on solid state diffuse reflectance data. The plots of  $[F(R)hv]^2$  versus  $hv$  and  $[F(R)hv]^{1/2}$  versus  $hv$  were used to obtain direct and indirect band gaps, respectively (Fig. 3.10).

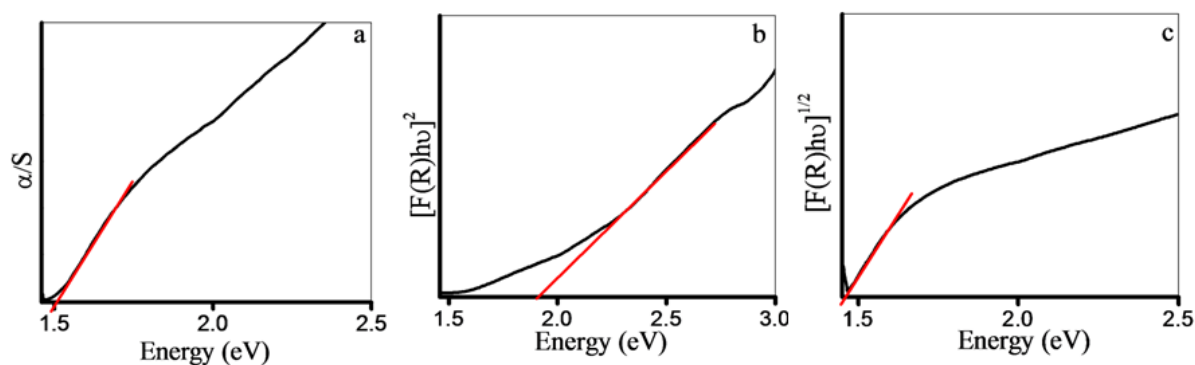


**Fig.3.10** a) Solid-state diffuse reflectance spectrum of SnS rectangular sheets obtained by thermolysis of  $[Et_2SnCl(SpymMe_2)]$  in OLA at 300 °C for 5 minutes and their Kubelka-Munk conversion plots of b)  $[F(R)hv]^2$  vs energy and c)  $[F(R)hv]^{1/2}$  vs energy from which direct and indirect band gaps were determined.

The band gaps were measured by extrapolating the linear portion of the plot to X (energy) axis. The direct gap estimated for hexagonal sheets (from  $[Et_2Sn(2-Spy)_2]$ ) is

1.62 eV while the values for that of rectangular sheets (from  $[\text{Et}_2\text{SnCl}(\text{2-SpymMe}_2)]$ ) are 1.90 (5 minutes) and 1.6 (10 minutes) eV. However, the indirect band gaps for all the samples are nearly 1.46 eV. The direct and indirect band gaps are blue shifted with respect to bulk SnS [ $E_g$  (direct) = 1.3 eV and  $E_g$  (indirect) = 1.1 eV] to the tune of 0.3-0.6 eV and 0.36 eV, respectively. The thicknesses of both the hexagonal and rectangular sheets are larger than the Bohr radius reported for bulk SnS (7 nm) and hence the blue shift in the direct band gaps cannot be accounted for quantum size effects. The increased band gaps may be attributed to the surface effect of the carriers, lattice distortions or surface lattice defects [188].

# Chapter 4

## Preparation of tin selenide nanostructure using organotin pyridyl and pyrimidyl selenolates

### Summary

Air stable, monomeric complexes of composition  $[\text{R}_2\text{Sn}(\text{2-Sepy}(5\text{-Me}))_2]$  ( $\text{R} = \text{Me}$ ,  $\text{Et}$ ,  $^t\text{Bu}$ ) and  $[\text{R}_2\text{Sn}(\text{2-SepymMe}_2)_2]$  ( $\text{R} = \text{Me}$ ,  $\text{Et}$ ,  $^n\text{Bu}$ ,  $^t\text{Bu}$ ) have been isolated by the reaction of  $\text{R}_2\text{SnCl}_2$  with 5-methyl-2-pyridylselenolate (2-Sepy(5-Me)) or 4,6-dimethylpyrimidylselenolate (2-SepymMe<sub>2</sub>). The treatment of  $[\text{R}_2\text{Sn}(\text{2-SepymMe}_2)_2]$  with  $\text{R}_2\text{SnCl}_2$  afforded chloro complexes,  $[\text{R}_2\text{SnCl}(\text{2-SepymMe}_2)]$  ( $\text{R} = \text{Me}$ ,  $^n\text{Bu}$  or  $^t\text{Bu}$ ). The complexes have been characterized by elemental analysis and multinuclear NMR ( $^1\text{H}$ ,  $^{13}\text{C}$ ,  $^{77}\text{Se}$ ,  $^{119}\text{Sn}$ ) spectroscopy. The molecular structure of  $(\text{Sepy}(5\text{-Me}))_2$ ,  $[\text{R}_2\text{Sn}(\text{2-Sepy}(5\text{-Me}))_2]$  ( $\text{R} = \text{Me}$ ,  $\text{Et}$ ,  $^t\text{Bu}$ ),  $[\text{Bu}_2\text{Sn}(\text{2-SepymMe}_2)_2]$  and  $[\text{Bu}_2\text{SnCl}(\text{2-SepymMe}_2)]$  have been established by single crystal X-ray analysis. These complexes have been utilized as molecular precursors for the preparation of tin selenide ( $\text{SnSe}$  and  $\text{SnSe}_2$ ) nanostructures and thin films. Phase and composition ( $\text{SnSe}$  and  $\text{SnSe}_2$ ) tunability of tin selenide nanostructure have been demonstrated from the thermolysis of  $[\text{Bu}_2\text{Sn}(\text{2-Sepy}(5\text{-Me}))_2]$  through proper choice of high boiling solvent whereas  $[\text{R}_2\text{Sn}(\text{2-SepymMe}_2)_2]$  complexes upon thermolysis afforded exclusively  $\text{SnSe}_2$  nanostructures. pXRD, SEM, TEM, EDX and DRS were used to investigate the phase purity, morphology, composition and band gap of nanostructures. The nanostructures showed photo response which make them promising candidate for alternative low-cost photon absorber material.

## 4.1 Introduction

Nanostructures with sheet like morphologies are important 2D materials which have received enormous attention in recent times [22,189,190]. Owing to their fascinating electronic band structure and remarkably layer dependent properties, these materials find applications in next generation optoelectronic, photovoltaic and thermoelectric devices [60,191,192]. Tin selenides are emerging members of 2D semiconducting materials due to their earth abundant, low cost and environmentally benign characteristics [22,60,61]. Tin selenides exist in two prominent narrow band gap forms, namely SnSe and SnSe<sub>2</sub>. SnSe possess an orthorhombic crystal structure with an optical band gap of around 0.9 eV whereas the SnSe<sub>2</sub> crystallizes in a CdI<sub>2</sub> hexagonal lattice with a band gap of  $\sim 1$  eV [80,193]. The distinctive combination of anisotropy and optical properties including slow carrier relaxation rate, provide SnSe as a suitable candidate for thermoelectric, photovoltaic and infrared optoelectronic devices [70,194,195], whereas the layered structure of SnSe<sub>2</sub> have been utilised for infrared photo detection, solar cells and anode material to improve lithium ion diffusivity in lithium ion battery [196-198].

Various multi-source routes which utilizes tin precursors (tin oleate, bis[bis(trimethylsilyl)amino]tin(II) or SnCl<sub>2</sub>) with a suitable selenium source (TOPSe, Se powder, 1,3-dimethylimidazoline- 2-selenone or SeO<sub>2</sub>) for the preparation of tin selenide nanostructures have been reported in literature [157,195,199,200]. In contrast to multi source methods, single source molecular precursors (SSP) route are often proven to be superior candidates. They are equally viable for the preparation of nanostructures and deposition of thin films [175,201]. Simultaneously the control over the stoichiometry, phase and morphology is also advantageous. Despite the above mentioned advantages of single source route, not many SSPs have been used for tin selenide nanostructures and thin films [137,138,144-147,149]. Few of the SSPs results in the final product

contaminated with elemental tin or selenium deficient tin selenide. SSP reported by O'Brien and co-workers bis(diphenylphosphinediselenoato)-tin(II)  $[\text{Sn}(\text{Ph}_2\text{PSe}_2)_2]$  for SnSe nanostructures involves expensive and toxic phosphine [144]. Moreover, presence of phosphine during thermolysis often leads to phosphorus contamination or unexpected products like metal phosphates or phosphide [202-204].

Successful utilization of tin complexes with internally functionalized pyridyl and pyrimidyl thiolates for the preparation of phase pure tin sulfide nanostructures and thin films motivated us to extend this strategy for the preparation of tin selenide nanostructures and thin films. In view of the above we have investigated the chemistry of organotin 2-pyridyl- and 2-pyrimidyl selenolate complexes and utilized them as molecular precursors for the preparation of tin selenide nanostructures. The results of this work are described herein.

## **4.2 Experimental**

### **4.2.1 General Consideration**

Materials and techniques used during the investigation were discussed in Chapter 2.

### **4.2.2 Synthesis of bis(5-methyl-2-pyridyl)diselenide [(2-Sepy(5-Me))<sub>2</sub>]**

To a vigorously stirred mixture of freshly grinded selenium (1.8 g, 22.8 mmol) in distilled water (50 ml),  $\text{NaBH}_4$  (862 mg, 22.8 mmol) was added in small portions. The solution was warmed and stirred for 2 h until a clear red solution appears. To this solution, 2-bromo-5-methylpyridine (1.96 g, 11.4 mmol) was added and refluxed the reaction mixture for 8 h. The crude diselenide was extracted using chloroform, washed with water and then dried over anhydrous sodium sulfate. The absence of monoselenide was checked by TLC and the crude product was purified by column chromatography after removal of solvent, using 60-120 mesh silica gel and hexane-ethyl acetate (5:1) as an eluent. The yellow residue was recrystallised from dichloromethane to yield yellow



crystals (yield: 3.620 g, 92.8%), m.p. 82 °C. Anal. Calcd. for  $C_{12}H_{12}N_2Se_2$ : C, 42.12; H, 3.50; N, 8.18%. Observed: C, 41.68; H, 3.48; N, 7.89%.  $^1H$  NMR ( $CDCl_3$ )  $\delta$ : 2.28 (s, 3H, 5-Me); 7.34 (d, 7.8Hz, 1H, H-4); 7.68 (d, 7.8Hz, 1H, H-3); 8.27 (s, 1H, H-6) (ring protons).  $^{13}C\{^1H\}$  NMR ( $CDCl_3$ )  $\delta$ : 17.8 (Me); 123.40, 130.91, 138.19, 149.81, 150.85 (ring carbons).  $^{77}Se\{^1H\}$  NMR ( $CDCl_3$ )  $\delta$ : 447.7 ppm.

#### 4.2.3 Synthesis of bis(4,6-dimethyl-2-pyrimidyl)diselenide [(2-SepymMe<sub>2</sub>)<sub>2</sub>]

To a vigorously stirred mixture of freshly grinded selenium (4.4 g, 55.72 mmol) in distilled water (150 ml),  $NaBH_4$  (2.1 g, 55.44 mmol) was added in small portions. The solution was warmed and stirred for 2 h until a clear red solution appears. To this mixture, ethanolic solution (20 ml) of 2-chloro-4,6-dimethylpyrimidine (7.3 g, 51.18 mmol) was added drop-wise with stirring at the room temperature. Once addition was completed, the contents were heated at 70 °C for 10 h with stirring. The progress of the reaction was monitored by TLC till its completion. Subsequently the solvent was removed under vacuum and the product was extracted in chloroform. The filtrate was evaporated under vacuum to yield a brown solid which was purified on a silica column. The product eluted in 5:1 hexane–ethyl acetate mixture gave red crystals of diselenide, [(2-SepymMe<sub>2</sub>)<sub>2</sub>] (yield 14.2 g, 68 %), m.p. 143 °C. Anal. Calcd. for  $C_{12}H_{14}N_4Se_2$ : C, 38.72; H, 3.79; N, 15.05% Found C, 38.70; H, 3.72; N, 15.15%.  $^1H$  NMR ( $CDCl_3$ )  $\delta$ : 2.38 (s, 12H, Me), 6.72 (s, 2H);  $^{13}C\{^1H\}$  NMR ( $CDCl_3$ )  $\delta$ : 23.1 (Me), 117.0 (C-5), 165.3 (C-Se), 167.5 (C-4,6).  $^{77}Se\{^1H\}$  NMR ( $CDCl_3$ )  $\delta$ : 488 ppm.

#### 4.2.4 Synthesis of [Me<sub>2</sub>Sn(2-Sepym(5-Me))<sub>2</sub>]

To a methanolic solution of sodium 5-methyl-2-pyridyl selenolates [prepared by reduction of bis(5-methyl-2-pyridyl)diselenide (200 mg, 0.58 mmol) by a methanolic solution of  $NaBH_4$  (44.2 mg, 1.17 mmol)], a toluene solution of  $Me_2SnCl_2$  (127mg, 0.58 mmol) was added with stirring which continued for 2 hours at room temperature. The

solvents were evaporated under vacuum and the residue was extracted with chloroform and filtered. The filtrate was reduced (4 ml) and methanol and diethylether (1:1, v/v, 1 ml) were added which on slow evaporation afforded colourless crystals of the title complex (190 mg, 67% yield) m. p. 105-106 °C. Anal Calcd. for  $C_{14}H_{18}N_2Se_2Sn$ : C, 34.25; H, 3.69; N, 5.70%. Found: C, 33.59; H, 4.02; N, 5.63%.  $^1H$  NMR ( $CDCl_3$ )  $\delta$ : 1.07 (s,  $Me_2Sn$ , 6H,  $^2J(Sn-H) = 78Hz$ ); 2.21(s,  $C_5H_3(5-Me)N$ , 6 H); 7.21 (d,d, CH-3, 2 H, 7.5, 4.8 Hz); 7.32 (d, CH-4, 2 H, 7.2 Hz); 7.98 (d, CH-6, 2 H, 4.5 Hz)  $^{77}Se\{^1H\}$  NMR ( $CDCl_3$ )  $\delta$ : 194 (s,  $^1J(^{119}Sn-^{77}Se) = 668$  Hz)  $^{119}Sn\{^1H\}$  NMR ( $CDCl_3$ )  $\delta$ : -141.3 (s,  $^1J(^{119}Sn-^{77}Se) = 683$  Hz).

#### 4.2.5 Synthesis of $[Et_2Sn(2-Sepym(5-Me))_2]$

Prepared similar to  $[Me_2Sn(2-Sepy(5-Me))_2]$  and was isolated as a white crystalline solid in (194 mg, 65% yield), m. p. 126 °C. Anal Calcd. for  $C_{16}H_{22}N_2Se_2Sn$ : C, 37.02; H, 4.27; N, 5.39%. Found: C, 36.78; H, 3.92; N, 5.21%.  $^1H$  NMR ( $CDCl_3$ )  $\delta$ : 1.28 (t, 7.5 Hz,  $SnCH_2CH_3$ ), 1.64 (q, 7.5 Hz,  $SnCH_2$ ), 2.22 (s, Me), 7.20 (d, 8 Hz) 7.33 (d, 8 Hz), 8.02 (s, H-6).  $^{13}C\{^1H\}$  NMR ( $CDCl_3$ )  $\delta$ : 11.2 (s,  $^2J(Sn-C) = 39$  Hz,  $SnCH_2CH_3$ ), 17.9 (s,  $^1J(Sn-C) = 522$  Hz,  $SnCH_2$ ), 18.0(s, Me), 127.3, 128.4, 137.6, 148.2, 153.9 (ring carbons).  $^{77}Se\{^1H\}$  NMR ( $CDCl_3$ )  $\delta$ : 156.3(s,  $^1J(^{119}Sn-^{77}Se) = 662$  Hz).  $^{119}Sn\{^1H\}$  NMR ( $CDCl_3$ )  $\delta$ : -108.7 (s,  $^1J(^{119}Sn-^{77}Se) = 673$  Hz).

#### 4.2.6 Synthesis of $[^tBu_2Sn(2-Sepym(5-Me))_2]$

Prepared similar to  $[Me_2Sn(2-Sepy(5-Me))_2]$  and was isolated as a white crystalline solid in (230 mg, 69% yield), m.p. 115°C Anal Calcd. for  $C_{20}H_{30}N_2Se_2Sn$ : C, 41.77; H, 5.26; N, 4.87%. Found: C, 40.57; H, 4.62; N, 4.38%.  $^1H$  NMR ( $CDCl_3$ )  $\delta$ : 1.39 (s,  $^3J(^{119}Sn-^1H) = 102$  Hz,  $^tBu-Sn$ ), 2.21(s, Me), 7.18 (d, 8 Hz), 7.34 (d, 8 Hz), 8.08 (s, H-6).  $^{13}C\{^1H\}$  NMR ( $CDCl_3$ )  $\delta$ : 17.9 (s,  $-CH_3$ ), 31.4 (s,  $^tBu-Sn$ ), 41.5 (Sn-C), 127.8, 128.9,

137.1, 148.9, 153.5 (ring carbons).  $^{77}\text{Se}\{^1\text{H}\}$  NMR ( $\text{CDCl}_3$ )  $\delta$ : 153.7 (s,  $^1\text{J}(^{119}\text{Sn}-^{77}\text{Se}) = 883$  Hz).  $^{119}\text{Sn}\{^1\text{H}\}$  NMR ( $\text{CDCl}_3$ )  $\delta$ : -13.0 (s,  $^1\text{J}(^{119}\text{Sn}-^{77}\text{Se}) = 887$  Hz).

#### 4.2.7 Synthesis of $[\text{Me}_2\text{Sn}(2\text{-SepymMe}_2)_2]$

To a freshly prepared solution of  $[\text{Na}(2\text{-SepymMe}_2)]$  (obtained by the reduction of  $\{\text{SeC}_4\text{H}(\text{Me-4,6})_2\text{N}_2\}_2$  (191 mg, 0.51 mmol) in toluene with methanolic  $\text{NaBH}_4$  (39 mg, 1.30 mmol)), solid  $\text{Me}_2\text{SnCl}_2$  (112 mg, 0.51 mmol) was added with vigorous stirring which continued for 3 h at room temperature. The solvents were evaporated under vacuum and the residue was washed thoroughly with toluene-hexane mixture (1:20 v/v). The pure product was extracted with chloroform and filtered to remove  $\text{NaCl}$ . The filtrate was dried under reduced pressure and recrystallized from toluene-dichloromethane mixture to give a white powder (yield: 160 mg, 60%), mp 163 °C. Anal. Calcd. for  $\text{C}_{14}\text{H}_{20}\text{N}_4\text{Se}_2\text{Sn}$ : C, 32.28; H, 3.87%. Found: C, 31.87; H, 3.90%.  $^1\text{H}$  NMR ( $\text{CDCl}_3$ )  $\delta$ : 1.12 (s,  $\text{Me}_2\text{Sn}$ , 6 H,  $^2\text{J}(^{119}\text{Sn}-^1\text{H}) = 72$  Hz;  $^2\text{J}(^{117}\text{Sn}-^1\text{H}) = 69$  Hz); 2.36 (s,  $\text{C}_4\text{H}(4,6\text{-Me})\text{N}_2$ , 12 H); 6.74 (s,  $\text{CH-5}$ ,  $\text{C}_4\text{H}(4,6\text{-Me})\text{N}_2$ ).  $^{13}\text{C}\{^1\text{H}\}$  NMR ( $\text{CDCl}_3$ )  $\delta$ : 4.8 ( $\text{SnCH}_3$ ,  $^1\text{J}(^{119}\text{Sn}-^{13}\text{C}) = 527$  Hz;  $^1\text{J}(^{117}\text{Sn}-^{13}\text{C}) = 503$  Hz), 23.3 ( $\text{C}_4\text{H}(4,6\text{-Me})\text{N}_2$ ), 115.7 (C-5), 166.4 (C-4,6), 169.81 (C-Se).  $^{77}\text{Se}\{^1\text{H}\}$  NMR ( $\text{CDCl}_3$ )  $\delta$ : 233 ( $^1\text{J}(^{119}\text{Sn}-^{77}\text{Se}) = 725$  Hz;  $^1\text{J}(^{117}\text{Sn}-^{77}\text{Se}) = 692$  Hz).  $^{119}\text{Sn}\{^1\text{H}\}$  NMR ( $\text{CDCl}_3$ )  $\delta$ : -135 ( $^1\text{J}(\text{Sn-Se}) = 724$  Hz) ppm.

#### 4.2.8 Synthesis of $[\text{Et}_2\text{Sn}(2\text{-SepymMe}_2)_2]$

Prepared similar to  $[\text{Me}_2\text{Sn}(2\text{-SepymMe}_2)_2]$  and recrystallized from toluene-dichloromethane mixture as colorless crystals in 70% yield, mp 146 °C. Anal. Calcd. for  $\text{C}_{16}\text{H}_{24}\text{N}_4\text{Se}_2\text{Sn}$ : C, 35.00; H, 4.41%. Found: C, 34.50; H, 4.40%.  $^1\text{H}$  NMR ( $\text{CDCl}_3$ )  $\delta$ : 1.26 (t,  $\text{SnCH}_2\text{CH}_3$ , 6 H, 7.8 Hz); 1.68 (q,  $\text{SnCH}_2\text{CH}_3$ , 4 H); 2.36 (s,  $\text{C}_4\text{H}(4,6\text{-Me})\text{N}_2$ , 12 H); 6.73 (s,  $\text{CH-5}$ ,  $\text{C}_4\text{H}(4,6\text{-Me})\text{N}_2$ ).  $^{13}\text{C}\{^1\text{H}\}$  NMR ( $\text{CDCl}_3$ )  $\delta$ : 11.0 ( $\text{SnCH}_2\text{CH}_3$ ,  $^2\text{J}(^{119}\text{Sn}-^{13}\text{C}) = 40$  Hz), 16.3 ( $\text{SnCH}_2\text{CH}_3$ ,  $^1\text{J}(^{119}\text{Sn}-^{13}\text{C}) = 502$  Hz;  $^1\text{J}(^{117}\text{Sn}-^{13}\text{C}) = 481$  Hz), 23.5 ( $\text{C}_4\text{H}(4,6\text{-Me})\text{N}_2$ ), 115.7 (C-5), 166.4 (C-4,6), 170.7 (C-Se).  $^{77}\text{Se}\{^1\text{H}\}$  NMR ( $\text{CDCl}_3$ )  $\delta$ :

180 ( $^1J(^{119}\text{Sn} - ^{77}\text{Se}) = 723 \text{ Hz}$ ;  $^1J(^{117}\text{Sn} - ^{77}\text{Se}) = 690 \text{ Hz}$ ).  $^{119}\text{Sn}\{^1\text{H}\}$  NMR ( $\text{CDCl}_3$ )  $\delta$ : -87 ( $^1J(^{119}\text{Sn} - ^{77}\text{Se}) = 726 \text{ Hz}$ ) ppm.

#### 4.2.9 Synthesis of [ $^t\text{Bu}_2\text{Sn}(\text{2-SepymMe}_2)_2$ ]

Prepared in a similar fashion to [ $\text{Me}_2\text{Sn}(\text{2-SepymMe}_2)_2$ ] and recrystallized from toluene-dichloromethane mixture as colorless crystals in 66% yield, mp 126 °C. Anal. Calcd. for  $\text{C}_{20}\text{H}_{32}\text{N}_4\text{Se}_2\text{Sn}$ : C, 39.69; H, 5.33%. Found: C, 40.23; H, 5.40%.  $^1\text{H}$  NMR ( $\text{CDCl}_3$ )  $\delta$ : 0.79 (t,  $\text{SnCH}_2\text{CH}_2\text{CH}_2\text{CH}_3$ , 6 H, 7.2 Hz); 1.33 (m), 1.58-1.75 (m) (SnBu); 2.37 (s,  $\text{C}_4\text{H}(\text{4,6-Me})\text{N}_2$ , 12 H); 6.74 (s,  $\text{CH-5}$ ,  $\text{C}_4\text{H}(\text{4,6-Me})\text{N}_2$ ).  $^{13}\text{C}\{^1\text{H}\}$  NMR ( $\text{CDCl}_3$ )  $\delta$ : 13.6 ( $\text{SnCH}_2\text{CH}_2\text{CH}_2\text{CH}_3$ ), 23.1 ( $\text{SnCH}_2\text{CH}_2\text{CH}_2\text{CH}_3$ ,  $^1J(^{119}\text{Sn} - ^{13}\text{C}) = 479 \text{ Hz}$ ;  $^1J(^{117}\text{Sn} - ^{13}\text{C}) = 458 \text{ Hz}$ ), 23.6 ( $\text{C}_4\text{H}(\text{4,6-Me})\text{N}_2$ ), 26.3 ( $\text{SnCH}_2\text{CH}_2\text{CH}_2\text{CH}_3$ ,  $^2J(^{119}\text{Sn} - ^{13}\text{C}) = 99 \text{ Hz}$ ), 28.7 ( $\text{SnCH}_2\text{CH}_2\text{CH}_2\text{CH}_3$ ,  $^3J(^{119}\text{Sn} - ^{13}\text{C}) = 35 \text{ Hz}$ ), 115.8 (C-5), 166.5 (C-4,6), 170.6 (C-Se).  $^{77}\text{Se}\{^1\text{H}\}$  NMR ( $\text{CDCl}_3$ )  $\delta$ : 194 ( $^1J(^{119}\text{Sn} - ^{77}\text{Se}) = 745 \text{ Hz}$ ;  $^1J(^{117}\text{Sn} - ^{77}\text{Se}) = 711 \text{ Hz}$ ).  $^{119}\text{Sn}\{^1\text{H}\}$  NMR ( $\text{CDCl}_3$ )  $\delta$ : -92 ( $^1J(^{119}\text{Sn} - ^{77}\text{Se}) = 746 \text{ Hz}$ ) ppm.

#### 4.2.10 Synthesis of [ $^t\text{Bu}_2\text{Sn}(\text{2-SepymMe}_2)_2$ ]

Prepared similar to [ $\text{Me}_2\text{Sn}(\text{2-SepymMe}_2)_2$ ] and recrystallized from toluene-dichloromethane as colorless crystals in 68% yield, mp 157 °C. Anal. Calcd. for  $\text{C}_{20}\text{H}_{32}\text{N}_4\text{Se}_2\text{Sn}$ : C, 39.69; H, 5.33%. Found: C, 39.40; H, 5.31%.  $^1\text{H}$  NMR ( $\text{CDCl}_3$ )  $\delta$ : 1.48 (s,  $^t\text{Bu}_2\text{Sn}$ , 18 H,  $^3J(\text{Sn-H}) = 99 \text{ Hz}$ ); 2.37 (s,  $\text{C}_4\text{H}(\text{4,6-Me})\text{N}_2$ , 12 H); 6.70 (s,  $\text{CH-5}$ ,  $\text{C}_4\text{H}(\text{4,6-Me})\text{N}_2$ ).  $^{13}\text{C}\{^1\text{H}\}$  NMR ( $\text{CDCl}_3$ )  $\delta$ : 23.7 ( $\text{C}_4\text{H}(\text{4,6-Me})\text{N}_2$ ), 31.9 ( $\text{Me}_3\text{C-Sn}$ ), 41.6 (C-Sn), 116.4 (C-5), 166.6 (C-4,6), 170.3 (C-Se).  $^{77}\text{Se}\{^1\text{H}\}$  NMR ( $\text{CDCl}_3$ )  $\delta$ : 182 ( $^1J(\text{Sn-Se}) = 977 \text{ Hz}$ ).  $^{119}\text{Sn}\{^1\text{H}\}$  NMR ( $\text{CDCl}_3$ )  $\delta$ : 28 ( $^1J(^{119}\text{Sn} - ^{77}\text{Se}) = 999 \text{ Hz}$ ) ppm.

#### 4.2.11 Synthesis of [ $\text{Me}_2\text{SnCl}(\text{2-SepymMe}_2)$ ]

To a toluene solution of [ $\text{Me}_2\text{Sn}(\text{2-SepymMe}_2)_2$ ] (100 mg, 0.192 mmol),  $\text{Me}_2\text{SnCl}_2$  (42 mg, 0.191 mmol) solution in the same solvent was added and the whole mixture was stirred at room temperature for 1 h. The solvents were evaporated under vacuum to yield

a solid (yield: 61.26 mg, 86%), mp 108 °C. Anal. Calcd. for C<sub>8</sub>H<sub>13</sub>N<sub>2</sub>ClSeSn: C, 25.95; H, 3.54%. Found: C, 25.87; H, 3.61%. <sup>1</sup>H NMR (CDCl<sub>3</sub>) δ: 1.14 (s, Me<sub>2</sub>Sn, 6 H, <sup>2</sup>J(Sn–H) = 71 Hz); 2.35 (s, C<sub>4</sub>H(*Me*-4,6)N<sub>2</sub>, 6 H); 6.84 (s, *CH*-5, C<sub>4</sub>H(4,6-*Me*)N<sub>2</sub>). <sup>13</sup>C{<sup>1</sup>H} NMR (CDCl<sub>3</sub>) δ: 5.6 (SnCH<sub>3</sub>, <sup>1</sup>J(<sup>119</sup>Sn-<sup>13</sup>C) = 532 Hz; <sup>1</sup>J(<sup>117</sup>Sn-<sup>13</sup>C) = 509 Hz), 23.0 (C<sub>4</sub>H(*Me*-4,6)N<sub>2</sub>), 116.5 (C-5), 167.1 (C-4,6), 170.4 (C-Se). <sup>77</sup>Se{<sup>1</sup>H} NMR (CDCl<sub>3</sub>) δ: 262 (<sup>1</sup>J(Sn–Se) = 724 Hz). <sup>119</sup>Sn{<sup>1</sup>H} NMR (CDCl<sub>3</sub>) δ: –90 (<sup>1</sup>J(<sup>119</sup>Sn-<sup>77</sup>Se) = 727 Hz) ppm.

#### 4.2.12 Synthesis of [<sup>n</sup>Bu<sub>2</sub>SnCl(2-SepymMe<sub>2</sub>)]

Prepared in a similar fashion to [Me<sub>2</sub>SnCl(2-SepymMe<sub>2</sub>)] and the complex was extracted with hexane and dried under vacuum to give a colorless liquid in 71% yield. <sup>1</sup>H NMR (CDCl<sub>3</sub>) δ: 0.89 (t, SnCH<sub>2</sub>CH<sub>2</sub>CH<sub>2</sub>CH<sub>3</sub>, 6 H, 7.2 Hz); 1.37 (m), 1.69-1.77 (m) (SnBu); 2.35 (s, C<sub>4</sub>H(4,6-*Me*)N<sub>2</sub>, 6 H); 6.84 (s, *CH*-5, C<sub>4</sub>H(4,6-*Me*)N<sub>2</sub>). <sup>13</sup>C{<sup>1</sup>H} NMR (CDCl<sub>3</sub>) δ: 13.6 (SnCH<sub>2</sub>CH<sub>2</sub>CH<sub>2</sub>CH<sub>3</sub>), 24.6 (SnCH<sub>2</sub>CH<sub>2</sub>CH<sub>2</sub>CH<sub>3</sub>, <sup>1</sup>J(<sup>119</sup>Sn-<sup>13</sup>C) = 486 Hz; <sup>1</sup>J(<sup>117</sup>Sn-<sup>13</sup>C) = 465 Hz), 23.2 (C<sub>4</sub>H(4,6-*Me*)N<sub>2</sub>), 26.2 (SnCH<sub>2</sub>CH<sub>2</sub>CH<sub>2</sub>CH<sub>3</sub>, <sup>2</sup>J(<sup>119</sup>Sn-<sup>13</sup>C) = 90 Hz), 27.8 (SnCH<sub>2</sub>CH<sub>2</sub>CH<sub>2</sub>CH<sub>3</sub>, <sup>3</sup>J(<sup>119</sup>Sn-<sup>13</sup>C) = 35 Hz), 116.7 (C-5), 167.2 (C-4,6), 170.7 (C-Se). <sup>77</sup>Se{<sup>1</sup>H} NMR (CDCl<sub>3</sub>) δ: 228 (<sup>1</sup>J(<sup>119</sup>Sn–<sup>77</sup>Se) = 748 Hz; <sup>1</sup>J(<sup>117</sup>Sn–<sup>77</sup>Se) = 713 Hz). <sup>119</sup>Sn{<sup>1</sup>H} NMR (CDCl<sub>3</sub>) δ: –74 (<sup>1</sup>J(<sup>119</sup>Sn-<sup>77</sup>Se) = 755 Hz) ppm.

#### 4.2.13 Synthesis of [<sup>t</sup>Bu<sub>2</sub>SnCl(2-SepymMe<sub>2</sub>)]

Prepared in a similar fashion to [Me<sub>2</sub>SnCl(2-SepymMe<sub>2</sub>)] and recrystallized from dichloromethane-hexane as colorless crystals in 82% yield, mp 101 °C. Anal. Calcd. for C<sub>14</sub>H<sub>25</sub>N<sub>2</sub>ClSeSn: C, 36.99; H, 5.54%. Found: C, 36.92; H, 5.59%. <sup>1</sup>H NMR (CDCl<sub>3</sub>) δ: 1.48 (s, <sup>t</sup>Bu<sub>2</sub>Sn, 18 H, <sup>3</sup>J(<sup>119</sup>Sn-<sup>1</sup>H) = 110 Hz; <sup>3</sup>J(<sup>117</sup>Sn-<sup>1</sup>H) = 108 Hz); 2.38 (s, C<sub>4</sub>H(4,6-*Me*)N<sub>2</sub>, 6 H); 6.81 (s, *CH*-5, C<sub>4</sub>H(4,6-*Me*)N<sub>2</sub>). <sup>13</sup>C{<sup>1</sup>H} NMR (CDCl<sub>3</sub>) δ: 23.9 (C<sub>4</sub>H(4,6-*Me*)N<sub>2</sub>), 30.9 (Me<sub>3</sub>C-Sn), 43.4 (C-Sn, <sup>1</sup>J(<sup>119</sup>Sn-<sup>13</sup>C) = 398 Hz; <sup>1</sup>J(<sup>117</sup>Sn-<sup>13</sup>C) = 380 Hz), 117.0 (C-5), 167.0 (C-4,6), 171.5 (C-Se). <sup>77</sup>Se{<sup>1</sup>H} NMR (CDCl<sub>3</sub>) δ: 197 (<sup>1</sup>J(<sup>119</sup>Sn–<sup>77</sup>Se)

= 910 Hz;  $^1J(^{117}\text{Sn} - ^{77}\text{Se}) = 870 \text{ Hz}$ .  $^{119}\text{Sn}\{^1\text{H}\}$  NMR ( $\text{CDCl}_3$ )  $\delta$ : -20 ( $^1J(\text{Sn-Se}) = 912 \text{ Hz}$ ) ppm.

#### 4.2.14 Preparation of tin selenide nanostructures

Tin selenide nanostructures were prepared by thermolysis of  $[\text{}^t\text{Bu}_2\text{Sn}(2\text{-Sepy}(5\text{-Me}))_2]$  and  $[\text{R}_2\text{Sn}(2\text{-SepymMe}_2)_2]$  ( $\text{R} = \text{Et}, ^n\text{Bu}, ^t\text{Bu}$ ) using a hot injection method.

Thermolysis of  $[\text{}^t\text{Bu}_2\text{Sn}(2\text{-Sepy}(5\text{-Me}))_2]$  was carried out in different high boiling solvents to evaluate the effect of solvent on the composition and morphology of nanostructures. In a typical experiment, 8 ml of high boiling solvent (OLA, ODE or OA either individually or in combination) was taken in a three-necked round bottom flask and degassed at  $100^\circ\text{C}$  under nitrogen flow for 30 min. The temperature was raised to  $220^\circ\text{C}$ . The required amount of  $[\text{}^t\text{Bu}_2\text{Sn}(2\text{-Sepy}(5\text{-Me}))_2]$  (100 mg, 0.17 mmol) dispersed in the same solvent (2ml) was rapidly injected into the preheated solvent. The reaction temperature was dropped in the range of  $\sim 195^\circ\text{C}$  upon injection which again raised to  $220^\circ\text{C}$  and maintained at this temperature for 10 min. The dark solution formed was cooled rapidly to  $70^\circ\text{C}$  where excess methanol was added into the flask. The resulting nanocrystals were separated by centrifugation and purified by washing several times with 2:1 mixture of methanol and toluene solution.

In a different set of experiments,  $[\text{R}_2\text{Sn}(2\text{-SepymMe}_2)_2]$  ( $\text{R} = \text{Et}, ^n\text{Bu}, ^t\text{Bu}$ ) were thermolysed in OLA at  $210^\circ\text{C}$  to study the effect of different “R” and growth duration (2, 5 and 10 minutes) on the phase purity and crystallite size of nanostructures. In a typical experiment, an OLA (2 ml) dispersion of complex  $[\text{R}_2\text{Sn}(2\text{-SepymMe}_2)_2]$  (100 mg) was injected rapidly into a preheated ( $210^\circ\text{C}$ ) OLA (8 ml) in a three-necked flask with vigorous stirring under flowing argon. The temperature of the reaction mixture was dropped in the range of  $\sim 185^\circ\text{C}$  upon injection which again raised to  $210^\circ\text{C}$ . The reaction mixture was kept at  $210^\circ\text{C}$  for different durations (2, 5 and 10 minutes). After

the desired growth time, the reaction mixture was cooled down rapidly to 95-98 °C and quenched by injecting toluene (4 ml). The resulting nanocrystals were separated by precipitating with excess methanol followed by centrifugation to give a black powder.

#### **4.2.15 Preparation of thin films by Aerosol Assisted Chemical Vapor Deposition (AACVD)**

A toluene solution (25 ml) of [<sup>t</sup>Bu<sub>2</sub>Sn(2-SepymMe<sub>2</sub>)<sub>2</sub>] (125 mg, 0.21 mmol) was used to generate aerosol by an ultrasonic humidifier. The aerosol was transported over a period of 1 h using argon as a carrier gas (flow rates of 180 sccm) to a preheated silicon wafer (110) orientation placed in a turbo furnace at 375 °C.

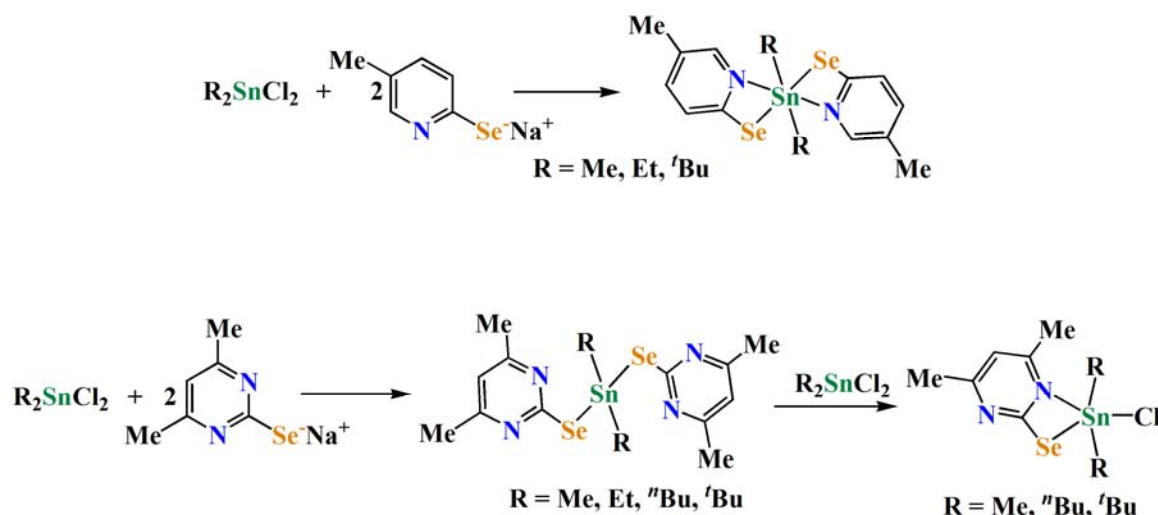
#### **4.2.16 Crystallography**

Intensity data for [R<sub>2</sub>Sn(2-Sepy(5-Me))<sub>2</sub>] (R = Me, Et, <sup>t</sup>Bu), [<sup>n</sup>Bu<sub>2</sub>Sn(2-SepymMe<sub>2</sub>)<sub>2</sub>], [<sup>t</sup>Bu<sub>2</sub>Sn(2-SepymMe<sub>2</sub>)<sub>2</sub>] and [<sup>t</sup>Bu<sub>2</sub>SnCl(2-SepymMe<sub>2</sub>)] were collected at room temperature (298 ± 2K) on a Rigaku AFC7S diffractometer using graphite monochromated Mo-Kα (λ = 0.71069 Å) radiation so that θ<sub>max</sub> = 27.5°. The unit cell parameters were determined from 25 reflections measured by a random search routine and are given in Tables 2.3 and 2.4 of Chapter 2.

### **4.3 Results and Discussion**

#### **4.3.1 Synthesis and Spectroscopy**

Treatment of R<sub>2</sub>SnCl<sub>2</sub> (R = Me, Et, <sup>n</sup>Bu, <sup>t</sup>Bu) with two equivalents of sodium 5-methyl-2-pyridyl selenolate [Na(2-Sepy(5-Me))] and sodium 4,6-dimethyl-2-pyrimidyl selenolate, [Na(2-SepymMe<sub>2</sub>)], in a toluene-methanol mixture gave diorganotin selenolate complexes, of type [R<sub>2</sub>Sn(2-Sepy(5-Me))<sub>2</sub>] (R = Me, Et and <sup>t</sup>Bu) and [R<sub>2</sub>Sn(2-SepymMe<sub>2</sub>)<sub>2</sub>] (R = Me, Et, <sup>n</sup>Bu, <sup>t</sup>Bu) (Scheme 4.1), respectively. The latter when treated with an equivalent of R<sub>2</sub>SnCl<sub>2</sub> in toluene mixture gave chloro complexes, [R<sub>2</sub>SnCl(2-SepymMe<sub>2</sub>)] (R = Me, <sup>n</sup>Bu, <sup>t</sup>Bu).



**Scheme 4.1** Synthesis of organotin pyridyl and pyrimidyl selenolate complexes

The  $^1\text{H}$ ,  $^{13}\text{C}\{^1\text{H}\}$ ,  $^{77}\text{Se}\{^1\text{H}\}$  and  $^{119}\text{Sn}\{^1\text{H}\}$  NMR spectra were recorded in  $\text{CDCl}_3$ . The  $^1\text{H}$  and  $^{13}\text{C}\{^1\text{H}\}$  NMR spectra showed expected resonances and peak multiplicities. The pyridyl and pyrimidyl ring protons shifted to downfield with reference to the corresponding signals for the diselenide. The magnitudes of  $^1J(^{119}\text{Sn}-^{13}\text{C})$  and  $^2J(^{119}\text{Sn}-^1\text{H})$  for dimethyltin complexes ( $[\text{Me}_2\text{Sn}(2\text{-SepymMe}_2)_2]$  and  $[\text{Me}_2\text{SnCl}(2\text{-SepymMe}_2)]$ ) are similar to other dimethyltin(IV) derivatives with seleno-pyridine ligands [149].  $^1J(\text{Sn}-\text{C})$  values in case of pyrimidyl complexes decreases gradually on replacing methyl groups attached to tin by Et,  $^n\text{Bu}$  or  $^t\text{Bu}$  which may be due to the increasing steric hindrance resulting in diminishing the electron acceptor property of tin [205].

The  $^{77}\text{Se}\{^1\text{H}\}$  NMR spectra displayed a single resonance in the range 153 – 194 and 170-262 ppm which were flanked by tin satellites with  $^1J(^{119}\text{Sn}-^{77}\text{Se})$  couplings varying between 668-887 and 723-977 Hz for pyridyl and pyrimidyl derivatives, respectively. The  $^{77}\text{Se}\{^1\text{H}\}$  resonance within the series is shielded while the  $^1J(^{119}\text{Sn}-^{77}\text{Se})$  increased on replacing methyl groups on tin with  $^t\text{Bu}$  group. This can be attributed to increasing +I effect of the larger alkyl group. The  $^{77}\text{Se}$  resonance for chloro derivatives  $[\text{R}_2\text{SnCl}(2\text{-SepymMe}_2)]$  are deshielded (~30-20 ppm) with respect to the corresponding bis



complexes. The magnitude of  $^1J(^{119}\text{Sn}-^{77}\text{Se})$  coupling constant of pyridyl derivatives  $[\text{R}_2\text{Sn}(2\text{-Sepy}(5\text{-Me}))_2]$  is reduced with reference to the analogous pyrimidyl derivatives,  $[\text{R}_2\text{Sn}(2\text{-SepymMe}_2)_2]$  indicative of weaker Sn-Se interaction consequently longer Sn-Se bond lengths in the pyridyl selenolate complexes. A representative  $^{77}\text{Se}\{^1\text{H}\}$  NMR spectra of pyridyl and pyrimidyl derivatives is shown in Fig. 4.1.

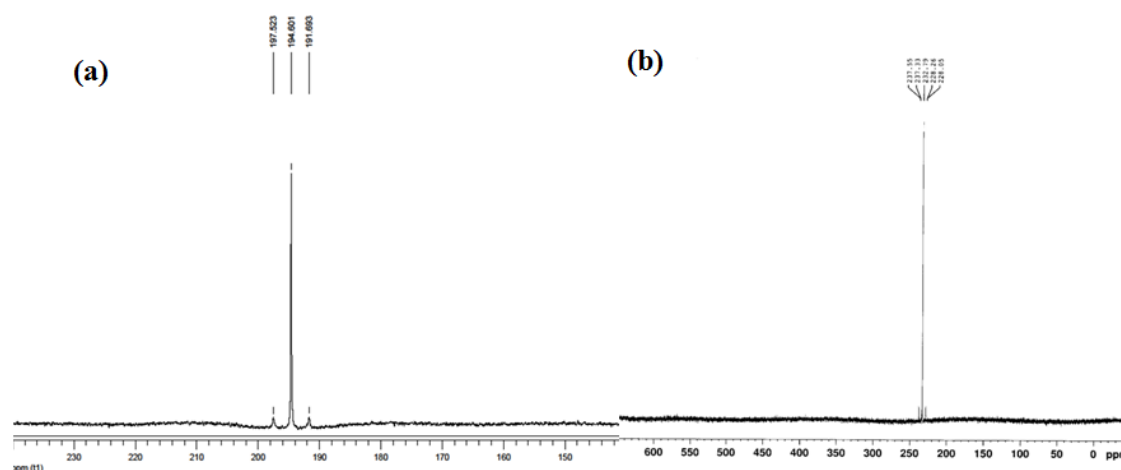


**Fig. 4.1**  $^{77}\text{Se}\{^1\text{H}\}$  NMR spectra of a)  $[\text{Me}_2\text{Sn}(2\text{-Sepy}(5\text{-Me}))_2]$  and b)  $[\text{Me}_2\text{Sn}(2\text{-SepymMe}_2)_2]$ .

The  $^{119}\text{Sn}\{^1\text{H}\}$  NMR spectra displayed a single resonance for all the complexes confirming the existence of only one tin containing species in solution. The  $^{119}\text{Sn}\{^1\text{H}\}$  resonances appeared in the range of  $-141$  to  $-13$  and  $-135$  to  $28$  ppm which were flanked by  $^{77}\text{Se}$  satellite with the coupling constant values between  $673\text{-}887$  and  $724\text{-}999$  Hz for pyridyl and pyrimidyl derivatives, respectively. A representative  $^{119}\text{Sn}\{^1\text{H}\}$  NMR spectra of pyridyl and pyrimidyl derivatives is shown in Fig. 4.2.

The resonances for pyrimidyl complexes are deshielded with reference to the  $^{119}\text{Sn}$  NMR signal for the corresponding 5-pyridylselenolate complexes indicating weaker Sn...N interactions in the former. The resonance within the series (bis or chloro) is

deshielded on replacing methyl group on tin by bulkier R group (Et,  $^n\text{Bu}$  or  $^t\text{Bu}$ ) which could be due to +I effect of the larger alkyl group, and is in conformity with the trend noted for diorgaotin dichlorides (e.g.,  $\text{R}_2\text{SnCl}_2$ ;  $\text{R}/\delta^{119}\text{Sn}$  (in ppm) = Me/141; Et/126;  $^n\text{Bu}$ /122;  $^t\text{Bu}$ /52) [206,207]. The variable temperature  $^{119}\text{Sn}$  NMR spectra of  $[\text{tBu}_2\text{SnCl}(2\text{-SepymMe}_2)]$  were recorded in methanol- $\text{d}_4$  to assess whether there is any interaction between tin and nitrogen. There was a slight shift in the  $^{119}\text{Sn}$  NMR resonance on lowering the temperature from RT to  $-40^\circ\text{C}$  ( $^{119}\text{Sn}$  NMR  $\delta$ : -18 at RT and -22 ppm at  $-40^\circ\text{C}$ ) (Fig. 4.3) indicating that there is no change in the coordination around tin. Temperature dependent  $^{119}\text{Sn}$  NMR chemical shifts of diorganotin carboxylates have been attributed to change in the coordination environment around tin [208].

In general,  $^{119}\text{Sn}$  signals for four-coordinate compounds are observed in the range of  $\delta = +200$  to  $-60$  ppm [208,209]. The  $^{119}\text{Sn}$  NMR signals for  $[\text{R}_2\text{Sn}(2\text{-Sepy}(5\text{-Me}))_2]$  ( $\text{R} = \text{Me, Et}$ ),  $[\text{R}_2\text{Sn}(2\text{-SepymMe}_2)_2]$  ( $\text{R} = \text{Me, Et, } ^n\text{Bu}$ ) and  $[\text{R}_2\text{SnCl}(2\text{-SepymMe}_2)]$  ( $\text{R} = \text{Me, } ^n\text{Bu}$ ) are out of this range, indicating higher coordination around tin atom in these complexes which is attained by weak tin-nitrogen intra-molecular interactions.

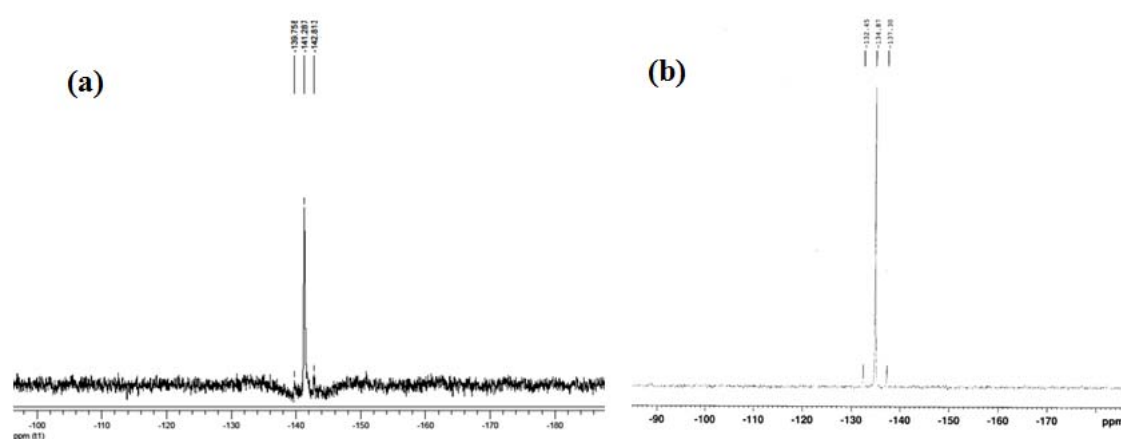


**Fig. 4.2**  $^{119}\text{Sn}\{^1\text{H}\}$  NMR spectra of a)  $[\text{Me}_2\text{Sn}(2\text{-Sepy}(5\text{-Me}))_2]$  and b)  $[\text{Me}_2\text{Sn}(2\text{-SepymMe}_2)_2]$ .

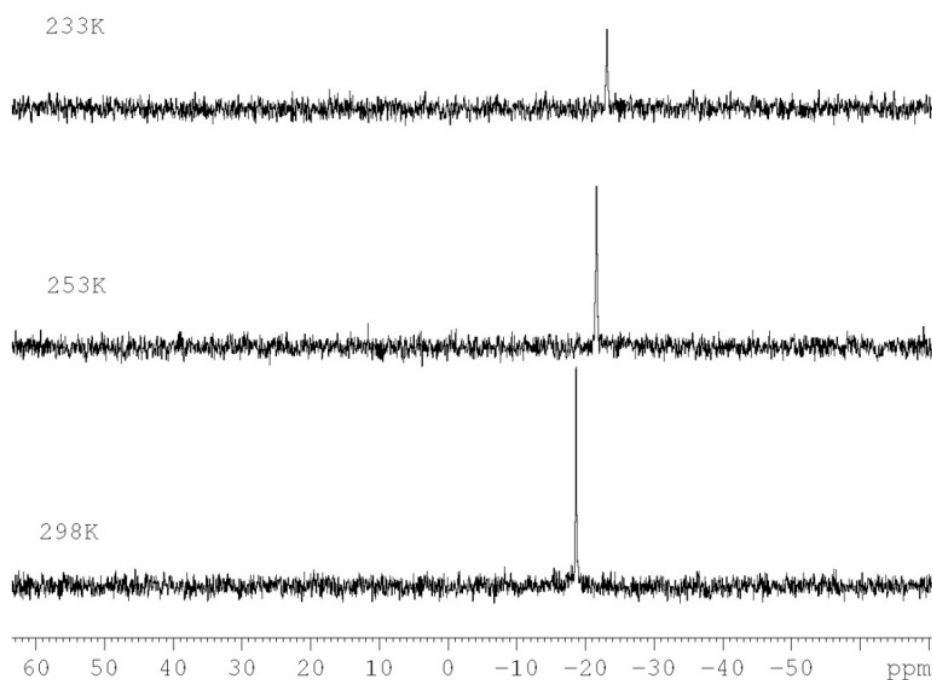


**Fig. 4.3** Variable temperature  $^{119}\text{Sn}\{^1\text{H}\}$  NMR spectrum of  $[\text{tBu}_2\text{SnCl}(2\text{-SepymMe}_2)]$  acquired in  $\text{CDCl}_3$ .

Only  $\text{tBu}_2$  derivatives resonance peak are appearing in this range, suggesting four-coordination around tin. This can be attributed to steric demand of  $\text{tBu}_2$  groups attached to tin which forces two pyridyl or pyrimidyl ring to occupy space at a larger distance from the tin atoms. Selected NMR data for the complexes have been tabulated in Table 4.1.

**Table 4.1**  $^{77}\text{Se}\{^1\text{H}\}$  and  $^{119}\text{Sn}\{^1\text{H}\}$  NMR data in  $\text{CDCl}_3$  of diorganotin selenolate complexes with coupling constant values.

Complexes in $\text{CDCl}_3$	$\delta$ $^{77}\text{Se}\{^1\text{H}\}$ NMR	$\delta$ $^{119}\text{Sn}\{^1\text{H}\}$ NMR
$[\text{Me}_2\text{Sn}(2\text{-Sepy}(5\text{-Me}))_2]$	$\delta$ : 194 ( $^1\text{J}(^{119}\text{Sn} - ^{77}\text{Se}) = 658 \text{ Hz}$ )	$\delta$ : -141 ( $^1\text{J}(^{119}\text{Sn} - ^{77}\text{Se}) = 663 \text{ Hz}$ )
$[\text{Et}_2\text{Sn}(2\text{-Sepy}(5\text{-Me}))_2]$	$\delta$ : 156 ( $^1\text{J}(^{119}\text{Sn} - ^{77}\text{Se}) = 662 \text{ Hz}$ )	$\delta$ : -108 ( $^1\text{J}(^{119}\text{Sn} - ^{77}\text{Se}) = 673 \text{ Hz}$ )
$[\text{tBu}_2\text{Sn}(2\text{-Sepy}(5\text{-Me}))_2]$	$\delta$ : 153 ( $^1\text{J}(^{119}\text{Sn} - ^{77}\text{Se}) = 883 \text{ Hz}$ )	$\delta$ : -13 ( $^1\text{J}(^{119}\text{Sn} - ^{77}\text{Se}) = 887 \text{ Hz}$ )
$[\text{Me}_2\text{Sn}(2\text{-SepymMe}_2)_2]$	$\delta$ : 233 ( $^1\text{J}(^{119}\text{Sn} - ^{77}\text{Se}) = 725 \text{ Hz}$ )	$\delta$ : -135 ( $^1\text{J}(^{119}\text{Sn} - ^{77}\text{Se}) = 724 \text{ Hz}$ )
$[\text{Et}_2\text{Sn}(2\text{-SepymMe}_2)_2]$	$\delta$ : 180 ( $^1\text{J}(^{119}\text{Sn} - ^{77}\text{Se}) = 723 \text{ Hz}$ )	$\delta$ : -87 ( $^1\text{J}(^{119}\text{Sn} - ^{77}\text{Se}) = 726 \text{ Hz}$ )
$[\text{nBu}_2\text{Sn}(2\text{-SepymMe}_2)_2]$	$\delta$ : 194 ( $^1\text{J}(^{119}\text{Sn} - ^{77}\text{Se}) = 745 \text{ Hz}$ )	$\delta$ : -92 ( $^1\text{J}(^{119}\text{Sn} - ^{77}\text{Se}) = 746 \text{ Hz}$ )
$[\text{tBu}_2\text{Sn}(2\text{-SepymMe}_2)_2]$	$\delta$ : 182 ( $^1\text{J}(^{119}\text{Sn} - ^{77}\text{Se}) = 977 \text{ Hz}$ )	$\delta$ : 28 ( $^1\text{J}(^{119}\text{Sn} - ^{77}\text{Se}) = 999 \text{ Hz}$ )
$[\text{Me}_2\text{SnCl}(2\text{-SepymMe}_2)]$	$\delta$ : 262 ( $^1\text{J}(^{119}\text{Sn} - ^{77}\text{Se}) = 724 \text{ Hz}$ )	$\delta$ : -90 ( $^1\text{J}(^{119}\text{Sn} - ^{77}\text{Se}) = 727 \text{ Hz}$ )
$[\text{nBu}_2\text{SnCl}(2\text{-SepymMe}_2)]$	$\delta$ : 228 ( $^1\text{J}(^{119}\text{Sn} - ^{77}\text{Se}) = 748 \text{ Hz}$ )	$\delta$ : -74 ( $^1\text{J}(^{119}\text{Sn} - ^{77}\text{Se}) = 755 \text{ Hz}$ )
$[\text{tBu}_2\text{SnCl}(2\text{-SepymMe}_2)]$	$\delta$ : 197 ( $^1\text{J}(^{119}\text{Sn} - ^{77}\text{Se}) = 910 \text{ Hz}$ )	$\delta$ : -20 ( $^1\text{J}(^{119}\text{Sn} - ^{77}\text{Se}) = 912 \text{ Hz}$ )

### 4.3.2 X-ray Crystallography

The ligand  $(2\text{-Sepy}(5\text{-Me}))_2$  is a discrete monomer as shown in Fig. 4.4. Selected inter-atomic parameters are given in Table 4.2 In the equatorial conformation of the ligand, C-Se-Se bond angles of  $104.5^\circ$  and  $102^\circ$  are in the range reported for other organic diselenides ( $92^\circ$  for  $(3\text{-CF}_3\text{-pySe})_2$ ,  $102.7^\circ$  for  $(5\text{-CF}_3\text{-pySe})_2$ ,  $104.7^\circ$  for  $(\text{pySe})_2$ , etc.)

[210]. The C-Se and Se-Se bond lengths are also in the range reported to most of the organic diselenides, i.e. (1.91–1.97 Å) and (2.285–2.33 Å), respectively [211].

The molecular structures of  $[\text{R}_2\text{Sn}(\text{2-Sepy}(5\text{-Me}))_2]$  ( $\text{R} = \text{Me, Et, } ^t\text{Bu}$ ),  $[\text{R}_2\text{Sn}(\text{2-SepymMe}_2)_2]$  ( $\text{R} = ^t\text{Bu, } ^n\text{Bu}$ ) and  $[\text{}^t\text{Bu}_2\text{SnCl}(\text{2-SepymMe}_2)]$  with atomic numbering scheme are shown in (Fig. 4.5 and 4.6). Selected inter-atomic parameters are given in Tables 4.3-4.6.

The structures of  $[\text{R}_2\text{Sn}(\text{2-Sepy}(5\text{-Me}))_2]$  ( $\text{R} = \text{Me, Et, } ^t\text{Bu}$ ) are isomorphous to  $[\text{R}_2\text{Sn}(\text{SeC}_5\text{H}_4\text{N})_2]$  ( $\text{R} = \text{Me, } ^t\text{Bu}$ ) described recently [149]. The tin atom in these complexes lies on a two-fold rotation axis. The coordination around tin can be defined by the carbon atoms of two R groups and selenium from 5-methyl-2-pyridyl selenolate ligands. The overall geometry around tin can be considered as a skew trapezoidal bipyramidal. There are weak tin-nitrogen intra-molecular interactions. The Se...N distances are longer than the sum of their covalent radii (2.15 Å) but are shorter than the sum of van der Waal's radii (3.72 Å). The Sn-C distances (2.106(9)–2.227(5) Å) are well in agreement with those reported for diorganotin complexes [149,181]. The Sn-Se distances vary between 2.5694(11) and 2.6237(15) Å and can be compared with analogous diorganotin 2-pyridyl selenolates [149]. The Se-Sn-Se angles in these complexes are slightly reduced as compared to 2-pyridylselenolates,  $[\text{R}_2\text{Sn}(\text{SeC}_5\text{H}_4\text{N})_2]$  ( $\text{R} = \text{Me}$  (94.25(8), 91.23(8)°),  $^t\text{Bu}$  (89.14(11)°) [149]. The crystal lattice of  $[\text{Et}_2\text{Sn}(\text{2-Sepy}(5\text{-Me}))_2]$  contains two independent molecules which differ slightly in their inter-atomic parameters (Table 4.4).

On the other hand, the coordination geometry around tin in pyrimidyl derivative  $[\text{}^t\text{Bu}_2\text{Sn}(\text{2-SepymMe}_2)_2]$  can be defined by carbon atoms of two  $^t\text{Bu}$  groups and selenium from monodentate 2-pyrimidylselenolate ligands. The overall geometry can be considered as distorted tetrahedral. The Sn...N distances are longer than the sum of their covalent

radii (2.15 Å) but are shorter than the sum of van der Waal's radii (3.72 Å). The Sn...N separation in [<sup>t</sup>Bu<sub>2</sub>Sn(2-SepymMe<sub>2</sub>)<sub>2</sub>] is longer than the [<sup>t</sup>Bu<sub>2</sub>Sn(2-Sepy(5-Me))<sub>2</sub>] (Sn...N = 2.877 Å) and the one reported in [<sup>t</sup>Bu<sub>2</sub>Sn(SeC<sub>5</sub>H<sub>4</sub>N)<sub>2</sub>] (Sn...N = 2.425(9) Å) [149], indicating a weaker Sn...N interaction in the former case. A similar structure is observed for [<sup>n</sup>Bu<sub>2</sub>Sn(2-SepymMe<sub>2</sub>)<sub>2</sub>] except there are four molecules present in the crystallographic asymmetric unit which differs slightly in their inter-atomic parameters. The Sn–Se bond distance (2.5800(6)) is shorter than those reported in [Sn(SeC<sub>5</sub>H<sub>4</sub>N)<sub>2</sub>]<sub>2</sub> (2.681, 2.759 Å) [148], <sup>1</sup>[Sn(SePh)<sub>2</sub>] (2.668, 2.675, 2.683, 2.673 Å) [201] and [<sup>t</sup>Bu<sub>2</sub>Sn(2-SeC<sub>5</sub>H<sub>4</sub>N)<sub>2</sub>] (2.622(2) Å) [149]. The Se–Sn–Se angle (86.19(3)°) is contracted by 3° to that of [<sup>t</sup>Bu<sub>2</sub>Sn(2-SeC<sub>5</sub>H<sub>4</sub>N)<sub>2</sub>] (89.14(11)°) [149] and [<sup>n</sup>Bu<sub>2</sub>Sn{SC<sub>5</sub>H<sub>3</sub>N(5-NO<sub>2</sub>)<sub>2</sub>}<sub>2</sub>] (89.9(1)°) [184]. The Sn–C<sub>butyl</sub> bond distance (2.205(4) Å) is slightly shorter than that of [<sup>t</sup>Bu<sub>2</sub>Sn(2-SeC<sub>5</sub>H<sub>4</sub>N)<sub>2</sub>] (2.246(10) Å) while it is comparable to the value reported for [<sup>t</sup>Bu<sub>2</sub>Sn(μ-OH){O(S)P(OEt<sub>2</sub>)<sub>2</sub>}<sub>2</sub>] (av. 2.16 Å) [213].

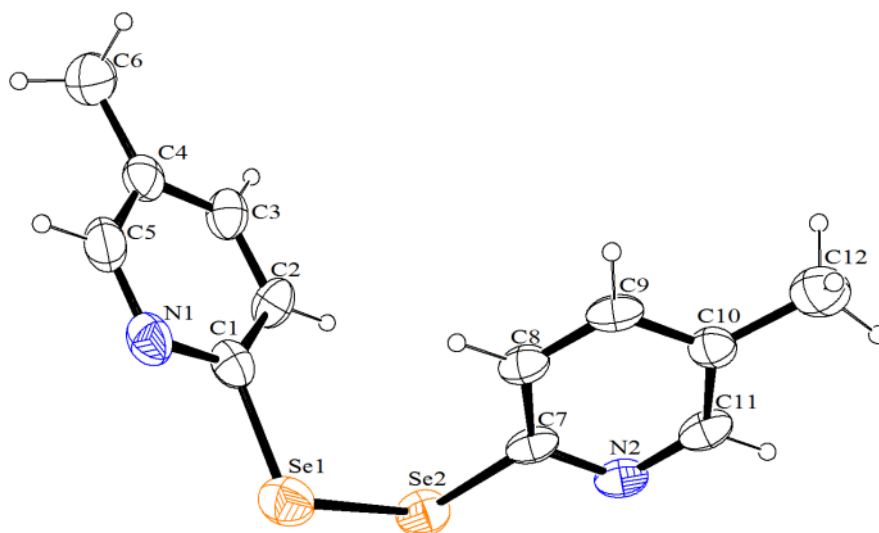


**Fig 4.4** Molecular structure of (2-Sepy(Me-5))<sub>2</sub>, with atomic number scheme .

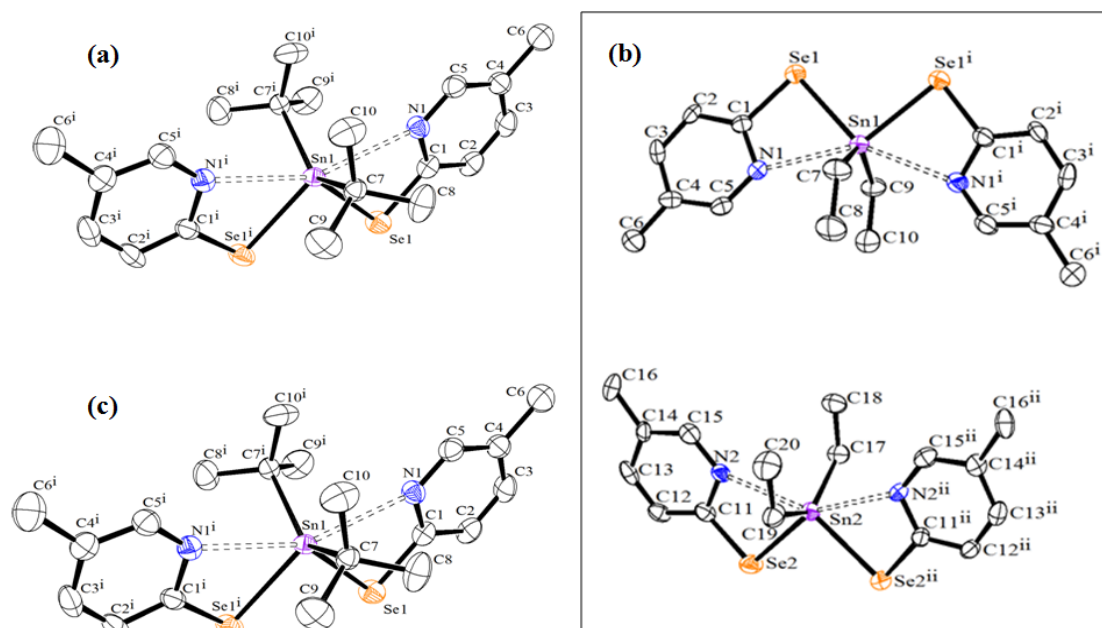


**Fig. 4.5** Crystal structure of a)  $[\text{Me}_2\text{Sn}(2\text{-Sepy}(5\text{-Me}))_2]$ , b)  $[\text{Et}_2\text{Sn}(2\text{-Sepy}(5\text{-Me}))_2]$  and c)  $[\text{tBu}_2\text{Sn}(2\text{-Sepy}(5\text{-Me}))_2]$  with partial atomic number scheme. Ellipsoids are drawn with 25% probability.

The tin in  $[\text{tBu}_2\text{SnCl}(2\text{-SepymMe}_2)]$  acquires a distorted trigonal bipyramidal geometry defined by a Cl, two  $\text{tBu}_2$  and Se, N of a selenopyrimidine ligand where the chloride atom and chelating pyrimidylselenolate occupy the equatorial plane while two *tert*-butyl groups are directed axially. The Sn...N distance (2.784 Å) is shorter than the sum of their van der Waals radii [214]. The Sn–N (2.784 Å) separation is larger than the one reported in  $[\text{Me}_2\text{SnCl}(\text{SepyMe})]$  (2.425(9) Å) [149],  $[\text{Ph}_2\text{SnCl}(\text{SC}_5\text{H}_4\text{N})]$  (2.413 Å) [180] and  $[\text{R}_2\text{SnCl}(\text{SpyMe}_2)]$  (R = Me or Et) (~2.51 Å) but is comparable to  $[\text{tBu}_2\text{Sn}(2\text{-SeC}_5\text{H}_4\text{N})_2]$  (2.827 Å) [149] and  $[(\text{c-Hex})_2\text{Sn}(\text{SC}_5\text{H}_4\text{N})_2]$  (2.72 Å) [183]. The Sn–Cl bond distance (2.418(3) Å) is as expected and is comparable to the values reported for  $[\text{Ph}_2\text{SnCl}(\text{SC}_5\text{H}_4\text{N})]$  (2.45 Å) [184] and  $[\text{SnCl}_4(\text{Et}_2\text{Se})_2]$  (2.42, 2.43 Å) [215].

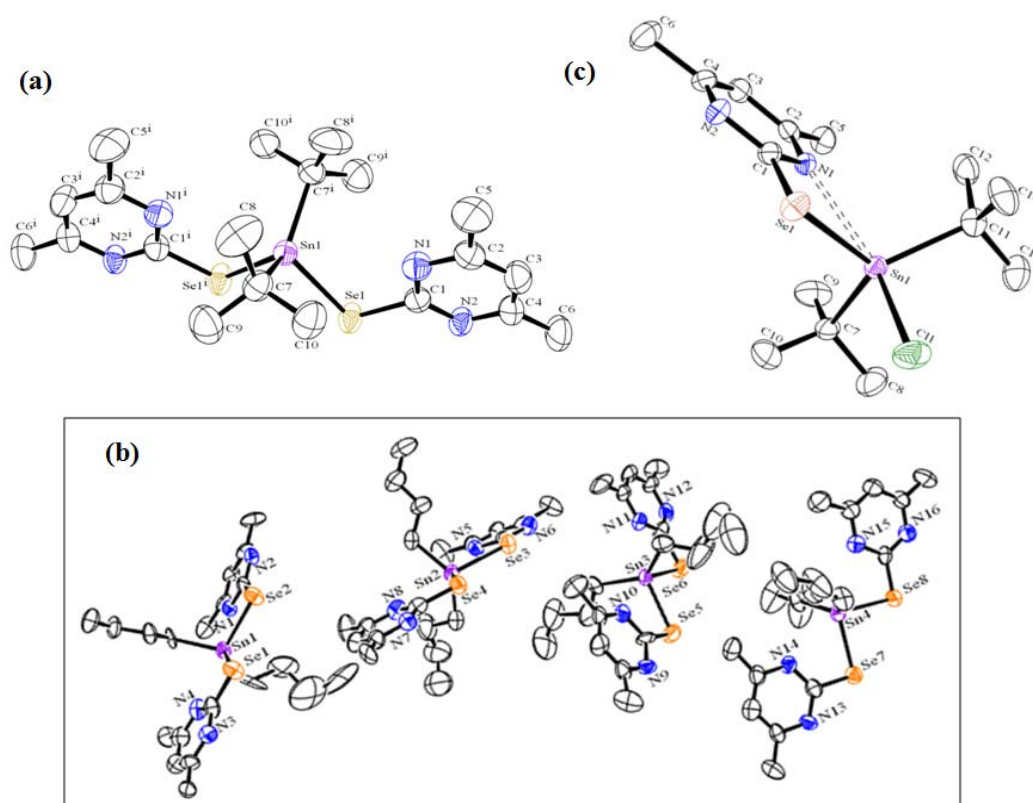


**Fig. 4.6** Crystal structure of a) [ $t\text{-Bu}_2\text{Sn}(2\text{-SepymMe}_2)_2$ ], b) [ $n\text{-Bu}_2\text{Sn}(2\text{-SepymMe}_2)_2$ ] and c) [ $t\text{-Bu}_2\text{SnCl}(2\text{-SepymMe}_2)$ ] with partial atomic number scheme. Ellipsoids are drawn at 50%, 25% and 10% probability for a), b) and c), respectively.

**Table 4.2** Selected bond lengths ( $\text{\AA}$ ) and angles ( $^\circ$ ) of [ $(2\text{-Sepy}(5\text{-Me}))_2$ ].

C(1)-N(1)	1.313(7)	C(1) Se(1) Se(2)	104.5(3)
C(1)-Se(1)	1.927(7)	C(7) Se(2) Se(1)	102.0(2)
C(5)-N(1)	1.341(8)	C(2) C(1) Se(1)	124.3(7)
C(7)-N(2)	1.334(7)	C(8) C(7) Se(2)	125.9(7)
C(7)-Se(2)	1.914(7)	N(1) C(1) Se(1)	111.1(6)
Se(1)-Se(2)	2.299(13)	N(2) C(7) Se(2)	111.2(6)



**Table 4.3** Selected bond lengths ( $\text{\AA}$ ) and angles ( $^\circ$ ) of  $[\text{Me}_2\text{Sn}(2\text{-Sepy}(5\text{-Me}))_2]$  and  $[\text{tBu}_2\text{Sn}(2\text{-Sepy}(5\text{-Me}))_2]$ .

$[\text{Me}_2\text{Sn}(2\text{-Sepy}(5\text{-Me}))_2]$		$[\text{tBu}_2\text{Sn}(2\text{-Sepy}(5\text{-Me}))_2]$	
Sn1-C7	2.106(9)	Sn1-C7	2.227(5)
Sn1-Se1	2.5694(11)	Sn1-Se1	2.6169(8)
Sn1-N1	2.972	Sn1-N1	2.877
Sn1-C8	2.120(10)	Se1-C1	1.893(6)
Sn1-Se1 <sup>i</sup>	2.5694(11)		
Se1-C1	1.907(7)		
C7-Sn1-C8	117.9(4)	C7-Sn1-C7 <sup>i</sup>	130.7(3)
C7-Sn1-Se1	112.8(2)	C7-Sn1-Se1	108.28(13)
C7-Sn1-Se1 <sup>i</sup>	112.8(2)	C7-Sn1-Se1 <sup>i</sup>	106.64(14)
C7-Sn1-N1	78.9	C7-Sn1-N1	85.8
C1-Se1-Sn1	93.0(2)	C1-Se1-Sn1	90.74(19)
C8-Sn1-Se1	110.7(2)	Se1-Sn1-Se1 <sup>i</sup>	88.07(4)
C8-Sn1-Se1 <sup>i</sup>	110.6	N1-Sn1-N1 <sup>i</sup>	151.8
C8-Sn1-N1	87.3		
Se1-Sn1-Se1 <sup>i</sup>	88.09(5)		
N1-Sn1-N1 <sup>i</sup>	151.5		

**Table 4.4** Selected bond lengths ( $\text{\AA}$ ) and angles ( $^\circ$ ) of  $[\text{Et}_2\text{Sn}(2\text{-Sepy}(5\text{-Me}))_2]$ .

Molecule 1		Molecule 2	
Sn1-C7	2.136(16)	Sn2-C17	2.121(16)
Sn1-C9	2.160(17)	Sn2-C19	2.154(18)
Sn1-Se1	2.6047(14)	Sn2-Se2	2.6237(15)
Sn1-N1	2.741	Sn2-N2	2.696
Se1-C1	1.921(11)	Se2-C11	1.897(12)
C7-Sn1-C9	130.2(7)	C17-Sn2-C19	133.5(7)
C7-Sn1-Se1	107.9(3)	C17-Sn2-Se2	108.1(3)
C7-Sn1-N1	81.5	C17-Sn2-N2	82.04
C9-Sn1-Se1	105.9(3)	C19-Sn2-Se2	103.5(3)
C9-Sn1-N1	83.63	C19-Sn2-N2 <sup>i</sup>	83.6
Se1-Sn1-Se1 <sup>i</sup>	92.45(6)	Se2-Sn2-Se2 <sup>i</sup>	92.68(7)

**Table 4.5** Selected bond lengths ( $\text{\AA}$ ) and angles ( $^\circ$ ) of  $[\text{}^t\text{Bu}_2\text{Sn}(\text{2-SepymMe}_2)_2]$  and  $[\text{}^t\text{Bu}_2\text{SnCl}(\text{2-SepymMe}_2)]$ .

[ ${}^t\text{Bu}_2\text{Sn}(\text{2-SepymMe}_2)_2$ ]		[ ${}^t\text{Bu}_2\text{SnCl}(\text{2-SepymMe}_2)$ ]	
Sn1–Se1	2.5800(6)	Sn1–C7	2.21
Sn1–C7	2.205(4)	Sn1–C11	2.19(1)
Sn1–N1	3.234(4)	Sn1–Cl1	2.418(3)
Se1–C1	1.910(4)	Sn1–Se1	2.545(1)
		Sn1–N1	2.784(7)
		Se1–C1	1.887(9)
C7–Sn1–C7 <sup>i</sup>	125.6(2)	C7–Sn1–C11	126.7(4)
C7–Sn1–Se1	108.3(1)	C7–Sn1–Cl1	98.1(3)
C7–Sn1–Se1 <sup>i</sup>	110.7(1)	C7–Sn1–Se1	115.7(3)
C7 <sup>i</sup> –Sn1–Se1	110.7(1)	C7–Sn1–N1	91.9(3)
C7 <sup>i</sup> –Sn1–Se1 <sup>i</sup>	108.3(1)	C11–Sn1–Se1	114.4(3)
Sn1–Se1–C1	98.4(2)	Cl1–Sn1–Se1	92.10(9)
N1 <sup>i</sup> –Sn1–N1	161.85	C11–Sn1–Cl1	97.2(3)
Se1 <sup>i</sup> –Sn1–Se1	86.19(3)	C11–Sn1–N1	95.7(3)
		Cl1–Sn1–Se1	92.1(9)
		Se1–Sn1–N1	62.6(2)
		Cl1–Sn1–N1	154.1(2)

**Table 4.6** Selected bond lengths (Å) and angles (°) of [*n*Bu<sub>2</sub>Sn(2-SepymMe<sub>2</sub>)<sub>2</sub>].

Molecule a		Molecule b		Molecule c		Molecule d	
Sn1-Se1	2.609(4)	Sn2-Se3	2.581(4)	Sn3-Se5	2.599(4)	Sn4-Se7	2.575(4)
Sn1-Se2	2.601(4)	Sn2-Se4	2.583(4)	Sn3-Se6	2.595(4)	Sn4-Se8	2.582(4)
Sn1-N1	2.747(13)	Sn2-N5	2.844(16)	Sn3-N11	2.778(16)	Sn4-N15	2.979(16)
Sn1-N3	2.722(16)	Sn2-N7	3.042(18)	Sn3-N9	2.732(17)	Sn4-N13	2.885(16)
Sn1-C13	2.09(3)	Sn2-C33	2.25(3)	Sn3-C53	2.12(3)	Sn4-C73	2.05(2)
Sn1-C17	2.18(2)	Sn2-C37	2.15(2)	Sn3-C57	2.17(2)	Sn4-C77	2.12(2)
Se1-C7	1.769(14)	Se3-C21	1.801(13)	Se5-C41	1.815(14)	Se7-C61	1.812(15)
Se2-C1	1.806(11)	Se4-C27	1.800(14)	Se6-C47	1.832(14)	Se8-C67	1.812(13)
Se1-Sn1-Se2	91.43(15)	Se3-Sn2-Se4	89.68(12)	Se5-Sn3-Se6	92.49(16)	Se7-Sn4-Se8	90.26(12)
Se1-Sn1-N1	153.0(4)	Se4-Sn2-N5	150.8(4)	Se5-Sn3-N9	154.2(5)	Se8-Sn4-N13	59.9(4)
Se1-Sn1-N3	61.1(4)	Se4-Sn2-N7	58.6(4)	Se5-Sn3-N11	61.1(4)	Se8-Sn4-N15	149.6(3)
Se2-Sn1-N3	152.4(4)	Se3-Sn2-N7	148.3(4)	Se6-Sn3-N11	153.5(4)	Se7-Sn4-N15	59.6(3)
C13-Sn1-C17	126.9(11)	C37-Sn2-C33	126.0(10)	C57-Sn3-C53	125.5(11)	C73-Sn4-C77	125.6(11)
C13-Sn1-Se2	110.3(8)	C37-Sn2-Se3	111.5(6)	C57-Sn3-Se6	108.7(7)	C73-Sn4-Se7	107.5(9)
C17-Sn1-Se2	106.7(7)	C33-Sn2-Se3	109.2(9)	C53-Sn3-Se6	109.9(8)	C77-Sn4-Se7	111.3(8)
C13-Sn1-Se1	105.5(9)	C37-Sn2-Se4	109.3(7)	C57-Sn3-Se5	106.9(6)	C73-Sn4-Se8	108.1(8)
C17-Sn1-Se1	110.4(5)	C33-Sn2-Se4	104.8(10)	C53-Sn3-Se5	108.2(9)	C77-Sn4-Se8	108.3(7)
C7-Se1-Sn1	88.4(7)	C21-Se3-Sn2	89.8(6)	C41-Se5-Sn3	89.6(6)	C61-Se7-Sn4	92.9(6)
C1-Se2-Sn1	88.3(6)	C27-Se4-Sn2	94.3(7)	C47-Se6-Sn3	88.7(8)	C67-Se8-Sn4	91.6(7)
N1-Sn1-N3	145.9(6)	N5-Sn2-N7	150.5(5)	N9-Sn3-N11	144.7(6)	N13-Sn4-N15	150.5(5)
C13-Sn1-N1	84.6(9)	C37-Sn2-N5	84.6(8)	C57-Sn3-N9	84.9(7)	C73-Sn4-N13	80.9(10)
C17-Sn1-N1	80.8(6)	C33-Sn2-N5	85.3(11)	C53-Sn3-N9	81.1(10)	C77-Sn4-N13	84.0(8)
C13-Sn1-N3	81.3(8)	C37-Sn2-N7	81.6(7)	C57-Sn3-N11	80.8(7)	C73-Sn4-N15	86.8(9)
C17-Sn1-N3	83.2(7)	C33-Sn2-N7	81.9(10)	C53-Sn3-N11	80.8(7)	C77-Sn4-N15	81.6(8)

### 4.3.3 Thermogravimetric Studies

In order to gain insight into relative volatilities and thermal stabilities of these complexes, thermogravimetric analyses (TGA) (Fig. 4.7) were performed under a flowing argon atmosphere.

The pyridyl complexes  $[R_2Sn(2-Sepy(5-Me))_2]$  decomposed in the range of 260-295 °C to give tin selenide. The ethyl and methyl derivatives, underwent a single-step decomposition, in contrast to  $[^tBu_2Sn(2-Sepy(5-Me)_2)]$  which showed a two-step decomposition. From the weight loss in the TG pattern it can be inferred that  $[Et_2Sn(2-Sepy(5-Me))_2]$  (weight loss: found 61.8%, calcd. 62.5%) and  $[Me_2Sn(2-Sepy(5-Me))_2]$  (weight loss: found 73.0%, calcd. 75.0%) gave SnSe on decomposition. In contrast, to  $[^tBu_2Sn(2-Sepy(5-Me)_2)]$  underwent decomposition via two overlapping steps initially forming SnSe<sub>2</sub> (weight loss: found 50.8%, calcd. 52.0%) before the formation of SnSe (weight loss: found 66.0%, calcd. 63.0%).

The bis pyrimidyl complexes,  $[R_2Sn(2-SepymMe_2)_2]$  underwent a single step decomposition. From the weight loss in the TG pattern it can be inferred that the complexes  $[Me_2Sn(2-SepymMe_2)_2]$  (weight loss: found 62.0%, calcd. 58.8%) and  $[^tBu_2Sn(2-SepymMe_2)_2]$  (weight loss: found 68.0%, calcd. 67.3%) gave SnSe whereas  $[Et_2Sn(2-SepymMe_2)_2]$  (weight loss: found 54.8%, calcd. 49.6%) and  $[^nBu_2Sn(2-SepymMe_2)_2]$  (weight loss: found 54.5%, calcd. 54.3%) afforded SnSe<sub>2</sub>. The % weight loss of Et derivative is higher than expected for the formation of SnSe<sub>2</sub> which may be due to partial sublimation during major weight loss step prior to the formation of SnSe<sub>2</sub> [216]. The complex,  $[^tBu_2SnCl(2-SepymMe_2)_2]$  underwent decomposition via two overlapping steps leading to the formation of tin (weight loss: found 71.2%, calcd. 73.8).

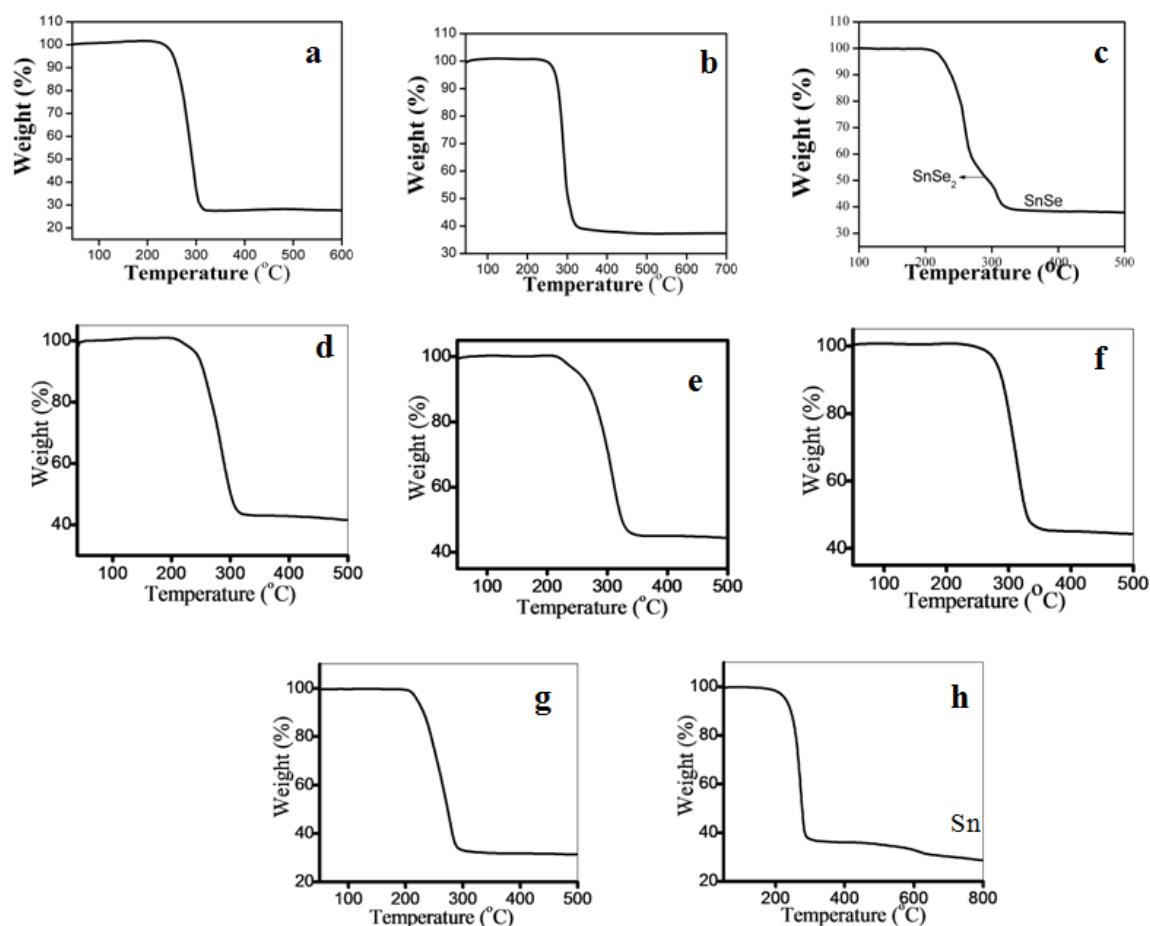


**Fig. 4.7** TG curve of a)  $[Me_2Sn(2-Sepy(5-Me))_2]$ , b)  $[Et_2Sn(2-Sepy(5-Me))_2]$ ,  $[tBu_2Sn(2-Sepy(5-Me))_2]$ , d)  $[Me_2Sn(2-SepymMe_2)_2]$ , e)  $[Et_2Sn(2-SepymMe_2)_2]$ , f)  $[nBu_2Sn(2-SepymMe_2)_2]$ , g)  $[tBu_2Sn(2-SepymMe_2)_2]$  and h)  $[tBu_2Sn(2-SepymMe_2)_2]$ , respectively.

#### 4.3.4 Preparation and characterization of tin selenide nanostructures

The thermogravimetric analyses revealed that  $[R_2Sn(2-Sepy(5-Me))_2]$  complexes yield SnSe on decomposition while in series  $[R_2Sn(2-SepymMe_2)_2]$ , Me and  $tBu$  gave SnSe whereas Et and  $nBu$  afforded SnSe<sub>2</sub>.

Therefore, from pyridyl series  $[R_2Sn(2-Sepy(5-Me))_2]$ , a representative complex  $[tBu_2Sn(2-Sepy(5-Me))_2]$  was chosen as single source precursor due to the fact that  $tBu$  is a good leaving group and also the complex showed a two-step decomposition processes which would enable us to isolate different compositions of tin selenide nanostructures.

The nanostructures were synthesised by thermolysis of [ $t\text{Bu}_2\text{Sn}(2\text{-Sepy}(5\text{-Me})_2)$ ] in different solvent systems (octadecene (ODE), oleylamine (OLA), oleic acid (OA) or in 1:1 (v/v) ODE:OLA and OA:OLA). Different solvents and their combination have been selected to investigate their effect upon the composition and morphology of the nanostructures. Initially, a non-coordinating and high boiling solvent ODE has been used for thermolysis of the precursor followed by OLA or OA which have different coordination capabilities to serve the role of solvent as well as capping agent.

While, from the pyrimidyl series [ $\text{R}_2\text{Sn}(2\text{-SepymMe}_2)_2$ ], Et,  $n\text{Bu}$  and  $t\text{Bu}$  were employed for the preparation of tin selenide nanostructures in OLA for different growth durations (2, 5, 10 min.) to assess the effect of different alkyl groups and growth durations on the morphology and composition of the nanostructures.

For clarity purpose first the preparation and characterization of nanostructures from [ $t\text{Bu}_2\text{Sn}(2\text{-Sepy}(5\text{-Me}))_2$ ] will be discussed followed by a detailed analysis of thermolysis experiments conducted using [ $\text{R}_2\text{Sn}(2\text{-SepymMe}_2)_2$ ] ( $\text{R} = \text{Et}, n\text{Bu}$  and  $t\text{Bu}$ ) for the synthesis of tin selenide nanostructures and deposition of thin film through aerosol assisted chemical vapour deposition (AACVD) using *tert*-butyl derivative as molecular precursor.

Thermolysis of [ $t\text{Bu}_2\text{Sn}(2\text{-Sepy}(5\text{-Me}))_2$ ] at 220 °C for 10 minutes using hot injection method in five distinct solvents/solvent mixtures was carried out for the preparation of tin selenide nanostructures which were characterized by p-XRD for determining phase and crystal structure (Fig. 4.8). Thermolysis of [ $t\text{Bu}_2\text{Sn}(2\text{-Sepy}(5\text{-Me}))_2$ ] (100 mg, 0.17 mmol) in 10 ml of ODE (8 ml of ODE in flask and 2 ml of ODE with the precursor during injection) afforded hexagonal phase of  $\text{SnSe}_2$  (JCDPS file no. 23-0602) while a similar experiment in 10 ml of OLA yielded orthorhombic phase of  $\text{SnSe}$  (JCPDS file no 48-1224) as evident from the reflection peaks of p-XRD and

corroborated by elemental composition analysis by EDX (Sn:Se atom ratio; 33.4:66.6 or 1:2 (in ODE); and 48.3:51.9 or 1:1.07 (in OLA)).

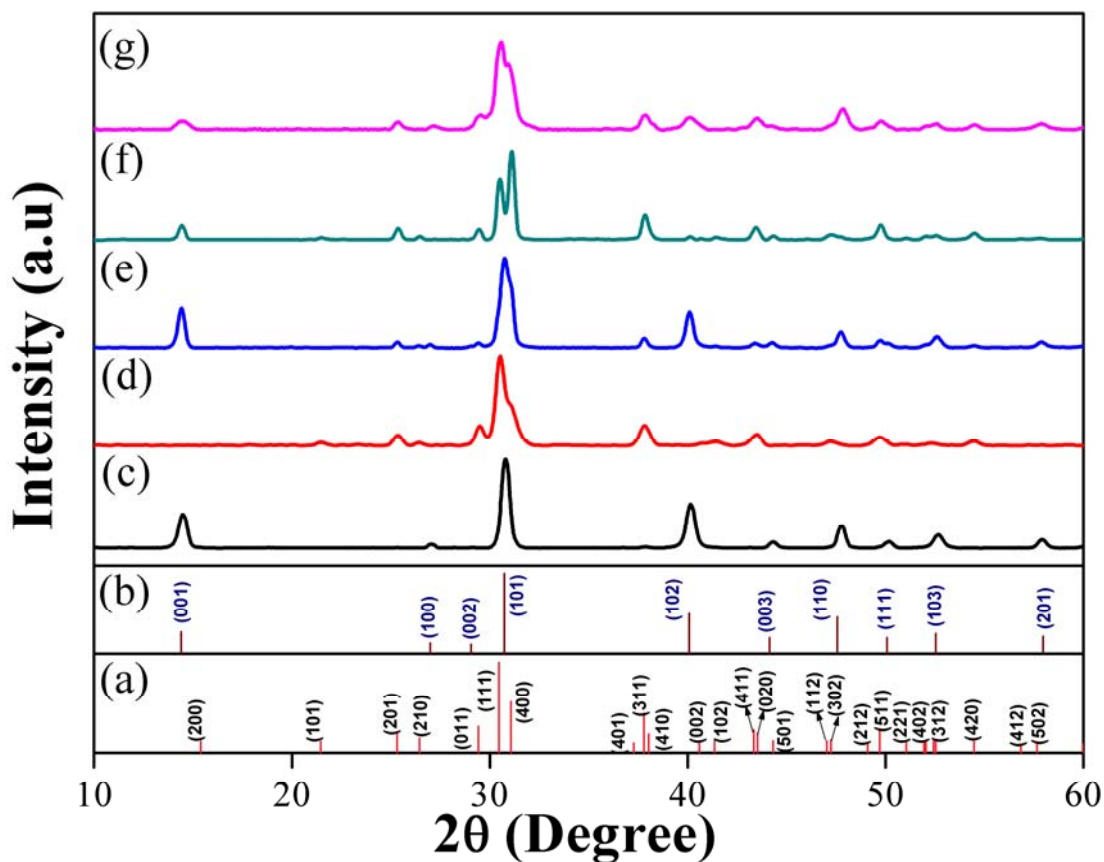


**Fig. 4.8** a) and b) Simulated XRD patterns of orthorhombic phase of SnSe (JCPDS no. 23-0602) and hexagonal SnSe<sub>2</sub> (JCPDS no. 48-1224), respectively. XRD profiles of tin selenide nanostructures obtained by thermolysis of [<sup>t</sup>Bu<sub>2</sub>Sn(2-Sepy(5-Me))<sub>2</sub>] at 220°C for 10 minutes in c) ODE, d) OLA, e) OA, f) 1:1 v/v mixture of OLA/ODE and g) 1:1 v/v mixture of OLA/ OA, respectively.

In contrast to thermolysis of [<sup>t</sup>Bu<sub>2</sub>Sn(2-Sepy(5-Me))<sub>2</sub>] in OLA or ODE, thermolysis in OA gave hexagonal phase of SnSe<sub>2</sub> as major product with little contamination from SnSe as deduced from p-XRD pattern. However when a mixture of ODE:OLA or OA:OLA (1:1; v/v) was used as solvent for thermolysis, slight contamination from hexagonal phase of SnSe<sub>2</sub> ( $2\theta = 14.44, 40.18, 47.34$ ) was found in orthorhombic phase of



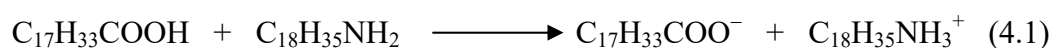
SnSe as evident from p-XRD pattern. Formation of different compositions can be attributed to the nature of the solvents. The presence of OLA provides strong reductive environment during thermolysis of  $[\text{tBu}_2\text{Sn}(\text{2-Sepy}(5\text{-Me}))_2]$  which facilitates the formation and stabilization of SnSe (Sn in +2 oxidation state) whereas thermolysis of  $[\text{tBu}_2\text{Sn}(\text{2-Sepy}(5\text{-Me}))_2]$  either in ODE or OA alone afforded  $\text{SnSe}_2$  (Sn in +4 oxidation state) as a pure/major product. The crystallite size of nanostructures (Table 4.7) was determined using Scherrer formula.

**Table 4.7** Reaction conditions, structural, compositional and optical parameters of tin selenides.

Solvent	Material composition (major + minor)	Morphology	Crystallite Size (nm)	EDX analyses (Sn:Se)	Direct Band Gap (eV)
ODE	$\text{SnSe}_2$	Hexagonal sheets	18	1:2.0	1.8
OLA	SnSe	Assembly of Irregular sheets giving flower like appearance	15	1:1.0	2.0
OA	$\text{SnSe}_2 + \text{SnSe}$	Hexagonal and rectangular sheets	13	1:1.9	-
OLA+ODE (1:1)	$\text{SnSe} + \text{SnSe}_2$	Rectangular sheets	20	1:1.2	-
OA+OLA (1:1)	$\text{SnSe} + \text{SnSe}_2$	nanoflakes	10	1:1.3	-

The non-coordinating (ODE) and weak coordinating (OLA) solvents could produce nanomaterials with larger crystallite size. When exclusively oleic acid (carboxylic acid groups are present as dimers because of hydrogen bonding interaction due to which

electron donation ability of oxygen is reduced resulting in weaker interaction between capping agent and the surface of nanoparticle [217]) was used, predominantly SnSe<sub>2</sub> with little amount of orthorhombic phase of SnSe was formed with average crystallite size of ~ 13 nm. On the other hand, thermolysis in OA/OLA could predominantly produce orthorhombic phase of SnSe with average crystallite size ~10 nm. This is attributed to the high electron donating and strong binding ability of oleate ion (C<sub>17</sub>H<sub>33</sub>COO<sup>-</sup>) resulted due to the deprotonation of oleic acid in the presence of OLA (C<sub>18</sub>H<sub>35</sub>NH<sub>2</sub>) as shown in the equation (4.1). To confirm whether Sn and Se are homogeneously distributed in the samples, 2-D elemental imaging of the all the nanostructures were performed which showed uniform distribution of the constituent elements.



The morphology of nanostructures was studied by scanning electron microscopy (SEM) and transmission electron microscopy (TEM). The SEM micrographs for SnSe<sub>2</sub> and SnSe nanostructures obtained by thermolysis of [tBu<sub>2</sub>Sn(2-Sepy(5-Me))<sub>2</sub>] in ODE and OLA, respectively showed hexagonal sheets (average thickness ~ 18 nm) and assembly of irregular sheets giving flower like appearance (average thickness ~ 12 nm) whereas the mixture of SnSe<sub>2</sub> (major part) and SnSe (minor part) obtained in OA revealed the formation of hexagonal and rectangular sheets, respectively (Fig. 4.9 a, d and g). The nanostructures synthesized from ODE:OLA (1:1 v/v) solvent mixture displayed smooth edged rectangular (Fig. 4.10 a, b and c) and irregular sheets while nanoflakes appeared in SEM images of nanostructures prepared in OA:OLA mixture (Fig. 4.10 d). The thickness of nanoflakes obtained in OA:OLA mixture is as small as 10 nm. This is attributed to the stronger binding ability of oleate group to the surface of nanostructures. The bright field

TEM images of the nanostructures obtained by the thermolysis of  $[\text{tBu}_2\text{Sn}(2\text{-Sepy}(5\text{-Me}))_2]$  in ODE and OLA revealed sheet like structure varying from hexagonal shape to irregular morphology (Fig.4.9 b and e). The interplanar distances of 2.94 and 2.96 Å (calculated from HRTEM images) for these samples correspond to (101) crystal plane of hexagonal  $\text{SnSe}_2$  (JCDPS file no. 23-0602) and (111) crystal plane of orthorhombic  $\text{SnSe}$  (JCPDS file no 48-1224) (Fig. 4.9 c and f).

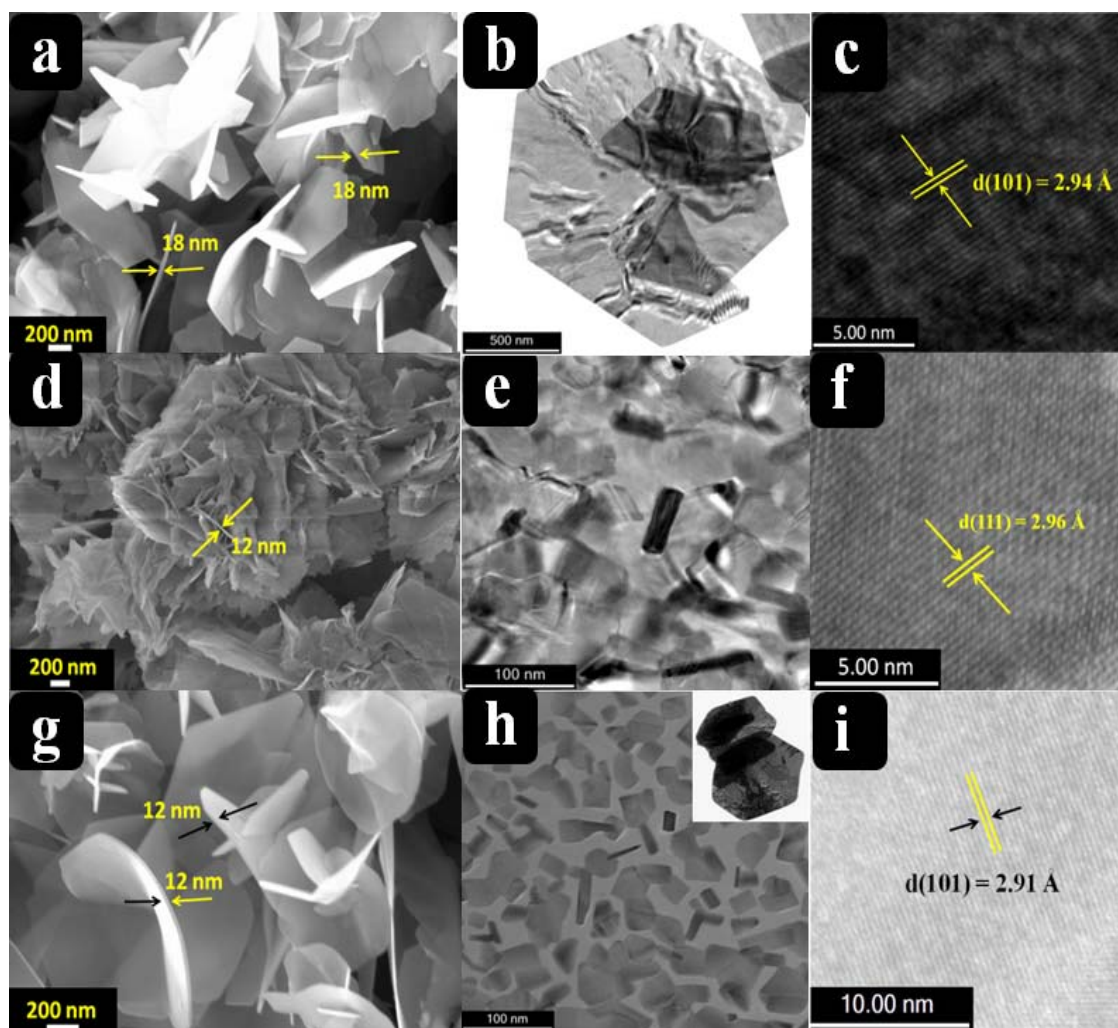


**Fig. 4.9** The SEM, TEM and HRTEM images of nanostructures obtained by thermolysis of  $[\text{tBu}_2\text{Sn}(2\text{-Sepy}(5\text{-Me}))_2]$  at  $220^\circ\text{C}$  for 10 minutes corresponds to (a, b, c) hexagonal  $\text{SnSe}_2$  in ODE, (d, e, f) orthorhombic  $\text{SnSe}$  in OLA (g, h, i) hexagonal  $\text{SnSe}_2$  contaminated with slight amount of orthorhombic  $\text{SnSe}$  in OA, respectively.

The TEM micrographs of nanostructures obtained using OA, however, showed a mixture of hexagonal and rectangular sheets which are consistent with SEM analysis (Fig. 4.9 h). The corresponding HRTEM images of hexagonal and rectangular sheets are depicted in (Fig. 4.9i and 4.10e) with lattice spacing of 2.91 and 2.98 Å indexed to (101) plane of SnSe<sub>2</sub> (JCDPS file no. 23-0602) and (111) plane of orthorhombic SnSe (JCPDS file no 48-1224).

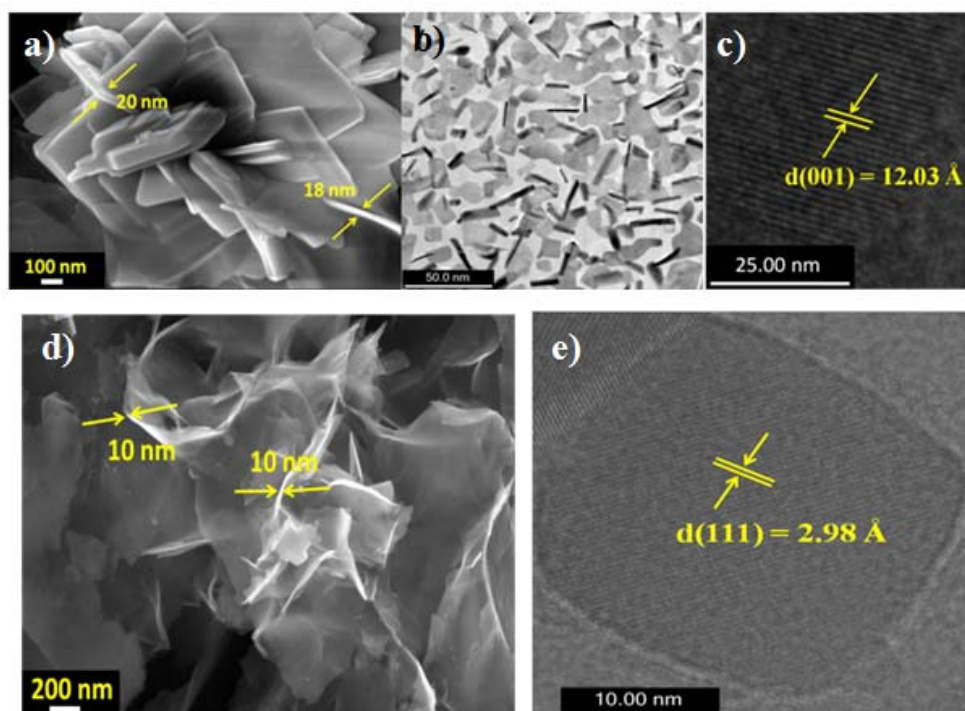


**Fig. 4.10** a), b), c) SEM, TEM and HRTEM of nanostructure obtained in (1:1) (v/v) mixture of ODE:OLA, d) SEM micrograph of nanostructure obtained in (1:1) (v/v) mixture of OLA:OA, e) HRTEM image of rectangular sheet obtained in OA from the thermolysis of [*t*Bu<sub>2</sub>Sn(2-Sepy(5-Me))<sub>2</sub>] at 220 °C for 10 minutes.

Thermolysis experiments of [R<sub>2</sub>Sn(2-SepymMe<sub>2</sub>)<sub>2</sub>] (R = Et, <sup>n</sup>Bu and <sup>t</sup>Bu) (100 mg each) in OLA (10 ml) for 2, 5 and 10 minutes, respectively at 210 °C gave black residue of tin selenides. The XRD profiles (Fig. 4.11) of the residues obtained by thermolysis for

2 minutes of  $[\text{Et}_2\text{Sn}(2\text{-SepymMe}_2)_2]$  and  $[\text{'Bu}_2\text{Sn}(2\text{-SepymMe}_2)_2]$  showed a set of reflections originating from (009), (104), (109), (1018), (0027), (0028), (111), (119), (1113), (0033), (209) (for thermolysis of  $[\text{Et}_2\text{Sn}(2\text{-SepymMe}_2)_2]$ ); (009), (109), (1018), (111), (119), (1113), (209) (for thermolysis of  $[\text{'Bu}_2\text{Sn}(2\text{-SepymMe}_2)_2]$ ) planes of hexagonal phase of  $\text{SnSe}_2$  (JCPDS File No. 40-1465) corroborated by elemental composition analysis by EDX [from  $[\text{Et}_2\text{Sn}(2\text{-SepymMe}_2)_2]$ : Sn:Se atom ratio is 31.6:68.4 or 1:2.2 and from  $[\text{'Bu}_2\text{Sn}(2\text{-SepymMe}_2)_2]$ : Sn:Se atom ratio is 30.9: 69.1 or 1:2.2]. Similar pattern [Brag reflections (009), (101), (108), (109), (1018), (1019), (0027), (1022), (110), (119), (209)] was observed for a product obtained from thermolysis of  $[\text{'Bu}_2\text{Sn}(2\text{-SepymMe}_2)_2]$  and was assigned for hexagonal  $\text{SnSe}_2$ . However, the XRD pattern displayed an additional peak at  $2\theta = 23.5^\circ$  which may be assigned to selenium impurity. The intensity of these Bragg reflections indicates their crystalline nature. The intensity of reflection from (009) plane indicates that structures has a preferential orientation in [001] direction. Such type of highly oriented 2D nanostructures is previously reported [197].

Similar Bragg's reflections with different lattice parameters (Table 4.8) were noted for the residues obtained from  $[\text{R}_2\text{Sn}(2\text{-SepymMe}_2)_2]$  ( $\text{R} = \text{Et}$ ,  $\text{'Bu}$  and  $\text{'Bu}$ ) by thermolysis carried out for 5 and 10 minutes (Fig. 4.12 and 4.13).

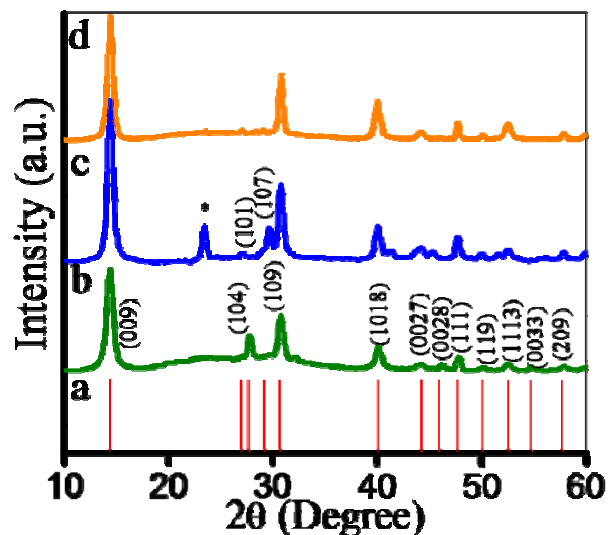


**Fig. 4.11** a) Simulated XRD pattern of hexagonal  $\text{SnSe}_2$  (JCPDS-40-1465). XRD profiles of  $\text{SnSe}_2$  nanosheets obtained by b) thermolysis of  $[\text{Et}_2\text{Sn}(2\text{-SepymMe}_2)_2]$ , c)  $[\text{nBu}_2\text{Sn}(2\text{-SepymMe}_2)_2]$  and d)  $[\text{nBu}_2\text{Sn}(2\text{-SepymMe}_2)_2]$  in OLA at 210 °C for 2 minutes (\* indicates the impurity peak of Se). Simulated pattern has been avoided for clarity.

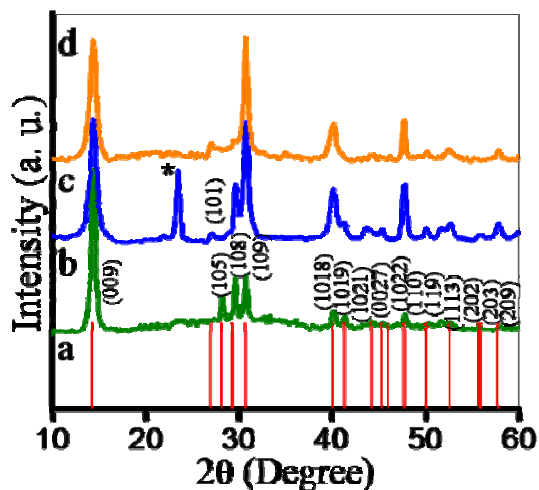


**Fig. 4.12** a) Simulated XRD pattern of hexagonal  $\text{SnSe}_2$  (JCPDS-40-1465). XRD profiles of  $\text{SnSe}_2$  nanosheets obtained by b) thermolysis of  $[\text{Et}_2\text{Sn}(2\text{-SepymMe}_2)_2]$ , c)  $[\text{nBu}_2\text{Sn}(2\text{-SepymMe}_2)_2]$  and d)  $[\text{nBu}_2\text{Sn}(2\text{-SepymMe}_2)_2]$  in OLA at 210 °C for 5 minutes (\* indicates the impurity peak of Se).

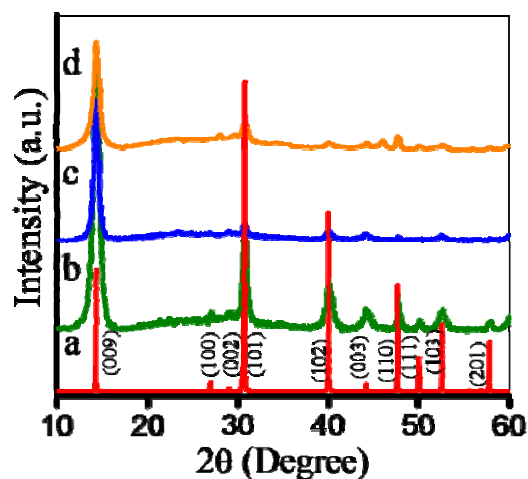


**Fig. 4.13** a) Simulated XRD pattern of hexagonal  $\text{SnSe}_2$  (JCPDS-23-0602). XRD profiles of  $\text{SnSe}_2$  nanosheets obtained by b) thermolysis  $[\text{Et}_2\text{Sn}(2\text{-SepymMe}_2)_2]$ , c)  $[\text{}^n\text{Bu}_2\text{Sn}(2\text{-SepymMe}_2)_2]$  and d)  $[\text{}^t\text{Bu}_2\text{Sn}(2\text{-SepymMe}_2)_2]$  in OLA at  $210^\circ\text{C}$  for 10 minutes.

SEM images (Fig. 4.14 and 4.15) of these residues revealed sheet like structures having smooth and rough edges. The residues obtained by thermolysis of  $[\text{Et}_2\text{Sn}(2\text{-SepymMe}_2)_2]$  displayed sheets which are uniformly distributed and have rough edges (Fig. 4.14a). The magnified image in the inset showed that the sheets have thickness in the range of 10-20 nm. SEM micrographs of the residues afforded by thermolysis of  $[\text{}^n\text{Bu}_2\text{Sn}(2\text{-SepymMe}_2)_2]$  and  $[\text{}^t\text{Bu}_2\text{Sn}(2\text{-SepymMe}_2)_2]$  revealed sharp edged sheets (Fig. 4.14b and c).

**Table 4.8** XRD data for tin selenide nanosheets obtained by the thermolysis of  $[R_2Sn(2\text{-SepymMe}_2)_2]$  ( $R = Et, {}^nBu$  and  ${}^tBu$ ).

S. No.	Complex	Duration of reaction in OLA	2 $\theta$	Corresponding plane	Lattice parameter	JCPDS File No.
1	$[Et_2Sn(2\text{-SepymMe}_2)_2]$	2	14.36, 27.81, 30.72, 39.97, 44.15, 45.98, 47.76, 50.01, 52.52, 54.72, 57.79	(009), (104), (109), (1018), (0027), (0028), (111), (119), (1113), (0033), (209)	3.811, 55.22(8)	40-1465
2		5	14.35, 28.18, 29.70, 30.73, 40.05, 41.33, 44.00, 47.84, 52.00, 55.74, 57.87	(009), (105), (108), (109), (1018), (1019), (1021), (110), (1112), (202), (209)	3.811, 55.21(40)	40-1465
3		10	14.35, 27.07, 29.08, 30.70, 40.09, 44.12, 47.76, 50.08, 52.60, 57.86	(001), (100), (002), (101), (102), (003), (110), (111), (103), (201)	3.810, 6.141(7)	23-0602
4	$[{}^nBu_2Sn(2\text{-SepymMe}_2)_2]$	2	14.47, 27.05, 29.73, 30.73, 40.20, 41.30, 44.16, 45.29, 47.69, 49.94, 57.86	(009), (101), (108), (109), (1018), (1019), (0027), (1022), (110), (119), (209)	3.811, 54.99(31)	40-1465
5		5	14.47, 27.05, 29.7, 30.73, 40.05, 41.18, 43.70, 45.29, 47.69, 52.49, 55.89, 57.87	(009), (101), (108), (109), (1018), (1019), (1021), (1022), (110), (1113), (203), (209)	3.811, 55.15(32)	40-1465
6		10	14.35, 29.00, 30.70, 40.09, 44.12, 47.66, 52.60	(001), (002), (101), (102), (003), (110), (103)	3810, 6.147(6).	23-0602
7	$[{}^tBu_2Sn(2\text{-SepymMe}_2)_2]$	2	14.46, 30.80, 40.14, 47.77, 50.06, 52.61, 57.82	(009), (109), (1018), (111), (119), (1113), (209)	3.811, 55.24(17)	40-1465
8		5	14.36, 27.08, 30.72, 40.17, 44.35, 47.79, 50.16, 52.52, 57.78	(009), (101), (109), (1018), (0027), (110), (119), (1113), (209)	3.811, 55.19(16)	40-1465
9		10	14.35, 30.7, 40.09, 44.3, 47.7, 50.08, 52.60, 57.86	(001), (101), (102), (003), (110), (111), (103), (201)	3811, 6.146(6)	23-0602



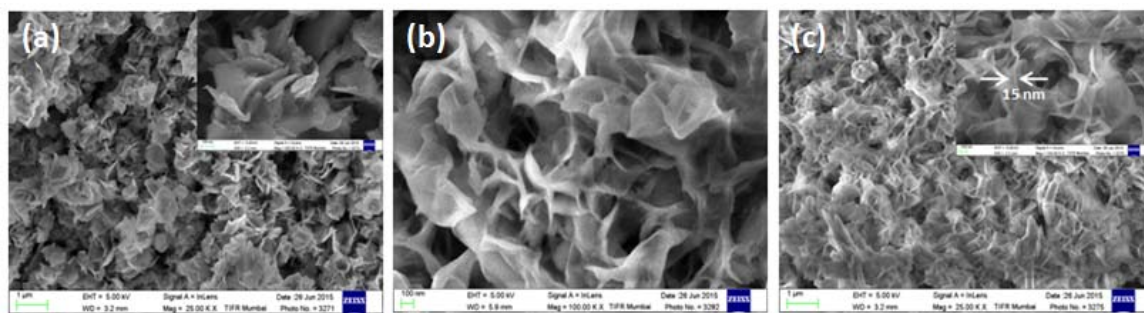


**Fig. 4.14** SEM images of  $\text{SnSe}_2$  nanosheets obtained by a) thermolysis of  $[\text{Et}_2\text{Sn}(2\text{-SepymMe}_2)_2]$ , c)  $[\text{nBu}_2\text{Sn}(2\text{-SepymMe}_2)_2]$  and d)  $[\text{tBu}_2\text{Sn}(2\text{-SepymMe}_2)_2]$  in OLA at  $210^\circ\text{C}$  for 2 minutes (Inset show magnified images of the same).

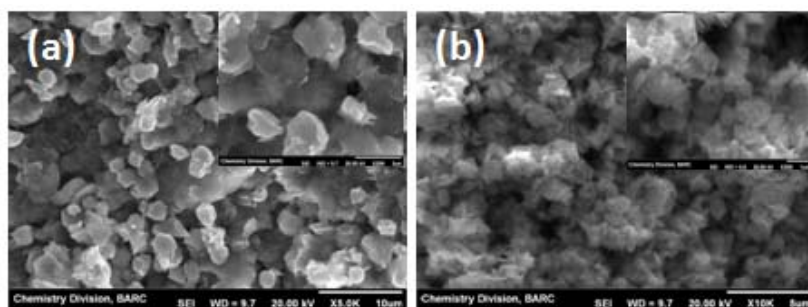


**Fig. 4.15.** SEM images of  $\text{SnSe}_2$  nanosheets obtained by a) thermolysis of  $[\text{Et}_2\text{Sn}(2\text{-SepymMe}_2)_2]$ , b)  $[\text{tBu}_2\text{Sn}(2\text{-SepymMe}_2)_2]$  in OLA at  $210^\circ\text{C}$  for 10 minutes (Inset show magnified images of the same).

Transmission electron microscopy has been used to find the morphology and phase of the residues. TEM image of the residue obtained by thermolysis of  $[\text{Et}_2\text{Sn}(2\text{-SepymMe}_2)_2]$  showed needle like structures (Fig. 4.16a) which are rolled forms of the sheets. The rolling of sheets happens due to the use of solvent during the preparation of TEM samples because of surface tension. The corresponding SAED pattern (Fig. 4.16b) exhibit set of lattice planes, (0010), (1021) and (1031) related to hexagonal phase of  $\text{SnSe}_2$  (JCPDS File No. 40-1465). The spot like pattern indicate single crystalline nature

of the rolled sheets. TEM image of the residue obtained by thermolysis of [ $t\text{Bu}_2\text{Sn}(2\text{-SepymMe}_2)_2$ ] revealed sheets like structures having the boundaries in sub micron range (other than thickness of sheets) and sharp needle like structures which are formed due to the rolling of the nano-sheets (Inset of Fig. 4.16c).

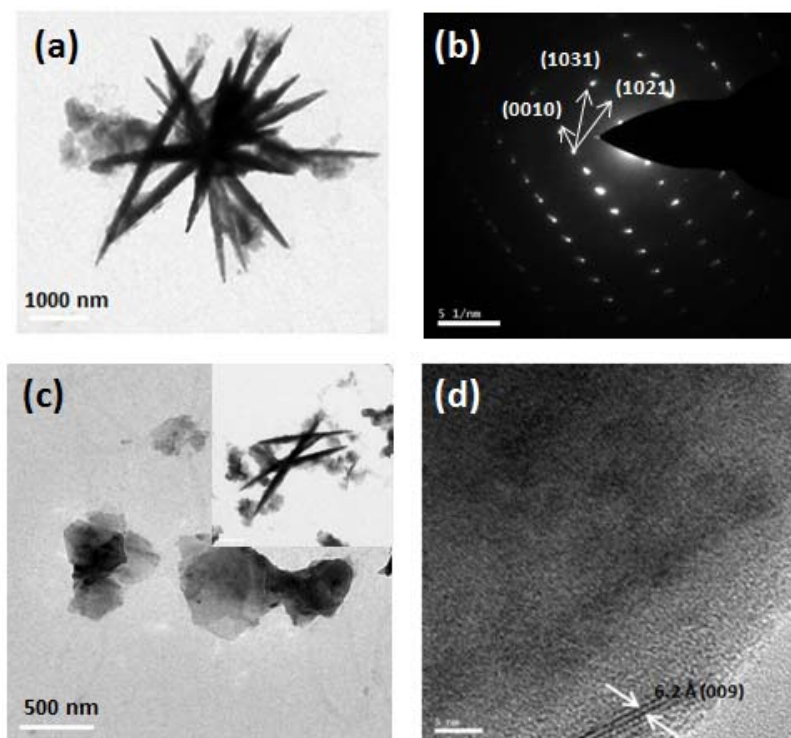


**Fig. 4.16** a) TEM image and b) SAED pattern of  $\text{SnSe}_2$  nanosheets obtained by thermolysis of  $[\text{Et}_2\text{Sn}(2\text{-SepymMe}_2)_2]$  in OLA at  $210^\circ\text{C}$  for 2 minutes while c) and d) are TEM and HR-TEM image of  $\text{SnSe}_2$  nanosheets obtained by thermolysis of  $[t\text{Bu}_2\text{Sn}(2\text{-SepymMe}_2)_2]$  in OLA at  $210^\circ\text{C}$  for 2 minutes (Inset show needle like structures formed by rolling of nanosheets).

Individual nanosheets were also observed in addition to the rolled sheets. HRTEM image of the sheets showed lattice plane with interplanar distance of  $6.20 \text{ \AA}$  corresponding to (009) plane of hexagonal phase of  $\text{SnSe}_2$  (JCPDS File No. 40-1465) (Fig. 4.16d).

### 4.3.5 Preparation and characterization of tin selenide thin films

One of the complexes, [ $t\text{Bu}_2\text{Sn}(2\text{-SepymMe}_2)_2$ ] was employed for deposition of  $\text{SnSe}_2$  thin film as  $t\text{Bu}$  is a good leaving group. Black tin selenide thin films were deposited on p-type silicon (110) substrate using toluene solution of [ $t\text{Bu}_2\text{Sn}(2\text{-SepymMe}_2)_2$ ] at  $375^\circ\text{C}$  for 1 h. There was no deposition below  $375^\circ\text{C}$  while very poor coverage at  $400^\circ\text{C}$  and above. XRD pattern of as prepared thin films (Fig. 4.17a) deposited at  $375^\circ\text{C}$  for 1 h showed peaks at  $2\theta = 25.8, 30.7, 33.9, 37.9, 41.2, 43.4, 47.7, 49.7, 51.8, 54.3$  and  $57.8^\circ$  which may be assigned to the reflections from (0016), (109), (0021), (1016), (1019), (1021), (111), (1025), (1112), (1115) and (209) planes of hexagonal phase of  $\text{SnSe}_2$  (JCPDS File No. 40-1465). This film annealed at  $375^\circ\text{C}$  for 1 h showed XRD reflections (Fig. 4.17b) from (009), (100), (109), (0021), (1016), (1021), (110), (1112), (0033) and (2010) planes of hexagonal  $\text{SnSe}_2$  (JCPDS File No. 40-1465). The composition is further confirmed by EDX analysis (for as prepared thin film: Sn:Se atom ratio is 36.9:63.1 or 1:1.7; for annealed prepared thin film: Sn:Se atom ratio is 38.4:61.6 or 1:1.6). The lattice parameters for as prepared and annealed thin films are  $a = 3.811(0)$ ,  $c = 55.36(36) \text{ \AA}$  (as prepared thin films) and  $a = 3.811(0)$ ,  $c = 55.05(3) \text{ \AA}$  (annealed thin films), respectively which are in accord with the hexagonal  $\text{SnSe}_2$  (JCPDS-40-1465). SEM micrographs (Fig. 4.17c) of as prepared thin films revealed irregular morphology. However, the annealed thin films revealed hierarchical flower like structures with an average size of  $\sim 15 \mu\text{m}$  (Fig. 4.17d).

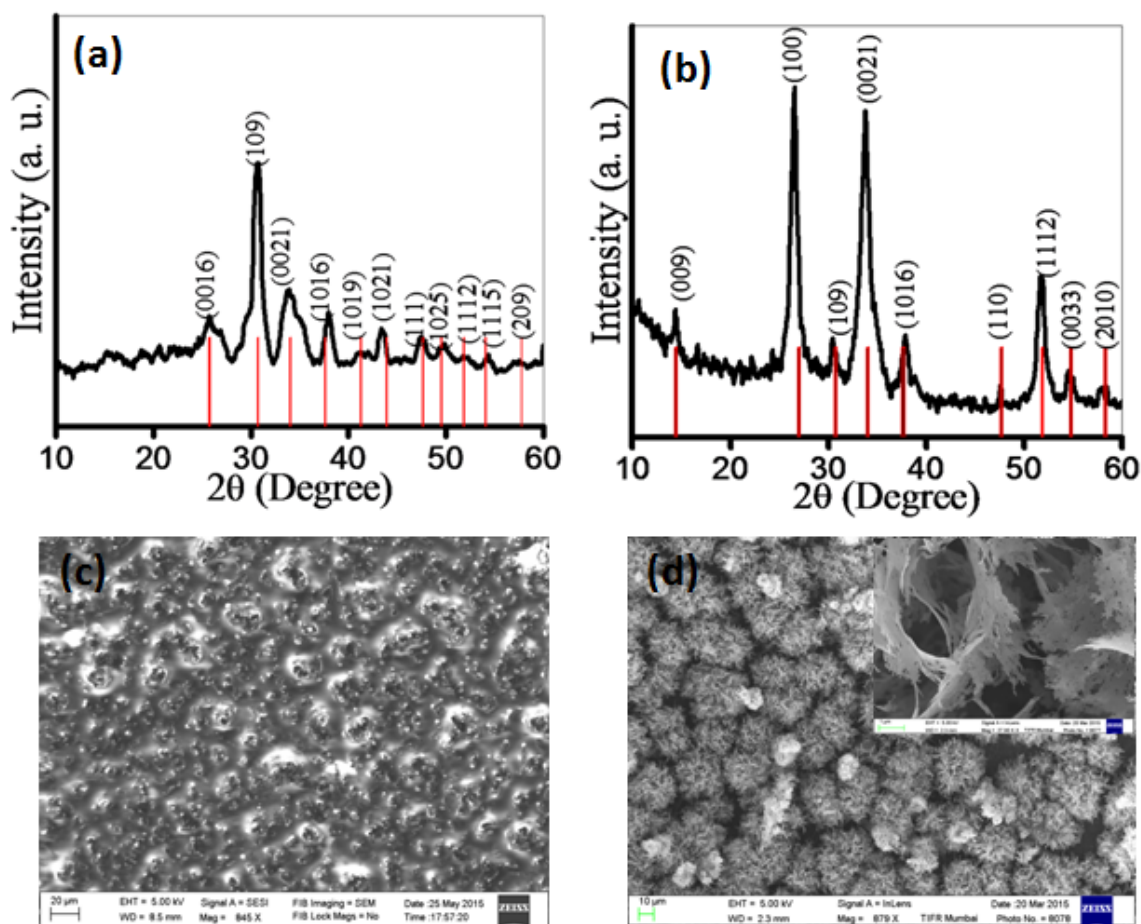


**Fig. 4.17** XRD profile and SEM images a) as prepared  $\text{SnSe}_2$  thin films obtained by AACVD of  $[\text{tBu}_2\text{Sn}(2\text{-SepymMe}_2)_2]$  on silicon substrate at  $375^\circ\text{C}$  for 1 h and b) annealed thin film of as prepared thin film at  $375^\circ\text{C}$  for 1 h.

#### 4.3.6 Optical properties

Considering the importance of  $\text{SnSe}$  and  $\text{SnSe}_2$  as narrow band gap materials, their optical properties were investigated by diffuse reflectance spectroscopy (DRS). The optical band gaps of these materials were determined by using a plot of Kubelka-Munk function,  $F(R)$  as given in equation 1.1.

The direct band gap was calculated using the Tauc's model (for  $n = 2$ ) and the indirect band gap can be calculated using Davis–Mott model (for  $n = 1/2$ ).

The direct band gaps of SnSe<sub>2</sub> hexagonal sheets (obtained in ODE) and SnSe assembly of irregular sheets (obtained in OLA) prepared from the thermolysis of [<sup>t</sup>Bu<sub>2</sub>Sn(2-Sepy(5-Me))<sub>2</sub>] were found to be 1.8 and 2.0 eV (Fig. 4.18).

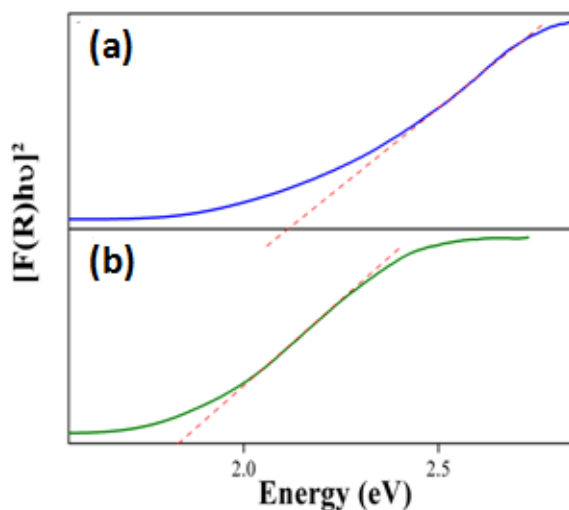


**Fig. 4.18** Plots of  $[F(R)h\nu]^2$  vs energy generated by Kubelka-Munk transformation of solid-state diffuse reflectance data of a) orthorhombic SnSe b) hexagonal SnSe<sub>2</sub> nanostructures obtained by thermolysis of [<sup>t</sup>Bu<sub>2</sub>Sn(2-Sepy(5-Me))<sub>2</sub>] at 220 °C for 10 minutes in OLA and ODE, respectively for determining direct band gap energies.

While the direct band gaps of the nanosheets obtained by thermolysis of [Et<sub>2</sub>Sn(2-SepymMe<sub>2</sub>)<sub>2</sub>] and [<sup>t</sup>Bu<sub>2</sub>Sn(2-SepymMe<sub>2</sub>)<sub>2</sub>] in OLA at 210 °C for 2, 5 and 10 minutes showed a gradual decrease from 2.22 to 1.82 (Fig. 4.19a) 2.30 to 1.76 (Fig. 4.19b), respectively, with the increase in reaction time. These values are blue shifted with respect to bulk SnSe<sub>2</sub> ( $E_g = 1.62$  eV) and [218] SnSe ( $E_g = 1.3$  eV) [23]. This increase in the band gap value of the nanostructures may be either due to quantum confinement or lattice distortion or surface lattice defects [188]. Since the thickness of the sheets obtained by thermolysis of [Et<sub>2</sub>Sn(2-SepymMe<sub>2</sub>)<sub>2</sub>] and [<sup>t</sup>Bu<sub>2</sub>Sn(2-SepymMe<sub>2</sub>)<sub>2</sub>] in OLA for 2

minutes are in the range of 10-20 nm and there is systematic increase of band gap with decreasing thickness of sheets, quantum confinement may not be ruled out.

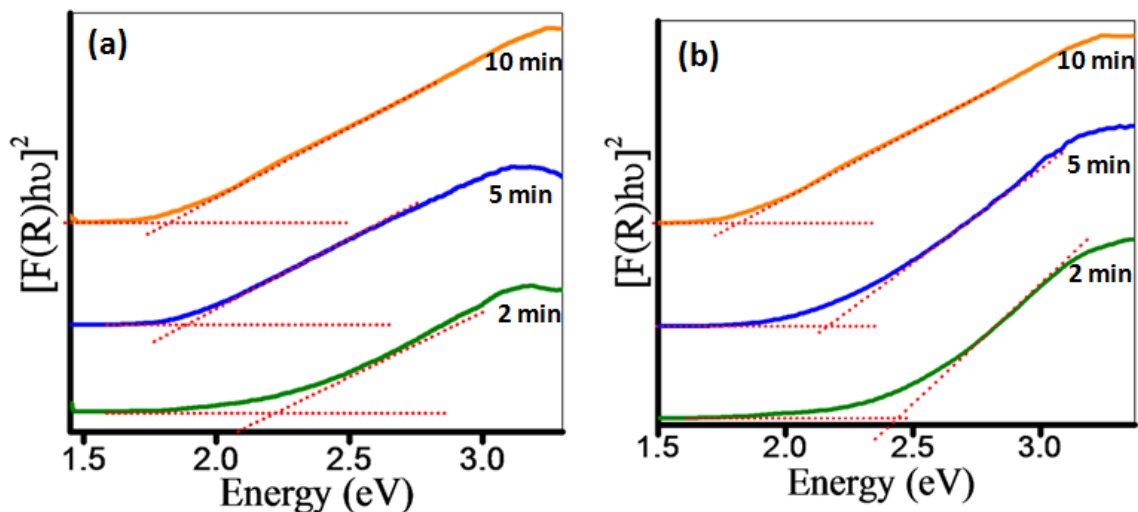


**Fig. 4.19** Plots of  $[F(R)hv]^2$  vs energy generated by Kubelka-Munk transformation of solid-state diffuse reflectance data of  $\text{SnSe}_2$  nano-sheets obtained by thermolysis of a)  $[\text{Et}_2\text{Sn}(2\text{-SepymMe}_2)_2]$  and b)  $[\text{tBu}_2\text{Sn}(2\text{-SepymMe}_2)_2]$  in OLA at 210 °C for 2, 5 and 10 minutes, respectively for determining direct band gap energies.

Direct band gap between 0.9 to 2.04 eV for  $\text{SnSe}_2$  has been reported in literature. For instance, Nanda and co-workers [61] observed that the band gap values for  $\text{SnSe}_2$  thin films depends upon their thickness which vary from 2.04 to 1.2 eV for a film thickness of 50 and 1200 nm, respectively. Pejova and Grozdanov [219] and Franzman et al. [220] demonstrated the effects of quantum confinement in  $\text{SnSe}$  by studying the optical properties of  $\text{SnSe}$  nanocrystals of average grain size of 14.8-20 nm. The nanocrystals possessed direct band gaps range of  $E_g = 1.70\text{-}1.75$  eV, respectively, which are both blue shifted from the band gaps of the bulk material. In the present investigation, direct band

gap values of phase pure SnSe<sub>2</sub> and SnSe, can be justified for the nanostructures having thickness in the range of 10 to 20 nm.

Similarly, the direct band gap values for as-deposited SnSe<sub>2</sub> thin films obtained by AACVD of [<sup>t</sup>Bu<sub>2</sub>Sn(2-SepymMe<sub>2</sub>)<sub>2</sub>] on silicon substrate at 375 °C for 1 h and annealed thin films are 2.12 and 2.06 eV (direct band gap) (Fig. 4.20), respectively. The decrease in the band gaps for annealed thin films compared to as-deposited thin films may be accounted for thermal expansion of the lattice and temperature dependent electron-phonon interactions [221].

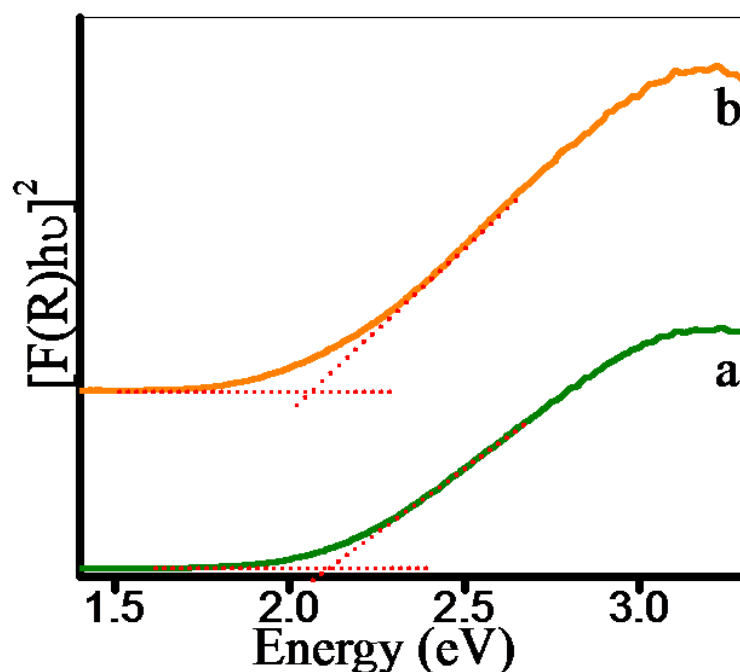


**Fig. 4.20** Plots of  $[F(R)hv]^2$  vs energy generated by Kubelka-Munk transformation of solid-state diffuse reflectance data of a) as-deposited SnSe<sub>2</sub> thin films obtained by AACVD of [<sup>t</sup>Bu<sub>2</sub>Sn(2-SepymMe<sub>2</sub>)<sub>2</sub>] on silicon substrate at 375 °C for 1 h and b) annealed thin films to determine direct band gap energies.

Similar trend in band gap values has been observed for the annealed thin films with respect to readily deposited thin films in the literature [222,223]. Although the deposition

and annealed temperatures are same, the total residence time in the furnace is different. As-deposited thin films are placed in furnace for 1 h during deposition while annealed thin films are obtained after heating the as-deposited thin films at 375°C for additional one hour after their deposition.

#### 4.3.7 Photo response measurements of Si/SnSe<sub>2</sub> based photoelectrochemical cell

Photo-response behaviour of SnSe and SnSe<sub>2</sub> obtained from the thermolysis of [t-Bu<sub>2</sub>Sn(2-Sepy(5-Me))<sub>2</sub>] in OLA and ODE were assessed by constructing a photo-electrochemical cell.

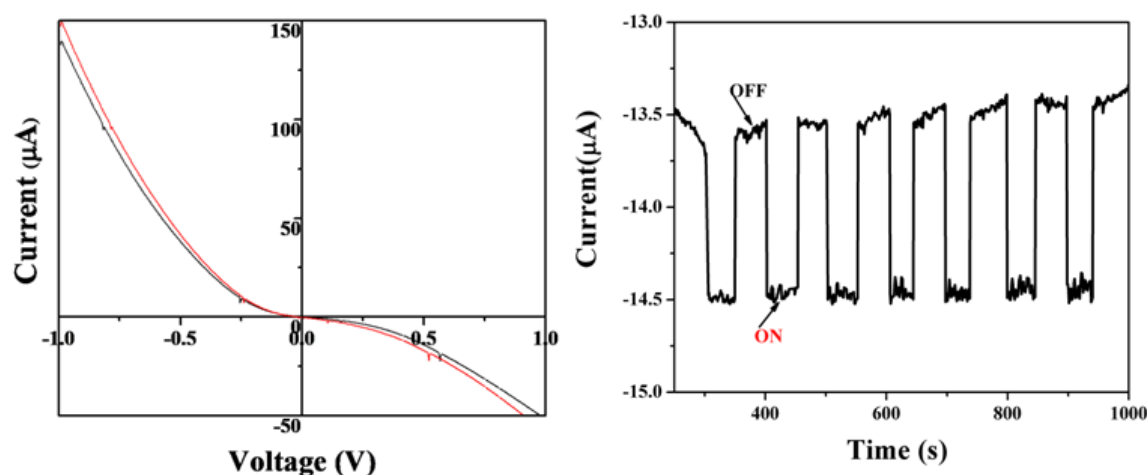


**Fig. 4.21** a) *I-V* characteristics of SnSe<sub>2</sub> nanostructures under dark (black) and light (red) conditions, b) Current vs. time plot of hexagonal SnSe<sub>2</sub> nanostructures under light intensity of 200  $\mu\text{W}/\text{cm}^2$  and bias voltage of 0.5 V.

The photocurrent increased when light was shined on Si/SnSe<sub>2</sub> working electrode relative to that of dark current due to the photo generated carriers. Nonlinear I-V characteristics (Fig. 4.21a) showed the junction properties with increase in the current due to the photoconductivity of the particles. The photo response as a function of time (Fig. 4.21b) was measured under light intensity of 200  $\mu\text{W}/\text{cm}^2$  with bias voltage of 0.5 V for



nanoparticles. The consistent switching characteristics during repeated cycles of on-off experiments demonstrate the photosensitivity of the nanostructure. The reproducibility of current suggests high stability of nanostructures under alternating light and dark conditions. The result indicates the potential application of hexagonal SnSe<sub>2</sub> in photo detector and photovoltaic applications. It is worth mentioning that no such switching characteristics were observed in case of orthorhombic SnSe under same set of conditions.

# Chapter 5

## Accessing ternary tin chalcogenide nanostructures from molecular precursors

### Summary

Synthesis of air stable tin(IV) and copper(I) complexes of 2-pyrazinylthiol (2-HSpyz), ( $[\text{tBu}_2\text{Sn}(\text{Spyz})_2]$  and  $[\text{Cu}(\text{Spyz})(\text{PPh}_3)_2]$ ) and bis(3-methyl-2-pyridylselenide) (2-Sepy(3-Me))<sub>2</sub> ( $[\text{Me}_2\text{Sn}(2\text{-Sepy}(3\text{-Me}))_2]$  and  $[\text{Cu}(2\text{-Sepy}(3\text{-Me}))_4]$ ), as molecular precursors for metal sulfide and metal selenide nanomaterials is described. The precursors for metal sulfide were isolated by the reactions of  $[\text{tBu}_2\text{SnCl}_2]$  and  $[\text{CuCl}(\text{PPh}_3)_3]$  with sodium 2-pyrazinylthiolate in methanol at room temperature, while the reactions of 3-methyl-2-pyridylselenolate with  $[\text{Me}_2\text{SnCl}_2]$  and CuCl afforded precursors for metal selenide nanostructures. The molecular structures of these complexes have been established by SCXRD and hetero nuclei NMR spectroscopy. TG analysis revealed that these complexes ( $[\text{tBu}_2\text{Sn}(\text{Spyz})_2]$  and  $[\text{Cu}(\text{Spyz})(\text{PPh}_3)_2]$ ), ( $[\text{Me}_2\text{Sn}(2\text{-Sepy}(3\text{-Me}))_2]$  and  $[\text{Cu}(2\text{-Sepy}(3\text{-Me}))_4]$ ) exhibit closely related decomposition temperatures. Utility of these complexes as molecular precursors for the preparation of binary (SnS/SnSe<sub>2</sub> and Cu<sub>1.8</sub>S/Cu<sub>2</sub>Se) and ternary  $[\text{Cu}_2\text{SnS}_3]$  (CTS) and  $[\text{Cu}_2\text{SnSe}_3]$  (CTSe) metal sulfide and selenide nanostructures has been assessed. The phase purity, morphology, composition and band gap of nanostructures were investigated by p-XRD, Raman, SEM, TEM, EDX and DRS analysis. It has been demonstrated that role of solvent is highly crucial for the phase purity of CTS nanostructures while reaction temperature has pronounced effect over the composition of CTSe nanostructures. The Photo-electrochemical studies revealed that ternary nanostructures pose as better photo responsive material as compared to binary one.

## 5.1 Introduction

Ever increasing environmental and energy concerns have led to an insatiable quest for non-toxic and earth abundant materials for solar cell applications [224]. In this context various copper based ternary  $\text{CuInSe}_2$  and quaternary  $\text{Cu(In,Ga)Se}_2$ ,  $\text{Cu}_2\text{ZnSnS}_4$  (CZTS) and  $\text{Cu}_2\text{ZnSnSe}_4$  (CZTSe) chalcogenides have been intensively explored as absorbing material for photovoltaic devices [225,226]. However, scarcity of gallium and indium and structural complexities associated with quaternary CZTS, may limit their use for practical applications [115,216]. Recently, ternary materials, such as  $\text{Cu}_2\text{SnS}_3$  (CTS) and  $\text{Cu}_2\text{SnSe}_3$  (CTSe), in their nano regime have attracted considerable attention due to solution processability and low cost. They are also projected as substitute for the technologically well-established solar cell materials which are based either on scarce (In,Te) or toxic (Cd, Pb) elements [115,116].

Dicopper tin trichalcogenides (CTS and CTSe), a p-type semiconductor, have structure isomorphous to  $\text{Cu}_2\text{SiS}_3$ , where S/Se anions are tetrahedrally bonded by four cations (Cu or Sn) [227]. Depending upon the distribution of these cations, different structural polymorphs viz. cubic, tetragonal, monoclinic, triclinic and wurtzite have been isolated [111]. The wurtzite polymorph which is a metastable phase has been isolated by wet chemical methods [120]. Dicopper tin trichalcogenides stands out for its high absorption coefficient ( $> 10^4 \text{ cm}^{-1}$ ), tunable band gap varying between 0.9-1.7 eV which covers the optimal solar spectrum [122], reasonably good electrical properties and composed of earth abundant elements making it cost effective [124,125]. While the fascinating properties of CTS and CTSe have garnered enormous attention as absorber material in solar cell application, it has also been utilised in other fields of great significance such as electrode material for Li-ion battery [228], infrared photodetection [128], thermoelectrics [129], supercapacitors [131], photocatalysis and gas sensing [132].

Recently the CTS nanoparticles were tested against Gram positive and Gram negative bacteria strains and found to possess excellent anti bacterial activity against both the strains [229].

CTS and CTSe nanostructures have previously been synthesized *via* chemical route such as hydrothermal [230], microwave [231,232], solvothermal [128,232,233] and hot injection method [120,229,234]. These synthesis routes mostly employ suitable sulphur source such as sulphur powder [229], thiourea, thioacetamide [230], 1-dodecanethiol [233], 1-octadecene/oleic acid – sulphur precursor [235] and metal halides or acetate.

However, synthesis of ternary or quaternary materials is generally encountered with problem of presence of binary impurities [216,132]. Moreover, the disadvantage with hydrothermal/ solvothermal is also evident, as relatively long duration is required to raise the temperature of solution in the autoclave to a preset value, during which the reaction has already taken place. This leads to difficulty in separating the nucleation stage from crystal growth step. Hence, final nanoparticles of uniform shape and size are not expected [236].

Molecular precursor route has remarkable potential to be used in the synthesis of ternary and quaternary compound due to some unique advantages associated with them in terms of lower defect concentration, phase purity, narrow size distribution and better control over the composition of complex material. There is hardly any report in the literature dealing with the preparation of CTS and CTSe materials from molecular precursors.

Successful accomplishment of the synthesis of binary tin chalcogenides through molecular precursors, prompted us to extend the strategy for the preparation of technologically important ternary tin chalcogenides (CTS and CTSe) as well. Accordingly, we have investigated the chemistry of tin and copper complexes with 2-

pyrazinylthiolate and 3-methyl-2-pyridylselenolate ligands. The results of the investigation are described herein.

## **5.2 Experimental**

### **5.2.1 General Consideration**

Materials and techniques used during the investigation were discussed in Chapter 2.

### **5.2.2 Synthesis of 2-pyrazinylthiol (2-HSpyz)**

The ligand was prepared according to reported method [237]. In a typical synthesis, sodium sulfide (250 mg) was added to dimethyl formamide (DMF) solution of 2-chloropyrazine (500 mg). The reaction mixture was refluxed for 6 hours, and the solvent was removed under vacuum. The resulting residue was dissolved in water, and then acidification with acetic acid gave a yellow precipitate which was extracted with 1N NaOH solution. Subsequently, insoluble material was removed and acidification of the filtrate gave 2-mercaptopyrazine [yield 422 mg, 84%; m.p.: 216 °C (decomp.); Anal Calcd. for  $C_4H_4N_2S$ : C, 42.83; H, 3.59; N, 24.97; Found: C, 42.97; H, 3.51; N, 24.83;  $^1H$  NMR (300 MHz,  $CDCl_3$ ) $\delta_H$ : 8.88 (d, 1H), 8.63 (dd, 1H), 8.42 (d, 1H)].

### **5.2.3 Bis(3-methyl-2-pyridyl)diselenide [(2-Sepy(3-Me))<sub>2</sub>]**

Freshly grinded elemental selenium (7.98 g, 101.1 mmol) was taken in 100 ml water, to which  $NaBH_4$  (3.82 g, 101.1 mmol) was slowly added with vigorous stirring. The solution was stirred for 1.5 hrs. A blood red color solution was obtained indicating the formation of  $Na_2Se_2$ . Subsequently, 2-bromo-3-methyl pyridine (17.2 g, 100 mmol) was added drop wise and the resultant reaction mixture was refluxed, till solution becomes yellow in color. The compound was then extracted with dichloromethane and the organic layer was dried over anhydrous sodium sulfate. The solvent was removed under vacuum to give a yellow residue. The yellow aqueous layer was left for 2-3 days to obtain yellow crystalline product at the bottom of beaker which was filtered and washed

with distilled water and dried under vacuum for few hours. The crude diselenide was purified by silica gel column chromatography and was recrystallized by slow evaporation from dichloromethane solution as a yellow needle shaped crystalline solid (yield 10.5 g, 62%), m.p. 142 °C.  $^1\text{H}$  NMR (300 MHz,  $\text{CDCl}_3$ )  $\delta$ : 2.46 (s, Me), 7.01 (d, 4.5 Hz; H-5), 7.32 (d, 7.5 Hz; H-4), 8.28 (d, 4.5 Hz; H-6) (each s, ring protons).  $^{13}\text{C}\{^1\text{H}\}$  NMR ( $\text{CDCl}_3$ )  $\delta$ : 21.1 (s, Me), 122.5 (CH-4), 134.3 (s), 137.0 (s, CH-5), 148.0 (s, CH-6).  $^{77}\text{Se}\{^1\text{H}\}$  NMR ( $\text{CDCl}_3$ )  $\delta$ : 436 ppm.

#### 5.2.4 Synthesis of [ $^t\text{Bu}_2\text{Sn}(\text{Spyz})_2$ ]

To a methanolic solution (20 ml) of sodium 2-pyrazinylthiolate, obtained from 2-mercaptopyrazine (200 mg, 1.78 mmol) in methanol and sodium methoxide (0.2 M, 9 ml), solid  $^t\text{Bu}_2\text{SnCl}_2$  (270 mg, 0.89 mmol) was added with stirring which continued for 2 hours at room temperature until a turbid solution appeared. The contents were filtered through a G-3 filtering unit and the filtrate on slow evaporation afforded pale yellow crystals of the title complex (yield: 298 mg, 74 %), mp 120 °C. Anal. Calcd for  $\text{C}_{16}\text{H}_{24}\text{N}_4\text{S}_2\text{Sn}$ : C, 42.21; H, 5.31; N, 12.3 %. Found: C, 42.08; H, 5.22; N, 12.11%.  $^1\text{H}$  NMR (300 MHz,  $\text{CDCl}_3$ )  $\delta_{\text{H}}$ : 1.35 (s,  $^t\text{Bu}_2\text{Sn}$ , 18H,  $^3\text{J}(^{119}\text{Sn}-^1\text{H}) = 110$  Hz;  $^3\text{J}(^{117}\text{Sn}-^1\text{H}) = 105$  Hz); 8.12 (dd, CH-5, 2H, 3.1 Hz); 8.2 (d, CH-5, 2H, 2.7 Hz); 8.58 (d, CH-3, 2H,  $^4\text{J} = 1.5$  Hz);  $^{119}\text{Sn}\{^1\text{H}\}$  NMR (111.92 MHz,  $\text{CDCl}_3$ )  $\delta_{\text{Sn}}$ : -18.4 ppm.

#### 5.2.5 Synthesis of [ $\text{Cu}(\text{Spyz})(\text{PPh}_3)_2$ ]

To a methanolic solution of sodium 2-pyrazinylthiolate (obtained by adding NaOH (aq, 80 mg, 2 mmol) to 2-mercaptopyrazine (225 mg, 2 mmol) in 15 mL methanol) [ $\text{CuCl}(\text{PPh}_3)_3$ ] (1.77 g, 2 mmol) dispersed in 15 ml acetonitrile was added with stirring which continued for 2 h at room temperature. Block-shaped orange single crystals were obtained after a few days upon slowly evaporating orange solution. Yield: 1.07 g (76.5%), mp 102 °C. Anal. Calcd for  $\text{C}_{40}\text{H}_{33}\text{CuN}_2\text{P}_2\text{S}$ : C, 68.70; H, 4.75; N, 4.00; S, 4.58

%. Found: C, 69.06; H, 4.98; N, 3.93; S, 3.6%.  $^1\text{H}$  NMR (300 MHz,  $\text{CDCl}_3$ ):  $\delta_{\text{H}} = 8.46$  (s, 1H), 7.73 (d, 1H, 2.4 Hz), 7.43 (d, 1H, 2.4 Hz), 7.35 – 7.21 (m, 30H,  $\text{PPh}_3$ ).  $^{31}\text{P}\{^1\text{H}\}$  NMR (121.49 MHz,  $\text{CDCl}_3$ ):  $\delta_{\text{P}} = -2.9$  ppm (Cu- $\text{PPh}_3$ ).

#### 5.2.6 Synthesis of $[\text{Me}_2\text{Sn}(2\text{-Sepy}(3\text{-Me}))_2]$

The complex was prepared according to reported method [149]. Solid  $\text{Me}_2\text{SnCl}_2$  (400 mg, 1.82 mmol) was added to a freshly prepared solution of  $[\text{Na}(2\text{-Sepy}(3\text{-Me}))]$  [from toluene solution of  $(2\text{-Sepy}(3\text{-Me}))_2$  (579 mg, 1.82 mmol) and  $\text{NaBH}_4$  (147 mg, 3.90 mmol) in methanol], with vigorous stirring. Stirring of the reaction mixture was continued for 3 h at room temperature and the solvents were evaporated under vacuum. The resultant residue was washed thoroughly with hexane:ether (1:1, v/v) mixture to remove excess ligand and the pure product was extracted with chloroform, which upon slow evaporation afforded colorless crystals of the title complex. (yield: 610 mg, 72%), mp 182 °C. Anal. Calcd for  $\text{C}_{14}\text{H}_{18}\text{N}_2\text{Se}_2\text{Sn}$ : C, 34.25; H, 3.70; N, 5.71%. Found: C, 34.29; H, 3.81; N, 5.68%. NMR (300 MHz,  $\text{CDCl}_3$ )  $\delta_{\text{H}}$ : 1.09 (s,  $\text{Me}_2\text{Sn}$ , 6 H,  $^2\text{J}(\text{Sn-H}) = 72$  Hz); 2.34 (s,  $\text{C}_5\text{H}_3(3\text{-Me})\text{N}$ , 6 H); 6.91 (d,d, CH-5, 2 H, 7.5, 4.8 Hz); 7.33 (d, CH-4, 2 H, 7.2 Hz); 7.94 (d, CH-6, 2 H, 4.5 Hz).  $^{13}\text{C}\{^1\text{H}\}$  NMR ( $\text{CDCl}_3$ )  $\delta$ : 6.3 ( $\text{Me}_2\text{Sn}$ ,  $^1\text{J}(\text{Sn-C}) = 562$  Hz), 22.1 ( $\text{C}_5\text{H}_3(3\text{-Me})\text{N}$ ), 118.9 (C-4), 135.1 (C-3), 136.3 (C-5), 144.4 (C-6), 158.8 (C-Se).  $^{77}\text{Se}\{^1\text{H}\}$  NMR ( $\text{CDCl}_3$ )  $\delta$ : 196 ( $^1\text{J}(\text{Sn-Se}) = 616$  Hz).  $^{119}\text{Sn}\{^1\text{H}\}$  NMR ( $\text{CDCl}_3$ )  $\delta$ : -184 ( $^1\text{J}(\text{Sn-Se}) = 618$  Hz).

#### 5.2.7 Synthesis of $[\text{Cu}(\text{sepy}(3\text{-Me}))_4]$

The complex was prepared according to reported method [175]. Solid  $\text{CuCl}$  (300 mg, 3.08 mmol) to a freshly prepared  $[\text{Na}(2\text{-Sepy}(3\text{-Me}))]$  [from toluene-methanol solution of  $(2\text{-Sepy}(3\text{-Me}))_2$  (519 mg, 1.5 mmol) and  $\text{NaBH}_4$  (123 mg, 3.2 mmol) in methanol] was added. The reaction mixture was stirred at room temperature for 3 h followed by removal of the solvents under vacuum. The residue was washed thoroughly with hexane:diethyl

ether (1:1, v/v) to remove excess ligand and extracted with chloroform and filtered. The filtrate was concentrated under reduced pressure and recrystallized by slow evaporation to yield yellow crystals (Yield: 576 mg, 79%), m.p. 236 °C. Anal. Calcd. for  $C_{24}H_{24}Cu_4N_4Se_4$ : C, 30.7; H, 2.6; N 6.0%. Found: C, 30.2; H, 2.9; N 6.3%.  $^1H$  NMR ( $CDCl_3$ )  $\delta$ : 2.24 (s, 3 H, 3-Me); 6.84 (t, 1 H, H-5); 7.18 (d, 1 H, H-4); 7.89 (d, 1 H, H-6) (ring protons).  $^{13}C\{^1H\}$  NMR ( $CDCl_3$ )  $\delta$ : 23.6 (Me), 118.8, 135.8, 137.2, 146.9, 162.0 (ring carbons).  $^{77}Se\{^1H\}$  NMR ( $CDCl_3$ )  $\delta$ : 82 ppm.

### 5.2.8 Preparation of CTS, SnS and $Cu_{1.8}S$ nanostructures

The CTS nanostructures were synthesized by heat up method using [ $tBu_2Sn(Spyz)_2$ ] and  $[Cu(Spyz)(PPh_3)_2]$  as molecular precursors. In a typical experiment, [ $tBu_2Sn(Spyz)_2$ ] (32.5 mg, 0.07 mmol) and  $[Cu(Spyz)(PPh_3)_2]$  (100 mg, 0.14 mmol) were dispersed in 8 ml of the high boiling solvent (OA and OLA either individually or in combination) in a three-necked flask and degassed under a nitrogen flow at room temperature. The reaction temperature was raised to 300 °C and kept at that temperature for 20 min. The dark turbid solution was rapidly cooled to 70 °C where excess methanol was injected into the flask. The resulting nanocrystals were separated by centrifugation and purified by washing several times with 2:1 mixture of methanol and toluene solution and dried.

A similar experiment was carried out in OLA at lower temperature 275 °C. The reaction mixture containing complexes [ $tBu_2Sn(Spyz)_2$ ] and  $[Cu(Spyz)(PPh_3)_2]$  were heated to 275 °C and kept at that temperature for 20 min. The nanostructures were isolated as mentioned above.

In addition to the preparation of CTS nanostructures, the thermolysis of molecular precursors [ $tBu_2Sn(Spyz)_2$ ] and  $[Cu(Spyz)(PPh_3)_2]$  were carried out separately in OLA at



300 °C for 20 min to obtain tin sulfide and copper sulphide nanostructures respectively which were used as references while assessing the phase purity of CTS nanostructures.

### 5.2.9 Preparation of $\text{Cu}_2\text{SnSe}_3$ , $\text{SnSe}_2$ and $\text{Cu}_2\text{Se}$ nanostructures

The CTSe nanostructures were prepared both by a) heat up and b) hot injection methods using  $[\text{Me}_2\text{Sn}(2\text{-Sepy}(3\text{-Me}))_2]$  and  $[\text{Cu}(2\text{-Sepy}(3\text{-Me}))_4]$  as molecular precursors.

#### a) Heat-up method

In a typical heat up experiment,  $[\text{Me}_2\text{Sn}(2\text{-Sepy}(3\text{-Me}))_2]$  (100 mg, 0.2 mmol) and  $[\text{Cu}(2\text{-Sepy}(3\text{-Me}))_4]$  (95.5 mg, 0.1 mmol) were dispersed in OLA (10 ml) in a three-necked flask and degassed under a nitrogen flow for 15 minutes at 100 °C. The reaction mixture was gradually heated to a required temperature (230, 260 and 300 °C) in three separate experiments and kept at that temperature for 10 minutes. The dark turbid solution was rapidly cooled down to 95-98 °C and toluene (4 ml) was injected to quench the reaction followed by the addition of methanol at 70 °C for precipitation of the nanostructures which were separated by centrifugation and washed thoroughly with toluene and methanol and dried.

A similar experiment was carried out by replacing OLA with TOPO. The reaction mixture containing complexes  $[\text{Me}_2\text{Sn}(2\text{-Sepy}(3\text{-Me}))_2]$  and  $[\text{Cu}(2\text{-Sepy}(3\text{-Me}))_4]$  were heated to 300 °C and kept at that temperature for 10 minute and isolated the nanostructures as mentioned above.

In addition to the synthesis of CTSe nanostructures, using this method thermolysis of  $[\text{Me}_2\text{Sn}(2\text{-Sepy}(3\text{-Me}))_2]$  (100 mg, 0.2 mmol) and  $[\text{Cu}(2\text{-Sepy}(3\text{-Me}))_4]$  (95.5 mg, 0.10 mmol) were carried out separately in OLA at 300 °C to obtain  $\text{Cu}_2\text{Se}$  and  $\text{SnSe}_2$

nanostructures which were used for comparing with CTSe nanostructures while assessing the phase purity.

#### **b) Hot injection method**

A mixture of  $[\text{Me}_2\text{Sn}(2\text{-Sepy}(3\text{-Me}))_2]$  (100 mg, 0.2 mmol) and  $[\text{Cu}(2\text{-Sepy}(3\text{-Me}))_4]$  (95.5 mg, 0.1 mmol) dispersed in OLA (2 ml) was injected into a preheated OLA (8 ml) at 300 °C with vigorous stirring under flowing argon. The reaction was continued at this temperature for 10 minutes whereupon the reaction was quenched by injecting toluene (4 ml) and allowed to cool the contents to room temperature. The resulting nanostructures were isolated by precipitating with excess methanol followed by centrifugation to give a black precipitate.

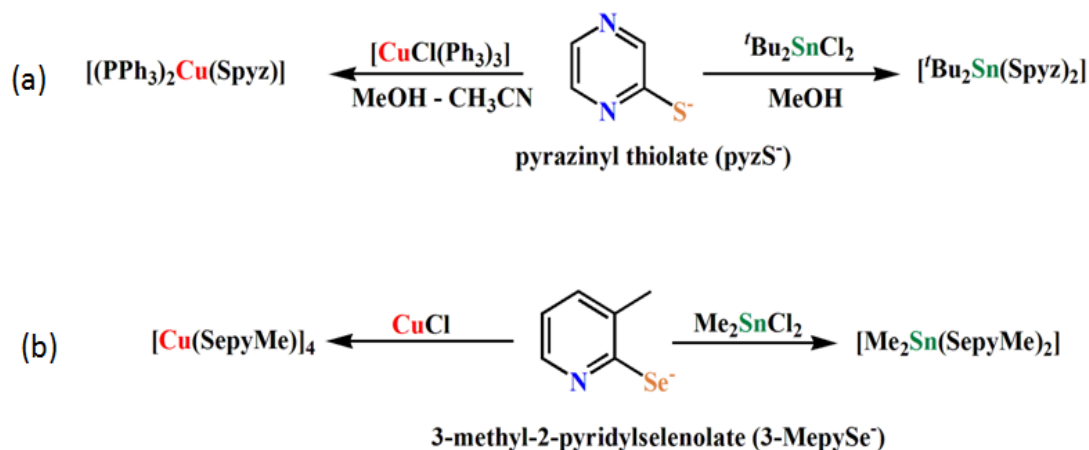
#### **5.2.10 Crystallography**

Intensity data for  $[\text{Cu}(\text{Spyz})(\text{PPh}_3)_2]$  was collected on a Agilent Super Nova microfocus X-ray source ( $\text{CuK}_\alpha$ ,  $\lambda = 1.5418 \text{ \AA}$ ) radiation while the data for  $[\text{Bu}_2\text{Sn}(\text{Spyz})_2]$  and  $[\text{Me}_2\text{Sn}(2\text{-Sepy}(3\text{-Me}))_2]$  were collected on a Rigaku AFC7S diffractometer using graphite monochromated ( $\text{MoK}_\alpha$ ,  $\lambda = 0.71069 \text{ \AA}$ ) radiation at room temperature ( $298 \pm 2 \text{ K}$ ) so that  $\theta_{\text{max}} = 27.5^\circ$ . The unit cell parameters (Table 2.5 and 2.6) were determined from 25 reflections measured by a random search routine and are given in chapter 2.

### **5.3 Results and discussion**

#### **5.3.1 Synthesis, Spectroscopy and X-ray crystallography**

Metal (Cu and Sn) complexes with chalcogenolate ligand were prepared according to scheme 5.1 and characterized:



**Scheme 5.1** Synthesis of metal (tin and copper) complexes with a) pyrazinyl thiolate and b) 3-methyl-2-pyridylselenolate ligands.

**a) Copper and tin complexes of pyrazinylthiolate ligand**

The  $^1H$ ,  $^{31}P\{^1H\}$ ,  $^{119}Sn\{^1H\}$  NMR spectra were recorded in  $CDCl_3$ . The  $^1H$  NMR spectra of the complexes exhibited expected resonances and peak multiplicities. The  $^{31}P$  spectrum (Fig. 5.1a) of complex  $[Cu(Spyz)(PPh_3)_2]$  displayed a resonance at  $\delta \sim -2.87$  due to coordinated  $PPh_3$  ligands. For complex  $[tBu_2Sn(Spyz)_2]$ , the  $^3J(^{119}Sn-^1H)$  is  $\sim 110$  Hz which is in close agreement with the values reported for di-*t*-butyl tin compounds [227,238].

The  $^{119}Sn\{^1H\}$  NMR spectrum (Fig. 5.1b) showed a single resonance ruling out any possibility of the existence of more than one species in solution.  $^{119}Sn$  signals for four and six coordinate compounds are observed in the range of  $\delta = +200$  to  $-60$  and  $-200$  to  $-400$  ppm, respectively [209,239]. The peak at  $\delta = -18$  ppm is well within the former range indicating a four-coordinated tin center devoid of any weak interaction between Sn and N of pyrazine ring in solution phase. This may be possibly due to the inductive and steric effects of the  $tBu$  group in organotin complexes which reduces the acceptor properties of tin [149].

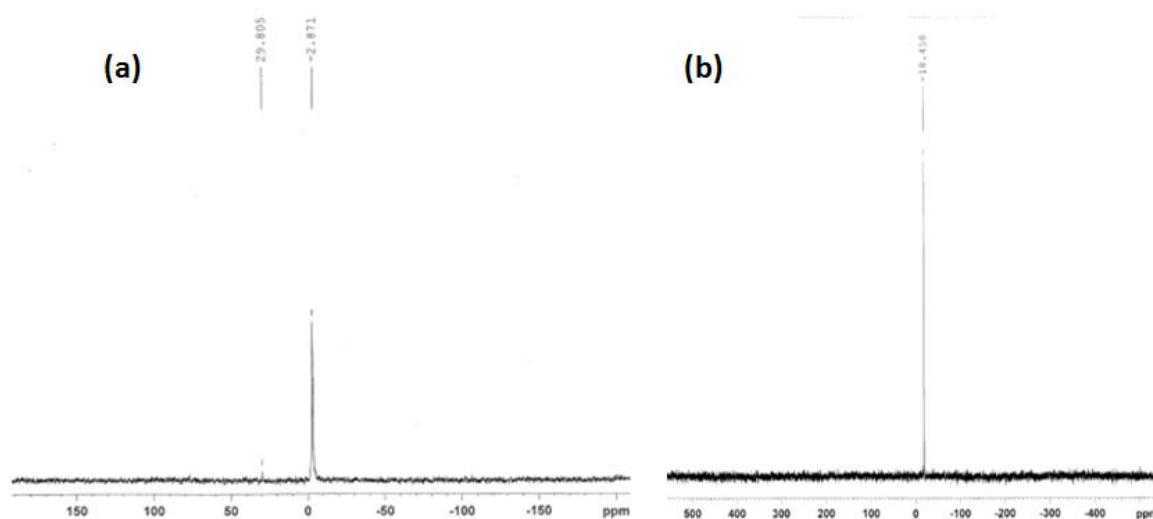


**Fig. 5.1** a)  $^{31}\text{P}\{^1\text{H}\}$  NMR (121.49 MHz,  $\text{CDCl}_3$ ) spectrum of  $[\text{Cu}(\text{Spyz})(\text{PPh}_3)_2]$  shows a resonance at -2.87 ppm. The minor peak at 29.80 is due to  $\text{Ph}_3\text{PO}$ . b)  $^{119}\text{Sn}\{^1\text{H}\}$  NMR (111.94 MHz,  $\text{CDCl}_3$ ) spectrum of  $[\text{tBu}_2\text{Sn}(\text{Spyz})_2]$  shows a single resonance at -18.45 ppm.

The molecular structures of  $[\text{tBu}_2\text{Sn}(\text{Spyz})_2]$  and  $[\text{Cu}(\text{Spyz})(\text{PPh}_3)_2]$ , established by single crystal X-ray diffraction analyses are shown in Fig. 5.2 and 5.3. Selected inter-atomic parameters are given in Table 5.1.

$[\text{tBu}_2\text{Sn}(\text{Spyz})_2]$  crystallizes in orthorhombic space group  $Pbca$ . The coordination sphere around tin is defined by two C atoms from  $\text{tBu}$  groups and two thiolate sulfur atoms. The Sn–C and Sn–S bond distances (Table 5.1) are well in agreement with those reported for diorganotin bis thiolates derived from N-heterocyclic thiolates ligands [181,182,184]. The distances between tin and ortho-N of pyrazinyl rings ( $\text{Sn1}\cdots\text{N1} = 2.88 \text{ \AA}$  &  $\text{Sn1}\cdots\text{N3} = 2.90 \text{ \AA}$ ) are longer than the sum of their covalent radii ( $2.15 \text{ \AA}$ ) but are shorter than the sum of van der Waal's radii ( $3.72 \text{ \AA}$ ) indicating a weak interaction between them, which appears to have been diminished in solution. Such interaction

between Sn and N is distinctly different from analogous diorganotin bis(2-pyridylthiolates),  $[R_2Sn(Spy)_2]$  ( $R = Me, Et, Ph$ ) and  $[^tBu_2Sn\{SC_5H_3(5-NO_2)N\}_2]$  [182,184] which exhibit relatively stronger Sn–N bonding interactions as evident from much shorter Sn $\cdots$ N distances (2.52–2.63 Å). This can be attributed to steric demand of  $^tBu$  groups attached to tin which forces two pyrazinyl ring to occupy space at a larger distance from the tin atoms.

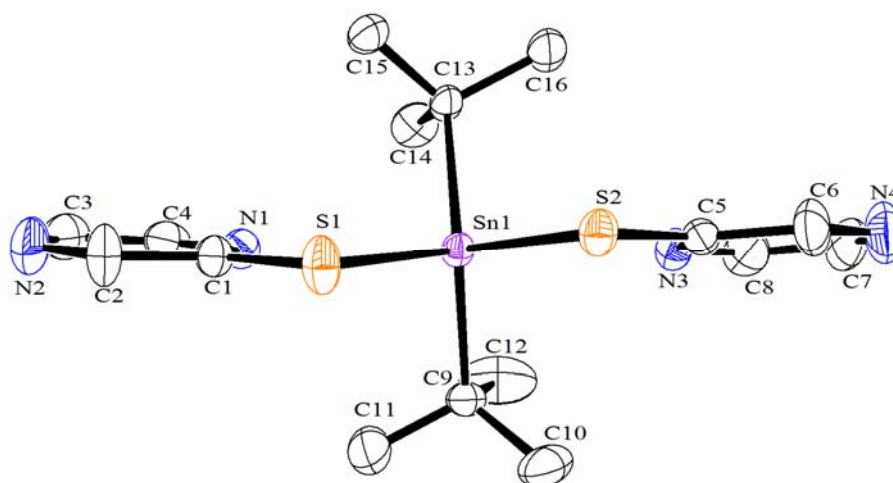


**Fig. 5.2** Molecular structure of  $[^tBu_2Sn(Spyz)_2]$  with partial atomic numbering scheme. Hydrogen atoms are omitted for clarity. Ellipsoids are drawn with 50% probability. The shorter distance between Sn and N atoms, Sn1–N1 and Sn1–N3 are 2.88 and 2.90 Å respectively, suggest weak interaction exist between them.

$[Cu(Spyz)(PPh_3)_2]$  crystallizes in triclinic space group  $P\bar{1}$ . The copper atom acquires a distorted tetrahedral configuration defined by two P atoms of  $PPh_3$  ligand and N and S atoms from chelating 2-pyrazinylthiolate group. There are two molecules of  $[Cu(Spyz)(PPh_3)_2]$  present in the crystallographic asymmetric unit which differs slightly in their inter-atomic parameters.

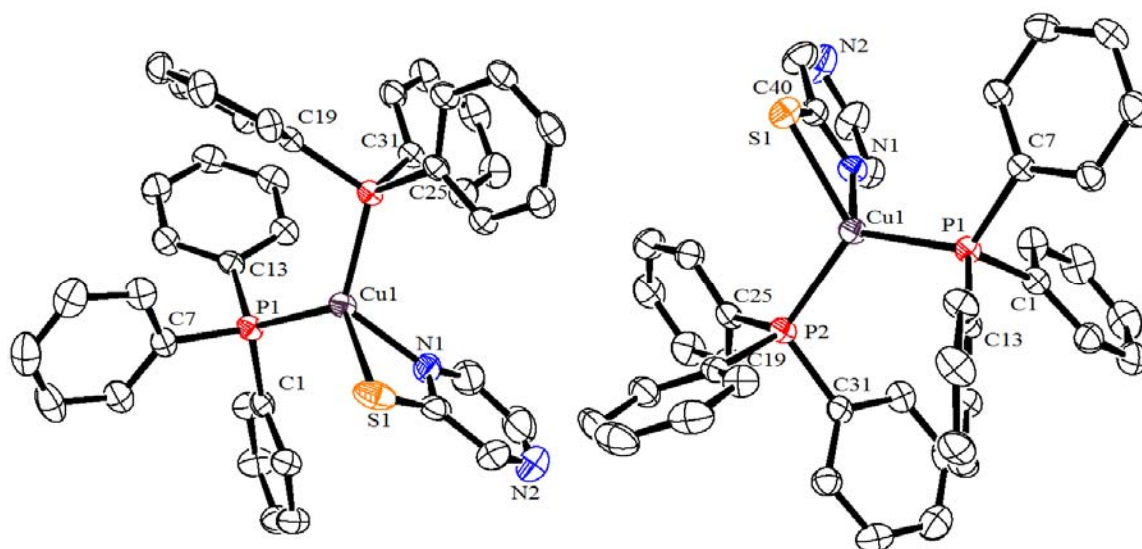


**Fig. 5.3** Molecular structure of  $[\text{Cu}(\text{Spyz})(\text{PPh}_3)_2]$  with partial atomic numbering scheme. There are two molecules in asymmetric unit. Hydrogen atoms are omitted for clarity. Ellipsoids are drawn with 50% probability.

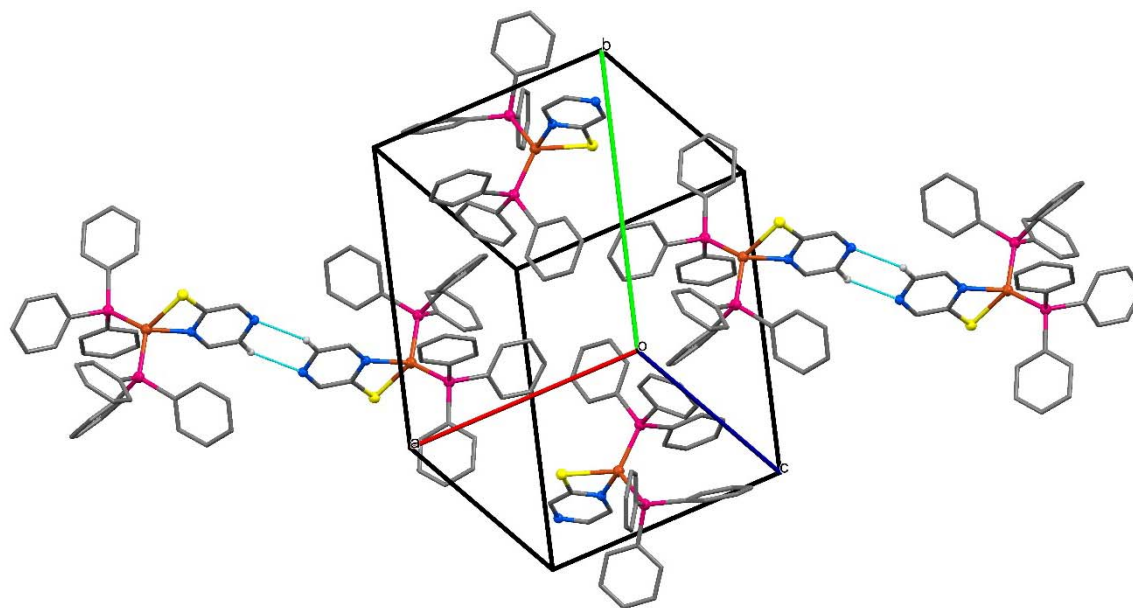


**Fig. 5.4** Packing diagram of  $[\text{Cu}(\text{Spyz})(\text{PPh}_3)_2]$ . One molecular complex unit exhibits weak intermolecular  $\text{N}\cdots\text{H}-\text{C}(\text{N})$  interaction. The parameters are:  $\text{N}-\text{C}$  distance 3.487 Å,  $\text{N}-\text{H}$  distance 2.632 Å,  $\text{N}-\text{H}-\text{C}$  angle 153.03°. The other molecule is devoid of any such interactions.

One of these molecule forms dimeric units with similar neighbouring molecule through weak attractive intermolecular  $N\cdots H-C(N)$  interactions between the pyrazinyl rings whereas the other one is devoid of any such intermolecular contacts (Fig. 5.4). The Cu–S, Cu–N, and Cu–P bond distances (Table1) are normal and are in conformity with those reported in literature [240, 241].

#### **b) Copper and tin complexes of pyridylselenolate ligand**

The precursors  $[Me_2Sn(2-Sepy(3-Me))_2]$  [149] and  $[Cu(2-Sepy(3-Me))]_4$  [175] were prepared according to literature methods.

The  $^1H$ ,  $^{13}C\{^1H\}$ ,  $^{77}Se\{^1H\}$  and  $^{119}Sn\{^1H\}$  NMR spectra of the complexes were recorded in  $CDCl_3$ . The  $^1H$  and  $^{13}C$  NMR spectra showed the expected resonances and peak multiplicities. The pyridyl ring proton resonances appeared at a lower field with reference to the corresponding signals for the diselenides. The  $^{77}Se\{^1H\}$  and  $^{119}Sn\{^1H\}$  NMR spectra of  $[Me_2Sn(2-Sepy(3-Me))_2]$  displayed single resonance peak flanked by  $^{119}Sn$  and  $^{77}Se$  satellites, respectively, indicating existence of only one tin containing specie in the solution with a direct bond between tin and selenium.

The X-ray structural characterization for the latter was reported in Ref. [175] while for the former is described here. The molecular structure of  $[Me_2Sn(2-Sepy(3-Me))_2]$  (Fig. 5.5) is isomorphous to  $[R_2Sn(2-Sepy)_2]$  ( $R = Me$  or  $tBu$ ) [149]. The complex is a discrete monomer with distorted tetrahedral geometry around tin defined by two Me groups and two selenium atoms of the selenolate ligand. The distortion is evident from Se–Sn–Se bond angle which is smaller than ideal tetrahedral angle ( $109.57^\circ$ ) whereas C13–Sn–C1 slightly opened up ( $122^\circ$ ) to compensates the contraction.

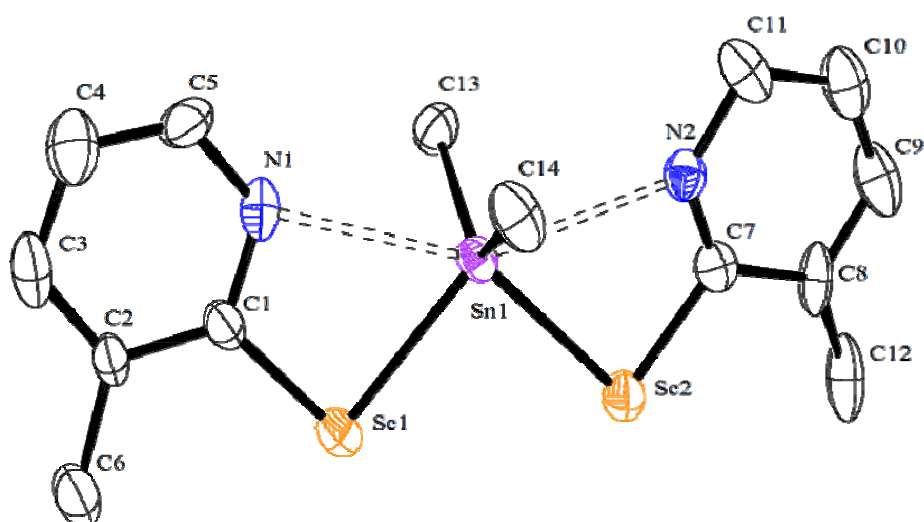


**Fig. 5.5** Crystal structure of  $[\text{Me}_2\text{Sn}(2\text{-Sepy}(3\text{-Me}))_2]$  with atomic number scheme. The ellipsoids were drawn at 25% probability (H atoms are omitted for clarity). Selected interatomic parameters: Bond distance ( $\text{\AA}$ ): Sn1-C13, 2.15(2); Sn1-C14, 2.128 (18); Sn1-Se1, 2.611 (2); Sn1-Se2, 2.666 (3); Sn1-N1, 2.74; Sn1-N2, 2.76. Bond angles ( $^\circ$ ): C13-Sn1-Se1, 109.4 (6); C13-Sn1-Se2, 110.4 (7); C14-Sn1-Se1, 111.0(6); C14-Sn1-Se2, 110.6 (7), Se1-Sn-Se2, 88.29 (8); N1-Sn1-N2, 146.86.

The Sn-N bond distances ( $\sim 2.75 \text{ \AA}$ ) are shorter than the sum of their van der Waal radii ( $3.72 \text{ \AA}$ ) [214] indicating a weak interaction between tin and nitrogen atom. The Sn-C bond distance is approximately equal to the reported values for  $[\text{Me}_2\text{Sn}(2\text{-Sepy})_2]$  [149]. However,  $\angle\text{Se-Sn-Se}$  ( $88.29 (8)^\circ$ ) is reduced while  $\angle\text{N-Sn-N}$  ( $146.36^\circ$ ) is widened as compared to the corresponding angles in  $[\text{Me}_2\text{Sn}(2\text{-Sepy})_2]$  ( $94.25 (8)$ ,  $142.38^\circ$ , respectively) [149].



**Table 5.1** Selected bond lengths (Å) and angles (°) of [*t*Bu<sub>2</sub>Sn(Spyz)<sub>2</sub>] and [Cu(Spyz)(PPh<sub>3</sub>)<sub>2</sub>].

[ <i>t</i> Bu <sub>2</sub> Sn(Spyz) <sub>2</sub> ]		[Cu(Spyz)(PPh <sub>3</sub> ) <sub>2</sub> ]			
		Molecule I		Molecule II	
C9–Sn1	2.203(6)	Cu1a–S1a	2.4395(11)	Cu1–S1	2.4358(13)
C13–Sn1	2.207(5)	Cu1a–N1a	2.141(3)	Cu1–N1	2.131(4)
S1–Sn1	2.5075(15)	Cu1a–P1a	2.2422(10)	Cu–P1	2.2504(11)
S2–Sn1	2.4939(16)	Cu1a–P2a	2.2591(11)	Cu1–P2	2.2407(11)
S1–C1	1.745(6)	S1a–C40a	1.728(4)	S1–C40	1.701(7)
S2–C5	1.724(6)				
Sn1–N1	2.886				
Sn–N3	2.902				
C9–Sn1–C13	128.6(2)	S1a–Cu1a–N1a	69.12(10)	S1–Cu1–N1	68.51(13)
C9–Sn1–S1	106.49(17)	S1a–Cu1a–P1a	120.99(4)	S1–Cu1–P1	117.12(5)
C9–Sn1–S2	110.42(16)	S1a–Cu1a–P2a	116.50(4)	S1–Cu1–P2	117.86(4)
C13–Sn1–S1	110.77(15)	N1a–Cu1a–P1a	115.77(10)	N1–Cu1–P1	109.35(11)
C13–Sn1–S2	107.29(17)	N1a–Cu1a–P2a	105.24(9)	N1–Cu1–P2	114.70(11)
S1–Sn1–S2	84.34(5)	P1a–Cu1a–P2a	117.60(4)	P1–Cu1–P2	118.42(4)
N3–Sn1–N1	160.47				

### 5.3.2 Thermogravimetric analyses

Thermogravimetric analyses (TGA) were carried out to evaluate the thermal decomposition behaviour of the complexes under flowing argon atmosphere (Fig. 5.6). TG curve for  $[^t\text{Bu}_2\text{Sn}(\text{Spyz})_2]$  shows a single step decomposition at around 275 °C with the weight of residue (33.7 %) corresponding to SnS (32.9 %). Similarly the TG curve of  $[\text{Cu}(\text{Spyz})(\text{PPh}_3)_2]$  showed a single step decomposition of the complex taking place at 335 °C with weight loss found (86.6 %) which is in agreement with the calculated weight loss (86.4 %) expected for the formation of CuS.

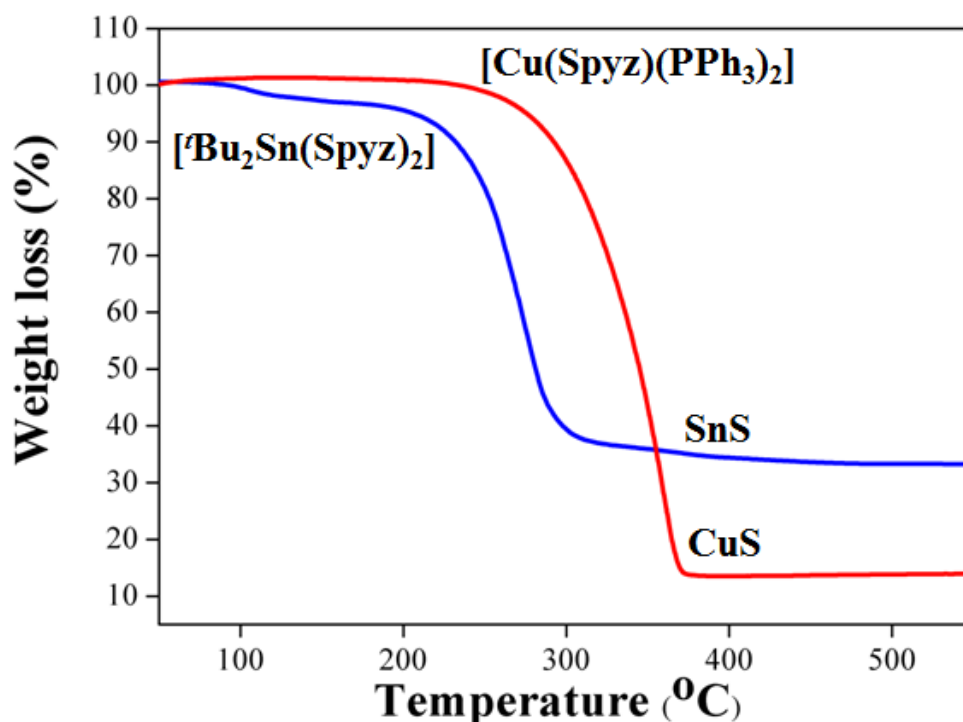


**Fig. 5.6** Thermogravimetric analysis data for complexes a)  $[^t\text{Bu}_2\text{Sn}(\text{Spyz})_2]$  and b)  $[\text{Cu}(\text{Spyz})(\text{PPh}_3)_2]$ , respectively.

Similarly,  $[\text{Me}_2\text{Sn}(2\text{-Sepy}(3\text{-Me}))_2]$  and  $[\text{Cu}(2\text{-Sepy}(3\text{-Me}))_4]$  were also underwent single step decomposition leading to the formation of Sn and  $\text{Cu}_{1.8}\text{Se}$ , respectively as evaluated in Ref. [149,175].

### 5.3.3 Preparation and characterization of the nanostructures

Metal sulfides (CTS, SnS, Cu<sub>1.8</sub>S) and metal selenides (CTSe, SnSe<sub>2</sub>, Cu<sub>2</sub>Se) were prepared from respective precursors and characterized as follows:

#### a) Metal sulfides (CTS, SnS, Cu<sub>1.8</sub>S)

Several synthetic methodologies have been developed for the preparation of CTS nanostructures. However, compared to binary chalcogenides, it is a challenging task to control stoichiometry and phase purity of ternary nanostructures due to the different reactivities of the metal precursors. To prepare ternary nanostructures, it is essential to select suitable combination of precursor material having similar kind of reactivities and comparable decomposition temperatures. The molecular precursors must shed the organic moieties during decomposition in order to produce the phase pure ternary material.

Complexes [Bu<sub>2</sub>Sn(Spyz)<sub>2</sub>] and [Cu(Spyz)(PPh<sub>3</sub>)<sub>2</sub>] shows closely related decomposition temperature and give respective metal sulfide upon decomposition as evident from thermogravimetric analysis. Thus, these complexes were chosen to assess their utility as molecular precursors for the preparation of ternary copper tin sulphide (CTS) nanostructures. The crystal structure, morphology, homogeneity and band gap of the resulting products were characterized by p-XRD, Raman spectroscopy, EDX, SEM, TEM, SAED techniques, diffuse reflectance spectroscopy.

The CTS nanostructures were prepared by heat up method in three distinct high boiling solvent systems (OA, OA-OLA mixture (1:1, v/v) and OLA). Different solvent systems were chosen to evaluate the effect of capping agents with different binding ability on the phase purity and morphology of nanostructures. Active –COOH group of OA and oleate ions, obtained from the mixture of OA-OLA has high electron donating and strong binding ability thus making them a strong capping agent whereas OLA is relatively weaker capping agent but provide strong reducing atmosphere at an elevated

temperature. In a typical heat up experiment, the  $[\text{tBu}_2\text{Sn}(\text{Spyz})_2]$  and  $[\text{Cu}(\text{Spyz})(\text{PPh}_3)_2]$  were dispersed in different high boiling solvent systems at room temperature and slowly heated whereupon a clear yellow solution formed at  $\sim 120^\circ\text{C}$ , which turned orange to red ( $\sim 190^\circ\text{C}$ ) finally became black ( $\sim 230^\circ\text{C}$ ). This colour change is indicative of the formation and growth of the metal chalcogenide nanostructures. The heating of reaction mixture continued to desired growth temperature, i.e.  $300^\circ\text{C}$  for 20 minutes followed by quenching and purification of the nanostructures.

The samples prepared in different reaction solvents are initially analysed by the p-XRD in order to assess phase purity, crystallinity and crystal structure of CTS nanostructures. The XRD patterns of CTS nanostructures synthesized at same growth temperature ( $300^\circ\text{C}$ ) and duration (20 minutes) using different solvent systems showed different profile suggesting the formation of different products (Fig. 5.7 d, e, f). Clearly the nature of the solvent affected the formation of desired product.

Thermolysis of complexes either in OA or in a mixture of OA-OLA revealed the formation of monoclinic phase of CTS as a major product slightly contaminated by cubic phase of  $\text{Cu}_{1.8}\text{S}$ . Low intensity peaks in p-XRD at  $2\theta = 32.43, 46.40$  and  $54.98^\circ$  are attributed to (200), (220) and (311) crystal planes confirming the presence of  $\text{Cu}_{1.8}\text{S}$  (JCPDS 04-006-0521) nanostructures in both the samples. The intense peak at  $2\theta = 28.45^\circ$  along with other peaks at  $32.90, 47.29$  and  $56.13^\circ$  originating from (200),  $(\bar{2}02)$ ,  $(\bar{1}33)$  and  $(\bar{3}33)$  crystal planes (JCPDS 04-010-5719) can be assigned to the formation of monoclinic CTS nanostructures (major product). The presence of binary impurity in the ternary nanostructures could be due to the strong binding ability of the capping agent which causes incomplete alloying of copper sulfide and tin sulfide. Possibility of existence of secondary phases  $\text{Cu}_{2-x}\text{S}$  or  $\text{SnS}$  in the desired  $\text{Cu}_2\text{SnS}_3$  has been predicted from the chemical potential diagram of Cu-Sn-S system generated by Guan et al. [242]. It

has also been observed that formation of CuS was more prominent than SnS (Fig. 5.7 d and e). This is possibly due to the preferential bonding of soft Lewis base ( $S^{2-}$ ) with soft Lewis acid ( $Cu^+$ ) rather than with hard Lewis acid ( $Sn^{4+}$ ). Similar type of observation was recently reported by Lokhande et al. [229]. The average crystallite size, calculated using Scherrer formula (Table 5.2) was  $\sim 15$  nm for the residue obtained from OA or OA-OLA mixture.

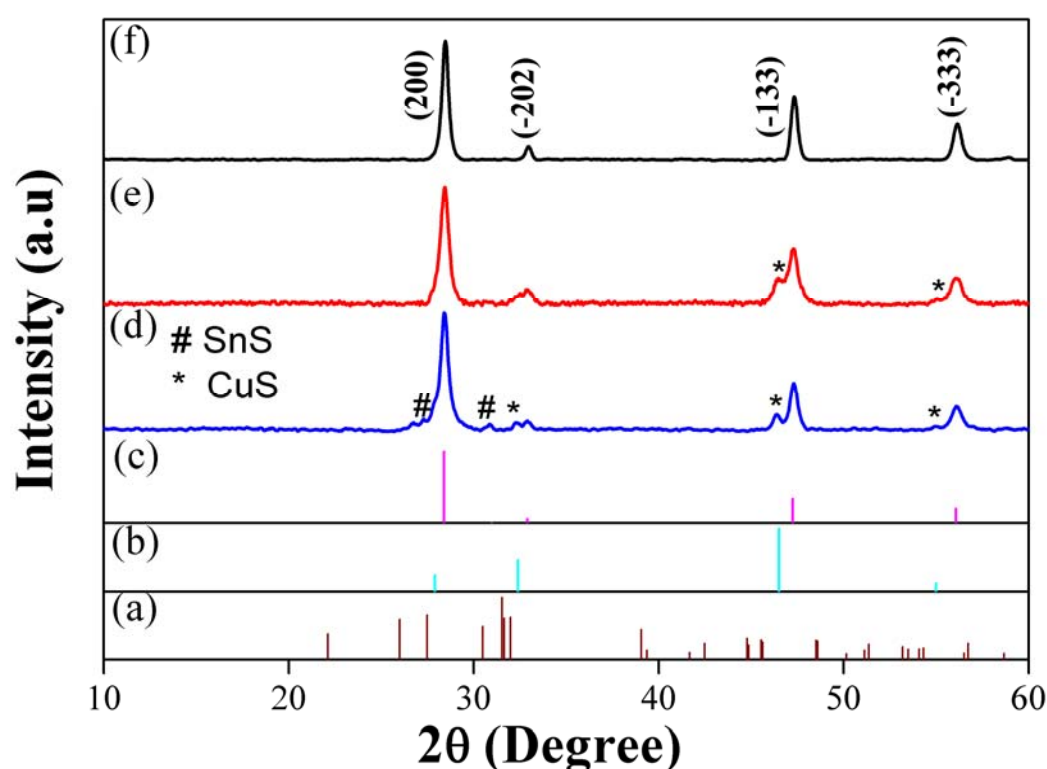


**Fig. 5.7** a), b), c) are the simulated XRD patterns of orthorhombic SnS (JCPDS no. 75-0925), cubic  $Cu_{1.8}S$  (JCPDS no. 04-004-7716), monoclinic CTS (JCPDS no. 04-010-5719) respectively. p-XRD profiles of CTS nanostructures obtained by co-thermolysis of  $[^tBu_2Sn(Spyz)_2]$  and  $[Cu(Spyz)(PPh_3)_2]$  at 300 °C for 20 minutes by heat up method in d) OA-OLA, e) OA and f) OLA as solvent/capping agent respectively. (# indicates impurity peaks of orthorhombic SnS while \* indicates the impurity peak of cubic  $Cu_{1.8}S$ ).

However, when relatively weak coordinating agent (OLA) was employed as a reaction solvent/capping agent, relatively larger CTS nanostructures were produced with average crystallite size  $\sim 22$  nm. The corresponding p-XRD (Fig. 5.7f) showed a set of reflections (200), ( $\bar{2}$ 02), ( $\bar{1}$ 33) and ( $\bar{3}$ 33) originating from the crystal planes of monoclinic CTS nanostructures (JCPDS 04-010-5719). Furthermore, the absence of peaks other than monoclinic CTS indicates that material is phase pure. The crystallinity of CTS material is reflected by sharpness of p-XRD peaks.

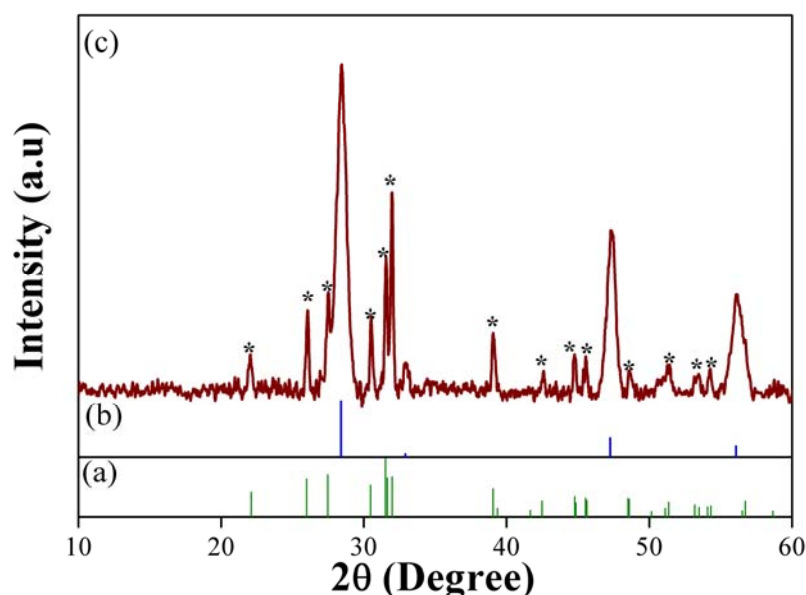


**Fig. 5.8** a), b) are the simulated XRD patterns of orthorhombic SnS (JCPDS no. 75-0925), monoclinic CTS (JCPDS no. 04-010-5719) respectively. c) XRD profiles of CTS nanostructures obtained by co-thermolysis of  $[^t\text{Bu}_2\text{Sn}(\text{Spyz})_2]$  and  $[\text{Cu}(\text{Spyz})(\text{PPh}_3)_2]$  at  $275^\circ\text{C}$  for 20 minutes by heat up method in OLA as solvent/capping agent. (\* indicates binary impurity from orthorhombic phase of SnS).

To reduce the dimensions of phase pure CTS, an effort was made by lowering down the reaction temperature to  $275^\circ\text{C}$ , however the related XRD analysis shows significant contamination from orthorhombic phase of SnS in CTS nanostructures (Fig. 5.8). The

lattice parameters of phase pure monoclinic CTS obtained in OLA are calculated by least square fitting and are listed in Table 5.3.

**Table 5.2** Reaction condition, structural, morphological, compositional and optical parameters of nanostructures.

Nanostructures	Reaction solvent	Crystallite size (nm)	Morphology	EDS analysis	Optical band gap (eV)
Phase pure CTS	OLA	22	Spherical particles	2.1:1.0:3.0 (Cu:Sn:S)	1.4
Phase pure SnS	OLA	27	Rectangular sheets	1:1 (Sn:S)	1.8
Phase pure Cu <sub>1.8</sub> S	OLA	13	Hexagonal discs	1.6:1 (Cu:S)	2.0
CTS with SnS and CuS impurity	OA	~ 15	Agglomeration of particles	3.4:1.0:3.8 (Cu:Sn:S)	
CTS with CuS impurity	OA-OLA	~ 15	Agglomeration of particles along with rectangular sheets	3.6:1.0:4.4 (Cu:Sn:S)	

**Table 5.3** Lattice parameter of nanostructures (CTS, SnS and Cu<sub>1.8</sub>S) synthesized in OLA at 300 °C.

Precursor	Nanostructures	Lattice parameter					
		a (Å)	b (Å)	c (Å)	α (°)	β (°)	γ (°)
[ <sup>t</sup> Bu <sub>2</sub> Sn(Spyz) <sub>2</sub> ] + [Cu(Spyz)(PPh <sub>3</sub> ) <sub>2</sub> ]	Monoclinic CTS	6.638(8)	11.513(6)	6.645(2)	90	109.29 (8)	90
[ <sup>t</sup> Bu <sub>2</sub> Sn(Spyz) <sub>2</sub> ]	Orthorhombic SnS	3.963(4)	4.350(8)	11.13(5)	90	90	90
[Cu(Spyz)(PPh <sub>3</sub> ) <sub>2</sub> ]	Cubic Cu <sub>1.8</sub> S	5.561(1)	5.561(1)	5.561(1)	90	90	90

CTS being a ternary semiconductor material, the presence of secondary binary phases (SnS, CuS) as impurity in final product are highly probable as predicted by Guan et al. [242]. In order to establish the absence of contamination from these binary phases, it is desirable to examine the formation of possible binary phases by carrying out the thermolysis of individual precursors which have been employed in the synthesis of phase pure CTS nanostructures under the similar conditions followed by the comparison of their p-XRD pattern with that of CTS. Thermolysis of individual precursors in OLA at 300 °C for 20 min resulted in the formation binary SnS and Cu<sub>1.8</sub>S nanostructures. p-XRD pattern of SnS and Cu<sub>1.8</sub>S are shown in Fig. 5.9. The diffraction peaks obtained in (Fig. 5.9c) are in good agreement with orthorhombic SnS (JCPDS pattern 75-0925) with preferred orientation along (013) plane. p-XRD pattern shown in Fig. 5.9d can be indexed to standard JCPDS pattern 04-004-7716 of cubic phase of Cu<sub>1.8</sub>S.



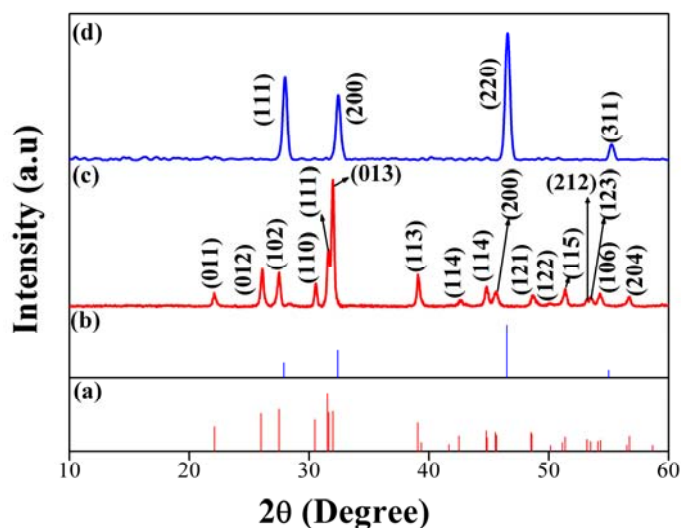


**Fig. 5.9** a), b) are the simulated XRD patterns of orthorhombic SnS (JCPDS no. 75-0925), cubic  $\text{Cu}_{1.8}\text{S}$  (JCPDS no. 04-004-7716), respectively. XRD profiles of c) orthorhombic SnS d) cubic  $\text{Cu}_{1.8}\text{S}$  nanostructures obtained by thermolysis of  $[\text{tBu}_2\text{Sn}(\text{Spyz})_2]$  and  $[\text{Cu}(\text{Spyz})(\text{PPh}_3)_2]$ , respectively, at 300 °C for 20 minutes by heat up method in OLA as solvent/capping agent.

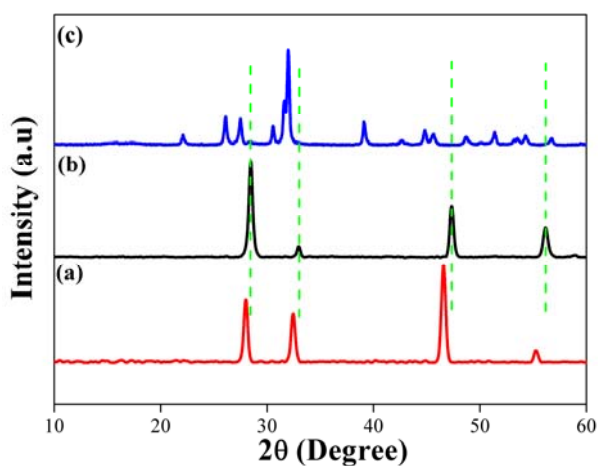


**Figure 5.10** XRD patterns of a) cubic  $\text{Cu}_{1.8}\text{S}$ , b) monoclinic CTS and c) orthorhombic SnS obtained by thermolysis of  $[\text{tBu}_2\text{Sn}(\text{Spyz})_2]$  and  $[\text{Cu}(\text{Spyz})(\text{PPh}_3)_2]$  either individually or in combination at 300 °C for 20 minutes by heat up method in OLA as solvent/capping agent.

Comparative p-XRD patterns of  $\text{Cu}_{1.8}\text{S}$ , SnS and CTS shown in Fig. 5.10 revealed that diffraction patterns of orthorhombic SnS and monoclinic CTS are distinctly different whereas the peak position in diffraction pattern are not markedly distinct from each other, making it difficult to distinguish CTS and  $\text{Cu}_{1.8}\text{S}$  using p-XRD.

However, CTS and  $\text{Cu}_{1.8}\text{S}$  has characteristic Raman spectra. Hence Raman spectroscopy is an important diagnostic tool to assess the phase purity of ternary CTS nanostructures.

The comparison of Raman spectra of CTS and  $\text{Cu}_{1.8}\text{S}$  nanostructures obtained at 300 °C in OLA are shown in Fig. 5.11.

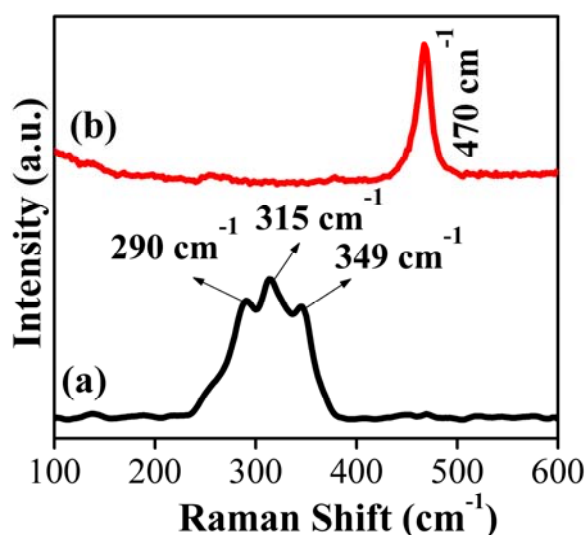


**Fig. 5.11** Raman spectra of a) monoclinic CTS and b) cubic  $\text{Cu}_{1.8}\text{S}$  obtained by thermolysis of precursors in OLA at 300 °C.

The Raman spectrum of the former (Fig. 5.11a) is characterized by the presence of three vibrational mode peaks at 290, 315 and 349 cm<sup>-1</sup> that corresponds to monoclinic phase of CTS and is in good agreement with reported literature [229,243]. The peak at 290 and 349 cm<sup>-1</sup> corresponds to A' symmetry modes while the peak at 315 cm<sup>-1</sup>

represents Cu-Sn atomic vibration [229,243]. The absence of characteristic vibration mode peak of  $\text{Cu}_{2-x}\text{S}$  [244] at  $470\text{ cm}^{-1}$ , (Fig. 5.11), rules out the possibility of contamination by binary  $\text{Cu}_{2-x}\text{S}$  in ternary CTS nanostructures. The Raman data are consistent with the XRD analysis and establish the formation of phase pure monoclinic CTS devoid of binary impurities.

To further elucidate the elemental composition of the CTS nanostructures prepared in different solvent systems, energy dispersive X-ray (EDX) analysis were performed at different locations (Table 5.3). The studies revealed that nanostructures prepared in OA, and mixture of OA-OLA, were rich in copper and sulfur, with elemental composition  $\text{Cu}_{3.4}\text{Sn}_{1.0}\text{S}_{3.8}$  (for nanostructures in OA) and  $\text{Cu}_{3.6}\text{Sn}_{1.0}\text{S}_{4.4}$  (for nanostructures in a mixture of OA-OLA), while nearly stoichiometric formation of CTS nanostructures ( $\text{Cu}_2\text{SnS}_3$ ) was observed when synthesized in OLA (Cu:Sn:S atom ratio is 33.4 : 15.5 : 47.8 or 2.1 : 1.0 : 3.0). For binary nanostructures SnS and  $\text{Cu}_{1.8}\text{S}$ , atomic percentage was 50.1 : 49.9 (Sn:S) and 58.5 : 38.3 (Cu:S) which is fairly close to the expected value of individual grains. The elemental composition obtained from EDX analysis supports the findings discussed from XRD and Raman results. To confirm the element distribution of the as synthesized CTS, SnS and  $\text{Cu}_{1.8}\text{S}$ , 2-D elemental mapping of the nanostructures were recorded revealing homogeneous distribution of constituent elements within the nanocrystals. A representative 2-D elemental mapping image and EDX spectrum of CTS nanostructures is shown in Fig. 5.12.

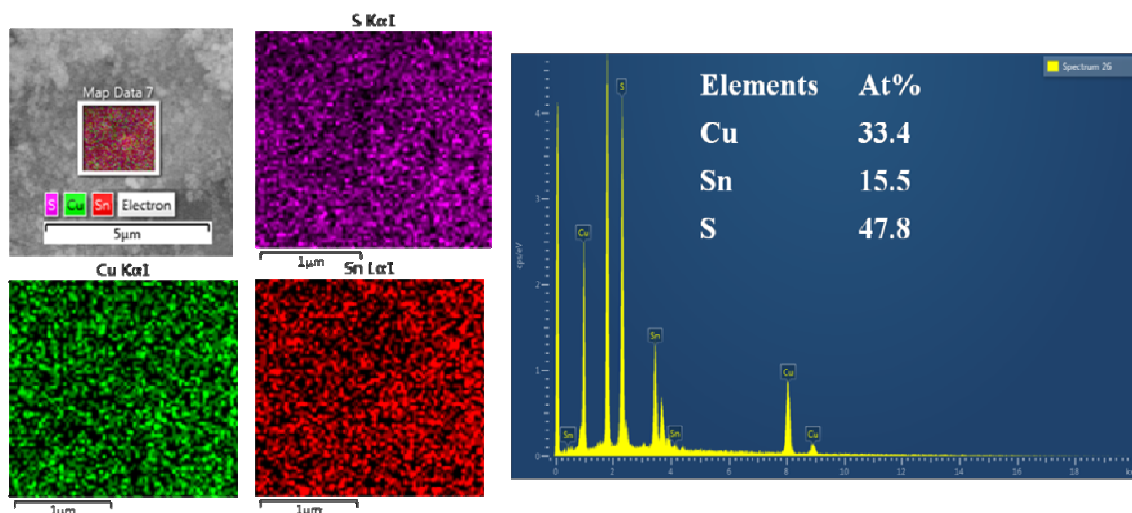


**Fig. 5.12** EDX and elemental imaging of nanostructures obtained from the co-thermolysis of  $[^t\text{Bu}_2\text{Sn}(\text{Spyz})_2]$  and  $[\text{Cu}(\text{Spyz})(\text{PPh}_3)_2]$  in OLA at 300 °C for 20 minutes.

Scanning electron microscopy (SEM) and transmission electron microscopy (TEM) has been used to find the morphology and phase of the nanostructures. The SEM micrographs of nanostructures synthesized using OA showed spherical agglomeration of particles (Fig. 5.13a).

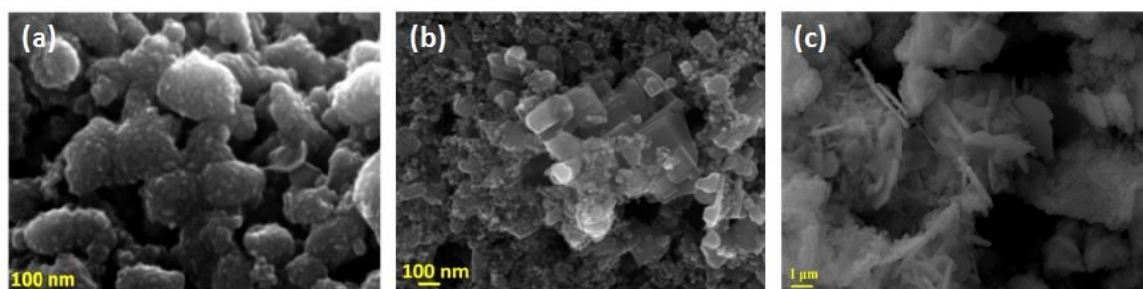


**Fig. 5.13** SEM of CTS nanostructures obtained from co-thermolysis of  $[^t\text{Bu}_2\text{Sn}(\text{Spyz})_2]$  and  $[\text{Cu}(\text{Spyz})(\text{PPh}_3)_2]$  in a) OA, b) OA-OLA at 300 °C and c) OLA at 275 °C for 20 minutes.

The SEM images shown in Fig. 5.13 b and c represent the nanostructures synthesized in mixture of OA-OLA at 300 °C and OLA at 275 °C, respectively, which clearly showed agglomeration of particles along with the formation of rectangular sheets in former case and irregular sheets with rough edges in the case of latter.

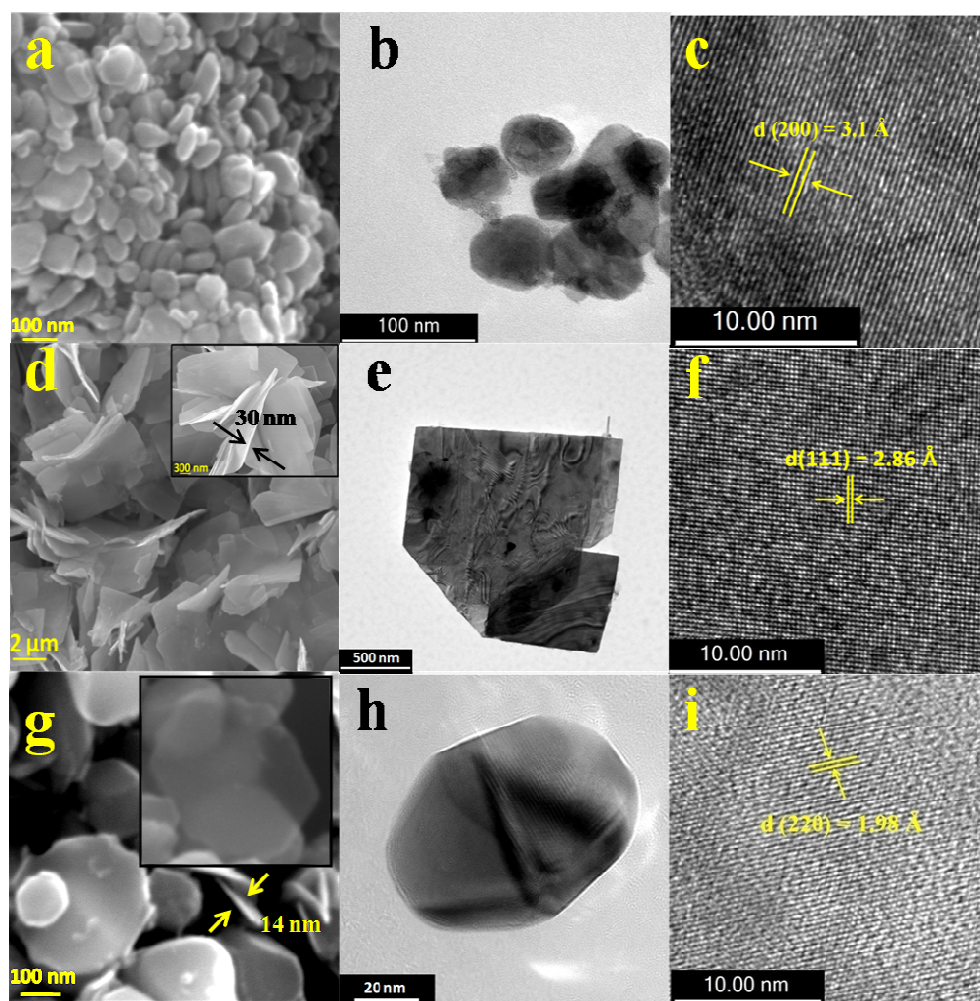


**Fig. 5.14** SEM, TEM and HRTEM of a), b), c) monoclinic CTS obtained from co-thermolysis of  $[^t\text{Bu}_2\text{Sn}(\text{Spyz})_2]$  and  $[\text{Cu}(\text{Spyz})(\text{PPh}_3)_2]$ ; d), e), f) orthorhombic SnS obtained from thermolysis of  $[^t\text{Bu}_2\text{Sn}(\text{Spyz})_2]$ ; g), h), i) cubic  $\text{Cu}_{1.8}\text{S}$  obtained from thermolysis of  $[\text{Cu}(\text{Spyz})(\text{PPh}_3)_2]$  at 300 °C for 20 minutes in OLA as solvent/capping agent.

SEM, TEM and HRTEM of phase pure ternary (CTS) and binary (SnS and Cu<sub>1.8</sub>S) nanostructures synthesized in OLA at 300 °C are shown in Fig. 5.14. The SEM and bright field TEM images of CTS nanostructures depicts the formation of nearly spherical particles with average diameter ~ 40 nm (Fig. 5.14 a, b). The morphology of SnS and Cu<sub>1.8</sub>S as deduced from SEM micrographs revealed the formation of rectangular sheets and nearly hexagonal discs with smooth edges having thickness as small as ~30 nm and 14 nm, respectively (Fig. 5.14 d, g). The TEM images of SnS and Cu<sub>1.8</sub>S shown in Fig. 5.14 e and h exhibit rectangular SnS sheets and hexagonal Cu<sub>1.8</sub>S discs that are almost semi-transparent under TEM electron beam due to thin thickness. The reduced thickness of Cu<sub>1.8</sub>S nanostructures is also evident from the inset of Fig. 5.14 g which shows the formation of nearly transparent hexagonal disc. The high resolution TEM (HRTEM) images of CTS, SnS and Cu<sub>1.8</sub>S in Fig. 5.14 c, f, i revealed the crystalline nature of nanostructures with lattice fringe spacing 3.1, 2.86 and 1.98 Å, respectively, which can be indexed to (200) plane of monoclinic CTS (JCPDS 04-010-5719), (111) plane of orthorhombic SnS (JCPDS 75-0925) and (220) plane of cubic Cu<sub>1.8</sub>S (JCPDS 04-004-7716).

#### **b) Metal selenides (CTSe, SnSe<sub>2</sub>, Cu<sub>2</sub>Se)**

CTSe nanostructures were prepared by co-thermolysis of [Me<sub>2</sub>Sn(2-Sepy(3-Me))<sub>2</sub>] and [Cu(2-Sepy(3-Me))]<sub>4</sub> in a high boiling coordinating solvent like OLA and TOPO. Initially, OLA was used as surface passivating agent due to the fact that amines have good affinity for copper as well as tin and ease of handling OLA during synthesis and purification of nanostructures. The average crystallite size of nanostructures obtained at different temperatures was in the range of 15-30 nm as estimated from p-XRD using Scherrer formula. However, when the growth temperature is less than 300 °C with

reaction time of 10 minutes, only a small amount of tin is incorporated than it is required for a  $\text{Cu}_2\text{SnSe}_3$  as revealed by EDX possibly due to incomplete decomposition of tin precursor. Therefore to synthesize nanostructures of still smaller dimensions with elemental composition close to  $\text{Cu}_2\text{SnSe}_3$ , either reduction in reaction growth time or a stronger coordinating solvent like TOPO need to be used for passivating the surface of nanostructures or a hot injection method in OLA at a temperature greater than or equal to  $300^\circ\text{C}$  serves the purpose. The growth temperature above  $300^\circ\text{C}$ , however only leads to particles of larger size and reducing the reaction time causes tin deficient  $\text{Cu}_2\text{SnSe}_3$ . Thus a strong coordinating solvent, TOPO was chosen to obtain nanostructures of smaller dimensions at a growth temperature of  $300^\circ\text{C}$  and a growth time of 10 minutes which resulted in obtaining tin deficient  $\text{Cu}_2\text{SnSe}_3$  nanostructures of  $\sim 15$  nm. Alternative route, hot injection method, was adopted to prepare nanostructures with smaller size and a composition close to  $\text{Cu}_2\text{SnSe}_3$ .

CTSe nanostructures prepared from  $[\text{Me}_2\text{Sn}(2\text{-Sepy}(3\text{-Me}))_2]$  and  $[\text{Cu}(2\text{-Sepy}(3\text{-Me}))_4]$  were characterized by solid state diffuse reflectance (DRS), p-XRD, SEM, EDX, TEM, X-ray photoelectron spectroscopy (XPS), electron paramagnetic resonance (EPR) and Raman spectroscopic techniques.

The p-XRD patterns of all the nanostructures prepared in OLA at 230, 260,  $300^\circ\text{C}$  for a duration of 10 minutes in a heat up synthesis exhibited peaks at  $2\theta$  of 27.2, 45.1 and  $53.4^\circ$  (Fig 5.15). The p-XRD peaks can be assigned to the reflections originating from (111), (220) and (311) Bragg planes, corresponding to diffraction characteristics of cubic  $\text{Cu}_2\text{SnSe}_3$  (ICDD file no. 03-065-4145) with space group  $F-43(m)$ . The broadness of all the peaks decreases with the increase in the growth temperature indicating the particle size is growing with the increase in temperature. The intensity of peaks clearly indicates

their crystalline nature. The calculated lattice parameters, unit cell volume and crystallite size as estimated by Scherrer formula is listed in Table 5.4.

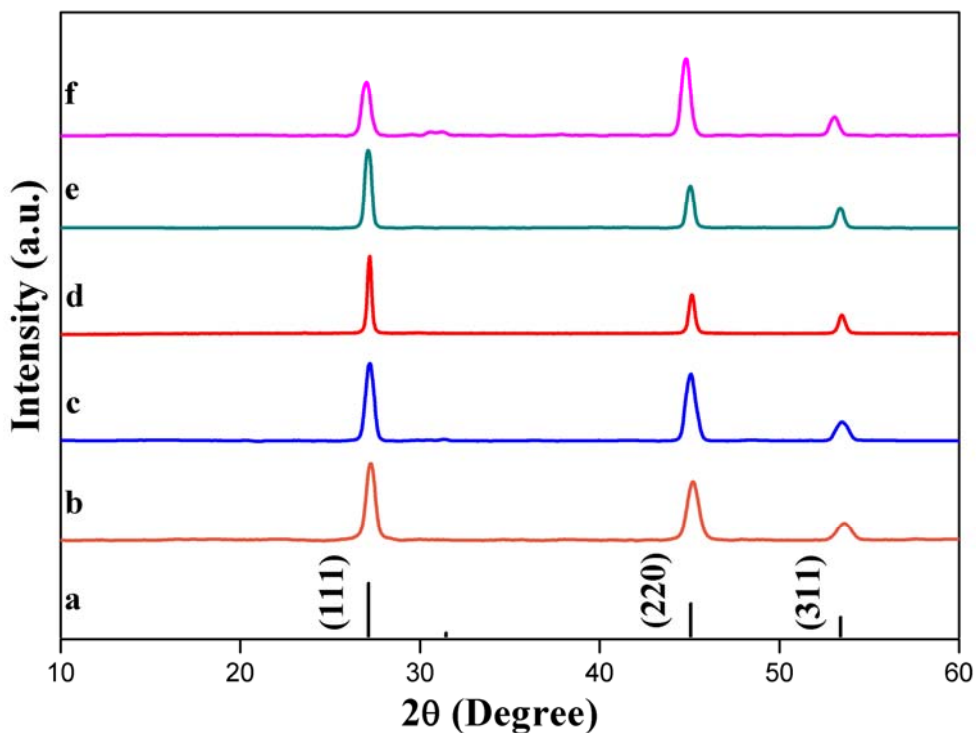


**Fig. 5.15** (a) Simulated XRD pattern of cubic  $\text{Cu}_2\text{SnSe}_3$  (ICDD file no. 03-065-4145). XRD profiles of CTSe nanostructures obtained by thermolysis of  $[\text{Me}_2\text{Sn}(2\text{-Sepy}(3\text{-Me}))_2]$  and  $[\text{Cu}(2\text{-Sepy}(3\text{-Me}))_4]$  in OLA at (b) 230, (c) 260 and (d) 300 °C using heat up method and (e) in OLA at 300 °C using hot injection method (f) 300 °C in TOPO using heat up method.

In order to ascertain the phase purity of CTSe nanostructures from possible binary copper and tin selenides impurities, p-XRD pattern of CTSe nanostructures were compared with that of  $\text{Cu}_2\text{Se}$  and  $\text{SnSe}_2$  prepared by thermolysis of individual precursors employing heat up method using the same conditions (Fig. 5.16). Although there is slight difference in the peak positions of CTSe and  $\text{Cu}_2\text{Se}$ , the intensity ratio of peaks at  $2\theta$  of



27.2 and 45.1° are distinctively different, indicating the diffraction peaks are from different materials.

**Table 5.4** Reaction conditions, structural and elemental composition and optical band gap data of nanostructures.

Method of thermolysis	Solvent	Temperature (± 2 °C)	Cell Constant (Å)	Crystallite size (± 1nm)	EDX Analysis Cu:Sn:Se	Direct band gap (eV)
Heat up	OLA	230	5.6631	15	28:1:21	-
Heat up	OLA	260	5.6762	16	2.5:1:3.6	-
Heat up	OLA	300	5.6846	30	2.1:1:3.3	1.73
Heat up	TOPO	300	5.7172	15	5.7:1:4.3	-
Hot Injection	OLA	300	5.6758	18	2.6:1: 4	1.87

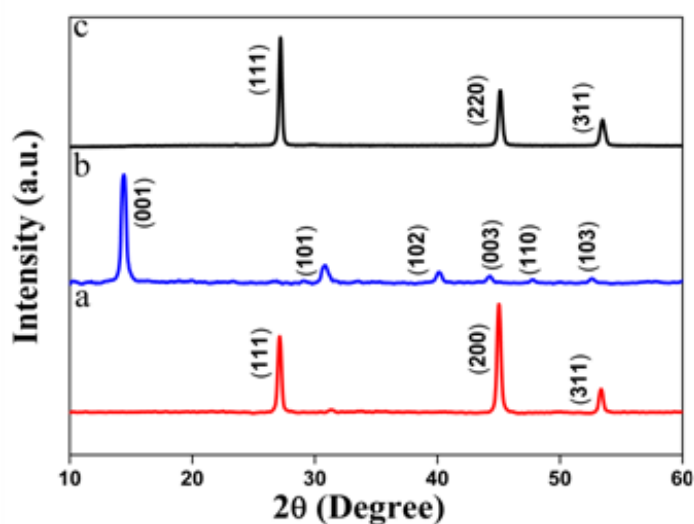


**Fig. 5.16** p-XRD pattern of (a)  $\text{Cu}_2\text{Se}$  obtained by thermolysis of  $[\text{Cu}(2\text{-Sepy}(3\text{-Me}))]_4$ , (b)  $\text{SnSe}_2$  obtained by thermolysis of  $[\text{Me}_2\text{Sn}(2\text{-Sepy}(3\text{-Me}))_2]$  and (c) cubic  $\text{Cu}_2\text{SnSe}_3$  obtained by co-thermolysis of  $[\text{Me}_2\text{Sn}(2\text{-Sepy}(3\text{-Me}))_2]$  and  $[\text{Cu}(2\text{-Sepy}(3\text{-Me}))]_4$  in OLA at 300 °C by heat up method.

Similar to heat up method, p-XRD peak pattern of nanostructures synthesized in OLA at 300 °C for 10 minutes in hot injection method revealed reflections from (111), (220) and (311) planes which matches with cubic  $\text{Cu}_2\text{SnSe}_3$  (ICDD file no. 03-065-4145). In contrast to  $\text{Cu}_2\text{SnSe}_3$  nanostructures obtained in OLA at 300 °C, the nanostructures obtained by co-thermolysis of  $[\text{Me}_2\text{Sn}(2\text{-Sepy}(3\text{-Me}))_2]$  and  $[\text{Cu}(2\text{-Sepy}(3\text{-Me}))_4]$  in TOPO at 300 °C for a duration of 10 minutes in a heat up synthesis displayed peaks at 27.0, 44.8 and 53.1°, which are slightly shifted with respect to diffraction characteristics of cubic phase  $\text{Cu}_2\text{SnSe}_3$  (ICDD file no. 03-065-4145) (Fig. 5.15f).

The morphology of CTSe nanostructures evaluated from SEM micrographs, obtained at 300 °C by heat up experiments in OLA, showed flower like structures made up of nanosheets with average thickness of  $11 \pm 1$  nm (Fig. 5.17a). Corresponding, TEM image of the CTSe nanostructures revealed the formation of nanosheets (Fig. 5.17b) while the SAED pattern of nanosheets showed circular patterns indicating the polycrystalline nature of nanostructures (Fig. 5.17c). The SAED pattern displayed a set of lattice planes, (111), (220) and (200) corresponding to the cubic phase  $\text{Cu}_2\text{SnSe}_3$ .

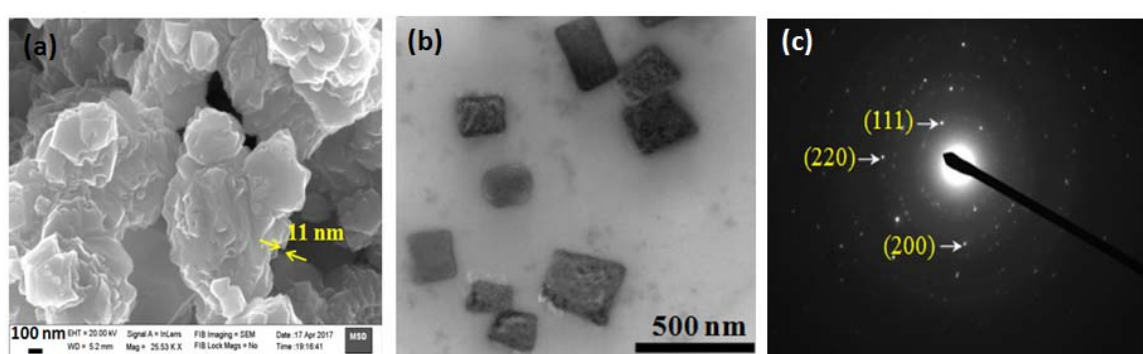


**Fig. 5.17** a) SEM, b) TEM and c) SAED pattern of CTSe nanostructures obtained by co-thermolysis of  $[\text{Me}_2\text{Sn}(2\text{-Sepy}(3\text{-Me}))_2]$  and  $[\text{Cu}(2\text{-Sepy}(3\text{-Me}))_4]$  in OLA at 300 °C by heat up method.

Co-thermolysis of  $[\text{Me}_2\text{Sn}(2\text{-Sepy}(3\text{-Me}))_2]$  and  $[\text{Cu}(2\text{-Sepy}(3\text{-Me}))_4]$  in TOPO afforded disc like structures (Fig. 5.18a). In contrast to the nanostructures obtained in OLA using heat up method at 300°C, SEM image of the sample obtained by hot injection method revealed a mixture of sheets and polyhedra (Fig. 5.18b).

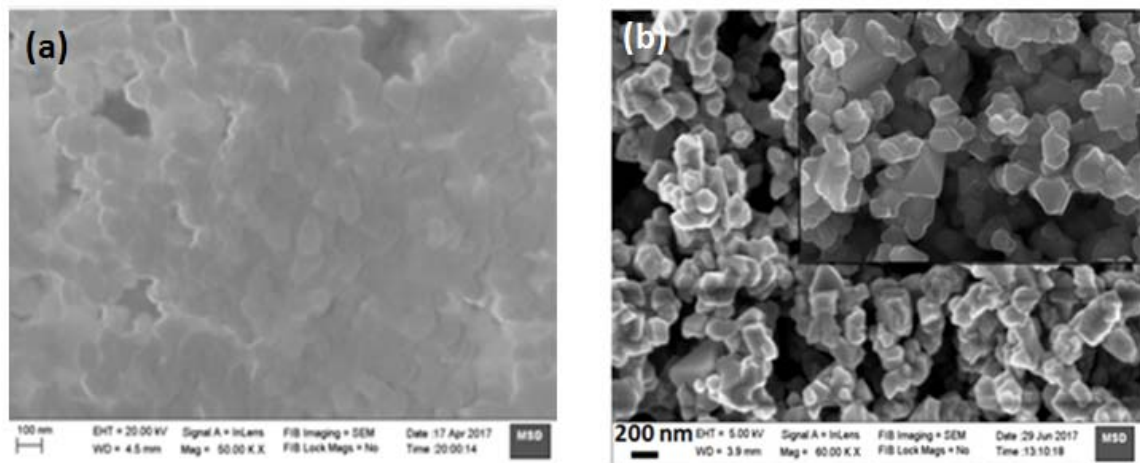


**Fig. 5.18** SEM micrographs of nanostructures obtained by co-thermolysis of  $[\text{Me}_2\text{Sn}(2\text{-Sepy}(3\text{-Me}))_2]$  and  $[\text{Cu}(2\text{-Sepy}(3\text{-Me}))_4]$  in a) TOPO (heat up method), b) OLA (hot injection method) at 300 °C.

It is difficult to make clear distinction between  $\text{Cu}_2\text{SnSe}_3$  and  $\text{Cu}_2\text{Se}/\text{Cu}_{1.8}\text{Se}$  by p-XRD alone because of similar p-XRD patterns for  $\text{Cu}_2\text{SnSe}_3$  and  $\text{Cu}_2\text{Se}/\text{Cu}_{1.8}\text{Se}$ . In order to identify the chemical composition unambiguously, EDX analyses (Table 5.4) were performed on all the samples on different locations. The EDX results for the sample prepared at 300 °C in OLA are in conformity with the composition of  $\text{Cu}_2\text{SnSe}_3$  whereas other samples prepared either at low temperatures in OLA or in TOPO revealed tin deficiencies (Table 5.4). Tin deficient CTSe in TOPO may be attributed to stronger coordinating nature of TOPO present either on the surface or in the vicinity of copper selenide formed initially by decomposition of copper precursor  $[\text{Cu}(2\text{-Sepy}(3\text{-Me}))_4]$

during heat up method which in turn hinders incomplete alloying *in situ* with tin selenide formed from  $[\text{Me}_2\text{Sn}(2\text{-Sepy}(3\text{-Me}))_2]$ . In contrast weaker OLA allows complete alloying of copper selenide and tin selenide *in situ* at 300 °C leading to the formation stoichiometric  $\text{Cu}_2\text{SnSe}_3$  nanostructures. Thus further investigations on the sample prepared by co-thermolysis of  $[\text{Me}_2\text{Sn}(2\text{-Sepy}(3\text{-Me}))_2]$  and  $[\text{Cu}(2\text{-Sepy}(3\text{-Me}))_4]$  in OLA at 300 °C for duration of 10 minutes in a heat up synthesis were carried out.

To confirm whether Cu, Sn, and Se are homogeneously distributed in the sample prepared at 300 °C in OLA, 2D-projected elemental mapping of the nanostructure was performed which showed uniform distribution of all the three elements (Fig. 5.19).

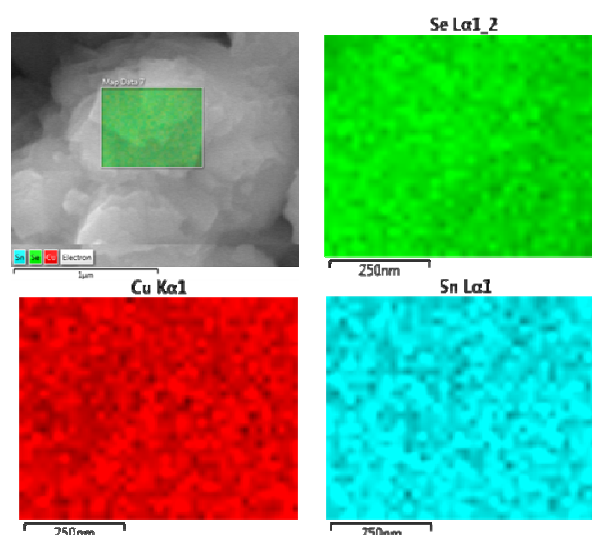


**Fig. 5.19** Elemental mapping of CTSe nanostructure obtained by co-thermolysis of  $[\text{Me}_2\text{Sn}(2\text{-Sepy}(3\text{-Me}))_2]$  and  $[\text{Cu}(2\text{-Sepy}(3\text{-Me}))_4]$  in OLA at 300 °C using heat up method.

To further substantiate the phase purity of CTSe nanostructures obtained in OLA at 300 °C by heat up method, Raman spectroscopic studies were carried out. Raman spectroscopy gives direct insight about the vibrational properties of crystalline material.

Raman spectrum of CTSe synthesized in OLA at 300 °C showed three peaks, an intense peak at  $\sim 174\text{ cm}^{-1}$  and relatively minor peaks at 206, 249 (Fig. 5.20a). These peaks are in good agreement with the previously reported data for  $\text{Cu}_2\text{SnSe}_3$  (Table 5.5) [42-45]. The intense peak corresponds to  $A_1$  symmetry mode related to the vibration of anion atom with cation at rest. The slight shift in the Raman peak positions could be due to either the size effects, or excitation intensity of the laser [120,246]. In order to ensure the absence of binary impurities, Raman spectra of as prepared colloidal  $\text{Cu}_2\text{Se}$  and  $\text{SnSe}_2$  nanostructures under the same conditions were recorded and compared with that of CTSe (Fig. 5.20). The comparative spectra confirmed the purity of CTSe phase without any additional binary compound impurity.

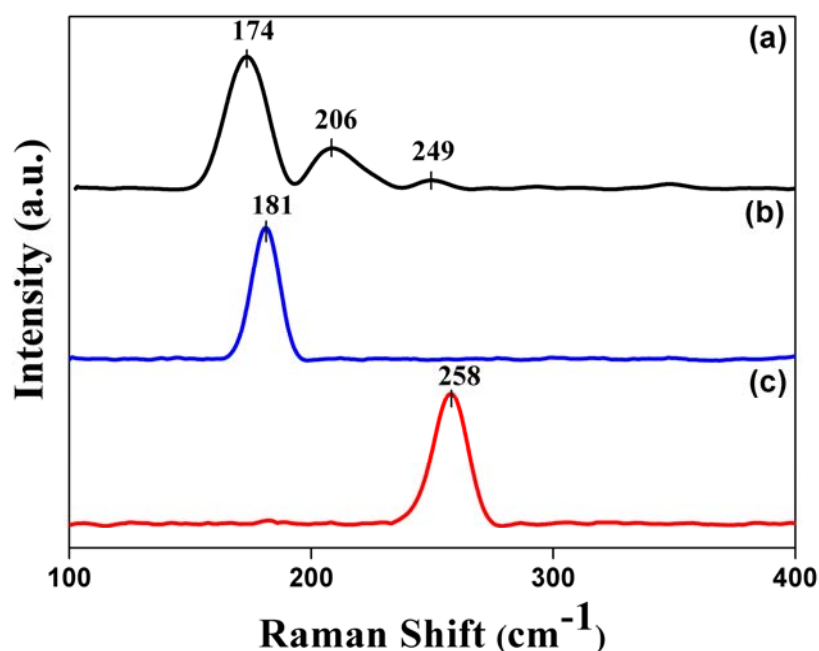


**Fig. 5.20** Raman spectra of a) CTSe, b)  $\text{Cu}_2\text{Se}$  and c)  $\text{SnSe}_2$  nanostructures obtained either by thermolysis of  $[\text{Me}_2\text{Sn}(2\text{-Sepy}(3\text{-Me}))_2]$  and  $[\text{Cu}(2\text{-Sepy}(3\text{-Me}))_4]$  individually or together in OLA at 300 °C by heat up method.

**Table 5.5** Raman spectroscopic data for CTSe.

	Raman Peaks (Present Work)	Raman Peaks [144]	Raman Peaks [126]	Raman Peaks [245]	Raman Peaks [246]
1	174	180	180	178	177
2	206	Not observed	200	204	Not calculated
3	249	Not observed	Not observed	244	246

X-ray photoelectron spectroscopy (XPS) was employed to investigate the chemical states and surface properties of  $\text{Cu}_2\text{SnSe}_3$  nanostructures. The survey scan was carried out in the binding energy range of 0-1000 eV and the core level photoelectron spectra of Cu2p, Sn3d, Se3d, along with the fitting profile are shown in Fig. 5.21.

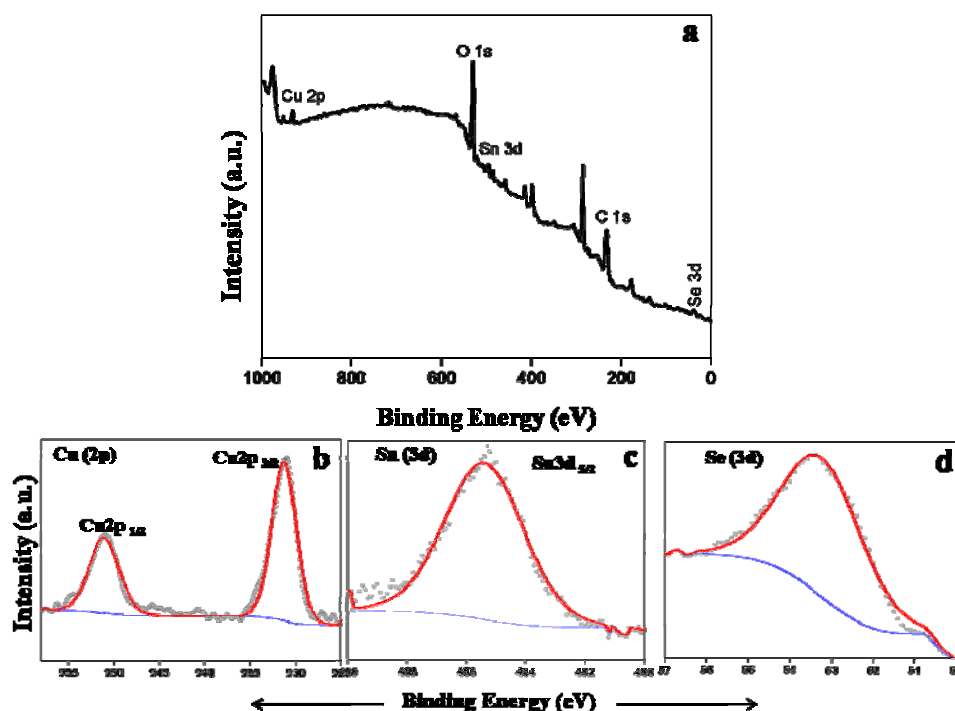


**Fig. 5.21** (a) X-ray photoelectron survey scan for CTSe nanostructures obtained by co-thermolysis of  $[\text{Me}_2\text{Sn}(2\text{-Sepy}(3\text{-Me}))_2]$  and  $[\text{Cu}(2\text{-Sepy}(3\text{-Me}))_4]$  in OLA at 300 °C by heat up method. (b) Cu 2p, (c) Sn 3d and (d) Se 3d core level spectra.

The binding energy of Cu 2p<sub>1/2</sub> and Cu2p<sub>3/2</sub> peaks are at 952 and 932 eV, respectively which are indicative of the presence of Cu<sup>+</sup> and can be compared with the binding energies reported for Cu<sub>2</sub>O and CuCl [247]. The absence of satellite peaks in the range of 936-942 eV implies the nonexistence of Cu<sup>2+</sup> ion. The binding energies for Sn3d<sub>5/2</sub> at 486 are closely related to Sn(IV). The Se 3d value at 56 eV is also in good agreement with those reported in literature [126]. Hence the XPS analysis shows the normal valence state of Cu, Sn and Se are +1, +4 and -2, which confirms the formation of Cu<sub>2</sub>SnSe<sub>3</sub> at 300°C in OLA.

Ge et al. [248] reported paramagnetic behaviour of Cu<sub>2</sub>SnSe<sub>3</sub> which can either be due to the presence of Cu<sup>2+</sup> in the form of Cu<sub>2</sub>SnSe<sub>4</sub> or due to other paramagnetic impurity phases/ presence of defect centres. Thus magnetization measurements as a function of temperature, T and applied magnetic field, H on nanostructures of Cu<sub>2</sub>SnSe<sub>3</sub> were carried out. Magnetization (magnetic moment per unit mass, M) vs T data is measured under high H, 5000 Oe in zero field cooled (ZFC) and field cooled (FC) modes (Fig. 5.22). At high temperature (>250K), M became negative in both the modes characteristic of diamagnetic behaviour as expected from 3d<sup>10</sup> configuration of Cu in Cu<sub>2</sub>SnSe<sub>3</sub>. With decreasing temperature it showed an increase in M value characteristics of paramagnetic behaviour also noted by Ge et al. [248]. A slight difference in M<sub>FC</sub> and M<sub>ZFC</sub> values in the temperature range 5 – 50 K was also noted indicative of weak magnetic ordering. The weak magnetic ordering was further confirmed by measurement of hysteresis loop (M vs H) at 5K (inset of Fig. 5.22). To ascertain whether the magnetism in otherwise diamagnetic Cu<sub>2</sub>SnSe<sub>3</sub> is due to the presence of any Cu<sup>2+</sup> (a d<sup>9</sup> configuration) impurity, an EPR investigation has been performed.

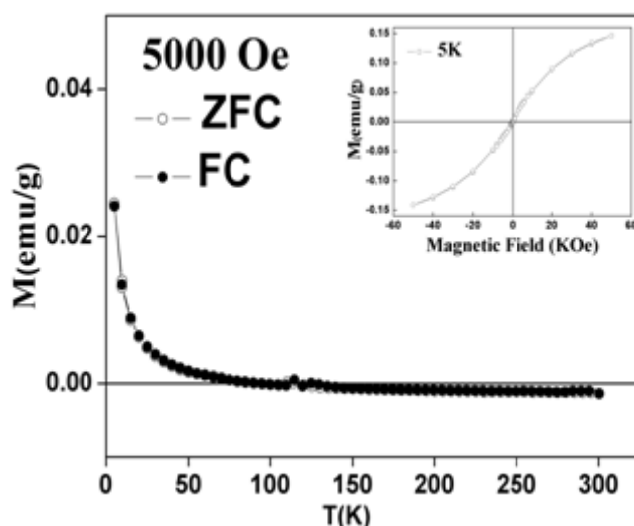


**Fig. 5.22** Temperature dependent magnetic susceptibility CTSe nanostructures obtained by co-thermolysis of  $[\text{Me}_2\text{Sn}(2\text{-Sepy}(3\text{-Me}))_2]$  and  $[\text{Cu}(2\text{-Sepy}(3\text{-Me}))_4]$  in OLA at 300 °C by heat up method. Inset shows field dependent magnetization curve for  $\text{Cu}_2\text{SnSe}_3$  at 5K.

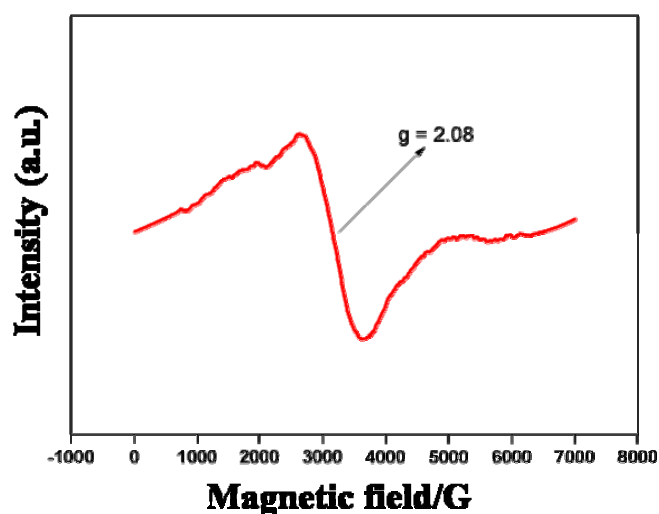


**Fig. 5.23** EPR spectrum of CTSe nanostructures obtained by co-thermolysis of  $[\text{Me}_2\text{Sn}(2\text{-Sepy}(3\text{-Me}))_2]$  and  $[\text{Cu}(2\text{-Sepy}(3\text{-Me}))_4]$  in OLA at 300 °C by heat up method.

EPR spectrum of CTSe nanostructure (Fig. 5.23) showed a weak signal at  $g = 2.08$  without any signature hyperfine splitting of  $\text{Cu}^{2+}$ , indicating the absence of  $\text{Cu}^{2+}$  in the sample. Therefore, the weak magnetization at low temperatures could be due to impurity



phases or the presence of some defect centres. The broad line width of the EPR signal indicates a certain degree of heterogeneity typically being observed at the surface of nanostructure crystals [249].

### 5.3.4 Optical properties

Considering the importance of CTS, CTSe, SnS, SnSe<sub>2</sub>, Cu<sub>1.8</sub>S and Cu<sub>2</sub>Se as photon absorber materials for photovoltaic cells, the optical properties of phase pure nanostructures obtained in OLA at 300 °C were investigated by diffuse reflectance spectroscopy (DRS). The optical band gaps of these materials were determined by using a plot of Kubelka-Munk function,  $F(R)$  as given in equation 4.2 of chapter 4.

#### a) Metal sulfides

The direct band gaps of CTS, SnS and Cu<sub>1.8</sub>S were estimated as 1.4, 1.8 and 2.0 eV, respectively by plotting the relation  $[F(R)h\nu]^2$  vs  $h\nu$  derived from Tauc's model (for  $n = 2$ ) (Fig. 5.24). These values are blue shifted with respect to bulk CTS (0.9 eV) [117], SnS (1.3 eV) [111] and Cu<sub>1.8</sub>S (1.2 eV) [250]. The increase in the band gap value of the nanostructures may be either due to quantum confinement or lattice distortion or surface lattice defects. The direct band gap values evaluated in present investigation are consistent with those reported in literature (0.9-1.77 eV for CTS [229,117], 1.3-1.9 eV for SnS [111], and 1.2-2.3 eV for Cu<sub>1.8</sub>S [251]).

#### b) Metal selenides

The direct band gap of CTSe (Fig. 5.25) nanostructures obtained in OLA at 300°C by heat up and hot injection method are 1.73 and 1.87 eV, respectively, which are in accordance with the literature data [144,252].

The direct band gaps of Cu<sub>2</sub>SnSe<sub>3</sub> nanostructures are shifted with respect to the direct band gap of bulk Cu<sub>2</sub>SnSe<sub>3</sub> 1.12 eV [253]. The increase in the band gap from 1.73

in heat up method to 1.87 eV in hot injection method may be attributed to decrease in the dimensions of the nanostructures.

The optimal band gap of these metal sulfide and metal selenide nanostructures reveals their suitability as a photo-absorber material for solar cell application.

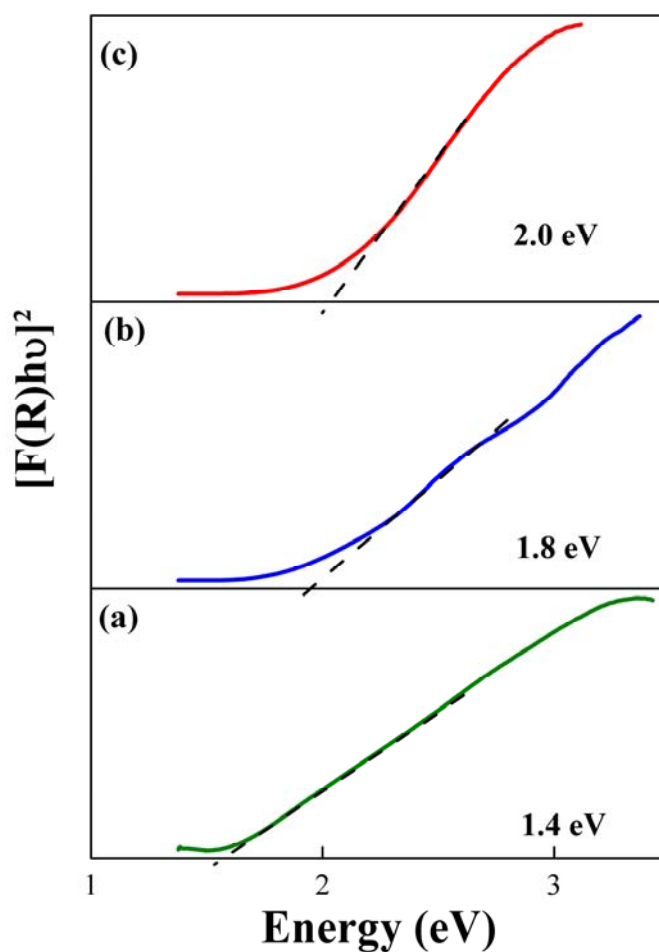


**Fig. 5.24** Plots of  $[F(R)hv]^2$  vs energy generated by Kubelka-Munk transformation of solid-state diffuse reflectance data of a) monoclinic CTS obtained from co-thermolysis of  $[^t\text{Bu}_2\text{Sn}(\text{Spyz})_2]$  and  $[\text{Cu}(\text{Spyz})(\text{PPh}_3)_2]$ , b) orthorhombic SnS obtained from thermolysis of  $[^t\text{Bu}_2\text{Sn}(\text{Spyz})_2]$  and c) cubic  $\text{Cu}_{1.8}\text{S}$  obtained from thermolysis of  $[\text{Cu}(\text{Spyz})(\text{PPh}_3)_2]$  at 300 °C for 20 minutes in OLA as solvent/capping agent, respectively for determining direct band gap energies.

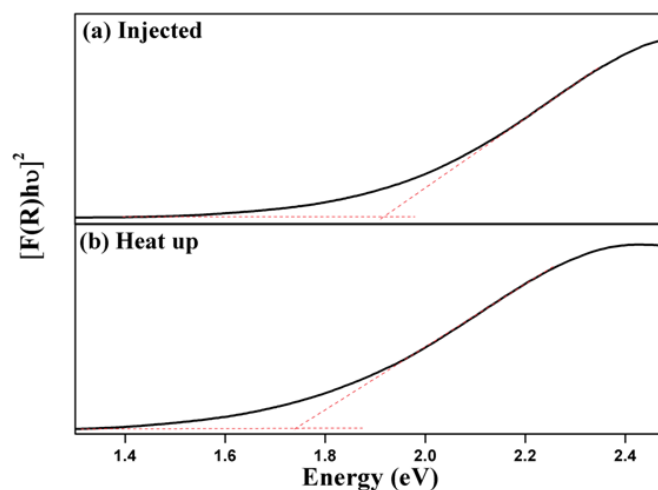


**Fig. 5.25** Stack Plots of  $[F(R)hv]^2$  vs energy generated by Kubelka-Munk transformation of solid-state diffuse reflectance data of CTSe nanostructures obtained by co-thermolysis of  $[Me_2Sn(2-Sepy(3-Me))_2]$  and  $[Cu(2-Sepy(3-Me))]_4$  in OLA at 300 °C by (a) hot injection method and (b) heat up method.

### 5.3.5 Photoelectrochemical studies

Photo-response of nanostructures (CTS, CTSe, SnS and  $Cu_{1.8}S$ ) has been evaluated by preparing photo electrochemical cell. Current-voltage (I-V) characteristics for the CTS, SnS and  $Cu_{1.8}S$  nanostructures showed nonlinear behaviour (Fig. 5.26 and 5.27). The nonlinear I-V characteristics exhibit the junction properties with increase in current under illumination conditions relative to that of dark current due to photo-generated carriers. It has been observed that increment in photocurrent under illumination is better in case of CTS nanostructure as compared to SnS and  $Cu_{1.8}S$  nanostructures. The absorber film showed a power conversion efficiency of 1.7% without any antireflection coating which is comparable to the reported values [254].

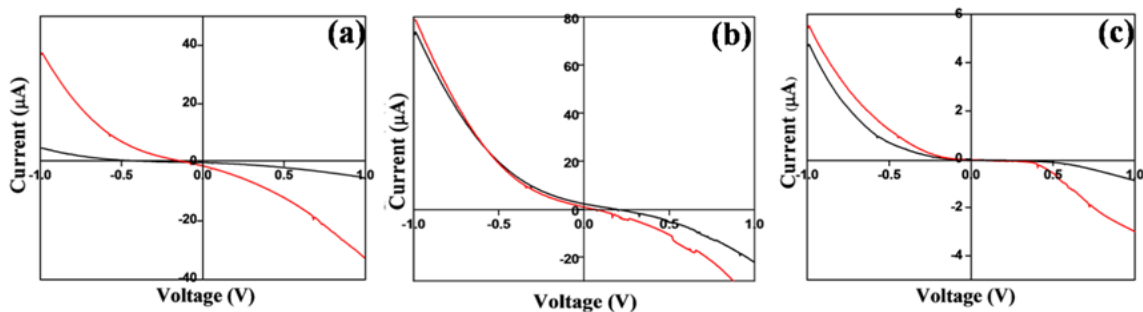


**Fig. 5.26** I-V characteristics of a) CTS, b)  $\text{Cu}_{1.8}\text{S}$  and c)  $\text{SnS}$  nanostructures obtained by thermolysis of precursors in OLA at 300 °C for 20 minutes under dark (black) and light (red) conditions

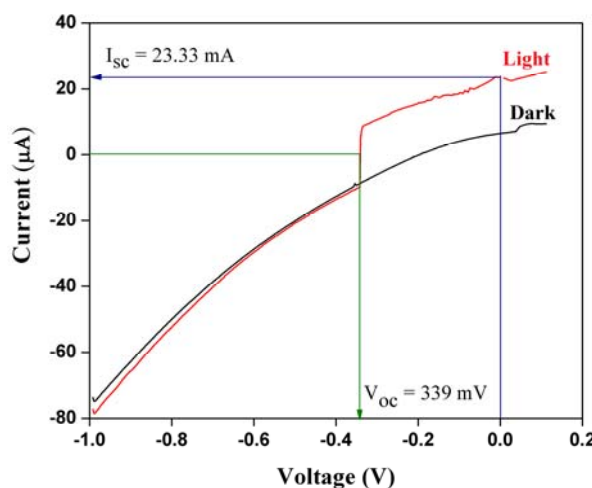


**Fig. 5.27** I-V characteristics of CTSe nanostructure (Efficiency = 1.7 %;  $V_{oc}$  = 339 mV;  $J_{sc}$  =  $33.3 \mu\text{A}/\text{cm}^2$ ; Fill factor = 0.3) obtained by co-thermolysis of  $[\text{Me}_2\text{Sn}(2\text{-Sepy}(3\text{-Me}))_2]$  and  $[\text{Cu}(2\text{-Sepy}(3\text{-Me}))_4]$  in OLA at 300 °C.

Photosensitivity and photo-stability are important criteria, to select an absorber material for photovoltaic applications. Fig. 5.28 and 5.29 shows the photo response of nanostructures (CTS,  $\text{Cu}_{1.8}\text{S}$ ) and CTSe, respectively as a function of time, measured under light intensity of  $200 \mu\text{W}/\text{cm}^2$  with bias voltages of 0.5 V. Both metal sulfide and metal selenide nanostructures showed switching characteristics during the repeated cycles

of on-off experiments. From Fig 5.28 it is clear that, CTS nanostructures showed better photosensitivity and enhanced photo-response over number of on-off cycles as compared to  $\text{Cu}_{1.8}\text{S}$  particles.

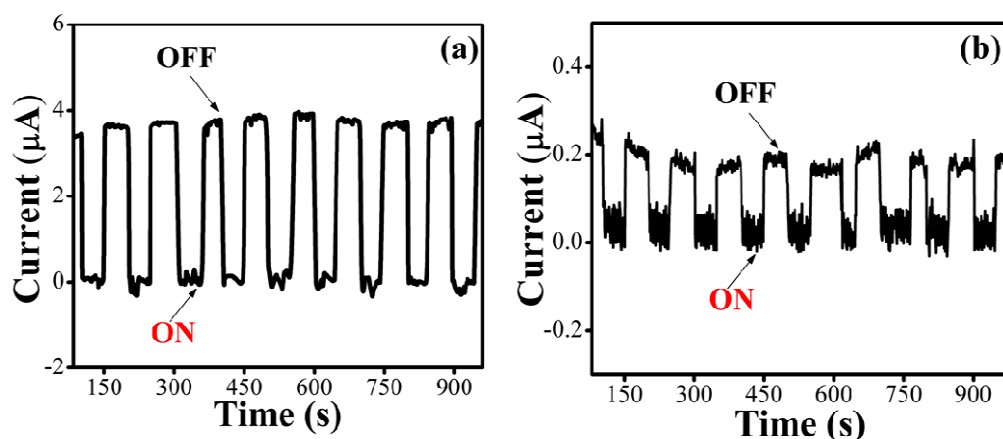


**Fig. 5.28** Current vs Time plot phase pure a) monoclinic CTS and b) cubic  $\text{Cu}_{1.8}\text{S}$ , nanostructures obtained at 300 °C for 20 minutes using OLA as reaction solvent.

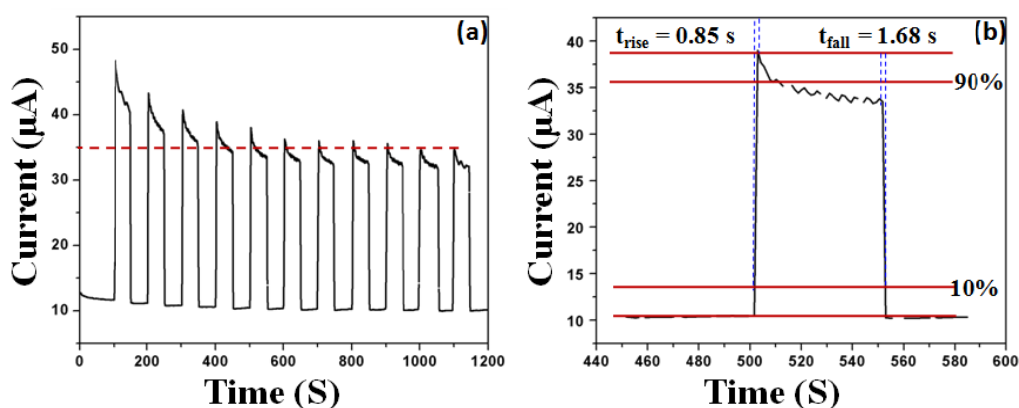


**Fig. 5.29** (a) Current vs. time plot of CTSe nanostructures obtained by thermolysis of co-thermolysis of  $[\text{Me}_2\text{Sn}(2\text{-Sepy}(3\text{-Me}))_2]$  and  $[\text{Cu}(2\text{-Sepy}(3\text{-Me}))_4]$  in OLA at 300 °C; (b) expanded view of one of the cycles.

Switching behaviour of CTSe nanostructures are shown in Fig. 5.29a, where 11 on and off cycles are presented, the fifth cycle (middle one) (Fig. 5.29b) has been chosen to calculate rise time and fall time, i.e the time required for the current to increase from 10

to 90% of the peak value is 0.85 and 1.68 s, respectively. The measurements revealed that rise times are faster than fall times and that may be due to the involvement of trap states and defects in switching process [255].

The reproducibility of photocurrent suggests high stability of CTS and CTSe nanostructures under alternating light and dark conditions. The result indicates the potential application of these nanostructures in photo detector and photovoltaic applications. It is worth mentioning that no such switching characteristics were observed in case of orthorhombic SnS under the same set of conditions.

# Chapter 6

## Conclusions and Future Work

The present thesis deals with the synthesis, characterization and utilization of precursors for the preparation of tin chalcogenide nanostructures. Binary and ternary tin chalcogenide materials being non toxic, low cost find relevance in the field of photovoltaics, thermoelectric devices, lithium ion batteries, etc. Considering the importance of tin chalcogenides, various wet chemical routes such as solvothermal, hydrothermal, polyol methods, etc. have been adopted for their synthesis. However, most of these methods involve the use of highly sensitive and toxic reagents during the preparation. Of late molecular precursor route has emerged as a versatile technique for the synthesis of metal chalcogenide nanoparticles and deposition of thin films which offer key advantages over other routes in terms of phase purity and better stoichiometry. However, this route has met with a little success in the case of tin chalcogenides and related ternary materials possibly due to limited exploration of tin complexes with chalcogen ligands as molecular precursors. Reported precursors have certain drawbacks including i) use of hazardous chemicals during the preparation (phosphine) or utilization ( $\text{H}_2\text{S}$ ) of precursors, ii) inappropriate stoichiometry and incorporation of impurities (elemental/ phase) in the final product and iii) poor solubility of precursors due to the formation of non-crystalline polymers stabilized through bridging chalcogenolate ligands. Hence it is important to develop molecular precursors with appropriate physico-chemical properties for the preparation of binary and ternary tin chalcogenide nanostructures. In this study, we have synthesized a series of organotin complexes with a variety of internally functionalized chalcogen ligands. All the complexes were characterized by

elemental analysis, multi-nuclear NMR spectroscopy while the structures of several complexes have been established unambiguously by single crystal X-ray diffraction analysis. Thermal behaviour of the complexes were analysed by TGA before employing them as molecular precursors for the preparation of nanomaterials and deposition of tin chalcogenide thin films by aerosol assisted chemical vapour deposition (AACVD). The summary of the key findings are listed below:

Chapter one gives a general introduction to semiconductor nanomaterials followed by a brief discussion about the structure and unique properties of binary and ternary tin chalcogenide nanomaterials which leads to their utility in the field of photovoltaics and thermoelectric devices. This chapter gives an overview of various solution based synthetic methodologies employed for the preparation of tin chalcogenide materials with special attention to molecular precursor route, its significance and the challenges associated with it. A review of various precursors reported in literature for the preparation of tin chalcogenide nanomaterials has also been included in this chapter. Last section of the chapter provides a brief note on the objective and motivation of the present work.

The second chapter describes general materials and chemicals used during the synthesis of complexes and nanomaterials followed by a brief discussion on experimental tools and techniques such as elemental analysis (CHNS analysis), multi-nuclear magnetic resonance (NMR) spectroscopy, single crystal and powder X-ray diffraction analysis (SCXRD and p-XRD), thermogravimetric analysis (TGA), electron microscopic studies (SEM and TEM), energy dispersive X-ray analysis (EDX), selective area electron diffraction (SAED), Raman spectroscopy, Diffuse reflectance spectroscopy (DRS), photoelectrochemical studies (PEC), etc. employed during the course of the present investigations.



The third chapter of thesis deals with the synthesis and characterization of air-stable monomeric diorganotin complexes of pyridyl and pyrimidyl thiolates. The synthesis of complexes involves a reaction of dialkyltin dichloride with sodium pyridyl/pyrimidyl thiolates. Single crystal X-ray structure of complexes  $[R_2Sn(2-Spy)_2]$  ( $R = Et, ^tBu$ ) and  $[R_2SnCl(2-SpymMe_2)]$  ( $R = Me, Et, ^tBu$ ) showed the central tin acquires a skew trapezoidal configuration in the former while the distorted trigonal-bipyramidal geometry in the latter complexes. Thermogravimetric analysis revealed that the complexes  $[R_2Sn(2-Spy)_2]$  ( $R = Me, Et$ ) underwent two step decomposition while the *tert*-Butyl derivative showed single step decomposition leading to the formation of elemental Sn and SnS, respectively. The complexes of the type  $[R_2SnCl(2-SpymMe_2)]$  ( $R = Me, Et$ ) underwent disproportionation leading to the formation of  $R_2SnCl_2$  and SnS. However,  $[^tBu_2SnCl(2-SpymMe_2)]$  undergoes a single step decomposition to form Sn. Some of these complexes have been employed as single source molecular precursors for the preparation of phase pure tin sulfide nano-sheets while  $[^tBu_2Sn(Spy)_2]$  was used for the deposition of tin sulfide thin films by aerosol assisted chemical vapour deposition (AACVD). Hexagonal and rectangular sheets were isolated by thermolysis of different precursors. The thickness of the sheets is in the range of 30-80 nm which showed direct spanning from 1.6-1.9 eV. A shift of 0.31-0.6 eV with respect to bulk band gaps can be accounted for the surface effect of the carriers, lattice distortions or surface lattice defects.

The fourth chapter describes the synthesis and characterization of diorganotin complexes with substituted pyridyl and pyrimidyl selenolates. The complexes are monomeric and air stable. Single crystal X-ray analysis revealed the overall geometry around tin as skew trapezoidal bipyramidal in case of  $[R_2Sn(2-Sepy(5-Me))_2]$  and distorted tetrahedral in case of  $[R_2Sn(2-SepymMe_2)_2]$ . TG analysis revealed that pyridyl

complexes  $[R_2Sn(2-Sepy(5-Me))_2]$  ( $R = Me, Et$ ) decomposed in the range of 260-295 °C to give SnSe, while  $[^tBu_2Sn(2-Sepy(5-Me))_2]$  underwent a two step decomposition, initially forming  $SnSe_2$  before the formation of SnSe. The bis pyrimidyl complexes showed single step decomposition either leading to the formation of SnSe or  $SnSe_2$ . These complexes have been used as single source molecular precursors for the preparation of tin selenide nanostructures in the form of nanomaterials and thin films. Thermolysis of  $[^tBu_2Sn(2-Sepy(5-Me))_2]$  in an appropriate solvent yielded tin selenide ( $SnSe$  and  $SnSe_2$ ) of different composition. Phase pure  $SnSe_2$  with hexagonal morphology was formed in ODE while use of OLA results in the formation of assembly of irregular sheets of orthorhombic SnSe. Experiments revealed that choice of solvent is highly crucial in deciding the phase purity of nanostructures. Thermolysis of  $[R_2Sn(2-SepymMe_2)_2]$  ( $R = Et, ^nBu, ^tBu$ ) in OLA for different time duration establish the effect of different alkyl groups and growth duration on the morphology and phase purity of nanostructures. In contrast to the thermolysis of  $[^tBu_2Sn(2-Sepy(5-Me))_2]$  in OLA which led to the formation of SnSe, thermolysis of  $[R_2Sn(2-SepymMe_2)_2]$  in OLA always afforded  $SnSe_2$  nanosheets and this can be attributed to the stronger Sn-Se bonds in the latter complexes compared to former one. The thickness of the nano sheets were in the range of 10-20 nm. *tert*-Butyl derivative of  $[R_2Sn(2-SepymMe_2)_2]$  was employed for the deposition of  $SnSe_2$  thin films with hierarchical flower like structures. The band gaps as deduced from diffuse reflectance spectroscopy (DRS) vary from 1.75 to 2.1 eV (direct) while that of thin films are in the range of 2.06-2.12 eV which are blue shifted compared to bulk  $SnSe_2$  and SnSe. Utility of these nanostructures as photon absorber materials for solar cell applications was assessed through photo-electrochemical studies.  $SnSe_2$  nanostructures exhibit good photo-stability and photo-response behaviour which has been

faster switching characteristics while no such behaviour was observed in case of SnSe nanostructures.

The fifth chapter documents the synthesis and characterization of molecular precursors for the preparation of technologically important ternary tin chalcogenide nanostructures ( $\text{Cu}_2\text{SnS}_3$  and  $\text{Cu}_2\text{SnSe}_3$ ). The molecular precursor route was underexplored and there is hardly any report in literature dealing with the preparation of these nanostructures *via* molecular precursor route. As part of our study, we wished to explore the precursor route for ternary materials as well. To this end, we synthesized tin and copper complexes with 2-pyrazinyl thiolate and 3-methyl-2-pyridyl selenolate. The synthesis involves a straight forward reaction of metal salts ( $t\text{Bu}_2\text{SnCl}_2$ ,  $\text{Me}_2\text{SnCl}_2$ ,  $(\text{PPh}_3)_2\text{CuCl}$ ,  $\text{CuCl}$ ) with sodium pyrazinyl thiolate/ pyridyl selenolates. Single crystal X-ray structure of complexes  $[t\text{Bu}_2\text{Sn}(\text{Spyz})_2]$ ,  $[(\text{PPh}_3)_2\text{Cu}(\text{Spyz})]$  and  $[\text{Me}_2\text{Sn}(2\text{-Sepy}(3\text{-Me}))_2]$  showed a distorted tetrahedral geometry around tin and copper. TG analysis of metal thiolates and metal selenolates complexes revealed closely related decomposition temperatures with the formation of the corresponding metal sulfide and metal selenide. The potential of the complexes as molecular precursors for the preparation of  $\text{Cu}_2\text{SnS}_3$  and  $\text{Cu}_2\text{SnSe}_3$  along with binary materials SnS, CuS,  $\text{SnSe}_2$  and  $\text{Cu}_2\text{Se}$  has been evaluated under different reaction conditions. p-XRD, EDX, Raman spectroscopy, SEM, TEM and HR-TEM provide clear evidence that co-thermolysis of precursors  $[t\text{Bu}_2\text{Sn}(\text{Spyz})_2]$  and  $[(\text{PPh}_3)_2\text{Cu}(\text{Spyz})]$  produced phase pure  $\text{Cu}_2\text{SnS}_3$  with nearly spherical shape, rectangular sheets of orthorhombic SnS and hexagonal morphology of cubic  $\text{Cu}_{1.8}\text{S}$  in OLA while thermolysis in OA or OA-OLA leads to  $\text{Cu}_2\text{SnS}_3$  contaminated with binary impurities. On the other hand, phase pure  $\text{Cu}_2\text{SnSe}_3$  nanostructures have been synthesized using air stable  $[\text{Me}_2\text{Sn}(2\text{-Sepy}(3\text{-Me}))_2]$  and  $[\text{Cu}(2\text{-Sepy}(3\text{-Me}))_4]$  molecular precursors. The effect of reaction temperature and the coordinating solvent on the composition of

nanostructures were investigated. The temperatures studies revealed that only tin deficient  $\text{Cu}_2\text{SnSe}_3$  nanostructures were formed when the reaction temperatures are below 300 °C both in OLA and TOPO. At 300 °C, stoichiometric  $\text{Cu}_2\text{SnSe}_3$  nanosheets with homogeneous distribution of elements were obtained in a weak coordinating solvent like OLA while tin deficient  $\text{Cu}_2\text{SnSe}_3$  nanostructures were formed in the case of strong coordinating solvent like TOPO. The reason for tin deficient  $\text{Cu}_2\text{SnSe}_3$  in TOPO may be due to the presence of TOPO either on the surface or in the vicinity of copper selenide leading to its incomplete alloying with tin selenide. Magnetization, XPS and EPR studies of stoichiometric  $\text{Cu}_2\text{SnSe}_3$  nanosheets were investigated to clear the ambiguity over the origin of weak magnetization in otherwise diamagnetic  $\text{Cu}_2\text{SnSe}_3$  nanostructures as reported earlier. The studies confirmed that weak magnetization in these structures is due to the presence of some defects and not due to Cu(II) impurities in the sample. The band gap of  $\text{Cu}_2\text{SnS}_3$  nanostructures (1.4 eV) and  $\text{Cu}_2\text{SnSe}_3$  nanosheets (1.73 eV) derived from DRS, is in the range of optimum band gap required for solar energy absorption. The band gaps of nanostructures are blue shifted relative to bulk counterpart. PEC studies revealed that  $\text{Cu}_2\text{SnS}_3$  and  $\text{Cu}_2\text{SnSe}_3$  exhibit better photo-response and superior photo-stability compared to binary nanomaterials.

Thus, overall this thesis presents the synthesis and characterization of novel tin complexes with various internally functionalized chalcogenolate ligands. The complexes have been explored as molecular precursors for the preparation of binary and ternary tin chalcogenides. The facile cleavage of C-E bond in these complexes serves them as versatile precursors for the preparation of tin chalcogenide nanostructures and deposition of thin films. Utilization of these precursors presents a robust synthetic route which demonstrates control over the composition, phase and band gap of the synthesized tin chalcogenide nanostructures through subtle variation in the precursor structure, reaction temperature,

growth duration and proper choice of high boiling solvent. PEC studies revealed that ternary nanostructures exhibit better photosensitivity compared to binary tin chalcogenides.

The knowledge from present thesis can be extended for large scale preparation of technologically important tin chalcogenide nanomaterials and thin films without involving toxic and sensitive chemicals.

### **Future Work**

The future work will focus on the large scale synthesis of tin chalcogenide nanostructures. Photovoltaic and thermoelectric properties of these nanostructures will be evaluated by constructing a prototype cell. Efforts will be made for the synthesis of single source molecular precursor for ternary materials like  $\text{Cu}_2\text{SnS}_3$ ,  $\text{Cu}_2\text{SnSe}_3$ ,  $\text{CuInSe}_2$ , etc.

The understanding from the present work will be used for the preparation of quaternary metal chalcogenide nanostructures including  $\text{Cu}_2\text{ZnSnS}_4$ ,  $\text{Cu}_2\text{ZnSnSe}_4$ ,  $\text{CuIn(Ga)Se}_2$  and their thin film deposition.

# References

1. A.S. Edelstein (ed), Nanomaterials: Synthesis, Properties and Applications, IOP publishing, Bristol, (1999).
2. J. Yacaman, L. Rendon, J. Arenas, M. C. S. Puche, Science, 273 (1996) 223.
3. M. Faraday, Philos. Trans. R. Soc., London, 147 (1857) 145.
4. R. Zsigmondy, Z. Phys. Chem., 56 (1906) 65.
5. R. Feynman, lecture entitled “There's Plenty of Room at the Bottom” given at American Physical Society meeting at Caltech on December 29, 1959.
6. M. H. Rashid and T. K. Mandal, J. Phys. Chem. C, 45 (2007) 16750.
7. J. Kim, C. Y. Wong and G. D. Scholes, Acc. Chem. Res., 42 (2009) 1037.
8. X. Peng, L. Manna, W. Yang, J. Wickham, E. Scher, A. Kadavanich, A. P. Alivisatos, Nature, 404 (2000) 59.
9. Y. Jun, J. Choi, J. Cheon, Angew. Chem. Int. Ed., 45 (2006) 3414.
10. C. Kittel, Introduction to solid state physics, John Wiley & sons, Inc., Singapore, 2002.
11. Holgate, Sharon Ann Understanding Solid State Physics, CRC Press, ISBN 1420012320, (2009), 177.
12. A. R. West, Solid State Chemistry and its Applications, 2014.
13. S. O. Kasap, Principles of electronic materials and devices, McGraw-Hill, 2006.
14. P. Kubelka, F. Munk-Aussig, Ein Beitrag zur Optik der Farban striche. Zeitschrift für Technische Physik, 12, (1931) 593.
15. M. R. Gao, J. Jiang, S. H. Yu, Small, 8 (2012) 13.
16. C. H. Lai, M. Y. Lu and L. J. Chen, J. Mater. Chem., 22 (2012) 19.
17. M. Yuan and D. B. Mitzi, Dalton Trans., (2009) 6065.
18. A. P. Alivisatos, Science, 271 (1996) 933.

19. S. Adachi, *Properties of Semiconductor Alloys: Group-IV, III-V and II-VI Semiconductors*, Wiley, (2009).
20. P. Y. Yu, M. Cardona, Springer, (1996).
21. X. Peng, J. Wickham, A. P. Alivisatos, *J. Am. Chem. Soc.*, 120 (1998) 5343.
22. X. Zhou, Q. Zhang, L. Gan, H. Li, J. Xiong, T. Zhai, *Adv. Sci.*, 3 (2016) 1600177.
23. P. D. Antunez, J. J. Buckley, R. L. Brutchey, *Nanoscale*, 3 (2011) 2399.
24. W. Zhang, R. Yu, H. J. Zhang, X. Dai, Z. Fang, *New J. Phys.*, 12 (2010) 065013.
25. X. Qiu, L. N. Austin, P. A. Muscarella, J. S. Dyck, C. Burda, *Angew. Chem. Int. Ed.*, 45 (2006) 5656.
26. P. Reiss, M. Carrière, C. Lincheneau, L. Vaure, S. Tamang, *Chem. Rev.*, 116 (2016) 10731.
27. P. Mir, M. Audiffred, T. Heine, *Chem. Soc. Rev.* 43 (2014) 6537.
28. S. C. Dhanabalan, J. S. Ponraj, Z. Guo, S. Li, Q. Bao, H. Zhang, *Adv. Sci.* 4 (2017) 1600305.
29. F. Wang, Z. Wang, L. Yin, R. Cheng, J. Wang, Y. Wen, T. A. Shifa, F. Wang, Y. Zhang, X. Zhana, J. He, *Chem. Soc. Rev.*, 47 (2018) 6296.
30. K. S. Novoselov, A. K. Geim, S. V. Morozov, D. Jiang, Y. Zhang, S. V. Dubonos, I. V. Grigorieva, A. A. Firsov, *Science*, 306 (2004) 666.
31. L. Gao, G. X. Ni, Y. Liu, B. Liu, A. H. Castro Neto, K. P. Loh, *Nature*, 505 (2014) 190.
32. W. Zhang, J. K. Huang, C. H. Chen, Y. H. Chang, Y. J. Cheng, L. J. Li, *Adv. Mater.*, 25 (2013) 3456.
33. R. Lv, J. A. Robinson, R. E. Schaak, D. Sun, Y. Sun, T. E. Mallouk, M. Terrones, *Acc. Chem. Res.* 48 (2015) 56.
34. D. Voiry, A. Mohite, M. Chhowalla, *Chem. Soc. Rev.* 44 (2015) 2702.

35. X. Duan, C. Wang, A. Pan, R. Yu, X. Duan, *Chem. Soc. Rev.* 44 (2015) 8859.
36. G. Xiao, Y. Wang, J. Ning, Y. Wei, B. Liu, W. W. Yu, G. Zoua, B. Zou, *RSC Advances*, 3 (2013) 8104.
37. D. Lembke, S. Bertolazzi, A. Kis, *Acc. Chem. Res.*, 48 (2015) 100.
38. Y. P. Venkata Subbaiah, K. J. Saji, A. Tiwari, *Adv. Funct. Mater.* 26 (2016) 2046.
39. Z. He, W. Xu, Y. Zhou, X. Wang, Y. Sheng, Y. Rong, S. Guo, J. Zhang, J. M. Smith, J. H. Warner, *ACS Nano*, 10 (2016) 2176.
40. S. J. Yun, S. H. Chae, H. Kim, J. C. Park, J. H. Park, G. H. Han, J. S. Lee, S. M. Kim, H. M. Oh, J. Seok, M. S. Jeong, K. K. Kim, Y. H. Lee, *ACS Nano*, 9 (2015) 5510.
41. S. Cui, H. Pu, S. A. Wells, Z. Wen, S. Mao, J. Chang, M. C. Hersam, J. Chen, *Nat. Commun.*, 6 (2015) 8632.
42. C. C. Mayorga-Martinez, Z. Sofer, M. Pumera, *Angew. Chem. Int. Ed.* 54 (2015) 14317.
43. S. Lei, F. Wen, L. Ge, S. Najmaei, A. George, Y. Gong, W. Gao, Z. Jin, B. Li, J. Lou, J. Kono, R. Vajtai, P. Ajayan, N. J. Halas, *Nano Lett.*, 15 (2015) 3048.
44. M. Lin, D. Wu, Y. Zhou, W. Huang, W. Jiang, W. Zheng, S. Zhao, C. Jin, Y. Guo, H. Peng, Z. Liu, *J. Am. Chem. Soc.*, 135 (2013) 13274.
45. S. R. Tamalampudi, Y. Y. Lu, U. R. Kumar, R. Sankar, C. D. Liao, B. K. Moorthy, C. H. Cheng, F. C. Chou, Y. T. Chen, *Nano Lett.*, 14 (2014) 2800.
46. Z. Wang, M. Safdar, M. Mirza, K. Xu, Q. Wang, Y. Huang, F. Wang, X. Zhan, J. He, *Nanoscale*, 7 (2015) 7252.
47. P. Hu, L. Wang, M. Yoon, J. Zhang, W. Feng, X. Wang, Z. Wen, J. C. Idrobo, Y. Miyamoto, D. B. Geohegan, K. Xiao, *Nano Lett.*, 13 (2013) 1649.
48. P. D. Matthews, P. D. McNaughten, D. J. Lewis, P. O'Brien, *Chem. Sci.*, 8 (2017) 4177.
49. J. Gao, A. F. Fidler, V. I. Klimov, *Nat. Commun.*, 6 (2015) 8185.



50. N. J. L. K. Davis, M. L. Böhm, M. Tabachnyk, F. W. R. Rivarola, T. C. Jellicoe, C. Ducati, B. Ehrler, N. C. Greenham, *Nat. Commun.*, 6 (2015) 8259.
51. R. Saran, R. J. Curry, *Nat. Photonics*, 10 (2016) 81.
52. P. Ramasamy , D. Kwak , D. H. Lim , H. S. Ra, J. S. Lee, *J. Mater. Chem. C*, 4 (2016) 479.
53. D. Parker, D. J. Singh, *Phys. Rev. B*, 82 (2010) 035204.
54. Y. Lee, S. H. Lo, C. Chen, H. Sun, D. Y. Chung, T. C. Chasapis, C. Uher, V. P. Dravid, M. G. Kanatzidis, *Nat. Commun.*, 5 (2014) 3640.
55. S. Hao, F. Shi, V. P. Dravid, M. G. Kanatzidis, C. Wolverton, *Chem. Mater.*, 28 (2016) 3218.
56. G. Ding, G. Gao, K. Yao, *Sci. Rep.*, 5 (2015) 9567.
57. L. Sharmer, M. S. Shackley and A. K. Harding, *J. Environ. Health*, 73 (2010) 8.
58. F. Bertolotti, D. N. Dirin, M. Ibanez, F. Krumeich, A. Cervellino, R. Frison, O. Voznyy, E. H. Sargent, M. V. Kovalenko, A. Guagliardi and N. Masciocchi, *Nat. Mater.*, 15 (2016) 987.
59. M. Ibanez, R. J. Korkosz, Z. Luo, P. Riba, D. Cadavid, S. Ortega, A. Cabot and M. G. Kanatzidis, *J. Am. Chem. Soc.*, 137 (2015) 4046.
60. Y. Huang, K. Xu, Z. Wang, T.A. Shifa, Q. Wang, F. Wang, C. Jiang, J. He, *Nanoscale* 7 (2015) 17375.
61. E. P. Mukhokosi, S. B. Krupanidhi, K. K. Nanda, *Sci. Rep.* 7 (2017) 15215.
62. R. P. Ryan and C. E. Terry, *Toxicology Desk Reference: The Toxic Exposure and Medical Monitoring Index*, ed. Taylor and Francis, Philadelphia, 1999.
63. W. R. Mateker and M. D. McGehee, *Adv. Mater.*, 29 (2017) 1603940.
64. M. I. Asghar, J. Zhang, H. Wang, P. D. Lund, *Renew Sust Energy Rev.*, 77 (2017) 131.

65. M. I. H. Ansari, A. Qurashi, M. K. Nazeeruddin, J. Photochem. Photobio. C: Photochem. Rev., 35 (2018) 1.
66. M. K. Assadi, S. Bakhoda, R. Saidurb, H. Hanaei, Renew. Sust. Energy Rev., 81 (2018) 2812.
67. V. R. M. Reddy, S. Gedi, B. Pejjai, C. Park, J. of Mater. Sci.: Mater. Electronics, 27 (2016) 5491.
68. X. Yu, J. Zhu, Y. Zhang, J. Weng, L. Hua, S. Dai, Chem. Commun., 48 (2012) 3324.
69. S. R. Popuri, M. Pollet, R. Decourt, F. D. Morrison, N. S. Bennett, J. W. G. Bos, J. Mater Chem C, 4 (2016) 1685.
70. Z. G. Chena, X. Shib, L. D. Zhaoc, J. Zou, Prog. Mater. Sci., 97 (2018) 283.
71. M. Jin, Z. Chen, X. Tan, H. Shao, G. Liu, H. Hu, J. Xu, B. Yu, H. Shen, J. Y. Xu, H. Jiang, Y. Pei, J. Jiang, DOI: 10.1021/acsenergylett.7b01259.
72. C. Vatsa, Ph. D. thesis, University of Mumbai, 1990.
73. A. G. Davies, M. Gielen, K. H. Pannell, E. R. T. Teikink, Tin Chemistry; Fundamentals, Frontiers and Applications; John Wiley and Sons, Ltd, Publication, 2008.
74. H. Zhong, G. Yang, H. Song, Q. Liao, H. Cui, P. Shen, C. X. Wang, J. Phys. Chem. C, 116, (2012) 9319.
75. I. Lefebvre, M. A. Szymanski, J. Oliver-Fourcade and J. C. Jumas, Phys. Rev. B: Condens. Matter Mater. Phys., 58 (1998) 1896.
76. N. S. Dantas, A. F. da Silva and C. Persson, Opt. Mater., 30 (2008) 1451.
77. A. Walsh and G. W. Watson, Phys. Rev. B: Condens. Matter Mater. Phys., 70 (2004) 235114.
78. B. Thangaraju, P. Kaliannan, J. Phys. D: Appl. Phys., 33 (2000) 1054.

79. T. Jiang and G. A. Ozin, *J. Mater. Chem.*, 8 (1998) 1099.
80. T. S. Pan, D. De, J. Manongdo, A. M. Guloy, V. G. Hadjiev, Y. Lin and H. B. Peng, *Appl. Phys. Lett.*, 103 (2013) 093108.
81. K. Ramasamy, V. L. Kuznetsov, K. Gopal, M. A. Malik, J. Raftery, P. P. Edwards, P.O'Brien, *Chem. Mater.*, 25 (2013) 266.
82. A. Okazaki, I. Ueda, *J. Phys. Soc. Jpn*, 11 (1956) 470.
83. N. K. Abrikosov, *Monographs in Semiconductor Physics*, 1969.
84. L.-D. Zhao, S.-H. Lo, Y. Zhang, H. Sun, G. Tan, C. Uher, C. Wolverton, V. P. Dravid, M. G. Kanatzidis, *Nature*, 508 (2014) 373.
85. H. Wiedemeier, H. Georg and G. V. Schnering, *Z. Kristallogr.*, 148 (1978) 295.
86. T. Chattopadhyay, J. Pannetier and H. G. V. Schnering, *J. Phys. Chem. Solid.*, 47 (1986) 879.
87. M. J. Peters and L. E. Mcneil, *Phys. Rev. B: Condens. Matter Mater. Phys.*, 41 (1990) 5893.
88. K. Adouby, C. Perez-Vicente, J. C. Jumas, R. Fourcade, A. A. Toure., *Z. Kristallogr.*, 213 (1998) 343.
89. A. A. Volykhov, V. I. Shtanov and L. V. Yashina, *Inorg. Mater.*, 44 (2008) 345.
90. M. Sist, J. Zhang and B. Brummerstedt Iversen, *Acta Cryst.*, B72 (2016) 310.
91. A. N. Mariano, K. L. Chopra, *Appl. Phys. Lett.*, 10 (1967) 282.
92. S. Sassi, C. Candolfi, J. B. Vaney, V. Ohorodniichuk, P. Masschelein, A. Dauscher, B. Lenoir, *Appl. Phys. Lett.*, 104 (2014) 212105.
93. N. K. Reddy, M. Devika, E. S. R. Gopal, *Crit. Rev. Solid State Mater. Sci.*, 40 (2015) 359.
94. W. Shi, M. Gao, J. Wei, J. Gao, C. Fan, E. Ashalley, H. Li, Z. Wang, *Adv. Sci.*, 5 (2018) 1700602.

95. M. Devika, K. T. Ramakrishna Reddy, N. Koteeswara Reddy, K. Ramesh, R. Ganesan, E. S. R. Gopal and K. R. Gunasekhar, *J. Appl. Phys.*, 100 (2006) 023518.
96. S. S. Kabalkina, N. R. Serebryanaya and L. F. Vereshchagin, *Sov. Phys. Solid State*, 10 (1968) 574.
97. M. B. Prince, *J. Appl. Phys.*, 26 (1955) 534.
98. J. J. Loferski, *J. Appl. Phys.* 27 (1956) 777.
99. P. Sinsermsuksakul, L. Sun, S. W. Lee, H. H. Park, S. B. Kim, C. Yang, R. G. Gordon, *Adv. Energy Mater.*, 4 (2014) 1400496.
100. J. Kim, J. Kim, S. Yoon, J.-Y. Kang, C.-W. Jeon, W. Jo, *J. Phys. Chem. C*, 122 (2018) 3523.
101. Y. Huang, E. Sutter, J. T. Sadowski, M. Cotlet, O. L.A. Monti, D. A. Racke, M. R. Neupane, D. Wickramaratne, R. K. Lake, B. A. Parkinson, P. Sutter, *ACS Nano*, 8 (2014) 10743.
102. H. Chang, E. In, K. J. Kong, J. O. Lee, Y. Choi, B. H. Ryu, *J. Phys. Chem. B*, 109 (2004) 30.
103. I. Lefebvre, J. Olivier, J. C. Jumas, P. Lavela, *Phys. Rev. B*, 61 (2000) 3110.
104. M.-J. Lee, J.-H. Ahn, J. H. Sung, H. Heo, S. G. Jeon, W. Lee, J. Y. Song, K.-H. Hong, B Choi, S.-H. Lee, M.-H. Jo, *Nat. Commun.*, 7 (2016) 12011.
105. E. Mooser, W. B. Pearson, *Phys. Rev.* 101 (1956) 492.
106. X. Zhou, L. Gan, W. Tian, Q. Zhang, S. Jin, H. Li, Y. Bando, D. Golberg, T. Zhai, *Adv. Mater.*, 27 (2015) 8035.
107. B. L. Evans, R. A. Hazelwood, *J. Phys. D. Appl. Phys.*, 2 (2002) 1507.
108. J. M. Gonzalez, I. I. Oleynik, *Phys. Rev. B* 94 (2016) 125443.
109. Y. Lei, S. Song, W. Fan, Y. Xing, H. Zhang, *J Phys Chem C*, 113 (2009) 1280.

110. J. M. Ma, D. N. Lei, X. C. Duan, Q. H. Li, T. H. Wang, A. M. Cao, RSC Adv,2 (2012) 3615.
111. A.C. Lokhande, K.V. Gurav, E. Jo, C.D. Lokhande, J. H. Kim, J. Alloy Compd, 656 (2016) 295.
112. G. Babu, Y. Kumar, Y. Reddy, V. Raja, Mater Chem Phys, 96 (2006) 442.
113. L. Wang, P. Hu, Y. Long, Z. Liu, X. He, J. Mater. Chem. A, 5 (2017) 22855.
114. D. Aldakov, A. Lefrançois, P. Reiss, J. Mater. Chem. C, 1 (2013) 3756.
115. Y. Park, H. Jin, J. Park and S. Kim Cryst Eng Comm, 16 (2014) 8642.
116. L. Wu, S. Chen, F. Fan, T. Zhuang, C. Dai, S. Yu, J. Am. Chem. Soc. 138 (2016) 5576.
117. Y. T. Zhai, S. Chen, J. H. Yang, H. J. Xiang, X. G. Gong, A. Walsh, J. Kang, S. H. Wei, Phys Rev B, 84 (2011) 075213.
118. C. Wang, S. Chen, J. Yang, L. Lang, H. Xiang, X. Gong, A. Walsh, S. Wei, Chem Mater 26 (2014) 3411.
119. J.Wang, K. Ryan, Cryst Eng Comm, 18 (2016) 3161.
120. U. V. Ghorpade, M. P. Suryawanshi, S. W. Shin, I. Kim, S. K. Ahn, J. H. Yun, C. Jeong, S. S. Kolekar, J. H. Kim; Chem. Mater. 28 (2016) 3308.
121. M. Norako, M. Greaney, R. Brutchey, J Am Chem Soc 134 (2012) 23.
122. W. Sun, Y. Ye, Y. You and J. Xu; J. Mater. Chem. A, 6 (2018) 8221.
123. M. Ibanez, D. Cadavid, U. A. Tamburini, R. Zamani, S. Gorsse, W. Li, A. Lopez, J. Morante, J. Arbiol, A. Cabot, J. Mater Chem A, 1 (2013) 1421.
124. M. Bouaziz, M. Amlouk and S. Belgacem, Thin Solid Films, 517 (2009) 2527.
125. M. P. Suryawanshi, U. V. Ghorpade, S. W. Shin, S. A. Pawar, I. Y. Kim, C. W. Hong, M. Wu, P. S. Patil, A. V. Moholkar, and J. H. Kim ACS Appl. Mater. Interfaces 8 (2016) 11603.

126. M. Ahmadi, S. S. Pramana, S. K. Batabyal, C. Boothroyd, S. G. Mhaisalkar, Y. M. Lam, *Inorg. Chem.*, 52 (2013) 1722.
127. H. C. Tao, S. C. Zhu, X. L. Yang, L. L. Zhang, S. B. Ni, *Journal of Electroanalytical Chemistry* 760 (2016) 127.
128. S. Dias, K. L. Kumawat, S. Biswas and S. B. Krupanidhi, *RSC Adv.*, 7 (2017) 23301.
129. Y. Shen, C. Li, R. Huang, R. Tian, Y. Ye, L. Pan, K. Koumoto, R. Zhang, C. Wan and Y. Wang, *Sci. Rep.* 6 (2016) 32501.
130. Y. Li, G. Liu, J. Li, K. Chen, L. Li, Y. Han, M. Zhou, M. Xia, X. Jiang, Z. Lin, *New J. Chem.*, 40 (2016) 5394.
131. C. Wang, H. Tian, J. Jiang, T. Zhou, Q. Zeng, X. He, P. Huang, and Y. Yao, *ACS Appl. Mater. Interfaces* 9 (2017) 26038.
132. A. C. Lokhande, A. A. Yadav, J. Y. Lee, M. He, S. J. Patil, V. C. Lokhande, C. D. Lokhande, J. H. Kim, *J. Alloys Compd.*, 709 (2017) 92.
133. M. Onoda, X. Chen, A. Sato, H. Wada, *Mater Res Bull*, 35 (2000) 1563.
134. M. A. Malik, M. Afzaal, P. O'Brien, *Chem. Rev.*, 110 (2010) 4417.
135. D. S. Koktysh, J. R. McBride, S. J. Rosenthal, *Nanoscale Res Lett*, 2 (2007) 144.
136. S. R. Bahr, P. Boudjouk and G. J. McCarthy, *Chem. Mater.*, 4 (1992) 383.
137. P. Boudjouk, D. J. Seidler, S. R. Bahr and G. J. McCarthy, *Chem. Mater.*, 6 (1994) 2108.
138. P. Boudjouk, D. J. Seidler, D. Grier, G. McCarthy, *J. Chem. Mater.*, 8 (1996) 1189.
139. D. C. Menezes, G. M. de Lima, A. O. Porto, C. L. Donnici, J. D. Ardisson, A. C. Doriguetto, J. Ellena, *Polyhderon*, 23 (2004) 2103.
140. I. P. Parkin, L. S. Price, T. G. Hibbert, K. C. Molloy, *J. Mater. Chem.*, 11 (2001) 1486.
141. G. Barone, T. G. Hibbert, M. F. Mahon, K. C. Molloy, L. S. Price, I. P. Parkin, A. M. E. Hardy, M. N. Field, *J. Mater. Chem.*, 11 (2001) 464.

142. A. T. Kana, T. G. Hibbert, M. F. Mahon, K. C. Molloy, I. P. Parkin, L. S. Price, *Polyhedron*, 20 (2001) 2989.
143. B. P. Bade, S. S. Garje, Y. S. Niwate, M. Afzaal, P. O'Brien, *Chem. Vap. Deposition*, 14 (2008) 292.
144. P. Kevin, S. N. Malik, M. A. Malik, P. O'Brien, *Chem. Commun.*, 50 (2014) 14328.
145. M. D. Khan, M. Aamir, M. Sohail, M. Sher, N. Baig, J. Akhtar, M. A. Malik, N. Revaprasadu, *Dalton Trans.*, 47 (2018) 5465.
146. M. D. Khan, M. Aamir, G. Murtaza, M. A. Malik, N. Revaprasadu, *Dalton Trans.*, 47 (2018) 10025.
147. I. Y. Ahmet, J. R. Thompson, A. L. Johnson, *Eur. J. Inorg. Chem.* (2018) 1670.
148. Y. Cheng, T. J. Emge and J. G. Brennan, *Inorg. Chem.*, 35 (1996) 342.
149. R. K. Sharma, G. Kedarnath, A. Wadawale, C. A. Betty, B. Vishwanadh and V. K. Jain, *Dalton Trans.*, 41 (2012) 12129.
150. C. H. Groot, C. Gurnani, A. L. Hector, R. Huang, M. Jura, W. Levason, G. Reid, *Chem. Mater.*, 24 (2012) 4442.
151. A. I. Vogel, *Textbook of Practical Organic Chemistry*, 4<sup>th</sup> ED., English Language Book Society, Longmann, London (1987).
152. T. Higashi, *ABSCOR-Empirical Absorption Correction based on Fourier Series Approximation*, Rigaku Corporation, 3-9-12 Matsubara, Akishima, Japan (1995).
153. G. M. Sheldrick, *SHELX 97-Program for Crystal Structure Analysis*, Göttingen, Germany (1997); Sheldrick, G. M. *Acta. Crystallogr. A*, 64 (2008) 112.
154. C. K. Johnson, *ORTEP II*, Report ORNL-5136, Oak Ridge National Laboratory, Oak Ridge TN (1976).
155. B. D. Cullity, *Elements of X-ray diffraction*, Addison – Wesley Inc., London (1978).
156. [https://en.wikipedia.org/wiki/Scanning\\_electron\\_microscope](https://en.wikipedia.org/wiki/Scanning_electron_microscope).

157. [https://en.wikipedia.org/wiki/Transmission\\_electron\\_microscopy](https://en.wikipedia.org/wiki/Transmission_electron_microscopy).
158. [https://en.wikipedia.org/wiki/Selected\\_area\\_diffraction](https://en.wikipedia.org/wiki/Selected_area_diffraction).
159. A. J. Bard, J. Phys. Chem., 86 (1982), 172.
160. D. Wei, G. Amaratunga, Int. J. Electrochem. Sci., 2 (2007) 897.
161. B. Philips-Invernizzi, D. Dupont, C. Caze, Opt. Eng., 40 (2001) 1082.
162. Q. Tan, L.-D. Zhao, J.-F. Li, C.-F. Wu, T.-R. Wei, Z.-B. Xing, M. G. Kanatzidis, J. Mater. Chem. A, 2 (2014) 17302.
163. P. Pramanik, P. K. Basu, S. Biswas, Thin Solid Films 150 (1987) 269.
164. T. Minemura, K. Miyauchi, K. Noguchi, K. Ohtsuka, H. Nakanishi, M. Sugiyama, Phys. Status Solidi C, 6 (2009) 1221.
165. E. C. Greyson, J. E. Barton, T. W. Odom, Small, 2 (2006) 368.
166. S. G. Hickey, C. Waurisch, B. Rellinghaus and A. Eychmuller, J. Am. Chem. Soc., 130 (2008) 14978.
167. Z. Deng, D. Han, Y. Liu, Nanoscale, 3 (2011) 4346.
168. J. Ning, K. Men, G. Xiao, L. Wang, Q. Dai, B. Zou, B. Liu, G. Zou, Nanoscale, 2 (2010) 1699.
169. H. Zhang, B. -R. Hyun, F. W. Wise, R. D. Robinson, Nano Lett., 12 (2012) 5856.
170. Deng, D. Cao, J. He, S. Lin, S. M. Lindsay, Y. Liu, ACS Nano, 6 (2012) 6197.
171. S. Dey, V.K. Jain, Platinum Met. Rev. 48 (2004) 16.
172. M. Bochmann, Chem. Vap. Deposition 2 (1996) 85.
173. G. Kedarnath, S. Dey, V.K. Jain, G.K. Dey, J. Nanosci. Nanotechnol. 6 (2006) 1031.
174. R. K. Sharma, G. Kedarnath, A. Wadawale, V. K. Jain, B. Vishwanadh, Inorganica Chimica Acta 365 (2011) 333.
175. R. K. Sharma, G. Kedarnath, V. K. Jain, A. Wadawale, C. G. S. Pillai, M. Nalliath, B. Vishwanadh, Dalton Trans., 40 (2011) 9194.



176. S. C. Nigam, G. S. Saharia and H. R. Sharma, *J. Indian Chem. Soc.*, 60 (1983) 583.
177. C. Vatsa, Ph. D. Thesis, University of Mumbai, 1990.
178. T. P. Lockhart and F. Davidson, *Organometallics*, 6 (1987) 2471.
179. T. P. Lockhart, W. T. Manders and E. M. Holt, *J. Am. Chem. Soc.*, 108 (1986) 6611.
180. R. Schmiedgen, F. Huber, H. Preut, G. Ruisi and R. Barbieri, *Appl. Organomet. Chem.*, 8 (1994) 397.
181. M. V. Castaño, A. Macías, A. Castiñeiras, A. S. González, E. G. Martínez, J. S. Casas, J. Sordo, W. Hiller and E. E. Castellano, *J. Chem. Soc., Dalton Trans.*, 1001 (1990).
182. R. Schmiedgen, F. Huber and H. Preut, *Acta Cryst. C*, 49 (1993) 1735.
183. M. Bouâlam, J. Meunier-Piret, M. Biesemans, R. Willem and M. Gielen, *Inorg. Chim. Acta* 198 (1992) 249.
184. G. Domazetis, B. D. James, M. F. Mackay and R. J. Magee, *J. Inorg. Nucl. Chem.*, 41 (1979) 1555.
185. O. Chen, Y. Yang, T. Wang, H. Wu, C. Niu, J. Yang and Y. C. Cao, *J. Am. Chem. Soc.*, 133 (2011) 17504.
186. L. Ding, S. He, S. Miao, M. R. Jorgensen, S. Leubner, C. Yan, S. G. Hickey, A. Eychmüller, J. Xu and O. G. Schmidt, *Sci. Rep.*, 4 (2014) 4647.
187. Y. Kim, K. Woo, I. Kim, Y. S. Cho, S. Jeong and J. Moon, *Nanoscale*, 5 (2013) 10183.
188. M. X. Wang, G. H. Yue, Y. D. Lin, X. Wen, D. L. Peng and Z. R. Geng, *Nano-Micro Lett.*, 5 (2013) 1.
189. Z. Zhang, H. Zhao, J. Fang, X. Chang, Z. Li, L. Zhao, *ACS Appl. Mater. Interfaces*, 10 (2018) 28533.
190. J. H. Han, S. Lee, J. Cheon, *Chem. Soc. Rev.*, 42 (2013) 2581.
191. J. Choi, H. Zhang, J. H. Choi, *ACS Nano*, 10 (2016) 1671.
192. C. Han, Q. Sun, Z. Li, S. X. Dou, *Adv. Energy Mater.*, 6 (2016) 1600498.

193. H. Zhang, D. V. Talapin, *Angew. Chem.*, 53 (2014) 9126.
194. C. Chang, M. Wu, D. He, Y. Pei, C.-Feng Wu, X. Wu, H. Yu, F. Zhu, K. Wang, Y. Chen, L. Huang, J. F. Li, J. He, L. D. Zhao, *Science*, (2018) 778.
195. S. Liu, X. Y. Guo, M. R. Li, W. H. Zhang, X. Y. Liu, C Li, *Angew. Chem.*, 50 (2011) 12050.
196. F. K. Butt, M. Mirza, C. Cao, F. Idrees, M. Tahir, M. Safdar, Z. Ali, M. Tanveera, I. Aslama, *Cryst Eng Comm.*, 16 (2014) 3470.
197. Z. Fang, S. Hao, L. Long, H. Fang, T. Qiang, Y. Song, *Cryst Eng Comm.*, 16 (2014) 2404.
198. S. Wen, H. Pan, Y. Zheng, *J. Mater. Chem.*, C 3 (2015) 3714.
199. C. Wang, Y. Li, G. Zhang, J. Zhuang, G. Shen, *Inorg. Chem.*, 39 (2000) 4237.
200. D. D. Vaughn, S.-I. In, R. E. Schaak, *ACS Nano*, 5 (2011) 8852.
201. L. D. Nyamen, V. R. Pullabhotla, A. A. Nejo, P. T. Ndifon, J. H. Warner, N. Revaprasadu, *Dalton Trans.*, 41 (2012) 8297.
202. Y.-F. Lin, H.-W. Chang, S.-Y. Lu, C. Liu, *J. Phys. Chem. C*, 111 (2007) 18538.
203. A. Panneerselvam, M. A. Malik, M. Afzaal, P. O'Brien, M. Helliwell, *J. Am. Chem. Soc.*, 130 (2008) 2420.
204. B. Philips-Invernizzi, D. Dupont, C. Caze, *Opt. Eng.*, 40 (2001) 1082.
205. T. A. K. Al-Allaf, *J. Organomet. Chem.*, 306 (1986) 337.
206. P. J. Smith and A. P. Tupciauskas, *Annual Reports on NMR on Spectroscopy*, 8 (1978) 291.
207. R. Hani and R. A. Geanangel, *Coord. Chem. Res.*, 44 (1982) 229-246.
208. S. Singh, S. Bhattacharya and H. Nöth, *Eur. J. Inorg. Chem.*, (2010) 5691.
209. C. Ma, J. Zhang, G. Tian, R. Zhang, *J. Organomet. Chem.*, 690 (2005) 519.

210. A. S. Pedrares, M. L. D. Carril, J. Romero, J. A. G. Vázquez, A. Sousa, *Inorg. Chim. Acta*, 363 (2010) 1212.
211. T. G. Back, P. W. Coddling, *Can. J. Chem.*, 61 (1983) 2749.
212. A. Eichhöfer, J. J. Jiang, H. Sommer, F. Weigend, O. Fuhr, D. Fenske, C. Y. Su, G. Buth, *Eur. J. Inorg. Chem.*, 2010, 410.
213. V. B. Mokal, V. K. Jain, E. R. T. Tiekink, *J. Organomet. Chem.*, 471 (1994) 53.
214. A. Bondi, *J. Phys. Chem.*, 18 (1964) 441.
215. S. D. Reid, A. L. Hector, W. Levason, G. Reid, B. J. Waller, M. Webster, *Dalton Trans.*, (2007) 4769.
216. P. Kevin, D. J. Lewis, J. Raftery, M. A. Malik, P. O'Brien, *J. Cryst. Growth*, 415 (2015) 93.
217. W. Bu, Z. Chen, F. Chen, J. Shi, *J. Phys. Chem.*, C113 (2009) 12176.
218. G. Dmingo, R. S. Itoga, C. R. Kannewurf, *Phys. Rev.*, 143 (1966) 536.
219. B. Pejova, I. Grozdanov, *Thin Solid Films*, 515 (2007) 5203.
220. M. A. Franzman, C. W. Schlenker, M. E. Thompson, R. L. Brutchey, *J. Am. Chem. Soc.*, 132 (2010) 4060.
221. R. Sachdeva, M. Sharma, A. Devi, U. Parihar, N. Kumar, N. Padha, C. J. Panchal, *J. Nano-electron. Phys.*, 3 (2011) 507.
222. M. M. El-Nahass, *J. Mater. Science*, 27 (1992) 6597.
223. V. P. Bhatt, K. Gireesan, C. F. Desai, *Cryst. Res. Technol.*, 25 (1990) 209.
224. X. Liu, Y. Feng, H. Cui, F. Liu, X. Hao, G. Conibeer, D. B. Mitzi, M. Green, *Prog. Photovolt: Res. Appl.*, 24 (2016) 879.
225. J. Ramanujam, U. P. Singh, *Energy Environ. Sci.*, 10 (2017) 1306.
226. C. Coughlan, M. Ibanez, O. Dobrozhan, A. Singh, A. Cabot, K. Ryan, *Chem. Rev.*, 117 (2017) 5865.

227. S. Dietzel, K. Jurkschat, A. Tzschach, A. Zschunke, Z. Anorg. Allg. Chem., 537 (1986) 163.
228. H. C. Tao, S. C. Zhu, X. L. Yang, L. L. Zhang, S. B. Ni, J. Electroanal. Chem., 760 (2016) 127.
229. A. C. Lokhande, A. Shelke, P. T. Babar, J. Kim, D. J. Lee, I. C. Kim, C. D. Lokhande, J. H. Kim RSC Adv., 7 (2017) 33737.
230. W. Li, X. Han, Y. Zhao, L. Liu, J. Wang, S. Yang, T. Tanaka, Mater. Lett., 125 (2014) 167.
231. M. Baghbanzadeh, L. Carbone, P.D. Cozzoli, C.O. Kappe, Angew. Chem. Int., 50 (2011) 2.
232. Q. Chen, D. Ma, Int. J. Photoenergy, (2013) 5, 593420.
233. Y. Liu, M. Liu, D. Yin, W. Wei, P. N. Prasad, M. T. Swihart Chem. Mater., 29 (2017) 3555.
234. Q. Liu, Z. Zhao, Y. Lin, P. Guo, S. Li, D. Pan, X. Ji, Chem. Commun., 47 (2011) 964.
235. X. Liu, X. Wang, M. T. Swihart Chem. Mater., 27(2015) 1342.
236. H. Chen, S.-M. Yu, D.-W. Shin, J.-B. Yoo, Nanoscale Res. Lett., 5 (2010) 217.
237. G. W. H. Cheeseman, J. Chem. Soc., 0 (1960) 242.
238. V. B. Mokal, V. K. Jain, J. Organomet. Chem., 441 (1992) 215.
239. J. Holecek, M. Nadvornik, K. Handlir, A. Lycka, J. Organomet. Chem., 315 (1986) 299.
240. P. Karagiannidis, P. Aslanidis, D. P. Kessissoglou, B. Krebs, M. Dartmann, Inorg. Chimica Acta, 156 (1989) 47.
241. S. C. Davies, M. C. Durrant, D. L. Hughes, K. Leidenberger, C. Stapper, R. L. Richards, J. Chem. Soc., Dalton Trans. (1997) 2409.
242. P. W. Guan, Z. K. Liu, Phys. Chem. Chem. Phys., 20 (2018) 256.

243. D. M. Berg, R. Djemour, L. G. Tay, S. Siebentritt, P. J. Dale, X. Fontane, V. I. Roca, A. P. Rodriguez, *App. Phys. Lett.*, 100 (2012) 192103.
244. T.S. Reddy, R. Amiruddin, M.C.S. Kumar; *Sol. Energy Mater Sol. Cells*, 143 (2015) 128.
245. G. Marcano, C. Rincón, S. A. López, G. Sánchez Pérez, J. L. Herrera-Pérez, J. G. M.-Alvarez, P. Rodríguez, *Solid State Commun.*, 151 (2011) 84.
246. J. J. Scragg, P. J. Dale, D. Colombara, L. M. Peter, *Chem Phys Chem*, 13 (2012) 3035.
247. J. F. Moulder, W. F. Stickle, P. E. Sobol, K. D. Bomben. “Handbook of X-ray Photoelectron Spectroscopy”, Minnesota: Physical Electronics (1995) 86.
248. Z. H. Ge, J. R. Salvador, G. S. Nolas, *Inorg. Chem.*, 53 (2014) 4445.
249. S. Livraghi, M. Chiesa, M. C. Paganini, E. Giamello, *J. Phys. Chem. C*, 115 (2011) 25413.
250. Y. Huang, H. Xiao, S. Chen, C. Wang, *Cer Inter.*, 35 (2009) 905.
251. A. Sagade, R. Sharma. *Sensors Actuators B-Chem.*, 133 (2008) 135.
252. M.E. Norako, M.J. Greaney, R. L. Brutchey, *J. Am. Chem. Soc.*, 134 (2012) 23.
253. G. S. Babu, Y.B. K. Kumar, Y. B. K. Reddy and V. S. Raja, *Mater. Chem. Phys.*, 96 (2006) 442.
254. D. Tiwari, T. K. Chaudhuri, T. Shripathi, U. Deshpande, R. Rawat, *Sol. Energy Mater Sol. Cells*, 113 (2013) 165.
255. C. Lan, C. Li, Y. Yin, H. Guo, S. Wang, *J. Mater. Chem. C*, 3 (2015) 8074.